ABSTRACT

Title of Document: QUANTATITIVE STUDY OF WATER DYNAMICS IN BIOMIMETIC MODELS AND LIVING TISSUE BY NMR AND MRI: PERSPECTIVES ON DIRECT DETECTION NEURONAL ACTIVITY

Ruiliang Bai, Doctor of Philosophy, 2015

Directed By: Professor and Chair, Robert M. Briber
Department of Materials Science and Engineering
Principle Investigator, Peter J. Basser
National Institutes of Health

Detection of neuronal activity noninvasively and *in vivo* is a *desideratum* in medicine and in neuroscience. Unfortunately, the widely used method of functional magnetic resonance imaging (fMRI) only indirectly assesses neuronal activity via its hemodynamic response; limiting its temporal and spatial accuracy. Recently, several new fMRI methods have been proposed to measure neuronal activity claiming to be more direct and accurate. However, these approaches have proved difficult to reproduce and are not widely applied mainly because of a dearth of "ground truth" experiments that convincingly establish the correlation between the magnetic resonance (MR) signals and the underlying neuronal activity. In addition, limited knowledge of water dynamics in living tissue restricts our understanding of the underlying biophysical sources of these candidate fMRI signals.

To address the first problem, we developed a novel test system to assess and validate fMRI methods, in which real-time fluorescent intracellular calcium images and MR recording were simultaneously acquired on organotypic rat-cortex cultures without hemodynamic confounds. This experimental design enables direct correlation of the candidate functional MR signals with optical indicia of the underlying neuronal activity. Within this test bed, MR signals with contrasts from water relaxation times, diffusion, and proton density were tested. Diffusion MR was the only one shown to be sensitive to the pathological condition of hyperexcitability, e.g., such as those seen in epilepsy. However, these MR signals do not appear to be sensitive or specific enough to detect and follow normal neuronal activity.

Efforts were made toward improving our understanding of the water dynamics in living tissue. First, water diffusivities and relaxation times in a biomimetic model were measured and quantitatively studied using different biophysical-based mathematical models. Second, we developed and applied a rapid 2D diffusion/relaxation spectral MR method, to better characterize the heterogeneous nature of tissue water. While the present study is still far from providing a complete picture of water dynamics in living tissues, it provides novel tools for advancing our understanding of the possibilities and limits of detecting neuronal activity via MR in the future, as well as providing a reproducible and reliable way to assess and validate fMRI methods.

QUANTATITIVE STUDY OF WATER DYNAMICS IN BIOMIMETIC MODELS AND LIVING TISSUE BY NMR AND MRI: PERSPECTIVES ON DIRECT DETECTION OF NEURONAL ACTIVITY

By

Ruiliang Bai

Dissertation submitted to the Faculty of the Graduate School of the
University of Maryland, College Park, in partial fulfillment
of the requirements for the degree of
Doctor of Philosophy
2015

Advisory Committee:
Professor Robert M. Briber, Chair
Dr. Peter J. Basser
Dr. Ferenc Horkay
Professor David Fushman
Professor Marco Colombini
Professor Srinivasa R. Raghavan

Dedication

The author dedicates this dissertation to his parents

Shengkuan Bai and Aixian Liu

for their unconditional love and support

Acknowledgements

I am grateful to my advisors, teachers, colleagues, family, and friends, who gave me immeasurable support and help in the many years I have spent working on my Ph.D. Without them, I cannot image how I could have succeeded in completing my dissertation.

I have always felt fortunate to have met and worked with my two advisors, Professor Robert M. Briber and Dr. Peter J. Basser, who together made this thesis happen by training me to develop my own scientific interests and helping me learn how to function in the academic world. There are so many things that I would like to thank Professor Briber for: leading me from background in physics to the wonderful world of biophysics, providing me with countless suggestions and endless help, and encouraging me to find my own interests and become an independent researcher. I admire and hope to emulate one day his broad knowledge in a variety of disciplines.

I am also deeply grateful to Dr. Basser for all his support in both academic and nonacademic spheres. I still remember our first conversation in the summer of 2011, when I had just completed my three research rotations and was still confused about what to do for my thesis. His academic insights into the fields of biomedical imaging and biophysics immediately attracted my interest and helped me make decisions about my dissertation and my academic career. Over the last four years, he has given me the freedom to explore different projects, inspired me to find and solve problems, and helped me find courage when I was facing difficulties and doubts about my own abilities.

I would also like to thank Dr. Ferenc Horkay. With him, I completed my first project and wrote my first published paper. I appreciate his patience in helping me—with my very limited background in chemistry—to perform polymer and gel experiments and thereby giving me the opportunity to learn this field. In that first project, I learned a lot from him, including how to design experiments, explain findings in a publication and value scientific rigor.

Many thanks to my colleagues at NIH (Beth, Alexandru, Miki, Evren, Okan, Dan, Jian, and Yuan) for the many interesting conversations about science and other topics and for their generous help whenever I encountered difficulties. I would also like to thank Professors Peter Kofinas and Isabel Lloyd and my fellow students in Professor Briber's group (Xin, Mert, Adam, and Omar). I am still profiting from many of their useful suggestions and comments now.

I am also grateful to my collaborators, Dr. Dietmar Plenz and his group (Craig, Andreas, and Tim) in NIMH, who helped me set up and test the fluorescence imaging system, kept providing us with high-quality organotypic cultures, and expanded my knowledge in neuroscience. I also acknowledge our collaborative activities with Professor Wojciech Czaja and Dr. Alex Cloninger in the Department of Mathematics at the University of Maryland.

I am also grateful to the faculty members and staff in our biophysics program. Special thanks to Professor David Fushman for serving as an advisor on my thesis committee, particularly for many interesting discussions on NMR theories and techniques, and to Professor Garegin Papoian for guiding me in one of my research rotations. I am also grateful to our previous and current program coordinators (Caricia

and Star) for helping me comply with many departmental requirements and reminding me about all the important academic deadlines.

Last, but not least, I thank my parents (Shengkuan Bai and Aixian Liu), my two sisters (Jing Bai and Jinglan Bai) and my brother-in-law (Weizhu Wang) for their concern, encouragement, and emotional support. You cannot imagine how hard it is for two farmers with very low incomes in my hometown to send their three children away from the poor village and to get the best education, but my parents did it. They did their best to give me the no better environments they can offer to grow up and passed their diligent and honest personality to me. It's their unconditional love and support that keep me moving forward and never stopped pursuing my dreams.

Table of Contents

List of Tables

List of Figures

Chapter 1: Emergence of new functional magnetic resonance imaging (fMRI) methods in the study of neuronal activity

This chapter provides a brief review of the pros and cons of the currently available noninvasive functional neuroimaging methods for the study of neuronal activity and introduces the motivation for this thesis project—to promote the use of magnetic resonance imaging (MRI) techniques for a more direct and accurate detection of neuronal activity. Some information on the physical background of MRI and its relation to water dynamics in tissue is also included to help readers understand MRI signal sources. The chapter is organized as follows: first, the importance of noninvasive neuroimaging of neuronal activity is introduced and the available methods, including electromagnetic-based electroencephalography (EEG) and magnetoencephalography (MEG), and hemodynamic-based optical imaging, positron emission tomography (PET) and functional MRI (fMRI), are briefly reviewed. Next, the basis of the signal sources for MRI and fMRI and the limitations of the current fMRI methods are briefly discussed. Then, the newly proposed fMRI methods for detecting neuronal activity more directly are reviewed and the strengths and limitations discussed. Finally, the motivations of this project—the need for "ground truth" experiments for testing and validating direct fMRI and the prerequisites necessary for future fMRI contrast design—are discussed.

1.1 Noninvasive neuroimaging of neuronal activity

1.1.1 Importance of large-scale noninvasive imaging of neuronal activity

With nearly 100 billion neurons, tenfold more glial cells, and an estimated 100 trillion connections, the workings of the human brain remains one of the greatest challenges in science and medicine [1]. Brain disorders, including Alzheimer's disease, Parkinson's disease, stroke, autism, depression, schizophrenia, traumatic brain injury, etc., are major causes of death and disability worldwide, placing a tremendous load on those suffering from these diseases and their families [2–4]. However, the cellular and pathological causes of these diseases are still poorly understood because of the complexity of the brain and our incomplete knowledge of its structure and function as well as the limited experimental tools and theoretical basis currently available to study the brain. Thus, developing new and efficient tools and techniques is essential for improving our understanding of the brain.

Neuronal excitation and transmission are the basis of information processing in the brain [5,6]. The study of neuronal activity can be traced back to 1780, when Luigi Galvani discovered that an electrical spark applied to an exposed nerve in a dead frog could cause its leg to twitch [7]. After more than two centuries of development of both the technology used to study the neural system and our understanding of the neural system, modern tools are now available to record or image neuronal activity in multiple spatial and temporal scales. At the cellular and subcellular levels, electrophysiology, whose tools include intracellular electrodes, extracellular single or multiple electrodes, and whole-cell patch recording, is a well-established discipline for studying the electrical properties of neuronal activity [1,6,8]. Since the discovery

of the green fluorescent protein (GFP) in the 1960s [9], a large number of new fluorescence proteins and related optical microscopy techniques have been developed to enable neuroscientists to study neuronal activity at multiple scales, e.g., ion channels, neurotransmitters, action potential generation and propagation, circuits and networks, etc. [10].

To study brain function at the level of large groups of neurons and networks, there are also several methods available for large-scale, noninvasive functional neuroimaging, which include electroencephalography (EEG), magnetoencephalography (MEG), optical imaging, positron emission tomography (PET), and functional MRI (fMRI) [11,12]. These techniques allow us to determine which brain regions are active during some stimuli or tasks, such as visual stimulation, electrical shock, finger movement, memory, etc.; this information is used widely in studies in the behavioral and cognitive neurosciences. However, all the methods mentioned above either have a spatial resolution of several millimeters or a temporal resolution of several seconds, and their representation of neuronal activity is indirect. Clearly, the methods for large-scale functional neuroimaging currently available cannot directly detect fine-scale neuronal activity or the precise time and the exact location of this activity within the brain [6,13–15].

Understanding the acute need to improve the understanding of brain function in time and space, the Brain Research through Advancing Innovative Neurotechnologies (BRAIN) Initiative (http://braininitiative.nih.gov/) was launched with the goal of advancing neuroimaging techniques that enable the measurement of brain function at multiple spatial and temporal scales. One important goal of this project is to promote

the invention of the next generation of large-scale brain imaging tools to detect neuronal activity more directly and accurately at both higher spatial scales and higher temporal resolution.

In this and the following sections, the currently available methods for large-scale, noninvasive functional brain imaging will be reviewed and their pros and cons discussed. Next, we will focus on fMRI, new developments in contrast design, and areas in which work is still required.

1.1.2 Electroencephalography (EEG) and magnetoencephalography (MEG)

EEG and MEG are two methods to record electrical and magnetic field fluctuations in the brain from the scalp; the sources of these fluctuations can be tracked back to electrical currents related to neuronal activity. There were two landmarks for the development of EEG: in 1875 the first animal EEG experiment was reported by an English physiologist Richard Caton [16], and in 1924, a German physiologist and psychiatrist, Hans Berger, performed the first EEG experiment on a human [17]. MEG was developed almost 100 years after EEG: in 1968, the first MEG experiments were reported by an American physicist, David Cohen [18]. Now both EEG and MEG have important clinical uses, such as detecting and localizing epileptic focal regions in the brain [14].

Electrical activity is an important part of neuronal activity and signal processing in the brain. After the neurotransmitter release and uptake in the synapse, postsynaptic action potentials and currents are generated and pass along dendrites and axons. When cells are activated in unison and the currents created are parallel, the combined current can be viewed as a single current dipole, which generates a

magnetic field detectable by the MEG outside the scalp [13,19]. The MEG signal mainly comes from the dendritic currents because the synaptic and terminal currents are randomly orientated to each other and their related magnetic fields cancel each other out [13,14,18,19]. As for the axonal currents, they generally move quickly, and it would, therefore, be very unlikely to have a sufficient number of synchronized axons to generate a detectable magnetic field [13,14,18,19].

Along with the intracellular currents mentioned above, extracellular currents flow in the opposite direction of the intracellular currents [14]. Together with transmembrane ionic and displacement electrical currents, they form a complete current pathway [14]. The extracellular currents spread out from their source, and some large-amplitude, synchronized currents might propagate to the scalp with enough amplitude to be picked up by the electrodes on the surface, which are the main signal sources of EEG [14,20,21]. It has been reported that glial cells may also contribute to the EEG signal as a secondary effect of neuronal activity, i.e., the increased extracellular potassium concentration caused by neuronal activity will increase intracellular and extracellular current by depolarization local cell membrane and creating local potential gradient across the membrane [14,20].

Although their spatial resolution is low, the main advantage of both EEG and MEG is their high temporal resolution, which can be faster than 1 millisecond. This makes them valuable for the study of fast neuronal events, which other available functional neuroimaging methods cannot capture [13,14,19,20]. Another advantage of both EEG and MEG is their ability to measure directly the electric output of neuronal activity rather than an indirect effect, such as the hemodynamic effects detected by

fMRI and PET [13–15,22]. The main disadvantage of both EEG and MEG is their poor spatial resolution, which is caused by the small amplitude of the neural current source, sensitivity of the detectors, and more importantly, the tendency for electric and magnetic fields to spread from their sources. These result in an ill-posed inverse problem for accurately localizing the signal sources [13,14,19,20,22,23]. Another limitation of both methods is the requirement of the signal sources to be highly synchronized and at a location close to the scalp (the signal decays as the distance from the source increases because of tissue conduction and the Biot-Savart law), which restricts their application in studying other types (nonsynchronized) of neuronal activity and brain function in deep brain regions [19,20,22,24].

1.1.3 Functional near-infrared spectroscopy (fNIR)

Functional near-infrared spectroscopy (fNIR) is a noninvasive brain imaging method based on the changes in the light–tissue interactions along the hemodynamic responses associated with neuronal activity [25]. The first *in vivo* near-infrared spectroscopy dates back to 1977 when Jöbsis proposed using it to monitor tissue oxygenation. The potential for use in detecting neuronal activity and brain function was first realized in the early 1990s when it was observed that the change in the oxygen level in blood flow caused by neuronal activity could be captured by near-infrared spectroscopy [26–29].

Neuronal activity involves many physiological processes, such as opening and closing of channels, diffusion and pumping of ions, sending of electrical signals, etc.; most of these activities consume energy and increase the metabolism's consumption and use of oxygen from the local capillary bed [15,30]. As consequences of the

neurovascular coupling, both the local cerebral blood flow and volume will increase as the amount of oxygenated hemoglobin increases to replace the deoxygenated hemoglobin [15,30]. The changes in the concentrations of the deoxygenated and oxygenated hemoglobin are the main signal sources for fNIR [25,30], which will be discussed below.

The interaction between light and biological tissue is complex and a popular research topic at present; current research involves light absorption, light scattering, fluorescence, etc. [31,32]. fNIR mainly makes use of the light absorption properties in tissue: light intensity attenuates as it is absorbed by molecules (water, lipid, protein, etc.) as it propagates inside the tissue [32,33]. The attenuation A of a light before (I_0) and after (I) it passes a volume of tissue is given by the Lambert–Beer law:

$$A = \ln \frac{I_0}{I} = \mu_a \cdot L = \sum_i \varepsilon_i \cdot c_i \cdot L \tag{1.1}$$

where μ_a is the bulk absorption coefficient, which is the product of the molar attenuation coefficient (ε_i) and the molar concentration (c_i) of all the absorbers, and L is the optical path length, which is a function of the geometric length, scattering coefficient and absorption coefficient [34,35]. ε_i for each molecule in the tissue is a function of the light wavelength [31,32]. In the near-infrared spectrum (700–1000 nm), water has a rather small molar attenuation coefficient while the hemoglobin absorbs a lot of light in this spectrum [27,34,35]. Inside the narrow spectral window of NIR, the oxygenated hemoglobin has a higher molar attenuation coefficient > ~810 nm, but a smaller value < ~810 nm, than deoxygenated hemoglobin [32,33]. According to Eq. 1.1, the relative concentration of the oxygenated and deoxygenated

hemoglobin can be estimated quantitatively with several absorption measurements at different wavelengths [27,29,30,33].

Compared with other methods for noninvasive functional brain imaging, fNIR has not shown many advantages in either temporal or spatial resolution [30]. The signal source of fNIR—the increased concentration of the oxygenated hemoglobin—has a delay of several seconds with respect to the neuronal activity and limits the temporal resolution of fNIR [22,30]. The spatial resolution of fNIR (in most cases no better than 5–10 mm) is limited by light scattering inside the tissue along the long pathway from the light source inside the brain to the detectors on the scalp [22,30,35]. Additionally, penetration is a problem for fNIR, as for most optical imaging methods, as the maximum detectable depth in the cortex is only 2–4 mm [22,30,35]. The main advantages of fNIR are its portability, low demand in terms of equipment, relative simplicity, and low cost [22,25,30,35].

1.1.4 Positron emission tomography (PET)

Positron emission tomography (PET) detects pairs of gamma rays emitted indirectly by the injected positron-emitting radionuclides (tracers), which are typically isotopes of an unstable nucleus, such as ^{11}C, ^{13}N, ^{15}O, ^{18}F, etc. [36]. Because there are not enough natural radionuclides in animals and humans to perform PET, radionuclides have to be produced in the cyclotron and then incorporated into molecules normally found in the body, such as water, glucose, ammonia, etc., or a specific molecule designed with biocompatibility [22,37,38]. The radioactive nuclide starts decaying and emitting positrons as soon as it is created; then the positron rapidly diffuses and collides with the electrons in the tissue until it is annihilated by

one of them [36,39,40]. This annihilation generates two 511-keV gamma rays in almost completely opposite directions; they are captured by an array of scintillation photoelectric detectors and provide the signal sources for reconstructing the 3D PET tomography [36,39,40].

PET was first used as a method for noninvasive functional brain imaging in the early 1980s by an ^{18}F tracer incorporated into glucose. This metabolic tracer, 2-[^{18}F] fluoro-2-deoxy-D-glucose ([^{18}F]FDG), accumulates in the brain region in which the most neuronal activity is occurring (see more discussion on this topic in Section 1.1.3) [41–43]. PET can also be used to detect neuronal activity indirectly by monitoring increased blood flow; this method involves the use of a short half-life tracer [^{15}O]water [44]. [^{15}O]water is freely diffusible in tissue, can pass the blood barrier, and has a half-life time of ~2 min. By estimation with tracer kinetic models, the blood flow can be mapped quantitatively in the brain [22]. In addition, PET can be used to study a neuroreceptor with a radiotracer that is designed to be the ligand to a specific subtype of this neuroreceptor [45,46].

The main advantage of using PET is the flexibility this method allows in designing the radiotracers, As a result PET is quite useful in mapping the neurotransmitter system and some brain diseases, such as epilepsy, dementia, stroke, tumors, etc. [36,38,39]. As for the real-time mapping of neuronal activity, PET is limited in both spatial and temporal resolution. In terms of spatial resolution, before annihilation, the positron must diffuse away from the source to collide with electrons in the tissue. Because this displacement is random and can be up to a millimeter or more, there is a natural limitation on the spatial resolution that can be achieved with

PET [22,40]. As for the temporal resolution, both the two methods currently used—glucose and blood flow mapping—are both indirectly related to neuronal activity. As discussed in Section 1.1.3, the delay of the hemodynamic response limits any further improvement of this method in terms of temporal resolution [22,40]. In addition, the long half-life time of the current radiotracer (the minimum is approximately several tens of seconds) also makes it difficult to track a single event of neuronal activity, which occurs on the sub-second scale, with this technique [47].

1.2 Functional magnetic resonance imaging

Functional MRI (fMRI) is another type of large-scale, noninvasive brain mapping methods that is currently the most widely used functional neuroimaging method in cognitive neuroscience [12]. In this section, first, the physical basics of nuclear magnetic resonance (NMR) are introduced. Following this, magnetic resonance (MR) contrast in tissue and its relation to water dynamics are briefly discussed. Finally, the biophysical signal sources of fMRI and its advantages and limits are discussed.

1.2.1 Basics of magnetic resonance

MR is a quantum phenomenon that occurs when a nucleus with net spin is left in the magnetic field. All nuclei with an odd number of either protons or neutrons, such as ^{1}H, ^{13}C, ^{15}N, etc., have a net spin, which is characterized by the nonzero spin quantum number *I*. Spin is also a form of angular momentum $\vec{S}$, which is an intrinsic property of the particle itself. The total angular momentum of a nuclear spin is $\vec{S} = h\sqrt{I\,(I+1)}/2\pi$, where h is the Planck constant. The projection of the angular

momentum in the z direction has two possible states I_z: $+h/4\pi$ and $-h/4\pi$ for the nuclei in ^{1}H with spin number I = ½. In this study, only the ^{1}H on the water molecules is used and studied, and the spin will stand for the nucleus of ^{1}H if no specific notation is provided. Each spin can be treated as a magnetic dipole, and its magnetic moment $\vec{\mu}$ is proportional to its spin angular moment, $h\vec{I}/2\pi$, by the gyromagnetic ratio, γ:

$$\vec{\mu} = \gamma h\vec{I}/2\pi \tag{1.2}$$

If an external magnetic field $\overrightarrow{B_0}$ is applied, the magnetic energy of the magnetic dipole at each quantum state I_z will be:

$$E = -\vec{\mu} \cdot \overrightarrow{B_0} = -\frac{\gamma h\vec{I} \cdot \overrightarrow{B_0}}{2\pi} = -\gamma I_z B_0 \tag{1.3}$$

The energy difference between the two quantum states is:

$$\Delta E = -\gamma \Delta I_z B_0 = \gamma h B_0/2\pi \tag{1.4}$$

In nuclear magnetic resonance (NMR), a group of spins rather than a single spin is studied. To move from a single spin to a group of spins, quantum statistics are required [48]. The half-spin protons in ^{1}H are *ferminos*, and the number of spins in the each quantum state follows the Boltzmann distribution. The number of spins in $+h/4\pi$ and $-h/4\pi$ are:

$$\begin{aligned} N_+ &= N\frac{1}{1+e^{-\frac{\Delta E}{kT}}} \\ N_- &= N\frac{e^{-\frac{\Delta E}{kT}}}{1+e^{-\frac{\Delta E}{kT}}} \end{aligned} \tag{1.5}$$

where N is the total number of spins, k is the Boltzmann constant and T is temperature. Thus the total magnetic momentum $\vec{M}$ (parallel to $\overrightarrow{B_0}$ direction) is:

$$\left|\vec{M}\right| = (N_+ - N_-)|\vec{\mu}| = N\frac{1-e^{-\frac{\Delta E}{kT}}}{1+e^{-\frac{\Delta E}{kT}}} \cdot \frac{\gamma h}{4\pi} \tag{1.6}$$

In current magnetic field strength of NMR (<= 21.1 T) and near room temperature, Eq. 1.6 can be simplified to:

$$\left|\vec{M}\right| = N\frac{\Delta E}{2kT} \cdot \frac{\gamma h}{4\pi} = N\left(\frac{\gamma h}{4\pi}\right)^2 \frac{B_0}{kT} \tag{1.7}$$

with the approximation $e^{-\frac{\Delta E}{kT}} \approx 1 - \frac{\Delta E}{kT}$.

At a macroscopic level, according to Eq. 1.7, a bulk magnetization parallel to the applied magnetic field is generated at equilibrium whose magnitude is linearly proportional to the magnetic field strength and the number of spins. This bulk magnetization is the signal source of all magnetic resonance systems. To detect this magnetization, an electromagnetic wave of the same energy as the energy difference between the two quantum states must be applied to perturb the equilibrium state. The frequency of this excitation electromagnetic wave ($\overrightarrow{B_1}$) is characterized by the Larmor frequency or resonant frequency based on Eq. 1.4:

$$\omega_0 = \gamma B_0 \tag{1.8}$$

In classical description, the evolution of the bulk magnetization can be described by the Bloch equations [49]:

$$\begin{aligned} \frac{dM_x}{dt} &= \gamma\left(\vec{M}\times\vec{B}\right)_x - \frac{M_x}{T_2} \\ \frac{dM_y}{dt} &= \gamma\left(\vec{M}\times\vec{B}\right)_y - \frac{M_y}{T_2} \\ \frac{dM_z}{dt} &= \gamma\left(\vec{M}\times\vec{B}\right)_z - \frac{M_z - M_0}{T_1} \end{aligned} \tag{1.9}$$

where $\vec{B}$ is the total applied magnetic field applied equal to $\overrightarrow{B_1} + \overrightarrow{B_0}$ when excitation is on and $\overrightarrow{B_0}$ when excitation is off, T_1 and T_2 are the spin–lattice (longitudinal) and the spin–spin (transverse) relaxation times, and M_0 is the equilibrium magnetization

under the main magnetic field $\overrightarrow{B_0}$. In general, after excitation, the magnetization parallel to the main magnetic field $\overrightarrow{B_0}$ will recover to M_0, while the magnetization perpendicular to $\overrightarrow{B_0}$ will decay to 0. These relaxation processes are determined by the two relaxation times, T_1 and T_2; their mechanisms and relation to water dynamics are discussed in the next section.

1.2.2 Water rotational motion and NMR relaxation times

Nuclear spin relaxation is caused by the fluctuations of the local magnetic field due to molecular rotation. The proton on the water molecules experiences an intramolecular dipole−dipole interaction with the proton on the same water molecule and an intermolecular dipole−dipole interaction with the proton on the neighboring water molecules or other types of molecules; these interactions induce the local magnetic field to fluctuate as the water molecule rotates. The intensity of the local magnetic field fluctuations can be described as a spectrum of frequency (w) as $J(w)$:

$$J(w) = \frac{\tau_c}{1+w^2\tau_c^2} \tag{1.10}$$

where τ_c is the water molecule's rotational correction time, which is the average time for a water molecule to rotate 1 radian and is approximately around 10^{-12} seconds for the free water at room temperature [48].

The relation between the relaxation times and the water rotational correlation time was given by the Bloembergen-Purcell-Pound (BPP) theory, which was developed in 1948 to explain the relaxation phenomenon in a pure substance [50]. According to the BPP theory, the spin–lattice relaxation time (T_1) and spin–spin relaxation time (T_2) are described as:

$$\frac{1}{T_1} = K[J(w_0) + 4J(2w_0)]$$
$$\frac{1}{T_2} = \frac{K}{2}[3J(0) + 5J(w_0) + 2J(2w_0)] \quad (1.11)$$

where w_0 is the resonance frequency of the main magnetic field B_0, and K is a constant determined by the distance between the two interacting nuclei. In general, T_1 characterizes the dipole–dipole interaction between the excited spins with its neighboring nuclei or other entities, in which excited spins lose their energy and recover back to their equilibrium state by stimulation of single- and double-quantum transitions. T_2 characterizes the dipole–dipole interaction between excited spins, which causes the excited spins to lose their coherence and involves all the three types of transitions: zero-, single- and double-quantum transitions. From Eq. 1.10 and Eq. 1.11, the two relaxation times are mainly determined by the molecule's rotational correlation time, and a decrease of the two relaxation times is expected as the molecule's rotational correlation time increases in the tissue [48].

T_1 and T_2 are very large values (~ seconds) for pure water [48]. However, these relaxation times measured in the tissue are much shorter than those measured in pure water [51]. This phenomenon is mainly caused by the interaction between water and other macromolecules, such as proteins, lipids, etc., which have a larger molecular mass and rotate at a much slower rate. The tumbling rate of the water located close to these macromolecules is reduced due to the water's interaction with the macromolecules. This "slow" water is called "bound water"; bound water relaxation times can be several milliseconds or less [48,52]. These bound water molecules can further affect the other water molecules by chemical exchange or translational exchange.

Biological tissue is highly heterogeneous, containing different types of cells, extracellular matrices, vasculature, etc. At the molecular level, there are a lot of macromolecules with a slow tumbling rate that are surrounded by water molecules, such as proteins, carbohydrates, RNA, lipids, etc. Thus, different chemical environments exist for water molecules, and these molecules may have different relaxation times. Indeed, different water relaxation compartments have been found in biological tissue. For example, the water trapped between the lipid membranes in the myelin sheath of the axons in the brain is shown to have much shorter relaxation times than intracellular and extracellular water. As a result it has been possible to use these shorter relaxation times to quantitatively map the myelin water content inside the brain [53]. Additionally, the water in different environments/compartments can undergo chemical exchange, diffusion, active motion, etc. [54,55]. Water relaxation as it relates to compartments and exchange is an area of MRI research that is currently receiving a great deal of attention [56–58] and which will be further discussed in the following sections.

1.2.3 Water translational motion and self-diffusion

At a microscopic view, particles in the liquid or gas state at above-zero temperatures are always moving randomly as a result of their rapid collisions with neighboring particles or molecules; this phenomenon is known as Brownian motion. Brownian motion was first discovered by a Scottish botanist, Robert Brown, in 1828 as he observed the motion of pollen grains in water under a microscope. Later in 1905, Albert Einstein provided a mathematical formulation to describe Brownian motion based on the statistical interpretation of microscopic motion [59]. There are

two parts to his theory. In the first part, Einstein described the displacement of the particles under Brownian motion by a parameter known as diffusion coefficient *D* with the following equation:

$$\langle x^2 \rangle = 2Dt \tag{1.12}$$

where $\langle x^2 \rangle$ is the mean square displacement of the particle in one dimension during the diffusion time *t*. In the second part of his theory, he related the diffusion coefficient *D* to the physical properties of the particle. In combination with Strokes' law, the diffusion coefficient *D* can be described using the Stokes–Einstein equation [60]:

$$D = \frac{kT}{6\pi\eta R} \tag{1.13}$$

where η is the dynamic viscosity, and *R* is the radius of the particle (assuming it is a sphere). From the Stokes–Einstein equation, it can be determined that, in a pure liquid or gas, the diffusivity of the particle is determined mainly by the size of the particle and the local viscosity.

Within the MR, it is possible to quantitatively measure the water diffusion coefficient based on the loss of coherence of the spins during the diffusion process in the presence of an applied external magnetic field gradient. Generally, a pair of identical magnetic field gradients with opposing directions is applied to measure the water's self-diffusion quantitatively. In the period of the first gradient, the spins in different locations experience different Larmor frequencies (Δf) and have different phases ($\Delta\phi = \Delta f$ * gradient duration) because the main magnetic field, $B_{0,}$ is

modulated by the presence of a magnetic field gradient. If the spins stayed at the same position without diffusion, the application of the second gradient with the opposite direction would cancel out the phase shift of each spin caused by the first gradient, and this gradient pair would have no effect on the MR magnetization. In reality, the particles are constantly diffusing; this movement causes a loss of phase coherence of the spins and attenuates the amplitude of the MR signal further. The MR signal attenuation caused by the gradient pair is commonly described by diffusion weighting, known as *b*-values:

$$S(b) = S_0 \exp(-bD) \tag{1.14}$$

where S_0 and $S(b)$ are the signals without and with the presence of the paired gradients and b is the diffusion weighting caused by the paired gradients. The *b*-values are determined by the strength and timing of the gradients and other characteristics of the MR pulse sequences (for more information see [61]).

The apparent diffusion coefficient (ADC) of water measured in tissue is two to ten times smaller than that measured in an aqueous water solution [62]. This "slowed-down" diffusion might be caused by several phenomena. First, the hydrodynamic interaction between water and other macromolecules (e.g., proteins, lipids, carbohydrate, etc.) with a much slower diffusivity reduces the diffusivity of the water in proximity to them [63]. Second, the presence of some diffusion obstructions (e.g., cell membranes, large macromolecules) can also produce a tortuosity effect on the water diffusion pathway, i.e., water has to diffuse along a longer diffusion pathway to move around the obstructions [64]. In addition, the lipid membrane might restrict the

water diffusion inside the cells, by a process known as the restriction effect [65].

For biological tissue, it has been found that Eq. 1.14 is not valid when *b* is acquired in multiple directions or in higher values. For multidirectional *b*, anisotropic properties of water diffusion, *D,* have been found in tissue, especially in white matter where water is more restricted perpendicular to the axon than parallel to it [65]. This phenomenon has been widely used for *in vivo* fiber tractography, an application of diffusion tensor imaging (DTI), although the underlying biophysical mechanisms between tissue microstructure and the diffusion signal are not entirely clear [65,66]. At higher *b* values, the diffusion attenuation cannot be described by a single exponential function such as Eq. 1.14. Rather, it was found that expanding Eq. 1.14 from a single-component to a multicomponent diffusion model fit the diffusion attenuation signals tissue very well, both *in vitro* and *in vivo* [62,67–70]. However, the underlying biophysical explanation of this multicomponent diffusion is poorly understood and under study; this type of diffusion might be the result of physical compartments (e.g., intracellular and extracellular) inside the tissue, of bound water close to macromolecules and cell membranes, of the heterogeneity of the tissue, or of some other unknown reason. It has also been reported that the water exchange among different water environments can play a role in the water diffusion signal [71–73].

1.2.4 Functional MRI contrast–hemodynamics

The discovery of an MRI application for detecting brain function can be tracked back to Ogawa and colleagues in 1990 [74–76]. In their studies, anesthetized rodents were scanned in a high-field MRI scanner (7T) with a gradient echo sequence. The gradient echo MRI is a relaxation-time-weighted image that is based on T_2^*, which is

a combination of the transverse relaxation time, T_2, and the local magnetic field inhomogeneity, ΔB_0:

$$\frac{1}{T_2^*} = \frac{1}{T_2} + \alpha \Delta B_0 \tag{1.15}$$

where α is positive constant. An interesting finding in their studies is that some brain regions containing blood vessels became darker in the T_2^*-weighted MRI images as the blood oxygen level was reduced. After a series of *in vivo* and *in vitro* studies, they concluded that the main cause of this change is the change in the relative concentration of the oxygenated and deoxygenated hemoglobin. The authors hypothesized that this blood-oxygen-dependent (BOLD) MRI could be used to detect brain activity through neurovascular coupling (as discussed in Sections 1.1.3 and 1.1.4).

Oxygenation changes the magnetic properties of hemoglobin: oxygenated hemoglobin is diamagnetic as is water, but deoxygenated hemoglobin is paramagnetic. Paramagnetic deoxygenated hemoglobin creates a local magnetic field gradient in blood vessels and their surrounding tissue, which reduces the local T_2^* (Eq. 1.15) and T_2^*-weighted signals at the region of high-concentration of deoxygenated hemoglobin. During neuronal activity, more oxygenated hemoglobin replaces the deoxygenated hemoglobin; this change reduces the local magnetic field inhomogeneity and increases the local T_2^* and T_2^*-weighted signals in the active regions in the brain. As a result of this mechanism, BOLD fMRI was successfully used in human brain function studies in 1992 [77–79], thus further establishing the reliability of this functional brain imaging method. Now fMRI is a widely used brain imaging tool for the study of brain functions in cognitive neuroscience [15].

1.2.5 Functional MRI limitations

The major limitation of the current functional MRI comes from the origin of its signal: changes in oxygen levels in the blood vessels. The hemodynamic origin of this method makes interpretation of the detected fMRI signals and the underlying neuronal activity problematic [80]. The relationship between the hemodynamic response and the underlying neuronal activity is complex. Experiments suggest that there is a nonlinear relationship between the fMRI signal changes and the level of neuronal activity [81–83]. For example, a saturation effect was observed in fMRI [82–84] indicating that fMRI, as currently used, cannot distinguish between the medium and maximum levels of neuronal activity if the fMRI response has saturated at the medium level. Further, the hemodynamic response cannot determine whether the underlying neuronal activity is from excitation or inhibition [80,85]. Recent studies found that glial activity can also contribute to the BOLD fMRI signal [86]. Clearly, this indirect-effect basis makes it challenging to correlate the observed fMRI signals to the underlying neuronal activity.

Moreover, the hemodynamic origin creates a natural limit to the temporal and spatial resolution of BOLD fMRI. There is normally a 1–2 second delay between the response of the oxygen level change and the start of the neuronal activity and another 5–10 seconds for the BOLD fMRI signal to reach its maximum level [87,88]. This slow hemodynamic response restricts any further improvement of this fMRI method (~ seconds) in temporal resolution, though fast MRI methods of several tens of milliseconds are already available. For spatial specificity, the vascular supply is regulated by a large group of neurons rather than a single neuron, which means that

the point spread function of BOLD fMRI is scaled in millimeters rather than micrometers [87,89,90]. Thus the maximum spatial resolution of the current BOLD fMRI is inferior to that of structural MRI, which at present can achieve a submillimeter voxel size.

1.3 Newly proposed functional MRI methods for direct detection of neuronal activity

Noninvasive, direct *in vivo* detection of neuronal activity by imaging with high temporal and spatial resolution is one of the major challenges in the neurosciences. Progress in this area is required to improve our understanding of brain function and, in the clinic, to develop new tools for diagnosing disease states and disorders of the brain. As the current fMRI method only indirectly reflects neuronal activity, and its hemodynamic origin limits its spatial and temporal resolution, physicists have begun looking for other MRI contrast mechanisms to detect intrinsic signals directly from neurons. Subsequently, several MRI methods have been proposed to provide more direct measures of neuronal activity; they include, but are not limited to: (a) functional diffusion MRI to detect water displacement [91–94]; (b) phase MRI to detect the changes in the local magnetic field caused by neuronal currents [95–97]; (c) Lorenz-force-effect MRI to detect displacements caused by neuronal currents [98,99]; (d) proton–density-weighted MRI to detect changes in proton pools [100,101]; and (e) spin-lock MR methods to detect oscillating neuronal current [102,103]. In this section, the biophysical signal sources and current stages of each method will be briefly reviewed.

1.3.1 Detection of the neuronal electromagnetic field

As discussed in Section 1.1.2 with respect to the EEG and MEG methods, electrical signaling is an important part of neuronal activity. Neuronal current occurs in most of the processes involved in a complete neuronal communication. After receiving the neurotransmitter from the synapses, dendrites generate neuronal current and potential and pass this electrical information to the soma. After getting enough current from the dendrites, the soma generates an action potential that propagates along the axons until they reach the axon terminal where the next synapse process starts. Typically, the neuronal current on a single neuron is on the order of a picoampere, and the local magnetic field generated by this current is on the order of 10^{-15} T [104], which is too small for any of the noninvasive brain imaging methods to detect. In the MEG study, the magnetic field detected on the scalp (2–4 cm from the neurons) is on the order of 10^{-13} to 10^{-12} T; the signal comes from a large group of highly synchronized neurons. In the MRI studies, the voxel size is approximately 2–4 mm, and an estimation of the magnetic field of the highly synchronized neuronal currents is on the order of 10^{-10} to 10^{-9} T [96].

One proposed MRI method for detecting the neuronal current is based on the Larmor frequency changes caused by the resulting local magnetic field changes. These frequency changes can be measured by the phase of the complex MR signal at a given imaging time, known as phase MRI. The first attempt to demonstrate the possibility of using MRI techniques to detect electrical current was made by Henkelman and his colleagues [105,106]. In their studies, a phase shift caused by the injection of two mA electrical current pulses into the forearm of a human subject was

picked up by phase MRI [88,105,106]. Later work further demonstrated that the current MRI system is capable of detecting the phase shifts on the order of 0.8 ± 0.1 degrees (1.7 ± 0.3 nT magnetic field changes) [107]. So far, several research groups have reported successful experiments using phase MRI to detect neuronal activity *in vivo* [96,108–110]. However, the debate about whether there are sufficient magnetic field changes detectable by phase MRI in a voxel containing a population of neurons has been ongoing since the method was first proposed. Recently, instances in which phase MRI failed to detect the expected neuronal activity *in vivo* [88,111] have been reported, casting further doubts on the reliability of this method.

In addition to detecting phase shifts, there are other MRI methods designed to detect neuronal current indirectly, e.g., using the Lorentz-force. The idea is that neurons carrying an electrical current would be displaced in a strong external magnetic field experiences by the Lorentz force [88,112]. Several phantom studies were performed by Song et al. designed to detect these proposed neural tissue displacements [88,112]. They also conducted one *in vivo* experiment in which responses to the electrical stimulation were detected in the median nerve of the forearm [98,113]. However, other research groups have cast doubts on the theoretical basis of this method and the detectable range of the Lorentz-force effect [99,114]. Recently, a new MRI method was developed to detect oscillating neuronal currents by matching the frequency of the applied spin lock magnetic field to the specific frequency of the oscillating neuronal currents [102,103,115]. In principle, this method should overcome the cancelation of the magnetic field that occurs when the currents are in opposite directions. However, this method is still in an early stage of

development and, to date, only a few demonstrations of the principles in artificial systems have been reported [102,103,115].

1.3.2 Functional diffusion MRI

Diffusion MRI is a method for measuring the apparent diffusivity of water within tissues [116–118]. As water undergoes diffusion in tissue, it samples many different local environments (e.g., barriers, macromolecules, cell membranes, etc.); this behavior makes diffusion measurement very sensitive to microenvironment changes [65]. Diffusion MRI is currently a gold-standard clinical neuroimaging method for diagnosing stroke clinically with an increase in diffusion-weighted image and a reduction in the ADC map [119,120]

Recently, diffusion MRI was suggested as a direct functional imaging method for detecting neuronal activity [91,121–123]. Early *in vivo* experiments in both humans and animals reported small but significant increases in diffusion-weighted MRI signals (in other words, decreases in the ADC of water), which were ascribed to changes induced by underlying neuronal activity directly rather than to blood-oxygen-level changes [91,121–123]. Similar reductions in water diffusivity under the conditions of extreme hyperexcitability achieved with strong biochemical stimulants were reported from *in vitro* experiments on brain slices [93,124] and spinal cord [92].

However, functional diffusion MRI (fDMRI) has not been widely adopted since its introduction approximately fifteen years ago mainly because of the dearth of convincing experiments establishing a biophysical basis for reported fDMRI changes. Recently, negative results have been reported with fDMRI: either the predicted changes were undetectable or there were strong hemodynamic contributions believed

to explain the observed changes [94,125–127]. Another obstacle in promoting diffusion MRI to detect brain function is that the underlying biophysical mechanism linking the potential diffusion MR signal changes to neuronal activity is still unclear. It was recently proposed that cell swelling during neuronal activity could be one cause of the reduction in water diffusivity [62]; however, the experimental evidence and biophysical explanation for this hypothesis are lacking. In addition to neuronal cell swelling, other physiological processes, such as cell membrane permeability changes, active pumping of water, microstreaming, etc., could all contribute to changes in the diffusion MRI signals, [71,92,128]. In conclusion, at least two problems must be solved before this potentially important direct functional brain imaging method can be shown to be viable: (1) conducting convincing experiments that directly correlate the diffusion MRI signal changes to the underlying neuronal activity and (2) understanding the biophysical mechanisms to connect the water diffusion to neuronal activity.

1.3.3 Proton-density MRI

Recently, several fMRI research groups realized there might be a proton-density contribution to the changes in the common BOLD fMRI measurements [129]. In BOLD fMRI, given the echo time (*TE*), the image is either T_2- or T_2^*-weighted:

$$S(TE) = S_0 \exp(-TE/T_2)$$

where S_0 is the signal intensity, known as proton density, when the relaxation process has not started. In BOLD fMRI, one uses a *TE* of several tens of milliseconds to make the observed signal either T_2- or T_2^*-weighted. In principle, there should be no signal changes as *TE* approaches zero as the T_2 or T_2^* contribution to observed signal

reduces to zero. However, starting from human spinal cord studies, Stroman and his colleagues found that there is also a signal change as *TE* approaches zero, which they defined as signal enhancement by extracellular protons (SEEP) [130]. The use of proton-density based MRI to detect neuronal activity has only been recognized by a small group of researchers in the functional MRI field [100,101,129–132]. Possible reasons for this lack of interest are: (1) this phenomenon is, at least partly, induced by the intravascular pressure increase during neuronal activity, which is also a hemodynamic process and thus, also an indirect assessment of neuronal activity [129,130]; (2) no other research groups have succeeded in reproducing this method in the detection of neuronal activity *in vivo*; and (3) the unexpected signal changes can be explained by some other mechanisms except for proton-density change [101,133]. All in all, the signal sources and biophysical mechanisms of this proposed fMRI method are still far from clear.

1.4 Toward direct detection of neuronal activity with MR

The noninvasive, *in vivo*, direct detection and imaging of neuronal activity is the essence in the neurosciences in terms of improving our understanding of brain function and, in the clinic, of diagnosing diseases and disorders of the brain. fMRI has been widely used in the cognitive neuroscience community since its invention in the 1990s [74–76]. The most widely used fMRI method, BOLD MRI, detects hemodynamic changes in the brain, which only indirectly reflect neuronal activity. The hemodynamic origin of the fMRI signal limits its spatial and temporal resolution and confounds its interpretation as a direct proxy for neuronal activity [80,85].

Recently, several MRI methods (described in Section 1.3) have been proposed to provide more direct measurement of neuronal excitation. On the other hand, during the past several decades, hardware used for MRI acquisition as well as image reconstruction and analysis has advanced. Now MRI images can be acquired rapidly (~ tens milliseconds) and with a high spatial resolution (sub millimeter). If a new MRI mechanism directly sensitive to neuronal activity with no time delay or location dispersion could be developed, it would become possible to detect neuronal activity via MRI more directly and accurately and with a much higher temporal and spatial resolution than is possible with the current fMRI. This breakthrough would provide scientists and doctors a much more powerful tool to explore and understand brain function.

Although proponents of these newly proposed fMRI methods have reported positive findings, most of these approaches are either still in development or have not yet been reproduced by a larger cohort of researchers. At least two problems must be solved before direct detection of neuronal activity via non-BOLD fMRI research can progress. Firstly, "ground truth" experiments potentially establishing a connection between the changes in these newly proposed fMRI methods and underlying neuronal activity are required to convincingly demonstrate one or more of these newly proposed mechanisms. Secondly, because the biophysical mechanisms between the observed MR signals and the underlying tissue microstructure and functions are still poorly understood, fundamental research to understand these connections is also critical. In this dissertation, the main goal is finding solutions for these two problems. Detailed plans are described in the following sections.

1.4.1 Needs and plans for "ground truth" experiments

A reliable and robust test system is needed to convincingly and conclusively vet and validate the proposed fMRI methods discussed in Section 1.3 and other new methods we or others may propose in future. At a minimum, such an fMRI test bed should include (a) a well-characterized biological model exhibiting neuronal activity free of hemodynamic, respiratory, and related physiological confounds and artifacts and (b) an independent, well-established neurophysiological method to detect neuronal activity directly and simultaneously with fMR/fMRI. To achieve the first goal, *in vitro* perfused brain slices are a good candidate system; these have been widely used in the neuroscience community as a biological model to study neural functions since the 1950s [134–136]. Indeed, successful MR spectroscopy and imaging experiments on perfused brain slices have already been reported in the study of metabolism, neurotransmitters, ions, tissue microstructure, tissue injury, and even neuronal excitation [69,70,93,124,131,137–143].

To achieve the second requirement, neuronal activity should be measured inside the NMR/MRI system during MR acquisitions with one or more standard neurophysiological method, which includes intracellular and extracellular electrical recording, calcium imaging, membrane surface voltage imaging, etc. [1,10]. Though the close configuration and potential electromagnetic interface in MR systems make it difficult to perform these recordings together with MR acquisition, there have been a few hybrid setups in which BOLD fMRI was recorded together with electrodes [144,145] or optical fibers [86]. In other fields, one group studied single cells or cell

cultures by a technically challenging setup with a combination of confocal and magnetic resonance microscopy [146–149]. However, to our knowledge, direct (non-BOLD) fMRI experiments satisfying the two requirements listed above have not yet been reported.

In this work we propose and demonstrate the use of such a test bed in which MR acquisition and calcium fluorescence imaging are performed simultaneously on organotypic cortical cultures obtained from rat brain. In this system, a single-sided MR system with permanent magnets was used [150]. Such systems, developed in the last two decades, are portable and have been used extensively to measure proton density, relaxation times, and diffusion coefficients in polymers and gels, foods, porous medium, and to a much more limited extent, biological materials [151–155]. One attribute of single-sided MR systems is the open access to the sample they provide, a feature we exploit in our design. This setup allows us to mount a fluorescence optical microscope with a long working distance above the biological specimen to simultaneously image intracellular Ca^{2+} transients. Fluorometric Ca^{2+} imaging detects caged or bound Ca^{2+} ions released during neuronal activity and represents a direct method for detecting neuronal activity [156,157].

In this study, our specimen were organotypic brain cultures of the rat cortex, which have been widely used in the neurosciences as a biological model of neuronal activity [158–162] and also in MRI studies [95,140,163]. Organotypic cortical cultures largely maintain their *in vivo* cortical cytoarchitecture including cortical layers and cortical cell types. They are stable and can be grown for several weeks in an incubator [159,160]. More importantly, organotypic cultures *in vitro* display bursts

of spontaneous neuronal activity, so-called up- and down-states that are similar to neural behavior observed *in vivo* [161,164,165]. No pharmacological manipulation is required to initiate neuronal activity; the culture remains in a long-term homeostatic state while exhibiting large transients of neuronal activity [162]. Organotypic cultures do not contain a cerebrovascular system and thus are free of artifacts of hemodynamic origin, such as pulsation and flow artifacts, effects caused by changes in blood pressure, or artifacts associated with respiration and variable oxygenation that are known confounds in fMRI studies *in vivo*.

In Chapter 2, we demonstrate the reliability and sensitivity of the single-sided NMR system by studying the water dynamics in a biomimetic model, a sodium polyacrylate solution and gel system, which is chemically well characterized. In Chapter 5, we provide a proof of principle of this novel instrument, demonstrating the reliability and performance of the proposed test bed by acquiring conventional MR data simultaneously with calcium fluorescence imaging, as a proxy for neuronal activity. In Chapter 6 and Chapter 7, use of this non-BOLD fMRI test bed to vet some candidate fMRI contrasts, which include water diffusion, relaxation times, and proton density, is described.

1.4.2 Prerequisites to studying neuronal activity via MR—water dynamics in living tissue

Water dynamics and the MR signal in biological tissue are complicated. At the molecular level, the dynamics of water molecules is highly correlated to that of other molecules (e.g., proteins, lipids, sugars, etc.) via the hydration effect or other interactions. The water molecules close to some macromolecules have been shown to

have reduced relaxation times and diffusivity, in other words, less rotational and translational freedom [48,52,62]. At the cellular level, there are different microenvironments for water, e.g., intracellular plasma, extracellular matrix, etc., which might cause water to have multiple components in both the relaxation and diffusion processes. More importantly, water in living tissue is not static, but rather is in continuous exchange with its neighboring water molecules via chemical exchange, diffusion, or active exchange.

In neuronal activity, numerous physiological processes might have an effect on the water dynamics and MR signals. In addition to the electrical signaling mentioned above, there is active exchange of ions (e.g., Na^+, Cl^-, K^+, Ca^{2+}, etc.), ion channels opening and closing, and ion pumps functioning [1]. More active water exchange might happen along with the ion exchange. Early morphological experiments showed that the neuron cell membrane might become "leaky" under intense excitation [166,167]; this leakiness might also modulate the water exchange between compartments. Cell volume changes have also been reported to occur during neuronal activity [166,168–172]. In addition, local temperature increases were also reported to be a simultaneous process of neuronal excitation [171].

However, there is very little information and knowledge about how these physiological processes affect the water dynamics and the resultant MR signals. Fundamental research on the underlying biophysical mechanisms between water dynamics and tissue microstructure and physiological processes is highly relevant and necessary to further promote the direct detection of neuronal activity via MR. The two aspects of our efforts to assist in achieving this goal are described below.

1.4.3 Method 1: The study of water dynamics in biomimetic models

One way to study the complicated water dynamics in tissue is by using biomimetic models to simplify the problem and isolate each part's contribution. In biological tissue the intracellular cytoplasm is more gel-like and the extracellular matrix is more solution-like [173]. Thus, a hydrogel or polymer solution with properties similar to those of living tissue is a good starting point for the study of water dynamics.

In particular, cross-linked sodium polyacrylate (NaPA) hydrogel has been proposed as a biomimetic model of living nerve fibers [174]. This anionic gel exhibits abrupt conformational changes by exchanging divalent counter-ions with monovalent cations, a behavior similar to that of the cortical gel layer of nerve fibers, which has been proposed to underlie the "all or none" nerve excitation and conduction [171,175]. The temporal variations of the swelling, heat production and absorbance, electric impedance, and potential associated with these changes in NaPA gels show a striking resemblance to those encountered during repetitive excitation of living nerve fibers [175,176]. Thus, the study of an NaPA model system by MR techniques may help further the understanding of the water dynamics inside tissue. Additionally, this model system might also provide insight into the ion exchange process underlying nerve excitation and its implication in water dynamics and MR signals. In Chapter 2, a systematic study of water's rotational and translational motions in this biomimetic model under physiological ionic solutions is presented.

1.4.4 Method 2: The development of 2D MR diffusion/relaxation spectra to characterize various microenvironments of water in tissue

Because of the heterogeneous nature of biological tissue, water in tissue is present in multiple microenvironments, in which it experiences various rotational and translational environments. Greater understanding of water dynamics in living tissue will be possible if there are MR methods capable of identifying these microenvironments and track water movement among them. However, conventional quantitative MRI (qMRI) methods represent the relaxation/diffusion properties inside each imaging voxel (~1 mm^3) as a single relaxation/diffusion value, which may produce incorrect and misleading results. For decades, 1D relaxation/diffusion spectra, a plot of component weightings as a function of relaxation/diffusion values, were used to attempt to identify water relaxation/diffusion compartments [177–181]. However, this method has limited resolution for distinguishing multiple water dynamic compartments, is inaccurate in the estimation of the compartment size/fraction, and is unable to track water exchange among compartments [55,182,183].

In molecular NMR, the power of NMR spectroscopy was significantly increased by the inclusion of a second dimension in the Fourier domain, expanding the ability to determine molecular structure, dynamics, and kinetics [184]. Based on the same principles, in recent years, there have also been several important developments in expanding the 1D MR diffusion/relaxation spectra to multidimensional MR diffusion/relaxation spectra to better characterize water dynamics [185]. Early studies in the porous medium and material sciences communities show the great advantages of this method in identifying water

compartments, monitoring water exchange between compartments, and studying the correlation of these diffusion/relaxation properties [186–192]. For instance, in our studies, we obtained 2D MR relaxation spectra (T_2–T_2) in a solution of urea and water. This method clearly distinguished the protons on the water molecules and urea molecules (Fig. 1.1) on the basis of their different transverse relaxation times. More importantly, the proton exchange process between these two chemical environments can be quantitatively monitored and characterized by changing the exchange time (a period designed in the MR sequence to allow for proton exchange with a minimal relaxation process) in the 2D T_2–T_2 experiments.

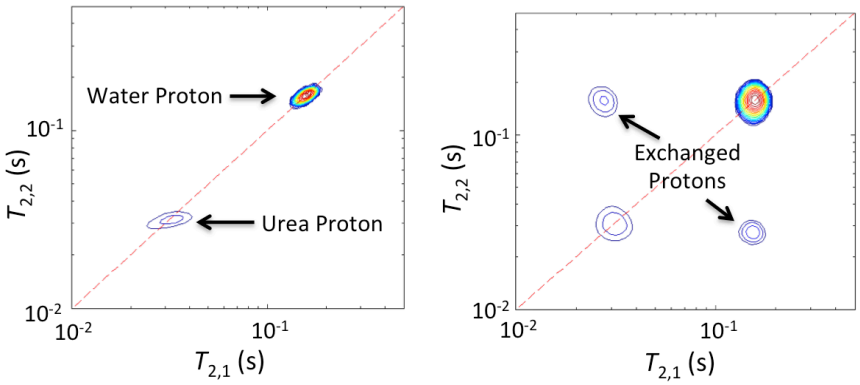

Figure 1.1. MR T_2–T_2 exchange spectra in a urea/water phantom with exchange time = 50ms (left) and 500ms (right), in which the on-diagonal pixels represent nonexchanging protons, while the off-diagonal pixels represent urea and water protons exchanged at the given exchange time.

Our preliminary results also show the great potential advantages of this type of method in characterizing the complex water dynamics in biological tissue. For instance, in Fig. 1.2, the T_2–T_2 exchange spectra obtained from fixed porcine spinal cord white matter clearly demonstrate a broad distribution of the T_2 relaxation times; this finding suggests there is microstructure heterogeneity inside the tissue and that the representation of the relaxation phenomenon with a single T_2 value is not correct

in conventional MRI relaxometry. Additionally, the increased intensity of the off-diagonal pixels as the exchange time increases shows that there is water exchange occurring among different water compartments and the exchange speed is in a detectable range (10 ms–1 s) when this type of MR method is used. The quantitative measurements of the microstructure heterogeneity and motion among different water microenvironments will be important in identifying some key biological information, such as cell size, extracellular matrix volume, cell membrane permeability, active water motion, etc. These characteristics are important to the understanding of water dynamics in living neural tissue and during the neuronal activity process.

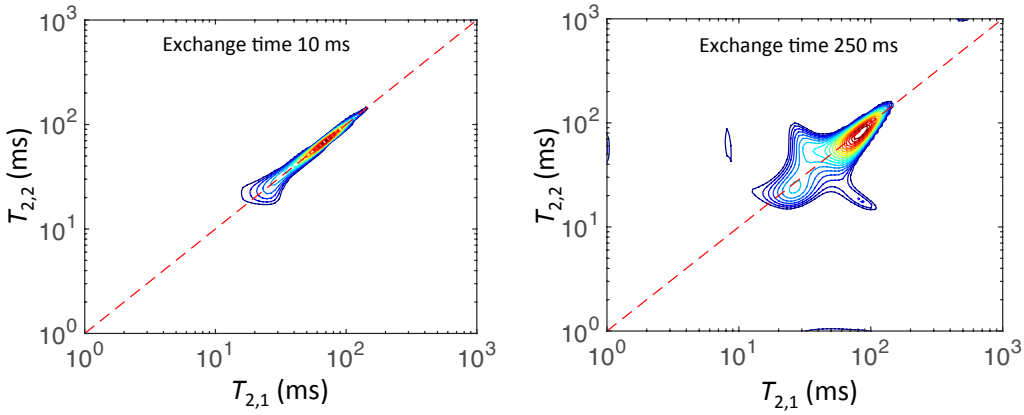

Figure 1.2. MR T_2–T_2 exchange spectra of the white matter (bundles of myelinated axons) from fixed porcine spinal cord with exchange time = 10 ms (left) and 250 ms (right), in which the on-diagonal pixels represent nonexchanging water molecules, while the off-diagonal pixels represent water molecules exchanged among different microenvironments.

While we recognize its potential for biological applications in living tissue, current 2D MR diffusion/relaxation spectra methods have two significant drawbacks, which limit its further application for *in vivo* studies. First, 2D MR diffusion/relaxation spectra have never been combined with MRI; this combination is

important for localizing and isolating different types of tissue and for further preclinical and clinical studies. Second, this type of method requires the acquisition of much more MR data than is currently feasible in preclinical or clinical time frames. To address the first problem, in Chapter 3, efforts were made to develop mathematical frameworks to overcome one of the problems in transferring the NMR spectroscopy method to MRI: correcting the artifacts caused by signal noise type changes that occur when NMR spectroscopy data (complex) are transferred to MRI magnitude data (magnitude). To address the second problem, in Chapter 4, we explored one way to dramatically reduce the data required to measure these 2D MR relaxation spectra, culminating our recent use of compressed sensing (CS), where we showed a 10-fold reduction in data to reconstruct a 2D MR relaxation spectra, reducing a 10-hour experiment to a one-hour experiment. Other problems and our planned solutions for further advancing the use of this type of important technique are discussed in Chapter 7.

Chapter 2: Initial effort: NMR water self-diffusion and relaxation studies on a biomimetic model of neuronal activity in physiologic ionic solutions

As discussed in Section 1.4.2, one way to study the complicated water dynamics in tissue is by using biomimetic models to simplify the problem and isolate each part's contribution. In this Chapter, sodium polyacrylate (NaPA) hydrogel in the physiological ionic solution was chosen as a biomimetic model of nerve excitation, which exhibits an abrupt volumetric phase transition in the presence of multivalent cations in the physiological concentration range. In this work, water self-diffusion coefficients and longitudinal relaxation rates in NaPA solutions and gels were measured by NMR, as a function of polymer content and structure in a physiological concentration range of monovalent and divalent cations, Ca^{2+} and Na^{+}. Several physical models describing the self-diffusion of the solvent were applied and compared. This work was adapted from our manuscript 1 published on *Journal of Applied Polymer Science* [155] (Appendix A).

2.1 Sodium polyacrylate (NaPA) hydrogel as a biomimetic model of nerve excitation

Knowledge of the dynamics of small molecules in polymeric materials is important to advance polymer-based technologies such as membrane separations, barrier materials, controlled drug release, ion-exchangers, packaging, biosensors, and chemical sensors [193–195]. Polyelectrolyte hydrogels are environmentally sensitive (pH and counterions), and can be used for site-specific drug delivery [196,197].

Many anionic polyelectrolyte gels exhibit an abrupt volumetric phase transition in the presence of multivalent cations in the physiological concentration range [198,199]. This phenomenon is believed to be related to important physiological processes such as nerve excitation and muscle contraction [174,175,198–201] where first-order phase transitions have been observed. Investigating the physical properties of synthetic polyelectrolyte gel model systems may lead to a better understanding of these phenomena. For these reasons, substantial work has been done to characterize the thermodynamic properties and structure of polyelectrolyte gels and the dynamics of small molecules in polymer matrices (e.g., concentrated solutions and gels).

It has been demonstrated that water plays an essential role in determining the physical properties of polyelectrolyte systems (e.g., solutions of RNA, carbohydrate, and proteins) [202,203]. Experimental studies as well as simulations demonstrated a strong coupling between the dynamics of polymer and solvent molecules [204,205]. It has been reported that the dynamics of biomolecules is strongly coupled to the onset of translational motions of hydration water [206,207], and the rotational dynamics of water molecules is changed by the polymer [208,209]. However, the mechanism of this coupling is poorly understood.

Previous studies have raised several important questions: Does the presence of the polyelectrolyte chain affect only the translational mobility of the water or does it also influence the orientational mobility? What is the molecular mechanism underlying these processes? Is the dynamics of water different in gels and in solutions of the same uncrosslinked polymer at the same polymer concentration? How does monovalent-divalent ion exchange affect the dynamics of water in

polyelectrolyte systems? To address these questions, we determined the mobility of the solvent (water) in model sodium polyacrylate (NaPA) solutions and gels by NMR spectroscopy. The self–diffusion coefficient and longitudinal relaxation rate of water were measured as a function of the polymer concentration. Water self-diffusion is governed by its local translational mobility while its longitudinal relaxation rate is sensitive to the local orientational mobility. The water density and order, and the interaction between polymer and solvent molecules affect both quantities. The results were analyzed in terms of different physical models of self-diffusion and longitudinal relaxation of solvent. The mobility of water was further investigated in the presence of mono- and divalent counterions (Na^+ and Ca^{2+}) in a physiological range of concentrations.

The paper is organized as follows. After describing our experimental methodology, we briefly review various physical models of solvent self-diffusion and evaluate their applicability to describe the experimental data. In the next section we focus on the analysis of the spin-lattice relaxation of water in salt free polyelectrolyte solutions and gels. This is followed by the discussion of the effect of added salts on the self-diffusion coefficient and spin-lattice relaxation rate of water.

2.2 NaPA solution and hydrogel synthesis and NMR setups

2.2.1 NaPA solution preparation

Aqueous solution of sodium polyacrylate (NaPA, M_w = 15 kDa, concentration: 35% w/w) was purchased from Sigma–Aldrich. No further purification steps were performed. The NaPA solution was diluted by deionized water to the designated concentrations. Salts (NaCl or $CaCl_2$) were added to the solutions during dilution.

2.2.2 NaPA hydrogel preparation

NaPA gels were made in aqueous solution by free–radical copolymerization of acrylic acid monomer and N, N'-methylenebis(acrylamide) cross-linker according to a procedure described previously [198]. The initial monomer concentration was 37% (w/w), and 31% of the monomers were neutralized by sodium hydroxide before polymerization. Dissolved oxygen was removed by bubbling nitrogen through the solution. Then, the monomer solution was diluted to the designated concentration and appropriate amounts of salts (NaCl or $CaCl_2$) were added. Finally, potassium persulfate (0.5 g/L) was added to initiate the polymerization reaction, and the solution was placed in an oven at 70^{o}C.

2.2.3 NMR-MOUSE

The NMR measurements were made by a single–sided NMR system (Profile NMR–MOUSE, ACT GmbH, Germany). Single-sided NMR systems developed in the last two decades possess the advantages that they are portable and reliable to study relaxation times and diffusion coefficients of various samples [150]. They are widely used in diverse fields such as in the rubber and polymer industries, food and materials processing applications [150,154,210–213].

A surface RF coil is placed on top of the magnet to excite and detect the NMR signal. The magnetic field strength at the selective volume is 0.32 T (corresponding to ^{1}H Larmor frequency of 13.79 MHz), with a strong and highly uniform magnetic field gradient of 15.3 T/m across the selective volume. The Kea spectrometer and Prospa acquisition software are provided by Magritek, New Zealand. All NMR measurements were made at ambient temperature (23 ^{0}C ± 1 ^{0}C).

2.2.4 Self-diffusion measurement

Self-diffusion coefficients were measured by Hahn spin echoes (90^o-τ-180^o-τ-echo) in the presence of a static and uniform magnetic field gradient [214]. To improve the sensitivity of these experiments, a Carr–Purcell–Meiboom–Gill (CPMG) pulse sequence was applied after the main diffusion-encoding period. The normalized signal attenuation for the Hahn echoes is [48],

$$I / I_0 = \exp(-bD) \tag{2.1}$$

with

$$b = \frac{2}{3}(\gamma G)^2 \tau^3 \tag{2.2}$$

where γ is the gyromagnetic ratio of protons, G is the strength of the static magnetic field gradient, D is the self-diffusion coefficient, and τ is the encoding period or echo time. Eight b–values (< 1200 s/mm^2) were used to produce a diffusion decay curve with 1024 echoes being added and 8 scans being performed for each b-value. This method was validated by measuring the self-diffusion coefficient, D, of various solvents, such as water, methanol, ethanol [214]. All the diffusion decay curves were well fit by a single exponential function.

2.2.5 Longitudinal relaxation time measurement

Longitudinal relaxation times (T_1) were measured by using a saturation recovery sequence (saturation – recovery time Δ - detection), followed by a CPMG train to improve the sensitivity, similar to the methods described above. Eight recovery times, Δ, were used to obtain a recovery curve, and 8 scans for each

recovery time, with 1024 echoes were added for each scan. The data were fitted to a mono-exponential function with a minor baseline [150]. The accuracy of our method was tested using a series of manganese chloride ($MnCl_2$) solutions and we found reasonable agreement to literature values [215,216].

2.3 Self-diffusion measurements in NaPA solution and gel as a function of polymer concentration

Various physical models have been proposed to describe self-diffusion of solvent molecules in polymer gels and solutions. These models fall into three general categories: 1) obstruction, 2) hydrodynamic, and 3) free volume [217].

First we analyze the experimental data using two obstruction models: the Maxwell [217], and the Mackie-Meares model [218]. Then, the validity of the cell model, a combination of obstruction and hydration models, is tested [219]. Finally, we apply the Vrentas-Duda free-volume model [220].

Fig. 2.1 shows the results obtained for NaPA solutions and gels in the absence of added salt. It can be seen that D is significantly greater in the gel than in the corresponding solution, and is practically independent of the cross-link density.

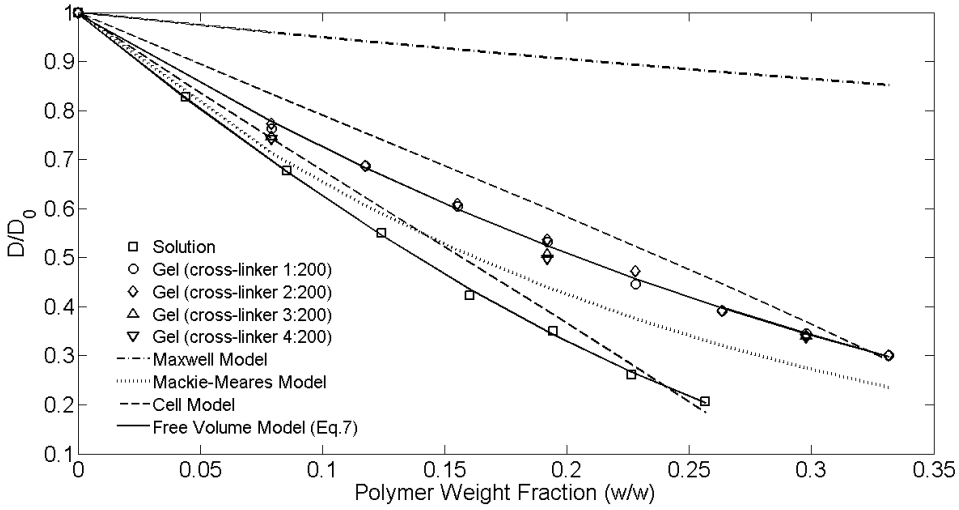

Figure 2.1. Self-diffusion coefficient D of NaPA solutions and gels with various cross-link densities normalized by the self-diffusion coefficient of the pure water D_0. The curves are fits of solution data and gel data with crosslink density 1:200 by different models (see text).

2.3.1 Obstruction model

In the obstruction models, the polymer chains are considered to be impenetrable and motionless relative to the small diffusing solvent molecules. The polymer hinders the diffusion of water molecules, increasing the path length required by a geometric tortuosity factor. Consequently, the apparent self–diffusion coefficient of small molecules decreases. In these models no interaction between the polymer and solvent molecules is taken into account. The obstruction effect is closely related to the shape of the obstructers; rod-like shapes obstruct more than spheres [221]. There are two main diffusion models based exclusively on the obstruction effect, 1) the Maxwell model, which assumes that the obstructers are spheres, and 2) the Mackie-Meares model [218], where the polymer chains are assumed to be impenetrable, motionless, infinitely long rods.

In the Maxwell model the self-diffusion coefficient D of the solvent is

expressed as [215],

$$\frac{D}{D_0} = \frac{1}{1+\Phi/2} \tag{2.3}$$

where D_o is the self-diffusion coefficient of the pure solvent and Φ is the volume fraction of the polymer

$$\Phi = \frac{m^{poly} v^{poly}}{m^{poly} v^{poly} + m^{water} v^{water}} \tag{2.4}$$

In Eq. 2.4, m^{poly} is the mass and v^{poly} (= 0.82 cm^3/g) is the specific volume of NaPA, and m^{water} and v^{water} are the mass of water and its specific volume, respectively.

The Mackie-Meares model yields the expression [218]:

$$\frac{D}{D_0} = \left[\frac{1-\Phi}{1+\Phi}\right]^2 \tag{2.5}$$

Fig. 2.1 clearly shows that the obstruction models do not adequately describe the concentration dependence of the self-diffusion coefficient. The Maxwell model seriously underestimates the obstruction effect of the NaPA. By contrast, the Mackie-Meares model reproduces the self-diffusion of water at low polymer concentration (c < 10% w/w) relatively well. The failure of these two obstruction models at high polymer concentrations may be due to either the complex geometry of the polymer chain or hydration effect that slows down water self-diffusion [217,222]. The gel data fall between the Maxwell and Mackie–Meares models. The reduced obstruction effect for the gel suggests that crosslinking may alter the effective geometry of the polymer chains with respect to water diffusion.

2.3.2 Combined obstruction and hydration model

A possible reason for the failure of obstruction models is that the interaction between water and polymer slows down the water self-diffusion close to the polymer. The cell-diffusion model of Jönsson, et al. takes into account both obstruction and hydration effects [219]. The model successfully predicts the self-diffusion of water in casein dispersions [223], in various surfactant-water systems [224], and also in whey protein solutions [225]. The macroscopic system is divided into identical cells containing one polymer molecule surrounded by water. In each cell, a distinction is made between hydration water and bulk water that may have different densities and mobilities. The macroscopic self-diffusion constant is represented by an apparent diffusion coefficient obtained by solving the diffusion equations for the cell with appropriate boundary conditions [219,225]. The cell model yields for a solution of spherical particles

$$D_{eff} = D_0\left(1+0.75\frac{m^{poly}}{m^{water}}\right)\frac{\left(1+0.75\frac{m^{poly}}{m^{water}}-k\frac{m^{poly}}{m^{water}}\right)}{1+0.75\frac{m^{poly}}{m^{water}}+0.5\frac{m^{poly}}{m^{water}}} \tag{2.6}$$

where k is a fitting parameter.

Eq. 2.6 was used to fit the NaPA solution and gel (with cross-link density 1:200) data with different values of k. Fig. 2.1 shows that this model fails to estimate the experimental diffusion coefficients over the entire concentration range. The observed discrepancy may be related to the deviation of the geometry of the NaPA chains from the assumed spherical shape.

2.3.3 Free volume model

The free volume model is based on the concept that molecular transport is

mainly governed by the occurrence of two events: 1) a hole of sufficient size (free volume) should appear adjacent to the small molecule, and 2) the molecule should have enough energy to jump into it [226]. The polymer reduces the free volume of the solution, which explains the observed decrease in the solvent self-diffusion coefficient with increasing polymer concentration [227]. This model satisfactorily describes self-diffusion of small molecules in numerous polymer solutions such as (polyvinyl acetate)–toluene [228], polystyrene-benzene systems [229,230], water–gelatin [231], water–PEG [232] and water-Poly(N,N-dimethylacrylamide) (PDMAA) gels [233].

The Vrentas-Duda theory [220,234] predicts that the self-diffusion coefficient of small molecule (solvent) in a binary system is

$$\frac{D}{D_0} = \exp\left\{ \frac{-(w_1\hat{V}_1^* + w_2\xi\hat{V}_2^*)}{\left(\frac{K_{11}}{\gamma}\right)w_1\left(K_{21} - T_{g1} + T\right) + \left(\frac{K_{12}}{\gamma}\right)w_2\left(K_{22} - T_{g2} + T\right)} - \frac{-\hat{V}_1^*}{\left(\frac{K_{11}}{\gamma}\right)\left(K_{21} - T_{g1} + T\right)} \right\} \tag{2.7}$$

where w_1 and w_2 are the weight fractions of the solvent and the polymer, T is the absolute temperature, and K_{11}, K_{12}, K_{21}, K_{22}, T_{g1}, T_{g2}, $\hat{V}_1^*$, $\hat{V}_2^*$, ξ, γ are constants (free volume parameters of polymer and solvent). For water the free volume parameters known from the literature [231] are listed in Table 2.1. The two independent parameters for the polymer, $\xi\hat{V}_2^*$ and $(K_{22} - T_{g2} + T)K_{12}/\gamma$, were obtained by fitting Eq. 2.7 to the experimental data.

Parameters	Value	Note
K_{11}/γ ($cm^3g^{-1}K^{-1}$)	2.33×10^{-3}	From ref [231]
$K_{21}-T_{g1}$ (K)	-156.9	From ref [231]
$\hat{V}_1^*$ (cm^3g^{-1})	1.071	From ref [231]
$\xi\hat{V}_2^*$ (cm^3g^{-1})	0.95 (±0.10)	By fitting Eq. 2.7 (in solution)
$\xi\hat{V}_2^*$ (cm^3g^{-1})	1.37 (±0.10)	By fitting Eq. 2.7 (in gel)
$K_{12}(K_{22}-T_{g2}+T)/\gamma$ (cm^3g^{-1})	-0.01 (±0.02)	By fitting Eq. 2.7 (in solution)
$K_{12}(K_{22}-T_{g2}+T)/\gamma$ (cm^3g^{-1})	0.16 (±0.02)	By fitting Eq. 2.7 (in gel)

Table 2.1. Parameters used and obtained in free volume model.

Fig. 2.1 also shows the fits of Eq. 2.7 (solid line) to the NaPA solution and gel (with cross-link density 1:200) data. In Table 2.1 are listed the fitting parameters of Eq. 2.7. In both systems the agreement between the prediction of Eq. 2.7 and the experimental data is reasonable. The difference in the fitting parameters may reflect the presence of cross-links. Cross-linking causes the redistribution of the polymer chains and modifies the thermodynamics of the polymer/solvent system [235,236]. However, further experiments and theories are needed to understand the underlying physical difference between the polymer solution and gel and the influence on water self-diffusion.

It might be that obstruction effects dominate water self-diffusion in NaPA solutions and gels at low polymer concentrations, while at high polymer concentrations, the interaction between polymer and solvent molecules becomes nonnegligible. *D* is observed to be greater in gels than in polymer solutions at the same concentration, and although the free-volume models satisfactorily describe the water self-diffusion data, the underlying physical mechanisms for the difference remain unclear.

In what follows we investigate the effect of polymer concentration and ions on

the spin-lattice relaxation of water in NaPA solutions and gels.

2.4 Spin-lattice relaxation time, T_1, in NaPA solution and gel as a function of polymer concentration

In water–polymer systems two types of water are present: 1) polymer-associated water; and 2) "free" water that is not influenced by the presence of the polymer. The spin–lattice relaxation rate of water is sensitive to both the structure of the polymer and the interaction between the polymer and water. Neutron and X-ray scattering measurements indicate that the density of water is greater near the polymer than in the bulk [237]. It was also reported that the translational and orientational mobility of polymer-associated water was slower than that of the free water, and orientation became anisotropic due to interaction with macromolecules [238].

In polymer systems, the relaxation behaviour of water nuclei has been described in terms of a fast-exchange two-site model [239–241]. The effective spin–lattice relaxation rate is given by [181,242]

$$\frac{1}{T_{1,eff}} = \frac{f_b}{T_{1,b}} + \frac{1-f_b}{T_{1,f}} \tag{2.8}$$

where f_b and $T_{1,b}$ are the fraction and average longitudinal relaxation time of polymer-associated water, and $1\text{-}f_b$ and $T_{1,f}$ are the fraction and longitudinal relaxation time of the free water.

In Fig. 2.2 we plot the spin-lattice relaxation rate $1/T_1$ as a function of the polymer concentration. The data indicate that at low polymer concentration, the dependence of spin-lattice relaxation rate on polymer concentration can be

approximated as linear. This finding implies that $T_{1,b}$ is constant and f_b is proportional to the fraction of the polymer. At higher concentrations (above 0.12 g/g in the solution and gel), however, $1/T_1$ increases faster than linear. Similar behavior was reported for other polyelectrolyte solutions such as low molecular weight PAA-water [238], protein–water [225], and β-lactoglobulin-water solutions [243]. Based on the two-site model, the deviation from linearity may be caused either by the increased number of polymer-associated water molecules or the faster relaxation rate $1/T_{1,b}$ of this water.

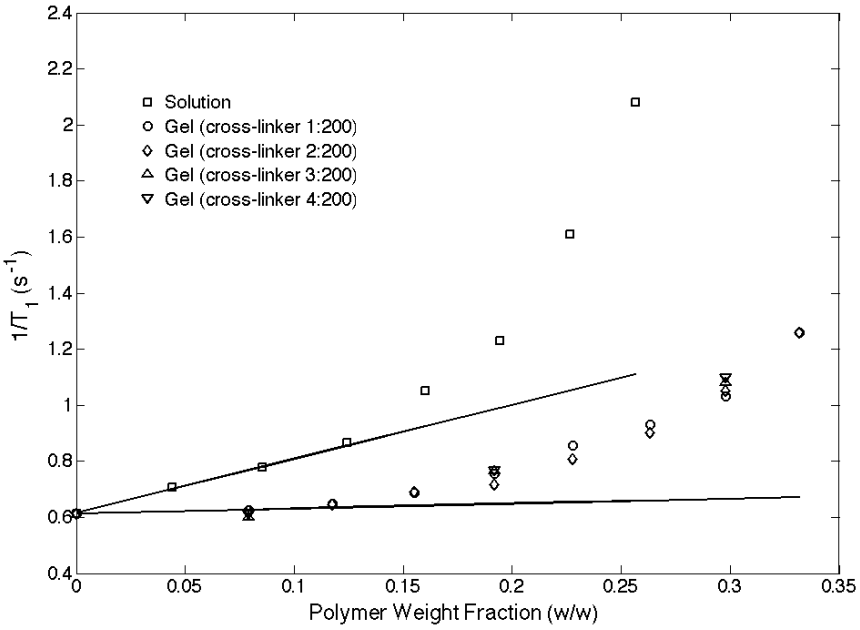

Figure 2.2. Variation of the spin-lattice relaxation rate $1/T_1$ as a function of the NaPA weight fraction in solutions and gels with various cross-link densities. Continuous lines are fits of Eq. 2.8 to the experimental data.

In summary, the results show that D is greater and the relaxation time T_1 is longer in the gel than in the polymer solution at the same concentration. These findings imply that the crosslinked polymer has a smaller effect on water mobility

than its uncrosslinked counterpart. The variation of the cross-link density of the gel does not have significant effect on either D or $1/T_1$.

There are two possible explanations for the difference of solvent mobility between the uncrosslinked polymer and the crosslinked state: (1) the solvent mobility is dependent on polymer molecular weight, which changes from limited value in solution (15 kDa) to infinite in the gel. However, in concentrated polymer solutions (above 0.12 g/g), the effect of polymer molecular weight should be minimal due to the strongly overlapped chains. Previous experiments on small molecule' self-diffusion in polymer solutions as a function of polymer molecular weight showed solvent mobility is independent of, or only weekly dependent on polymer molecular weight especially when the chains are high molecular weight [232,244]. In the present study, NaPA with 15 kDa was chosen to avoid this effect. (2) The cross-linking process modifies the chemical properties of polymer chains and the polymer-solvent interaction. Our present observation is consistent with evidence from previous macroscopic experiments and theory: there are important thermodynamic differences between the two states, and these changes are not simply proportional to the number of cross-linking points [235,245,246]. Osmotic pressure measurements on poly(vinyl acetate) gel were found to be almost independent of the cross-linking density of the gel [235]. A similar change in the self-diffusion coefficient from the uncrosslinked state to the crosslinked state was also reported for polydimethylsiloxane (PDMS)–toluene systems [245]. The difference was attributed to structural inhomogeneities created by the crosslinking process. During crosslinking polymer rich regions are formed, which coexist with regions of diminished polymer concentration. The NaPA

gels have been observed to contain large inhomogeneities (greater than 1000 Å) as detected by small-angle neutron scattering measurements [247]. More experiments are needed to validate these hypotheses and elucidate the underlying chemical and physical mechanisms.

2.5 Effect of ions on the dynamic properties of water in NaPA solution and gels

We determined the self–diffusion coefficient and the longitudinal relaxation rate of water in polymer-free salt solutions [248] and in NaPA solutions and gels. The data listed in Table 2.2 show that monovalent salt (NaCl) has no significant effect on D and $1/T_1$.

Polymer Concentration (w/w)	NaCl Concentration (M)	D (10^{-9} m^2/s)	$1/T_1$ (s^{-1})
0% (solution)	0	2.12 (0.02)	0.56 (0.02)
0% (solution)	1.0	2.06 (0.02)	0.55 (0.02)
16% (solution)	0	1.16(0.01)	0.89(0.02)
16% (solution)	0.6	1.11(0.01)	0.92(0.02)
26% (gel)	0	0.99(0.01)	0.85(0.02)
26% (gel)	0.6	0.91(0.01)	0.89(0.02)

Table 2.2. Self-diffusion and spin-lattice measurements on NaPA solutions and gels in pure water and in NaCl solutions

Addition of divalent salt ($CaCl_2$) slightly modifies the self–diffusion coefficient (Fig. 2.3a) and significantly enhances the longitudinal relaxation rate (Fig. 2.3b). The latter increases by more than 70% as the $CaCl_2$ concentration varies from 0 to 0.4 M. The curves in Fig. 2.3b can be satisfactorily described by a 2^{nd}-order polynomial. The results also indicate that the enhancement of $1/T_1$ is more pronounced at higher polymer concentration (at constant $CaCl_2$ concentration).

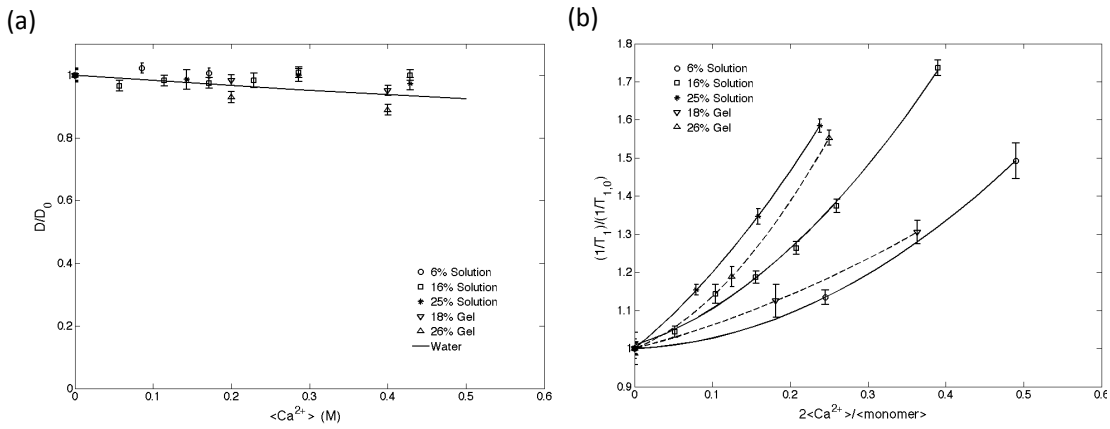

Figure 2.3. (a) Self-diffusion coefficient and (b) spin-lattice relaxation rate as a function of $CaCl_2$ concentration in both NaPA solutions and gels (crosslink density 2:200). All the data are normalized by the initial values.

The data shown in Fig. 2.3a and b reveal important differences between the effects of Na^+ and Ca^{2+} ions on the mobility of water. The weak influence of NaCl suggests that the diffuse monovalent ion cloud does not affect the conformation of the polymer and the interaction between the polymer and solvent. In the case of Ca^{2+} ions the increased spin-lattice relaxation rate reflects the more effective charge compensation when calcium ions replace sodium ions.

Previous studies indicate that ions in polyelectrolyte systems affect the thickness and degree of order of the polymer-associated hydration shell [249–252]. Increasing salt concentration may decrease the hydration strength due to increased screening of charges on the polymer backbone [249]. Reduction of the hydration stress increases both the self-diffusion coefficient and relaxation time. However, the observed reduction of the relaxation time shows that in the present system the interaction between Ca^{2+} and NaPA has no significant effect on the hydration strength between charged polymer and water.

Recent molecular dynamics simulation and anomalous small-angle X-ray scattering (SANS) measurements show that divalent cations are preferentially condensed onto oppositely charged polyelectrolyte chains while monovalent cations move more freely [201,253]. In calcium ion containing systems the orientational mobility of the polyelectrolyte molecule may be slowed due to electrostatic attraction between the calcium ion and two negative charges on the polymer backbone, which may further slow the tumbling rate of polymer-associated water molecules and result in a shorter relaxation time.

2.6 Discussions and conclusions

The self–diffusion coefficient and longitudinal relaxation rate of water in NaPA solutions and gels were determined by NMR. The self-diffusion measurements were analyzed in terms of different physical models of solvent self-diffusion in polymer systems. It was found that the free volume model provides a satisfactory fit of both solution and gel results.

To describe the relaxation response of water a linear two–site fast exchange model was adopted. In gels the self–diffusion coefficient is greater and the relaxation time of water is longer than in the corresponding (uncrosslinked) polymer solutions. The observed difference can be attributed to chemical and structural changes caused by cross-linking, however their influence on solvent mobility is almost independent of the number of cross-linking points. Na^+ only slightly affects the relaxation rate and self-diffusion coefficient of water. Addition of Ca^{2+} enhances the relaxation rate but only weakly modifies the self-diffusion coefficient. Further studies are required to understand the differences between the dynamic behaviour of polyelectrolyte gels and

solutions and to clarify the effect of monovalent and divalent cations on the NMR relaxation properties of charged polymer systems.

Chapter 3: Combining MR diffusion/relaxation spectra with imaging: a framework for accurate determination of the relaxation spectra from magnitude MRI images

The multidimensional MR diffusion/relaxation spectra shows great potential in the quantitative characterization of the microstructure heterogeneity and motions among different water microenvironments. This type of information will be very helpful in detecting some key biological information, such as cell size, extracellular matrix volume, cell membrane permeability, active water motion, etc., which is very important to understanding the water dynamics in living neural tissue and during the neuronal activity process. To further promote this type of technique for the study of living tissue, the first step would be to combine it with imaging to isolate different types of tissues and localize the regions of interest to us. A typical problem for transferring the NMR spectroscopy methods to MRI methods is the change in the data format and properties. The data from NMR spectroscopy is normally in complex format and the noise is Gaussian distributed, while the data from MRI only contains the magnitude of the data with low SNR and its noise is in Rician distribution. In this chapter, I will discuss a mathematical framework we developed to accurately determine the transverse relaxation (T_2) spectra from multiple echo magnitude MRI images. Though only one-dimensional T_2 spectra were tested and validated here in this study, this method is general and can be applied to other one-dimensional or multi-dimensional diffusion/relaxation spectra with proper adaption. This chapter was

adapted from our manuscript 2 published in the *Journal of Magnetic Resonance* [254] (Appendix A).

3.1 Artifacts caused by the low-SNR magnitude MRI data in the estimation of T_2 relaxation spectra

NMR relaxation measurements have been widely applied to study molecular dynamics in porous media [255,256], polymers and gels [155,211,225], food sciences [257], material sciences [258], plant tissue [259], and animal and human tissue studies [181,260]. NMR relaxometry, combined with MR imaging, is a powerful tool for characterizing the detailed microstructure of animal and human tissue *ex vivo* and *in vivo*, revealing complex microstructure in the brain [53,178,261], a layered structure in the cartilage [262], distinct domains in bone [263], etc.

Magnitude, rather than complex MRI signals, is widely used in quantitative MRI studies. This choice is primarily due to the fact that the phase of MRI signals is sensitive to many experimental factors, such as scanner type, field inhomogeneity, temperature, coil type, pulse sequence design, motion, etc. [264–267]. While magnitude MRI is preferred in relaxation experiments, the signal-to-noise ratio (SNR) in MRI is usually much lower than in its NMR counterpart. Ideally, the distribution of the NMR and MRI signal is Rician rather than Gaussian [264,268,269]; this distribution can cause problems in estimating relaxation parameters accurately, such as the T_1 and T_2 in MRI [270,271], particularly as the MRI signal approaches the background noise levels.

Quantitative T_2 (qT_2) MRI spectroscopy has attracted more attention in recent years due to its ability to identify microstructure-dependent T_2 components empirically without invoking prior modeling assumptions [177–181]. Specifically, the T_2 distribution—a plot of component weightings as a function of T_2—can provide information about the relative fraction of different distinct components in a material, such as the myelin water fraction within nerve samples. Calculated maps can yield potentially important biomarkers of pathology in demyelination diseases such as multiple sclerosis [53,177,272,273].

Typically, to obtain the T_2 distribution, a multi-echo MRI acquisition is performed on a single slice or multiple slices, and then the magnitude MRI data is directly fitted to an inverse Laplace transform (ILT) algorithm. This transformation is achieved by decomposing the signal into a sum of discrete exponential components, each with a unique relaxation time and amplitude. Estimates derived through ILT are generally sensitive to the presence of noise [58,182,185,271]. Furthermore, conventional ILT algorithms are based on least-squares methods that assume the signals are Gaussian distributed with a constant variance. Since the ideal magnitude MR signal is Rician distributed it is biased more toward a higher value than the noise-free signal intensity, while the signal variance is artificially decreased as the SNR approaches zero [268,269,271,274,275].

Specifically, noise in qT_2 MRI acquisitions can produce spurious cerebrospinal fluid (CSF)-like long T_2 components, bias of the true geometric mean T_2 (gmT_2) values and relative fractions of various components, and blurring of nearby T_2 peaks [275], all of which limit the accuracy of qT_2 MRI. Recently, a temporal phase

correction algorithm was developed to separate the relevant decay information from the noisy complex signal into the real channel, leaving only noise in the imaginary channel [275]. Although this strategy may improve some aspects of qT_2 MRI, the phase of the complex MRI signal may differ on the basis of the equipment used (scanners, coils, etc. [264–267]). The magnitude of the complex MR signal remains the most commonly used data in quantitative measures in MRI. Ideally, we would like to develop a scheme that maps the noisy magnitude MRI data to a Gaussian-distributed signal.

In our previous work, a signal transformation framework was proposed to map noisy Rician-distributed magnitude diffusion weighted MRI (DWI) signals into Gaussian-distributed DWI signals without using the phase information [274]. This framework has been applied successfully in quantitative diffusion MRI studies [274,276]. Generally, the first step includes estimation of noise variance and underlying signal, followed by transformation of the signal distribution to a Gaussian.

Here we adapt and extend this framework from DWI applications, most of which are model-based, to multi-echo qT_2 MRI spectral data that invokes no prior modeling assumptions. The artifacts in the T_2 distribution caused by the Rician MRI signals were systematically studied in simulations and real multi-echo MRI experiments within different SNR. The effectiveness of the modified signal transformational framework was investigated in this new application and our proposed framework was found to yield more accurate estimates of the T_2 distribution over a large range of SNR than direct use of magnitude MRI.

3.2 A signal transformation framework to map noisy Rician-distributed magnitude MRI signals into Gaussian-distribution signals

3.2.1. Distribution of the magnitude MR signals

It is well known that that using the magnitude of the Gaussian-distributed complex MRI data follows a Rician distribution, which is characterized by the following probability density function (PDF) [264,277]:

$$p(m \mid \eta, \sigma_g) dm = \frac{m}{\sigma_g^2} \exp\left(-\frac{\eta^2 + m^2}{\sigma_g^2}\right) I_0\left(\frac{m\eta}{\sigma_g^2}\right) dm \ , \tag{3.1}$$

where m is the noisy magnitude data, η is the underlying signal intensity, σ_g is the Gaussian noise standard deviation, and I_0 is the 0^{th}-order modified Bessel function of the first kind. The corresponding cumulative distribution function (CDF) can be expressed as [274]:

$$\begin{aligned} p_r(\alpha \mid \eta, \sigma_g) &= \int_0^{\alpha} p(m \mid \eta, \sigma_g) dm \\ &= 1 - \int_{\alpha}^{\infty} p(m \mid \eta, \sigma_g) dm \\ &= 1 - Q(\eta / \sigma_g, \alpha / \sigma_g) \end{aligned} \tag{3.2}$$

where Q is the generalized Marcum-Q function.

An important special limiting case of the Rician distribution is when the SNR (SNR = η / σ_g) is high enough that the PDF of Eq. 3.1 approaches the Gaussian distribution with a sample mean η and standard deviation σ_g [269]. Another important special case is when the underlying signal is zero, so that the Rician distribution in Eq. 3.1 reduces to a Rayleigh distribution [269]:

$$p_r(m \mid 0, \sigma_g) dm = \frac{m}{\sigma_g^2} \exp\left(-\frac{m^2}{2\sigma_g^2}\right) dm \ . \tag{3.3}$$

3.2.2 The framework for accurate determination of the T_2 distribution from multi-echo magnitude MRI images

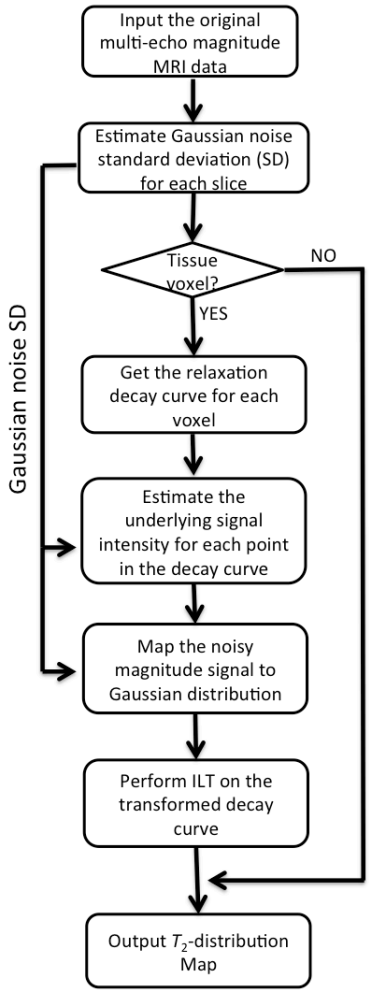

Figure 3.1. Framework to determine the T_2 distribution for each voxel.

The framework we proposed to accurately estimate T_2 distribution from multi-echo magnitude MRI images is described in Fig. 3.1. There are four essential steps: 1) the variance of the noise is estimated taking advantage of the multidimensional data structure (3.2.2.1), 2) the underlying signal intensity is estimated using an adapted

fixed point formula (3.2.2.2), 3) the estimated variance and underlying signal intensity are then used to transform the noisy magnitude signal to a noisy Gaussian-form signal by using the probability integral transform to match the cumulative distribution functions (3.2.2.3), and 4) an ILT algorithm is then performed on the transformed data to estimate the T_2 distribution for each voxel (3.2.2.4).

3.2.2.1 Estimation of the noise standard deviation (SD)

The accuracy of the noise variance estimation affects the accuracy of the estimate of the underlying signal intensity and of the transformed signal. Most current methods to estimate noise variance are based on applying the Rayleigh distribution Eq. 3.3 to fit the noise within a selected region of interest (ROI) on the magnitude MR image [264,277–280]. However, the additional information contained in the multi-dimensional data structures, such as the additional T_2 dimension in multi-echo MRI, provides an opportunity to use more advanced noise estimation approaches. Recently, we proposed a coherent framework for the probabilistic identification and estimation of noise (also known as PIESNO [281]). This approach was developed for the simultaneous identification of the noise-only pixels and estimation of the noise variance by taking advantage of the special data structure similar to multi-echo MRI for qT_2. The method can be briefly described as follows.

For a measurement $m_{i,j,k}$, where i,j are the x-y spatial coordinates and k is the added experimental dimension, for example, different echo times with K measurements. Assuming that the Gaussian noise SD, σ_g, across the added dimension is uniform, we may write the sample mean $s_{i,j}$ as:

$$s_{i,j} = \frac{1}{K}\sum_{1}^{K} t_{i,j,k} = \frac{1}{2\sigma_g^2 K}\sum_{1}^{K} m_{i,j,k}^2 \quad . \tag{3.4}$$

If $s_{i,j}$ is in the acceptable range of the corresponding CDF of Eq. 3.3, the corresponding pixels along k will be designated noise only. This is a self-consistent method, where the collection of identified noise-only pixels will be used to determine the underlying Gaussian SD; then a new iteration begins in which the new estimate of the Gaussian SD is used in Eq. 3.4. The iteration continues until the Gaussian SD converges or the iteration reaches the maximum threshold.

3.2.2.2. A fixed point formula for the estimation of the underlying signal intensity

The estimation of the underlying signal intensity η follows the fixed point formula developed in our previous work [268,274] by finding the solution of the following equation:

$$\eta = g\left(\eta \mid \langle m \rangle, \sigma_g\right) = \sqrt{\langle m \rangle^2 + \left[\zeta\left(\eta \mid \sigma_g\right) - 2\right]\sigma_g^2} \tag{3.5}$$

where $<m>$ is the first moment of m, which is estimated by smoothing the decay curve, and ζ is an analytical function of signal intensity η and noise SD σ_g. More details about Eq. 3.5 are summarized in Section 3.7. This formula has been modified for qT_2 MRI application by assigning the underlying signal intensity η to be 0 rather than a negative value as in our previous framework when the estimated $<m>$ is occasionally below the noise floor $\sqrt{\pi/2}\sigma_g$ when the SNR is close to 0 (for details see Section 3.7).

3.2.2.3 Mapping the noisy magnitude signal to Gaussian distribution

Using the Gaussian SD σ_g and the underlying signal η estimated in Section 3.2.2.1 and 3.2.2.2, respectively, the corresponding CDF for measurement m can be calculated from Eq. 3.2. The inverse cumulative probability function of a Gaussian random variable and the cumulative probability function of noisy Rician magnitude

signals using the probability integral transform [282,283] are then used to map from the noisy magnitude signal to a Gaussian form. The final transformed noisy Gaussian signal χ would be:

$$\chi = P_G^{-1}\left(P_r\left(m\middle|\eta,\sigma_g\right)\middle|\eta,\sigma_g\right) \tag{3.6}$$

where P_G^{-1} is the inverse cumulative distribution function of a Gaussian distribution. More details can be found in [274].

3.2.2.4. ILT algorithm

A nonnegative least squares (NNLS) algorithm with Tikhonov regularization was then applied on the transformed relaxation decay signals [284,285]. In the absence of noise, the ideal T_2 relaxation decay curve can be described as a multi-exponential function:

$$\eta(t_k) = \eta_0 \sum_{n=1}^{N} F\left(T_{2,n}\right)\exp\left(-t_k / T_{2,n}\right), \qquad k = 1,2,.....,K \tag{3.7}$$

where η_0 is the proton density, F is the probability function at each T_2 value and is assumed to be non-negative, t_k are the K echo times, and $T_{2,n}$ are the N logarithmically spaced T_2 time spacing. A robust and relatively stable solution of $F(T_{2,n})$ in the presence of noise can be obtained by minimizing Ξ

$$\Xi = \sum_{k=1}^{K}\left(\eta\left(t_k\right) - \chi_k\right)^2 + \mu\sum_{n=1}^{N} F\left(T_{2,n}\right)^2 \tag{3.8}$$

where χ_k is the transformed signal χ at echo time t_k, and μ is the parameter controlling the Tikhonov regularization. A Butler-Reeds-Dawson (BRD) method [286] based on the Morozov discrepancy principle [287], which compares $d(\log_{10}\Xi)/d(\log_{10}\mu)$ against a user-defined tolerance, TOL [288], was used to robustly determine the value of μ.

3.2.3. Simulations of multi-echo MRI magnitude data

The decay curves of the multi-echo MRI magnitude data at different SNRs were simulated by Monte Carlo methods to explore their artifacts on qT_2 MR and the efficacy of our proposed framework in correcting them. The noisy multi-echo MRI magnitude signal m at echo time t_k was generated by the following function:

$$m_k = \sqrt{\left(\eta(t_k) + \varepsilon_1\right)^2 + \varepsilon_2^2} \tag{3.9}$$

where $\eta(t_k)$ is the ground truth calculated by Eq. 3.7 with targeted T_2 distribution and ε_1 and ε_2 are the Gaussian random variables with mean zero and targeted standard deviation. Two different T_2 distributions were explored to simulate different tissue properties: one contains only a single component with gmT_2 equal to 51.6 ms; the other contains two components whose gmT_2 and weightings are (15.7 ms, 50%) and (51.6 ms, 50%). In both cases, the underlying T_2 distributions have a narrow Gaussian shape in the logarithmic T_2 space. The initial SNR (iSNR $\equiv \eta_0/\sigma_g$) ranges from 10 to 400 for single-component cases and from 30 to 410 for the double-component simulations.

In each simulation, 50 echo times *TE* were uniformly sampled from 5 ms to 250 ms with a gap of 5 ms. The noisy magnitude data and their transformed signals were then analyzed to get the T_2 distributions using the ILT algorithm in Section 3.2.2.4. The T_2 distribution consisted of 50 T_2 bins logarithmically spaced between half of the shortest *TE* (2.5 ms) and two times the longest *TE* (500 ms). TOL in the BRD method was set to 0.003. To achieve stability in statistics, 1000 realizations were performed at each SNR level and each targeted T_2 distribution.

3.2.4 Multi-echo MRI experiments of a gel phantom and fixed spinal cord tissue

Two samples were prepared for MRI experiments: a composite agarose and $CuSO_4$ phantom and an excised porcine spinal cord. The phantom was made using a filled spherical insert in a 10mm NMR tube. Each sample was filled with a different $CuSO_4$ doped agar gel. The spherical insert was filled with 1% agar gel doped with 100mM $CuSO_4$ and the NMR tube was filled with 0.5% agar gel doped with 50mM $CuSO_4$. The porcine spinal cord was excised and immediately immersion fixed in a 4% formalin solution. The spinal cord was fully rehydrated with phosphate buffered saline (PBS) prior to the MRI experiments and then contained within a 10mm susceptibility-matching Shigemi tube (Shigemi Inc., Japan) with Fluorinert (3M, St. Paul, MN) filling the unoccupied space during the MRI experiments.

Multi-echo acquisitions were performed on a 7T Bruker Avance III vertical bore MRI scanner equipped with a micro2.5 gradient system (Bruker BioSpin, Billerica, MA). For both the gel phantom and the porcine spinal cord, a single slice was selected with 50 echoes starting at 7 ms and continuing to 350 ms in 7 ms increments. The other acquisition parameters for the gel phantom were: TR = 2000 ms, matrix size = 128x128, slice thickness = 0.2 mm, FOV = 12 mm × 12 mm, and repetitions = 50, and for the spinal cord were: TR = 3000 ms, matrix size = 128x128, slice thickness = 1.00 mm, FOV = 12 mm × 12 mm, and repetitions = 64. In both experiments, Hermite pulse shapes were applied for both excitation and refocusing pulses with bandwidth (5400 Hz) matching.

To achieve different SNR levels, the complex data were averaged using different numbers of repetitions from the whole set initially. The magnitude images were then processed according to the framework detailed in Section 2.2. The T_2

distribution also consisted of 50 T_2 bins logarithmically spaced between half of the shortest *TE* (3.5 ms) and twice of the longest *TE* (700 ms) with TOL= 0.003.

3.2.5 Analysis of the T_2 distributions

In the simulations, the T_2 distribution at each SNR level was determined by averaging the T_2 distributions of 1000 identical simulations with random noise. In the MRI experiments, ROIs were selected at first; then a T_2 distribution was calculated for each ROI by averaging the T_2 distributions for all of the voxels inside each ROI. In the phantom experiments, two ROIs were selected: one containing all of the shorter-T_2 gel and the second containing all of the longer-T_2 gel. In the spinal cord experiments, three ROIs (dorsal, lateral and ventral) in white matter (WM) and one ROI in gray matter (GM) with relative homogenous gmT_2 were selected for further analysis.

In both simulations and experiments, the T_2 distributions with a single component were divided into two regimes: 1) tissue-associated water, from the shortest T_2 bin to 200 ms and 2) CSF-like water, from 200 ms to the longest T_2 bin. As for the T_2 distributions with multiple components, the tissue-associated water was further divided into myelin water (MW, from the shortest T_2 bin to 27 ms) and intracellular/extracellular water (IEW, from 27 ms to 200 ms).

3.3 Validation of the framework

3.3.1 Estimation of the underlying Gaussian noise SD

To determine the accuracy of PIESNO in estimating the Gaussian noise SD from the multi-echo MRI data, both synthetic signals and the data from the

experiments with porcine spinal cord were investigated. The synthetic signals contained the same data structure (128x128x50) as the signals in the single-slice multi-echo experiment on the spinal cord. The T_2 relaxation decay curve in each voxel was generated following Eq. 3.9 with the single-component T_2 distribution with gmT_2 equal to 51.6 ms. The proton density η_0 was set to be 1 for the centered 64x64 square matrix and 0 for the other regions.

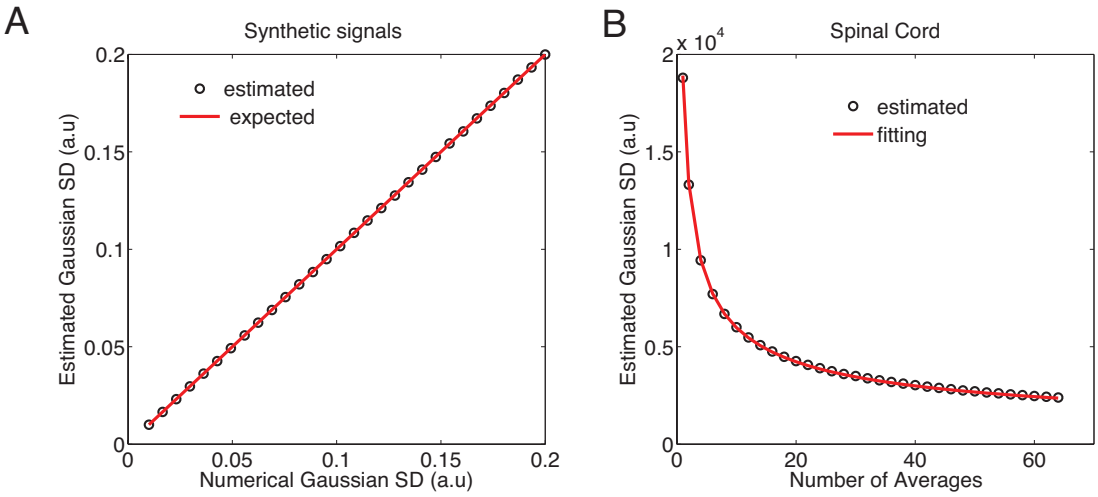

Figure 3.2. The estimated Gaussian SD via PIESNO from the synthetic signals with various noise levels (A) and from the spinal cord multi-echo MRI experiments with various averaging steps (B), where the red curve is the nonlinear fit of the data via Eq. 3.10.

The values of estimated Gaussian noise SD were plotted against the known SD σ_g from 0.01 to 0.2 (arbitrary units) in Fig. 3.2A, and it was found that the estimated values deviated less than 0.3% from the known values. In the spinal cord experiments, the underlying Gaussian noise SD in different SNRs was also estimated via PIESNO. The different SNRs were achieved by averaging the complex data with a step of two. The estimated Gaussian SD (Fig. 3.2B) was well fitted with the expected function:

$$\sigma_g(N) = \sigma_{g,0} / \sqrt{N} \tag{3.10}$$

via the nonlinear least squares method with $R^2 = 0.9999$.

3.3.2 Signal transformation from Rician distribution to Gaussian distribution

The efficacy of the proposed framework in correcting the multi-echo MRI magnitude data was validated by performing Monte Carlo simulations similar to those in Section 3.2 of [274]. 50,000 sets of the simulations described in Section 3.2.3 with a single T_2 (gmT_2 = 51.6 ms) were performed with the following parameters: proton density $\eta_0 = 1000$, *TE* ranges from 5 ms to 250 ms with a gap of 5 ms, and Gaussian noises with mean zero and SD = 100 in real and imaginary channels.

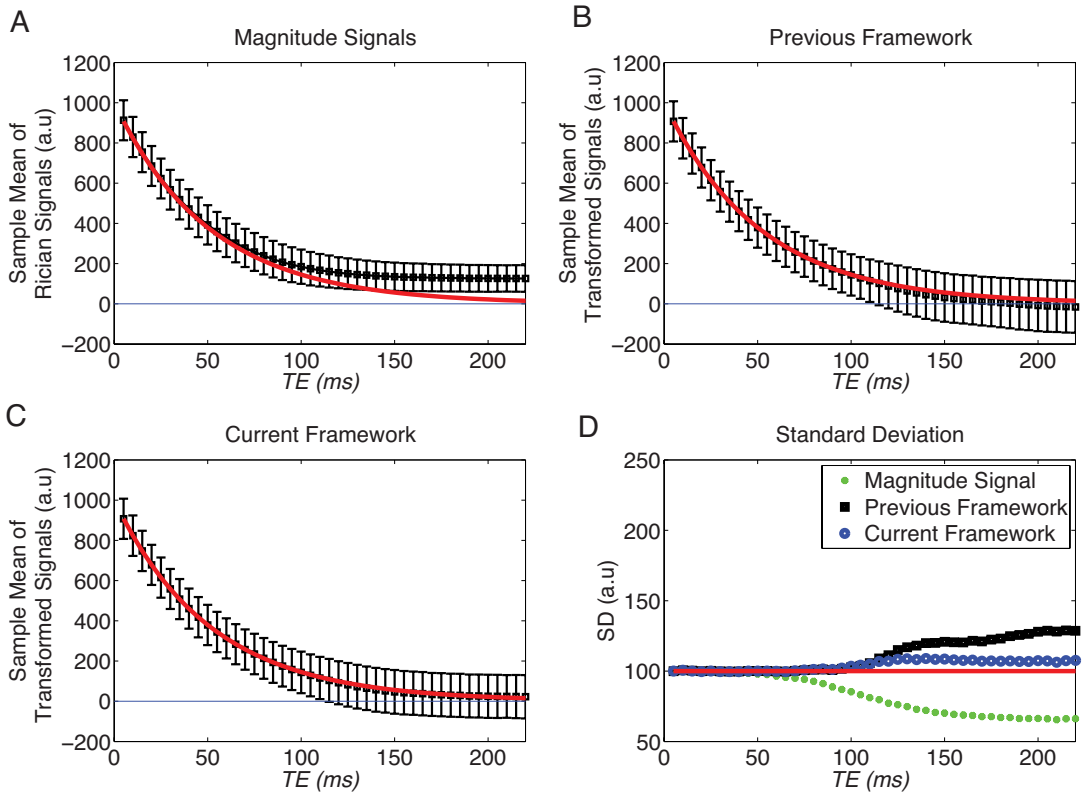

Figure 3.3. The black box and the error bar at each *TE* are the sample mean and the sample standard deviation of the noisy magnitude signals (A), the transformed signals via our previous framework (B), and the proposed modified framework here (C). The red continuous curves in (A-C) are the ground truth. The sample SD of the three sets of signals at each *TE* (D).

In Fig. 3.3A, the sample mean and sample SD of the 50,000 measurements at each *TE* are shown, where the maximum offset caused by the nature of the Rician distribution can be 117 from the ground truth as the SNR approaches 0. The underestimation problem of our original framework becomes apparent when the *TE*s are longer than 100 ms, with a corresponding SNR of 1.5 (Fig. 3.3B). In our current framework (Fig. 3.3C), the maximum distance and the mean distance between the sample mean of the transformed signals and the ground truth of all the *TE*s were reduced from 30 to 19 and from 14 to 5 (arbitrary units) compared with our previous framework. The SD of the Rician signals is far from the ground truth (100); it can be up to 35% lower than the ground truth as SNR approaches 0 (Fig. 3.3D). As for the transformed signals, the maximum and mean biasing of the variances' SD from the ground truth were 56% and 14% higher in our previous framework and only 16% and 5% higher in our current framework.

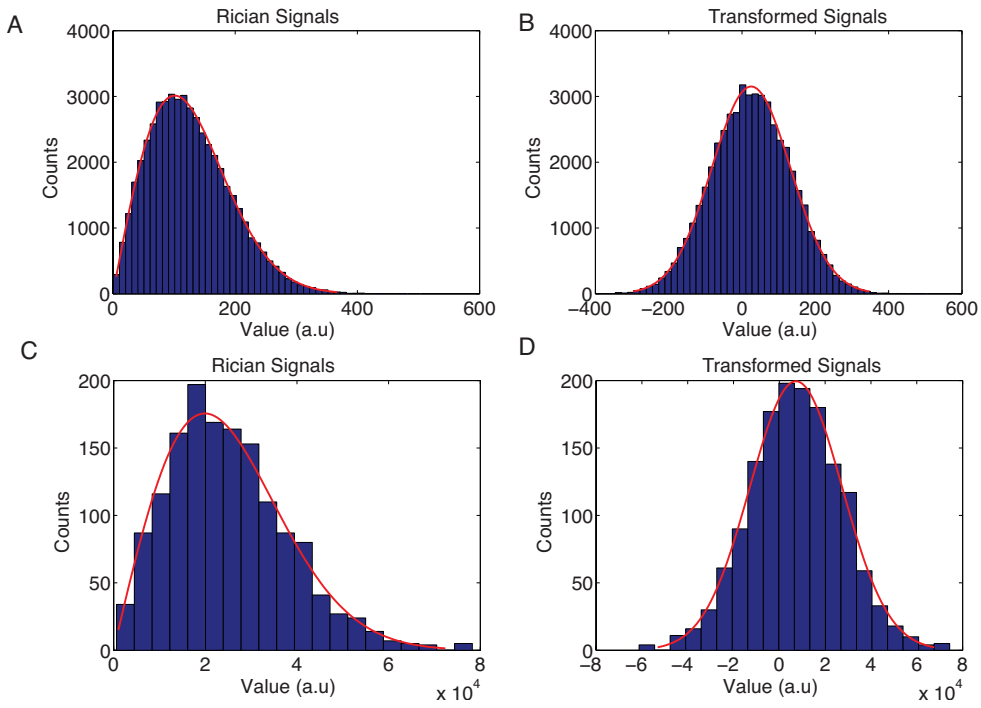

Figure 3.4. Histograms of the noisy magnitude signals (A, C) and their transformed values (B, D) of the simulation data at TE = 200 ms (A, B) and short-T_2 gel MRI data at TE = 140 ms (C, D). The red curves are the fittings to Rician distributions (A, C) and Gaussian distributions (B, D).

The histograms of the noisy magnitude signals and their transformed values via the scheme proposed here at TE = 200 ms are shown in Fig. 3.4A and Fig. 3.4B. The noisy magnitude data have a sample mean of 126 and a sample SD of 66, while the transformed signal was successfully corrected back to a Gaussian distribution ($p > 0.1$ for any random 2000 samples) with a sample mean of 15 and a sample SD of 108, where the ground truth is 22 and the SD 100. Similar histograms of the shorter T_2 gel at TE = 140 ms are also shown in Fig. 3.4C and Fig. 3.4D. The noisy magnitude intensity was well fit with a Rician distribution (red curve) with sample mean and SD equal to 2.5 x 10^4 and 1.3 x 10^4, while the transformed signal was successfully described by a Gaussian distribution (p = 0.96) with sample mean and SD equal to

(7.3 x 10^3 and 2.0 x 10^4), where the ground truth is 5.8 x 10^3 with an SD of 1.9 x 10^4 (the results from the data with 50 averages).

3.4 Numerical simulation of T_2 spectra MRI experiments

3.4.1 Simulations of the T_2 distribution with a single T_2 component

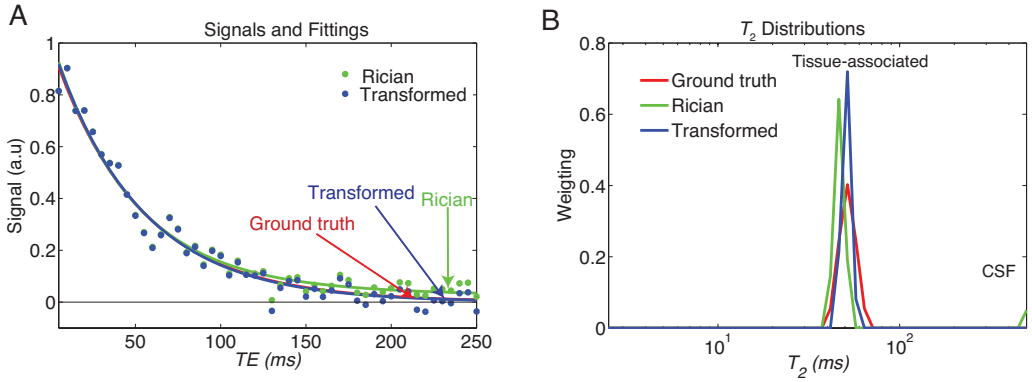

Figure 3.5. An example of the simulations with a single T_2 component at iSNR = 25. (A) The noisy magnitude signals (green dots) and the transformed signals (blue dots). The green and blue continuous curves are the fitting results obtained with the NNLS algorithm. (B) The T_2 distribution using the original Rician signals (green) and the transformed signals (blue). The continuous red curve in both (A) and (B) is the ground truth.

A demonstration of the effects of signal transformation on the T_2 distribution with an initial SNR (iSNR) equal to 25 is shown in Fig. 3.5. There is a clear offset in the magnitude signal when the underlying signal is approaching zero, which is reflected in the T_2 distribution as a tail in the CSF-like regime (relative fraction 2.5%). This offset in the magnitude signal also causes the tissue-associated peak (51.6 ms) to occur at a shorter relaxation time (46.6 ms). When the transformed signal is used in the NNLS algorithm, the spurious CSF-like tail disappears and the tissue-associated peak is corrected back to 50.9 ms.

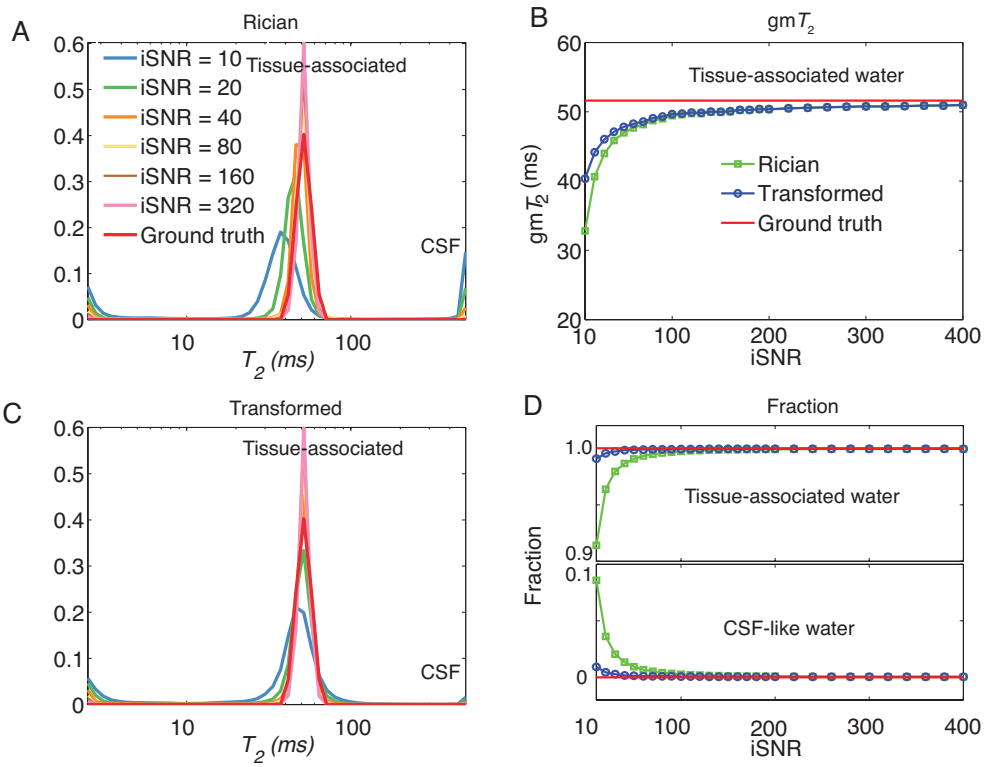

Figure 3.6. T_2 distributions using the Rician signals (A) and the transformed signals (C) at various iSNR. The gmT_2 values of the tissue-associated water (B) and the relative fractions of both the tissue-associated water and the CSF-like water (D) were plotted as a function of iSNR.

The statistical results of estimating T_2 distributions with various iSNR are shown in Fig. 3.6. Apparently, the bias of the tissue-associated water peak worsens as SNR goes down (Fig. 3.6A), while the proposed signal transformation makes the T_2 distributions more consistent over the entire range of SNR (Fig. 3.6C). Even at the lowest iSNR (iSNR=10), the gmT_2 and relative fraction of the tissue-associated water are successfully corrected from (32.8 ms, 91.4%) to (40.3 ms, 99.1%), where the ground truth is (51.6 ms, 100%). To achieve the relative fraction of the spurious CSF-like water less than 1% of the total water, an iSNR higher than 50 is necessary using

the Rician signal directly; however, iSNR>=10 is sufficient with our proposed framework.

3.4.2 Simulations of the T_2 distributions with two T_2 components

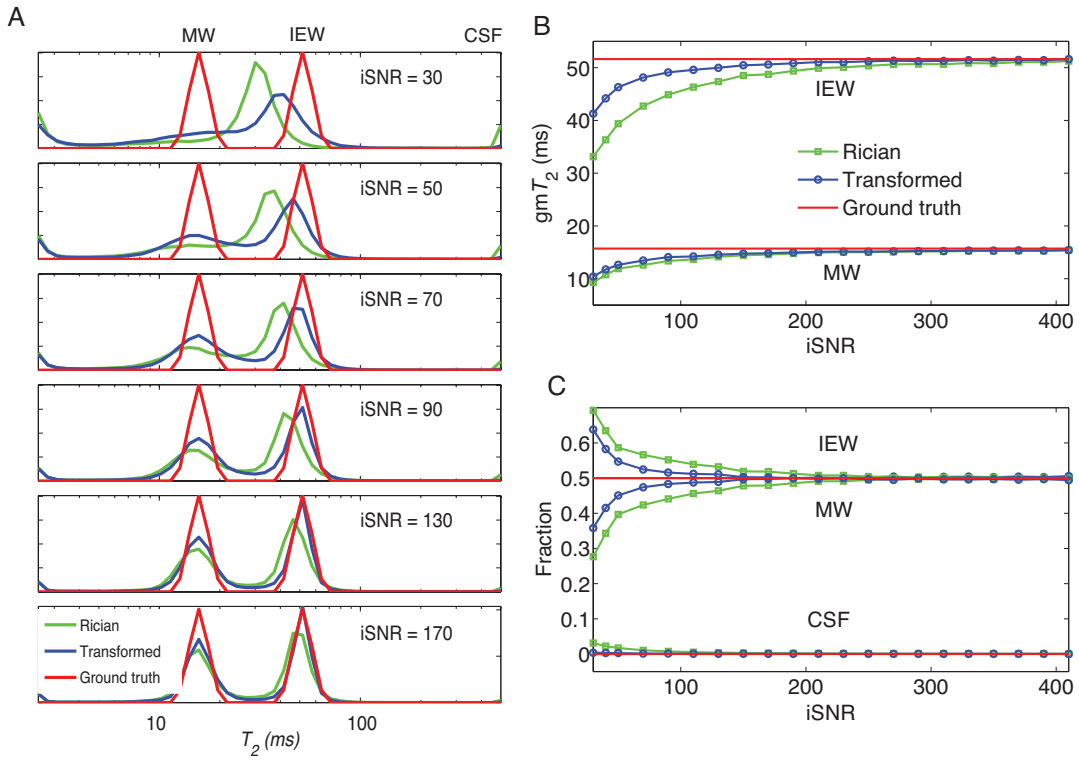

Figure 3.7. (A) The T_2 distributions of the simulations of two T_2 components with various iSNR and their corresponding gmT_2 values (B) and relative fractions (C) of different regimes. The red curves in (A–C) are the underlying ground truth.

In Fig. 3.7A, the averaged T_2 distribution of each 1000 realizations with the original Rician signals (green) and transformed signals (blue) are shown against the ground truth with different iSNRs. Except for the generation of the spurious CSF-like water, the gmT_2 of both MW and IEW and the relative fraction of MW are underestimated, and the relative fraction of IEW is overestimated, especially when iSNR goes down (Fig. 3.7B and Fig. 3.7C). At iSNR=30, the estimated gmT_2 of the

MW and IEW via directly fitting the Rician signals are 40.5% and 35.8 less than the ground truth, respectively, their relative fractions are 33.1% less and 38.5% higher than the ground truth. By implementing the proposed framework, the accuracy of both the gmT_2 and relative fraction estimations are improved. For example, to achieve 90% accuracy of the estimation of the MW fraction, iSNR>=110 is required when the Rician signals are used directly, while only iSNR>=50 is required when our proposed framework is implemented.

In Fig. 3.7A, at iSNR=30, the T_2 distribution calculated from the Rician signals only has one component in the tissue-associated water regime with gmT_2=20.8 ms and the relative fraction equal to 97.0%. In the T_2 distribution derived from the transformed signals, although the MW and IEW are still not clearly separable, the amplitude of $F(T_2)$ at the MW peak (T_2 =15.7 ms) position is 96% higher than that derived from the Rician signals. At iSNR=50, the peaks of MW and IEW are still blurred in the T_2 distribution calculated from the Rician signals, but they become visible in the T_2 distribution derived from the transformed signals, where the minimum amplitude between the two peaks is already 43% less than the amplitude of the smaller peak. At higher iSNRs (>50), the MW and IEW are separable in both T_2 distributions. However, the position and the relative fraction of each component approach the ground truth faster via the transformed signals as the iSNR increases.

3.5 T_2 spectra MRI experiments on gel phantom and fixed porcine spinal cord

3.5.1 Agar gel phantom

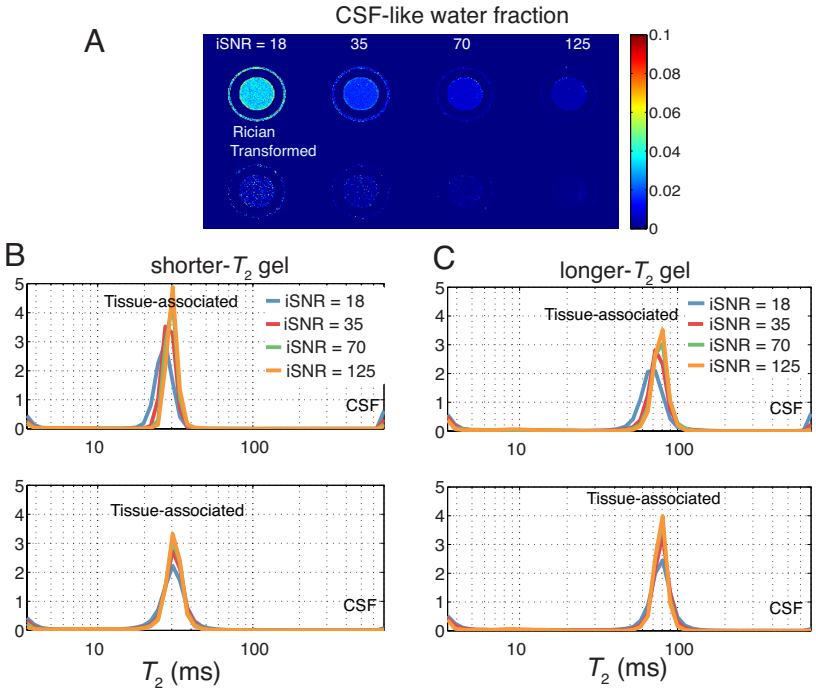

Figure 3.8. (A) Maps of the relative fractions of the CSF-like water with various iSNR. (B-C) T_2 distribution of the shorter-T_2 gel (B) and the longer-T_2 gel (C) with various iSNR.

The images of the CSF-like water fraction from the data with 1, 4, 16 and 50 averages (corresponding iSNR=18,35,70,125) are shown in Fig. 3.8A. Our proposed framework decreases the spurious CSF-like water fraction from 3.5% to 0.6% for the shorter-T_2 gel and from 4.3% to 0.6% for the longer-T_2 gel when iSNR=18. Similar to the simulations with a single T_2 component, an iSNR of no less than 70 is required to achieve 99% accuracy of the tissue-associated water fraction if the magnitude data are used with the NNLS algorithms directly, while the requirement of iSNR can be decreased to 18 by implementing our proposed framework.

The gmT_2 values of both gels were also corrected to more accurately reflect the ground truth: the gmT_2 of the shorter-T_2 gel was corrected from 24.8 ms to 27.5 ms at iSNR=18 where the ground truth is 28.7 ms, and for the longer-T_2 gel from 57.5

ms to 63.1 ms where the ground truth is 63.9 ms. More results with various iSNR are reported in Table 3.1.

Number of Averages		1	4	16	50
shorter-T_2 gel					
Rician signals	Tissue-associated	24.8 ms (96.5%)	27.1 ms (98.2%)	28.2 ms (99.1%)	28.5 ms (99.5%)
	CSF-like	3.5%	1.8%	0.9%	0.5%
Transformed signals	Tissue-associated	27.5 ms (99.4%)	28.2 ms (99.7%)	28.5 ms (99.8%)	28.7 ms (99.9%)
	CSF-like	0.6%	0.3%	0.2%	0.1%
longer-T_2 gel					
Rician signals	Tissue-associated	57.5 ms (95.6%)	61.5 ms (98.5%)	63.3 ms (99.6%)	63.8 ms (99.8%)
	CSF-like	4.4%	1.5%	0.4%	0.2%
Transformed signals	Tissue-associated	63.1 ms (99.4%)	63.3ms (99.8%)	63.7 ms (99.9%)	63.9 ms (99.9%)
	CSF-like	0.6%	0.2%	0.1%	0.1%

Table 3.1. Statistic results of the gmT_2 values and relative fractions for the agar gel phantom.

3.5.2 Spinal cord

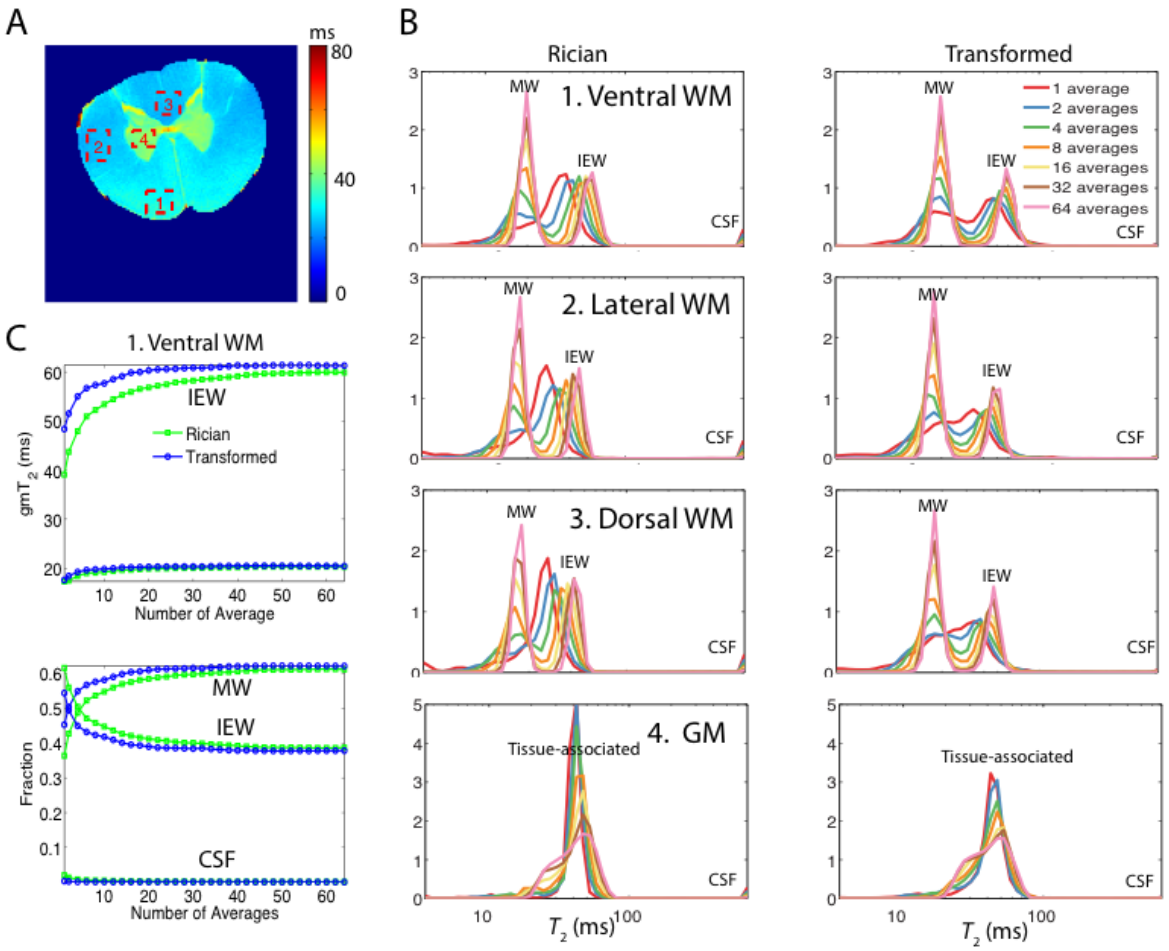

Figure 3.9. (A) The map of the gmT_2 from 3.5 ms – 700 ms of the spinal cord. (B) The T_2 distributions of the four ROIs (ventral WM, lateral WM, dorsal WM, and GM) with 1, 2, 4, 8, 16, 32 and 64 averages of the complex data using the original magnitude signals and the transformed signals. (C) The gmT_2 and relative water fractions of different water components in the ventral WM as a function of the number of averages.

Maps of the gmT_2 of the entire T_2 distribution from 3.5 ms to 700 ms with the highest SNR are shown in Fig. 3.9A. Not surprisingly, the GM shows a longer gmT_2 than the WM. Anatomy-related inhomogeneity of the gmT_2 is shown in both GM and WM, which agrees with other studies on spinal cords [56,289]. In Fig. 3.9B, the WM ROIs show two clear relaxation components with the gmT_2 and relative fraction (20.1

ms 62.3%, 59.1 ms 37.6%) for ventral WM, (17.8 ms 67.0%, 49.4 ms 33.0%) for lateral WM, and (17.8 ms 65.0%, 46.6 ms 35.0%) for dorsal WM, while the GM ROI shows a single T_2 component with a broad shape, whose gmT_2 and relative fraction were (40.7 ms 100.0%).

The development of the pattern of T_2 distributions under various SNR levels in each WM ROI match the simulations of the two T_2 components in Section 3.2.2, where the blurring of the MW and IEW peaks worsens as the SNR diminishes. For example, at the lowest SNR (iSNR=30), the MW peak and IEW peak of the ventral WM merge into a single peak with the averaged gmT_2 values (28.1 ms) of the two components, while the two components were clearly visible when the transformed signals were used (smallest amplitude between the two components is 64% of the smaller component's amplitude) with (17.4 ms, 45.3%) for the MW and (46.5 ms, 54.4%) for the IEW. More detailed SNR dependence for ventral WM are shown in Fig. 3.9C.

Consequently, the gmT_2 values and relative fractions of each regime are misestimated when the SNR is low; our framework makes these estimations more accurately. For example, our framework corrects the underestimation of the gmT_2 value and the overestimation of the relative fraction of the IEW in the ventral WM from 33.8% to 18.1% and from 63.8% to 44.7% at iSNR=30. To achieve 90% accuracy for the MW fraction estimation, our framework decreases the requirement of iSNR from 104 to 73.

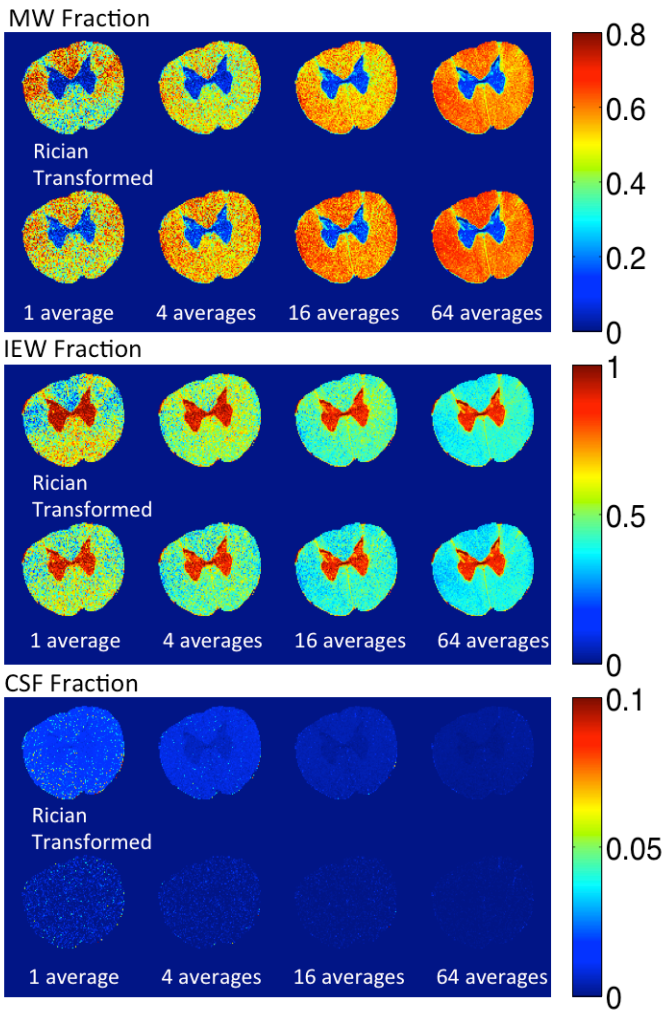

Figure 3.10. The maps of the relative water fraction of MW (top), IEW (middle), and CSF (bottom) in the spinal cord with the number of averages of the complex data equal to 1, 4, 16 and 64.

Fig. 3.10 shows the relative fraction of the MW, IEW, and CSF in the spinal cord with 1, 4, 16, and 64 averages of the complex data. The overestimation of the IEW fraction and underestimation of the WM fraction are more serious in the ventral WM, which has a longer gmT_2 for the MW. Clearly the CSF fraction is overestimated and the contrast between GM and WM is not accurate. The latter is due both to the overestimation of the CSF, which is SNR dependent as illustrated in Fig. 3.6, Fig. 3.7, and Table 3.1, and to the fact that GM has a higher SNR than does WM. Our

framework reduces not only the overestimation of the CSF fraction in both WM and GM but also the spurious contrast between the two.

3.6 Discussions and conclusions

In this work, our main objective is to adapt and extend our original signal transformational framework for qT_2 MRI spectral data and to determine its efficacy in transforming the Rician magnitude signals from multi-echo MRI experiments to Gaussian-distributed signals with the hope of improving the accuracy of the estimation of the T_2 distribution.

The additional dimension (T_2 dimension) of the multi-echo MRI data provides a much larger sample to estimate the Gaussian standard deviation; this larger sample improves the precision of the Gaussian noise SD estimation within PIESNO. As a consequence, the precision of the underlying signal intensity estimate also improves.

Both the multi-echo MRI simulations and agar gel phantom experiments clearly illustrate the efficacy of our proposed framework in mapping the noisy Rician signals to noisy Gaussian signals, with nearly constant SDs. The underestimation of the signal intensity in the very low SNR regime in our original framework has been ameliorated by adding a non-negative boundary in the fixed-point formula to estimate the underlying signal intensity, where the variance of the transformed signals are more stable. However, we believe further studies are still needed to investigate the best scheme to address a sample mean of the magnitude signals that is below the noise floor.

Our results confirm that the artifacts in the T_2 distribution arise from the magnitude data mentioned in the literature [271,275] and illustrate their dependence

on SNR. These artifacts include the generation of spurious CSF-like long T_2 tails, bias of the tissue-associated water peaks, blurring of nearby but distinct T_2 components, underestimation of the gmT_2 and relative fraction of myelin water, underestimation of the gmT_2 and overestimation of the relative fraction of intracellular/extracellular water. By implementing our proposed framework, the magnitude signals are transformed to meet the requirements of most ILT algorithms: that they be Gaussian distributed and have a constant standard deviation. As a consequence of this transformation, the associated artifacts of Rician signals are eliminated and the accuracy of the T_2 distribution is significantly improved.

It should be mentioned that the MW fraction of the porcine spinal cord used in this work (50%–70%) is higher than that found in other literature on rat spinal cord (10%–40%) [56,273,290]. To the best of our knowledge, no other quantitative study on the MW fraction of porcine spinal cord has been undertaken thus far. The larger MW fraction here may be the result of the differences between the two species or the different sample preparation procedures. As for GM, except for the correction of the biasing of the tissue-associated water and the generation of the spurious CSF components (see Fig. 3.9B), even the shape of T_2 distribution after implementation of our framework is more consistent over the entire range of SNR, though the underlying biophysical basis of this broad peak is still not clear.

Although SNR is still required to produce an accurate T_2 distribution, our framework decreases the SNR needed and improves the T_2 distribution over the entire range of SNR. Another advantage of our framework is its robustness; it does not require phase information and can be applied to the multi-echo MRI magnitude data

from all preclinical and clinical scanners (although other sources of noise, such as motion and physiological noise for *in vivo* applications, should be handled before using this framework).

The framework outlined in this work only illustrates the applications on multi-echo MRI data from a single transmit-receive RF coil. A similar framework can be adapted for a multi-receiver MRI system based on our original work on a multi-receiver MRI system with parallel imaging [274,281].

3.7 Supporting information: A fixed-point formula for the estimation of underlying signal intensity

The first step of the estimation is writing the first and the second moments of magnitude MRI signal *m* [268,270,291,292]:

$$\langle m \rangle = \frac{1}{2\sigma_g^2}\left(\exp(-\frac{\eta^2}{4\sigma_g^2})\sqrt{\frac{\pi}{2}}\sigma_g\left[\left(\eta^2+2\sigma_g^2\right)I_0\left(\frac{\eta^2}{4\sigma_g^2}\right)+\eta^2 I_1\left(\frac{\eta^2}{4\sigma_g^2}\right)\right]\right) \tag{3.11}$$

$$\left\langle m^2 \right\rangle = 2\sigma_g^2+\eta^2 \tag{3.12}$$

Then the variance of the noisy magnitude data is expressed as a product of a scaling factor and the squares of the Gaussian SD:

$$\sigma_r^2 = \left\langle m^2 \right\rangle - \langle m \rangle^2 = \zeta\left(\eta \,|\, \sigma_g\right)\sigma_g^2 \tag{3.13}$$

where the scaling factor ζ is an analytical function of SNR, i.e., $\theta \equiv \eta/\sigma_g$ [268]:

$$\zeta(\theta) = 2+\theta^2-\frac{\pi}{8}\exp\left(-\frac{\theta^2}{2}\right)\left(\left(2+\theta^2\right)I_0\left(\frac{\theta^2}{4}\right)+\theta^2 I_1\left(\frac{\theta^2}{4}\right)\right)^2 \tag{3.14}$$

By substituting Eq. 3.13 for Eq. 3.14, the underlying signal intensity can be estimated by finding the solution of this fixed-point equation:

$$\eta = g\left(\eta \mid \langle m \rangle, \sigma_g\right) = \sqrt{\langle m \rangle^2 + \left[\xi\left(\eta \mid \sigma_g\right) - 2\right]\sigma_g^2} \tag{3.15}$$

where the Gaussian SD, σ_g, is estimated by PIESNO, the method discussed in Section 3.2.2.1.

Specifically, the underlying signal intensity η is estimated as follows:

First, the decay data are smoothed using a penalized spline model, whose degree of freedom was chosen based on the method of generalized cross-validation (GCV) (see Appendices A and C of [274]). Next, the smoothed estimate $\hat{m}$ is substituted for <*m*> in Eq. 3.15, and the unique solution $\tilde{\eta}$ is determined for $\hat{m} \geq \sqrt{\pi/2}\sigma_g$, where $\sqrt{\pi/2}\sigma_g$ is the level of the noise floor, for which the underlying signal intensity is 0 but the first moment of the Rician distribution, <*m*>, is non-zero. When the estimated $\hat{m}$ is below the noise floor, the underlying signal intensity is assigned to be 0.

In our original framework [274], the estimate $\hat{\eta}$ was made to be $-\hat{\eta}_\delta$ when the estimated $\hat{m}$ is below the noise floor, where $\hat{\eta}_\delta$ is the signal intensity estimate obtained by solving a new equation, $\langle m \rangle = 2\sqrt{\pi/2}\sigma_g - \hat{m}$, to ensure the symmetry of the resultant distribution of $\hat{\eta}$ at zero SNR. However, the negative assignment of $\hat{\eta}$ biases the mean of the transformed noisy Gaussian signal by underestimating the ground truth signal when the SNR is close to 0 but not at 0 (around 0.15–2.0, see Section 3.3.2 in [274] and Fig. 3.3 in this paper). Unfortunately, the last several echoes of multi-echo MRI usually occur in this very low SNR regime rather than reaching zero. To improve the estimation of the underlying signal intensity in this very low SNR regime, rather than ensuring the symmetry at zero SNR, $\tilde{\eta}$ was

assigned to be 0 whenever $\tilde{m} < \sqrt{\pi/2}\sigma_g$. We adopt this assignment of $\tilde{\eta}$ based on the physical requirement that the variable $\tilde{\eta}$ be non-negative for typical multi-echo MRI experiments. The effect of this modification is shown in Fig 3.3.

Chapter 4: Accelerate 2D MR diffusion/relaxation spectra using compressed sensing

Potential applications of 2D diffusion/relaxation NMR and MRI to characterize complex water dynamics (e.g., compartmental exchange) in biological tissue have been realized in recent years. However, the large amount of data and long MR acquisition times required for conventional 2D MR diffusion/relaxation spectra limits its applicability for *in vivo* preclinical and clinical MRI. In this chapter, we present a new MR pipeline for 2D diffusion/relaxation spectra that incorporates compressed sensing (CS) as a means to vastly reduce the amount of 2D MR diffusion/relaxation spectra data needed for tissue characterization without compromising data quality. Here only two types of 2D MR diffusion/relaxation spectra, i.e., T_1–T_2 and T_2–T_2, were systematically tested and validated, but this MR pipeline can be generally applied to all other types of 2D MR diffusion/relaxation spectra, such as D–T_2, T_1–D, T_2^*–T_2^*, etc. This chapter was adapted from our manuscript 4 published in the *Journal of Magnetic Resonance* [293] (Appendix A).

4.1 Obstacles in 2D MR diffusion/relaxation spectra: slow acquisition

The power of NMR spectroscopy was significantly increased by the inclusion of a second dimension in the Fourier domain, expanding the ability to determine molecular structure, dynamics, and kinetics [184]. In recent years, there have also been increasing numbers of important developments and novel applications of multi-dimensional MR relaxometry to characterize the microstructure-related water dynamics (multiple components, exchange, correlations, etc.) in biological tissue

[54,294–301], food sciences [302,303], material sciences [186–189], porous media physics [190–192], and geophysics [304,305].

NMR relaxometry has been further advanced by the development of novel multi-dimensional diffusion/relaxation pulse sequences [185,186,192,299,306–309] and robust and accurate two-dimensional (2D) inverse Laplace transform (ILT) algorithms and data analysis methods [310–314]. However, the large amount of MR relaxation data and long scan times required for 2D relaxometry render this method infeasible and impractical for most preclinical and clinical applications. Faster data acquisition, improved experimental designs, more efficient data reconstruction methods requiring a reduced amount of data are highly desired to make 2D relaxometry practicable.

Recently, compressed sensing (CS) was introduced and successfully applied in the MRI field to accelerate data acquisition [315–320]. The conventional CS is mainly performed on the reconstruction in the Fourier space (k-space), which relies on the sparsity of the MRI images. However, to our best knowledge, no attention has been paid to the possibility of direct CS reconstruction from undersampled 2D relaxation signal, denoted as Laplace space.

One widely used 2D ILT algorithm used in 2D relaxometry was developed by Venkataramanan, et al. about a decade ago [310,311]. In their algorithm, it was shown that the 2D relaxometry signal could be compressed into a small matrix without losing useful information, which demonstrates the sparsity of the 2D relaxometry signal in some basis representations [315,321,322]. Noticing that, a natural question it raises is whether CS could be adopted to reduce the amount of data

required for 2D relaxometry. Unfortunately, the authors in [310,311] only focused on compressing data to reduce the computation memory required and accelerate the calculation of 2D relaxation spectra.

Recently, inspired by these findings, we proved the feasibility of the CS for the 2D relaxometry in theory and developed an efficient CS algorithm to reconstruct the 2D relaxometry from undersampled 2D relaxometry signals directly [322]. Using numerical simulations, the efficiency of the CS algorithm was used to recover 2D relaxometry using a vastly reduced number of MR measurements [322].

In this work, we develop and systematically demonstrate an MR experimental data analysis pipeline to apply this newly proposed CS algorithm to real experimental 2D relaxation spectra with a vastly reduced data set, suitable for material and tissue characterization without compromising data quality. This is an important step to find out the potential systematic artifacts in experiments and to determine the best acceleration factor that can be achieved for each 2D relaxation spectra from various samples.

We illustrate this new approach using MR data obtained on a 7T vertical wide-bore Bruker MRI scanner similar to those used in preclinical imaging applications. Both T_1-T_2 and T_2-T_2 relaxometry NMR data were acquired on a well-characterized urea/water phantom, which shows two exchanging components. T_1-T_2 MRI relaxometry was also performed on a fixed porcine spinal cord. In addition, numerical simulations of the 2D relaxation spectra were used to assess the effects of noise on the CS-based reconstruction of the 2D ILT.

4.2 2D MR relaxation spectra sequence and data acquisition

4.2.1 Urea/water phantom

The aqueous urea model system has been chosen for this study since it has two distinguishable types of protons in the transverse relaxation time (urea proton has a shorter T_2 than water proton) and urea is highly soluble in water [306,323]. A 7M-urea solution was made by dissolving urea powder (Sigma-Aldrich, Inc., USA) into phosphate buffered saline (PBS, pH = 7.4), resulting in a urea/water proton ratio of 20%/80%. Then, 0.2 mM Gd-DTPA (Magnevist®; Berlex, Inc.) and 0.025 mM $MnCl_2$ were added to the urea solution to reduce relaxation times. The pH of the urea solution was titrated to 8.1 with NaOH. An 80 μL solution was then transferred to a 5 mm susceptibility-matched Shigemi NMR tube (Shigemi Inc., Japan). All NMR experiments were completed within 24 hours after the solution was prepared to ensure stability of the phantom [306,323].

4.2.2 Porcine spinal cord

Porcine spinal cord was excised after necropsy and immediately immersion fixed in a 4% formalin solution. All animal handling protocols were approved by the NIH Heart, Lung and Blood Institute (NHLBI) Animal Care and Use Committee. Prior to the MRI experiments, the spinal cord was washed and fully rehydrated with PBS and then placed in a 10 mm susceptibility-matched Shigemi NMR tube (Shigemi Inc., Japan) with Fluorinert (3M, St. Paul, MN) filling the open spaces during the MRI experiments.

4.2.3 NMR and MRI measurements

Both the NMR measurements of the urea/water phantom and the MRI experiments on the fixed spinal cord were performed on a 7T Bruker vertical-bore microimaging μMRI scanner equipped with an Avance III console, and a micro2.5 microimaging gradient system (Bruker BioSpin, Billerica, MA). All specimens were kept at a bore temperature (≈17 ^{o}C) during scanning.

4.2.4 2D NMR of urea/water phantom

Two different 2D NMR relaxometry pulse sequences were performed on the urea/water phantom: (a) T_1–T_2 correlation relaxometry was performed using an inversion–recovery (IR) preparation "filter," followed by Carr–Purcell–Meiboom–Gill (CPMG) pulse trains (IR-CPMG) (Fig. 4.1a); (b) T_2–T_2 exchange relaxometry was performed using relaxation exchange spectroscopy (REXSY) (Fig. 4.1b), which consists of two CPMG pulse trains separated by a mixing time, τ_m, during which the magnetization is stored back along the longitudinal axis. A gradient spoiler was placed after the IR pulse in the IR-CPMG sequence and during the mixing period in the REXSY sequence to "crush" any remaining magnetization in the transverse plane. In the IR-CPMG pulse sequence, 50 IR points were sampled logarithmically from 50 ms to 5 s; 250 echoes were acquired in the CPMG pulse trains with a temporal spacing of τ = 2 ms. The pre-scan delay was set to 15 s to ensure full inversion recovery. A two-step phase cycling scheme was used (Fig. 4.1a), and only one repetition was acquired. An equilibrium CPMG echo train was also acquired with an inversion–delay of 15 s and four repetitions. In the REXSY experiments, the same parameters were used as in the IR-CPMG experiments, with the mixing time, τ_m,

starting from 50ms, and then 100ms and then in 100ms steps until reaching 1000ms. The repetition time (TR) was 8 s.

4.2.5 T_1–T_2 MRI of porcine spinal cord

T_1–T_2 correlation relaxometry was performed by an IR-prepared multiple spin echo (ME) sequence (Fig. 4.1c) with 36 inversion delays logarithmically distributed from 260 ms to 5000 ms and 50 spin echoes starting at 5 ms and continuing to 250 ms in 5 ms increments. The other acquisition parameters were: TR = inversion-delays + 12 s, matrix size = 64 × 64, slice thickness = 1 mm, field of view (FOV) = 10 mm × 10 mm and two-step phase cycling. Hermite pulse shapes were applied for both excitation and refocusing pulses with bandwidth (5400 Hz) matching and proper gradient crasher, and a 5 ms hyperbolic secant inversion pulse was used for uniform inversion of the sample. A magnetization equilibrium scan was also acquired with an inversion–delay equal to 12 s with four repetitions.

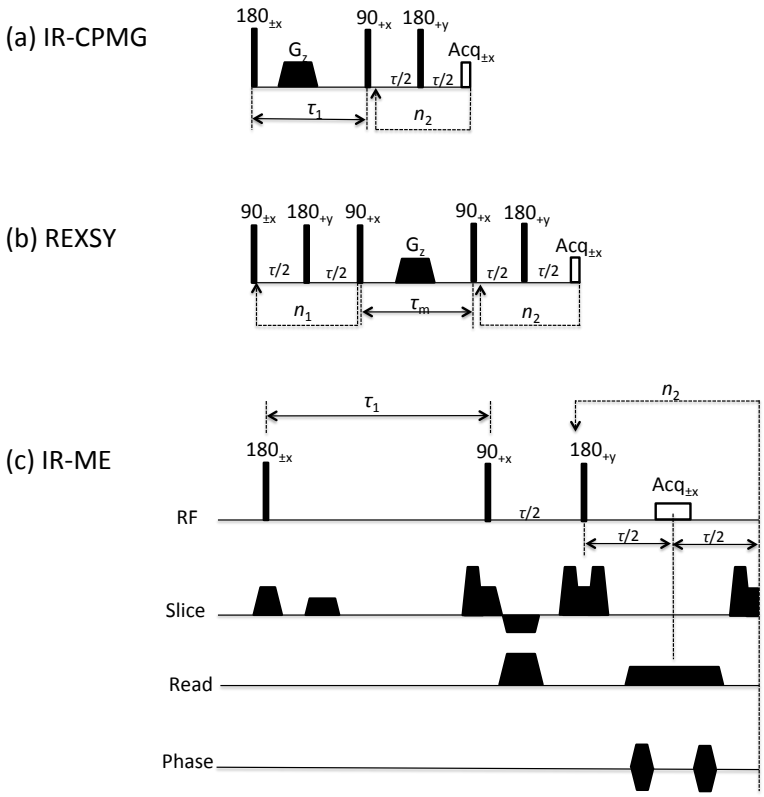

Figure 4.1. Pulse sequences diagrams for the three pulse sequences used in this work: (a) IR-CPMG, (b) REXSY, and (c) IR-ME with imaging. τ_1 is the inversion delay, τ is the echo time in the CPMG, τ_m is the mixing time in the REXSY, n_1 and n_2 are the number of loops in the first and second dimensions.

4.3 A MR pipeline to accelerate 2D MR diffusion/relaxation spectra via compressed sensing (CS)

The following data analysis flowchart (Fig. 4.2) was developed and used in this work to validate and test the efficiency of the CS framework. Experiments with dense sampling points were first performed to approximate the ground truth. After the raw data were preprocessed, 2D relaxation spectra were calculated from the full data set via 2D ILT. Random samples were then obtained from the preprocessed full data

with different acceleration factors, R (where $1/R$ is the fraction of the full data). The subsamples were then processed using two pipelines: CS reconstruction and conventional 2D ILT reconstruction. 2D relaxation spectra from each subsample were then compared to the result obtained from the full data, in the experiments, or to the ground truth, in the simulations.

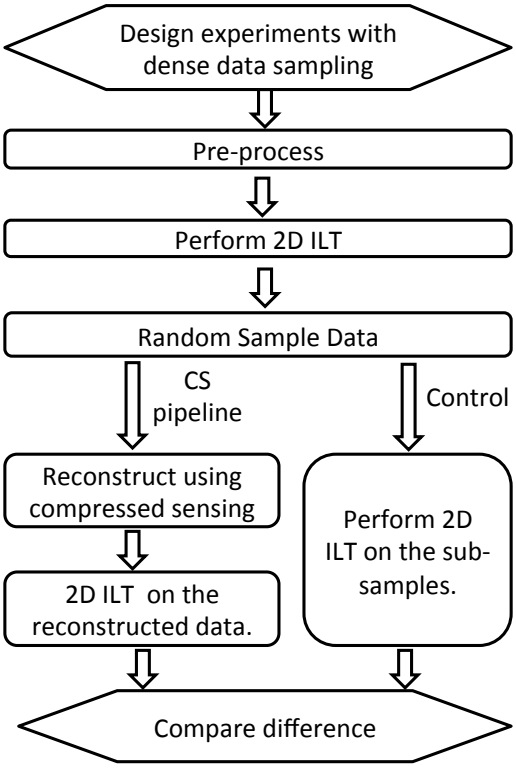

Figure 4.2. Flowchart of the pipeline used in this work.

4.3.1 Preprocessing

To remove the bias caused by Rician noise in the IR-ME MRI data, the noisy ME MRI magnitude data were first processed by a methodology we proposed and validated previously to transform 1D Rician magnitude data to Gaussian-distributed data [254,274,281]. Furthermore, ROI analysis was performed to satisfy the signal-to-noise ratio (SNR) requirements of the 2D ILT, which generally needs a high SNR to

obtain stable and accurate solutions. Here ROIs in white matter with a relatively homogenous geometric mean T_2 (gmT_2) were selected.

In the IR-CPMG and IR-ME experiments, the CPMG and ME data were subtracted from the corresponding equilibrium data to cancel the potential artifacts caused by imperfect 180° inversion pulses. Then, the experimental data from all the three pulse sequences can be written as:

$$M(\tau_1, \tau_2) = \sum_{m=1}^{N_m} \sum_{n=1}^{N_n} F(T_m, T_n) \exp\left(-\frac{\tau_1}{T_m}\right) \exp\left(-\frac{\tau_2}{T_n}\right) + \epsilon(\tau_1, \tau_2) \quad (4.1)$$

where τ_1 is the inversion delay in the T_1-T_2 sequences and the accumulated echo time $n_1\tau$ of the first CPMG in the T_2-T_2 sequences; τ_2 is the accumulated echo time $n_2\tau$ of the second CPMG or ME, $F(T_m, T_n)$ is the 2D probability density function (pdf) of the two corresponding relaxation parameters; N_m and N_n are the number of sampling points in each dimension of F; and $\epsilon(\tau_1, \tau_2)$ is the noise, which is assumed to be Gaussian in most 2D ILT algorithms. Here $N_m = 100$ and $N_n = 100$ were set for all of the following analysis.

4.3.2 2D ILT

Inversion of the 2D LT is generally ill–conditioned; a small change in M may result in large variations in $F(T_m, T_n)$. One practical technique to obtain a stable solution is minimizing Ξ:

$$\Xi \equiv \sum_{i=1}^{N_1} \sum_{j=1}^{N_2} \left[M(\tau_i, \tau_j) - \sum_{m=1}^{N_m} \sum_{n=1}^{N_n} F(T_m, T_n) \exp\left(-\frac{\tau_i}{T_m}\right) \exp\left(-\frac{\tau_j}{T_n}\right) \right]^2 + \alpha \sum_{m=1}^{N_m} \sum_{n=1}^{N_n} F(T_m, T_n)^2 \quad (4.2)$$

with a data-quality term with nonnegative constraints on F, and a second term for Tikhonov regularization. Above, N_1 and N_2 are the number of measurements in the

first and second dimension, and α is the regularization parameter. Eq. 4.2 can be rewritten in the form of a kernel matrix for the full data:

$$\Xi \equiv \|M - K_1 F K_2'\|^2 + \alpha \|F\|^2 \tag{4.3}$$

where || . || is the Frobenius norm of a matrix, and K_1 and K_2 are the kernels of the first and second dimension with the matrix size $N_1 \times N_m$ and $N_2 \times N_n$.

Here, a fast and widely used algorithm proposed by Venkataramanan, Song, and Hürlimann [311] to solve the minimization problem was applied. In this algorithm, the data are partially compressed by using the singular value decomposition (SVD) of K_i

$$K_i = U_i S_i V_i' \quad i \in \{1,2\} \tag{4.4}$$

By truncating the small singular values with a threshold (1×10^{-3} of the largest single value), S_i can be reduced to a much smaller matrix with dimensions $N_i \times s_i$. Then, the data matrix M can be projected onto the column space of K_1 and the row space of K_2 with a much smaller dimension: $\widetilde{M} = U_1' M U_2$ with the new matrix size $s_1 \times s_2$ [310,311]. Now Eq. 4.3 can be rewritten in an identical structure, but with the compressed data $\widetilde{M}$ and kernels of a much lower dimension [310,311,322].

For a given value of the regularization parameter, α, a unique solution can be obtained from Eq. 4.2 or Eq. 4.3 by solving the constrained optimization problem. An *S*-curve based method, which calculates the fitting error to the measurements $\chi(\alpha)$ with a series of α, was used to robustly determine the optimal value of α [286,310,314]. The best α is chosen within a user-defined tolerance, TOL :

$$d(log_{10}\chi(\alpha))/d(log_{10}\alpha) = \text{TOL} \tag{4.5}$$

Here TOL = 0.1 was used for both the simulated data and the experimental data.

4.3.3 Subsampling

After preprocessing the raw data, 1000 random subsamples were obtained from the full data at each different acceleration factor, *R*, by randomly sampling in the 2D relaxometry data matrix. The subsamples were then reconstructed using CS, and 2D relaxation spectra were then calculated from the reconstructed data via 2D ILT with data compression. As a control, conventional 2D ILT without data compression was directly performed on the subsamples as in Eq. 4.2.

4.3.4 Brief review of the CS algorithm for 2D-ILT reconstruction

The key concept behind CS reconstruction lies in the relationship between the full data matrix *M* and the compressed data $\widetilde{M}$. Because $M = U_1 \widetilde{M} U_2'$, and because U_1 and U_2 are left orthogonal and have energy spread out across *M*, these measurements form an incoherent, tight frame [322]. It means each element of *M* is an observation of a dense linear combination of every element of $\widetilde{M}$ simultaneously. $\widetilde{M}$ also has rapidly decaying singular values. For these reasons, and the fact that $\widetilde{M}$ has much smaller dimensions than *M*, one can capture all the information in $\widetilde{M}$ with a fraction of the number of measurements in *M*.

The reconstruction algorithm to recover $\widetilde{M}$ is also based on the fact that $\widetilde{M}$ has rapidly decaying singular values. The algorithm is a modification of the singular value thresholding algorithm from Cai et al. [324]. This optimization problem searches for the matrix *X* that minimizes the sum of the singular values, while matching the measurements $M = U_1 X U_2'$. The solution to this optimization problem, then, has a high probability, close to $\widetilde{M}$, of being up to a constant factor of the noise

[322]. Some brief steps of the proposed CS reconstruction were summarized in Section 4.8 and more information can be found in [322].

4.3.5 Comparison

Global similarities were obtained for the pdf, F, from the full data or the ground truth and one from each subsample by calculating a correlation coefficient (C) between all of the vectorized versions. In addition, the geometric mean (gm) relaxation parameters and the relative volume fraction (f) of each peak in each 2D relaxation spectra were also calculated and compared to the results from the full data or ground truth. The results of each 1000 realizations were displayed as Tukey box plots, in which the notch is the median, the edges of the box are the 25^{th} and 75^{th} percentiles, the whisker length is 1.5, and the outliers are plotted separately. Further, the paired Student's t-test was performed on the correlation coefficients from the results of the CS reconstruction and the control with the null hypothesis that C are equal in the results via the two methods and the alternative hypothesis that C is higher in the CS reconstruction than the control. Fisher z-transformation was applied on the correlation coefficients before the hypothesis test.

The median of the 1000 2D relaxation spectra data from all subsamples at each R is displayed and the variance of the results is characterized by interquartile range (IQR). The contrast between the two peaks is defined by the ratio of the smallest amplitude between the two components over the smaller component's amplitude in the T_2 projection of the displayed 2D relaxometry.

4.4 Numerical demonstration of the efficiency of compressed sensing in accelerating 2D relaxation spectra

4.4.1 Numerical simulation setups

T_1–T_2 relaxometry experiments were simulated by a Monte Carlo method to further test and validate the efficiency of the proposed CS reconstruction. The data acquisition protocol used in the T_1–T_2 MRI of spinal cord was applied here. Two broad peaks without exchange in the 2D T_1–T_2 relaxogram with positions and patterns similar to those obtained from spinal cord white matter were used as the joint pdf, F, to generate the data following Eq. 4.1 with Gaussian noise at various SNRs. Stable estimates were obtained by performing 1000 realizations for the full data with one random sample taken for each acceleration factor in each realization.

Furthermore, the potential artifacts caused by Rician noise were also simulated. An ROI consisting of 100 voxels with an IR-ME sequence was synthesized. Within each voxel, the data M_R were generated by changing the distribution of the signal in Eq. 4.1 from Gaussian to Rician at SNR = 200:

$$M_R(\tau_1, \tau_2) = \sqrt{\left[\sum_{m=1}^{N_m}\sum_{n=1}^{N_n} F(T_m, T_n)\exp\left(-\frac{\tau_1}{T_m}\right)\exp\left(-\frac{\tau_2}{T_n}\right) + \epsilon_1(\tau_1, \tau_2)\right]^2 + \epsilon_2(\tau_1, \tau_2)^2} \quad (4.6)$$

where ϵ_1 and ϵ_2 are Gaussian noise. The averaged data in the ROI were taken as the complete data set (SNR = 2000) with 1000 repetitions. The following subsampling and data analysis was the same as described in Section 4.3.2 and the simulations with Gaussian noise.

4.4.2 Noise type

For the full data with Gaussian noise at SNR = 2000, the 2D ILT algorithm yields a close estimate (Fig. 4.3b) of the ground truth (Fig. 4.3a) with a correlation coefficient C = 0.92 (Fig. 4.3g). Uncorrected Rician noise introduces spurious peaks in the long-T_2 regime, which are visible in both the T_1–T_2 relaxometry (red arrow in Fig. 4.3c) and its 1D projection onto the T_2 axis (red arrow in Fig. 4.3h). In addition, the two peaks are merged indistinguishably into one in both the T_1 and T_2 dimensions. The application of the signal transformation correction successfully removes the spurious peaks and makes the ground-truth peaks distinguishable (Fig. 4.3d and Fig. 4.3h) concomitant with the recovery of the correlation coefficient from 0.85 to 0.90 (Fig. 4.3g).

Subsampling was performed both on the data with Gaussian noise and on the data with the transformed signal. The results are shown in Fig. 4.3i, in which only the median was plotted for the data with Gaussian noise for display. Within the transformed data, the CS reconstruction successfully achieves a high correlation coefficient $C \sim 0.90$ with a small variance until R reaches 5, which is significantly higher than the results of the control ($p < 1\times10^{-9}$). Except for the higher correlation coefficients, better contrast is also observed with CS reconstruction. For example, at R = 5, the contrast between the two peaks is 69% with the CS reconstruction, but 89% in the control, where the ground truth is 34%.

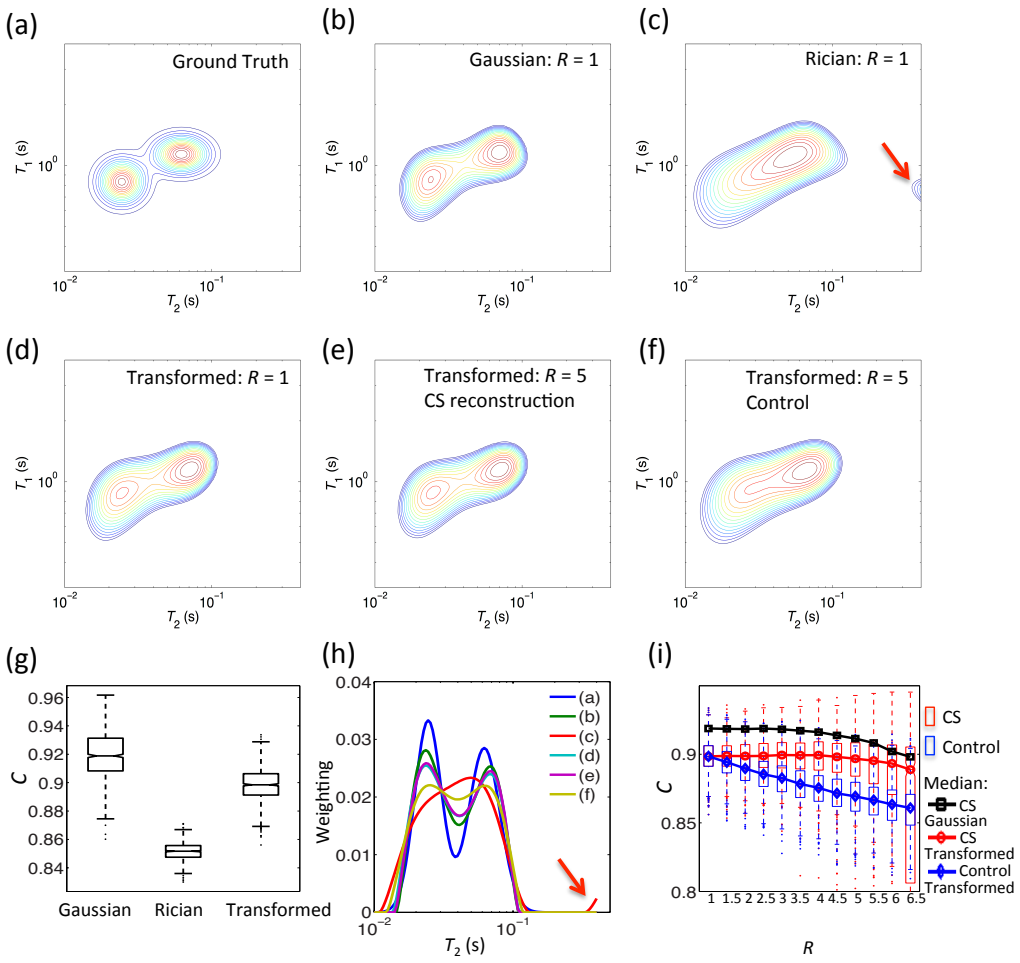

Figure 4.3. 2D T_1–T_2 relaxometry of (a) the simulated ground truth, (b) full data with Gaussian noise at SNR = 2000, (c) full data with magnitude signal, (d) full data with transformed (Rician noise corrected) signal, (e) CS reconstruction from the transformed data at R = 5 and (f) the corresponding control. (g) The results of the correlation coefficients of (b–d). (h) The normalized T_2 projections of (a–f). (i) The results of the correlation coefficients of the CS reconstruction from the data with Gaussian noise (black), the transformed signals from magnitude data (red) and its corresponding control (blue) at various acceleration factors, R.

4.4.3 Noise amplitude

The quality of the T_1-T_2 spectra from the full data itself decreases as the SNR in the simulations with Gaussian noise decreases (Fig. 4.4). For example, the

correlation coefficients drop from 0.94 to 0.84 when the SNR decreases from 10000 to 200 (Fig. 4.4l). Except for the decrease in the correlation coefficient, the contrast between the two peaks is also artificially reduced owing to the larger noise amplitude, which can be seen by comparing the T_1–T_2 spectrum with different noise amplitudes (Fig. 4.4a-c). The contrast in the 1D T_2 projection is changed from 60% to 85% when the SNR drops from 2000 to 800, where the two peaks are indistinguishable at SNR = 200.

The CS reconstruction from subsamples successfully maintains the quality of T_1–T_2 spectra at similar levels as the results form the full data when the SNR decreases. At R =3, the correlation coefficients from the subsample with CS reconstruction shows almost identical distributions as the results from the full data with slightly larger variance (≤1.5 times higher IQR) until the SNR drops below 800. At R =5, the correlation coefficients drops a little with larger variance, especially at lower SNR (<2000). Comparing to the control, the results from CS reconstruction shows much better quality at certain acceleration factors. For example, at SNR = 800, the correlation coefficients from the CS reconstruction results are significantly higher than the control ($p < 5\times10^{-9}$) until $R \geq 5.5$ (Fig. 4.4k). At higher R, the sample size is not large enough to generate good-quality T_1–T_2 spectra via either the CS reconstruction or the conventional 2D ILT.

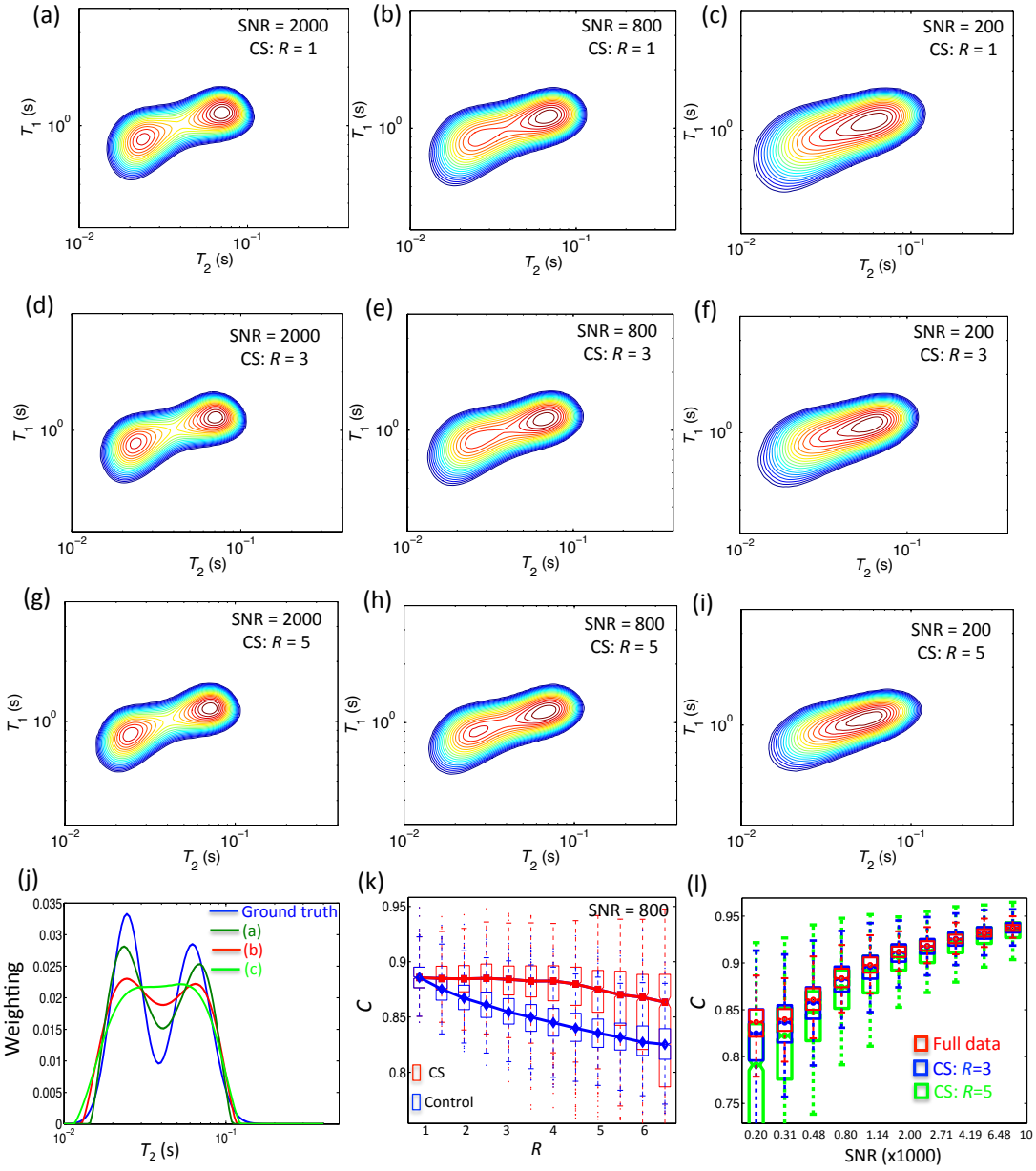

Figure 4.4. (a-i) T_1–T_2 relaxometry from the stimulated data with Gaussian noise at three SNR levels (SNR = 2000, 800 and 200) and three acceleration factors: R = 1, 3 and 5. (j) The normalized T_2 projections of (a–c) and the ground truth. (k) The boxplots of the correlation coefficients of the CS reconstruction (red) and the control (blue) from the simulated data with Gaussian noise at SNR = 800 at various acceleration factors, R, and the broader lines and dots are the median of the data at each R. (l) The boxplots of the correlation coefficients of the full data (red), CS reconstruction at R = 3 (blue) and R = 5 (green) at various SNR. For the display purpose, the outliers were not shown.

4.5 Accelerate urea/water MR T_1–T_2 and T_2–T_2 spectra experiments via CS

4.5.1 Urea/water T_1–T_2 spectra

Here, only the fourth echoes of the 250 CPMG echo trains were used; as a result the matrix size of the full data acquisition is 50 × 62 with SNR ≥ 5000. The T_1-T_2 spectrum from the full data is shown in Fig. 4.5a, in which two peaks are clearly observed: urea with gmT_2 = 30.9 ms, gmT_1 = 618 ms, and f = 18.9%; and the water with gmT_2 = 156 ms, gmT_1 = 614 ms, and f = 81.1%. The small bias of the relative volume fractions from 20%/80% is the result of exchange between the protons on the urea molecules and those on the water molecules. The projections of the T_1-T_2 distribution onto the T_1 and T_2 axes are shown along the axes in Fig. 4.5a and b. A single peak is observed in the projected 1D T_1 spectrum with gmT_1 = 614 ms for both the full data and CS reconstruction at R = 8. Two peaks are observed in the projected 1D T_2 spectra for which the full data set is used with f = 18.9% and gmT_2 = 30.9ms for the urea and f = 81.1% and gmT_2 = 156 ms for the water. The corresponding values at R = 8 with CS reconstruction are f = 18.6% and gmT_2 = 30.9 ms for the urea and f = 81.4% and gmT_2 = 156 ms for the water.

In Fig. 4.5b, the T_1–T_2 spectrum at acceleration factor R = 8 is presented; this spectrum has a very high correlation coefficient, C > 0.999. In contrast, the corresponding value of 1000 simulations in the control at R = 8 drops to 0.895 as shown in Fig. 4.5c, which is significantly smaller than the CS reconstruction (p < 1×10^{-9}). With CS reconstruction at R ≤ 8, the biases of the urea parameters are: ≤ 0.1% for the f, ≤ 0.1% for the gmT_1, and ≤1% for the gmT_2. The corresponding values for the water are: ≤0.02%, ≤0.02%, and ≤0.01%, respectively. In contrast, the

corresponding biases in the control at $R = 8$ are -3.1%, -0.2%, and -3.2% for the urea and 0.73%, 0.09%, and 0.80% for the water. In addition, the variance of the results obtained with 1000 random samples is much smaller than that of the control at $R \leq 6$ and comparable to the control at $R = 7$ and 8. At higher acceleration factor ($R \geq 9$), very large variance and growing bias are observed.

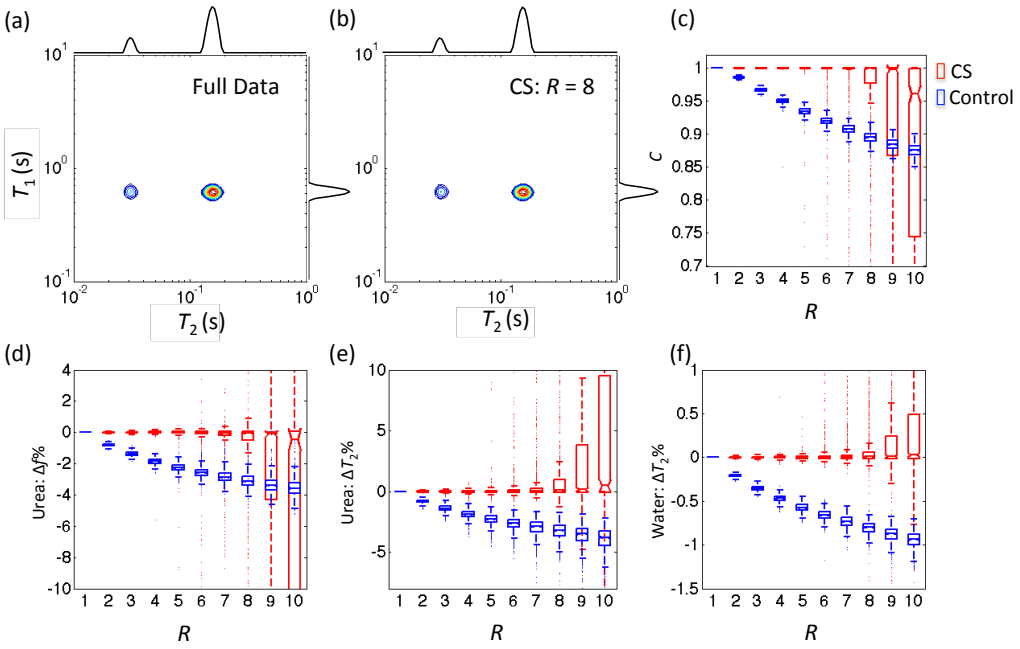

Figure 4.5. T_1–T_2 spectra of the urea/water phantom from (a) the full data and (b) the CS reconstruction at $R = 8$, in which the curves along the axes are the 1D projections onto each dimension. (c–f) are the Tukey box plots of the results from the 1000 realizations in each acceleration factor R, which includes (c) the correlation coefficients, the percentage of the biases of the urea's (d) relative volume fraction, (e) gmT_2, and (f) the water's gmT_2.

4.5.2 Urea/water T_2–T_2 spectra

T_2–T_2 spectra of the urea/water phantom at different mixing times are shown in Fig. 4.6a and Fig. 4.7a. As the mixing time becomes longer, the total signal

intensity decreases while the relative fraction of the off-diagonal peaks increases. A two-site exchange model was used to fit the amplitudes of the peaks following a similar protocol as proposed by Dortch et al. [306] with the estimate of the urea proton fraction being 19.6% and the exchange rate 0.35 s^{-1}. Two peaks at τ_m = 50 ms and τ_m = 1000 ms, with SNRs of ~ 5000 and 1000 respectively, were chosen to test the performance of the CS reconstruction.

At τ_m = 1000 ms, the off-diagonal peaks (P_{ab} and P_{ba}) appear with the total relative volume fraction 15.1%, for which the relative volume fractions of the unchanged urea (P_{aa}) and the water (P_{bb}) are 11.3% and 73.6% respectively. At $R \leq 9$, the correlation coefficients between the CS reconstructed T_2–T_2 spectra and the one from full data can be maintained as high as ≥ 0.989, which are significantly higher than the control ($p < 1\times10^{-9}$); this coefficient begins to fall quickly with larger variance at $R \geq 10$. In the control, there is a strong underestimation of the relative fraction of the off-diagonal peaks, $P_{ab} + P_{ba}$, and an overestimation of the water peaks P_{bb}, which can be as large as 14.5% and 1.8% at R = 9. CS reconstruction successfully corrects the biases back (e.g., 1.1% (overestimation) and 0.36% (overestimation) at R = 9), with almost the same variance at low R and a slightly larger variance at high R (e.g., ~ 1.8 times higher in IQR than the control at R = 9). Except for the precise reconstruction of each peak's relative fraction, the other relaxation parameters are also more accurate. For example, the gmT_2 of the peak P_{ab} is underestimated by 8.2% and 3.1% at the first and second dimension (gm$T_{2,1}$ and gm$T_{2,2}$) in the control case at R = 9, while the overestimations of peaks in the CS reconstruction are only 1.6% and 0.24%.

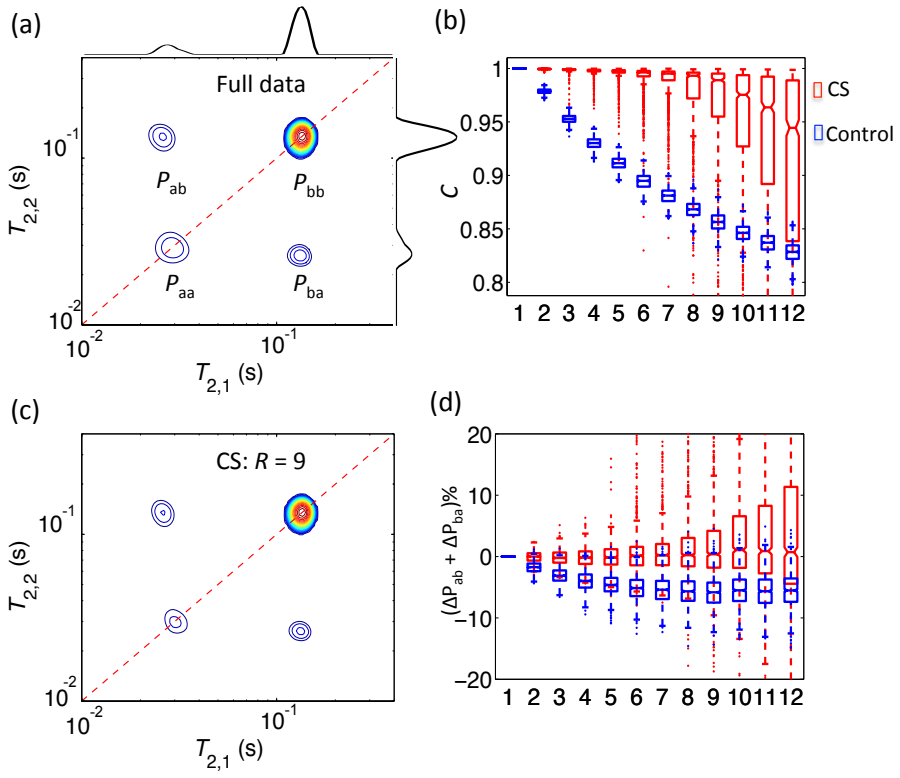

Figure 4.6. T_2–T_2 spectra of the urea/water phantom at mixing time τ_m = 1000 ms from (a) the full data and (c) the CS reconstruction at R = 9. (b, d) are the results of (b) the correlation coefficients and (d) the biases of the relative volume fractions of the off-diagonal peaks as a function of the acceleration factor R, for which the red is the CS reconstruction and the blue is the corresponding control.

At mixing time, τ_m = 50 ms, good CS reconstruction can be obtained until R = 12. Here the 125 × 125 data matrix was first evenly subsampled into a 62 × 62 matrix (R = 4); then additional subsampling was performed randomly on the 62 × 62 data matrix. In Fig. 4.7b, the statistical median of the 1000 T_2–T_2 spectra at R = 12 is shown; the correlation coefficient, C = 0.962, is very close to the corresponding value (0.964) at R = 4. At $R \leq 12$, the statistical estimations of the other relaxation and amplitude parameters are also accurate and precise: for example, the median biases of

the f, gm$T_{2,1}$ and gm$T_{2,2}$ of the urea peak are only ≤0.87%, ≤0.74%, and ≤ 0.45%, respectively, compared with the corresponding results from the full data.

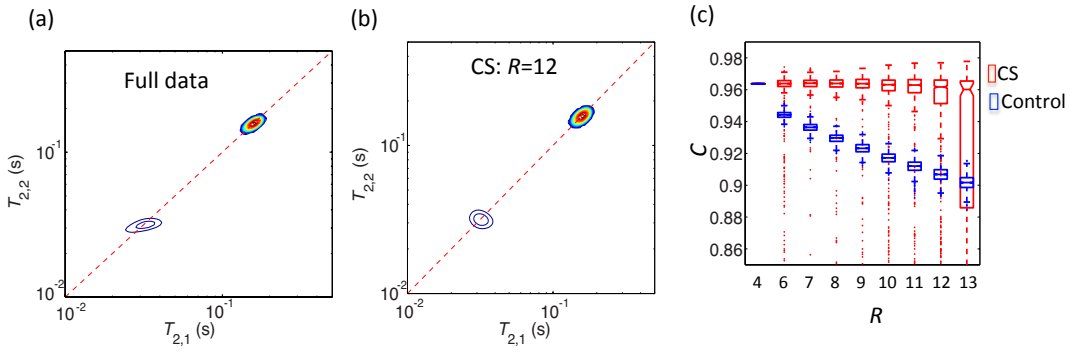

Figure 4.7. T_2–T_2 spectra of the urea/water phantom at mixing time τ_m = 50 ms from (a) the full data and (d) the CS reconstruction at R = 12. (c) Correlation coefficients as a function of the acceleration factor R, where the red is the CS reconstruction and the blue is the corresponding control.

4.6 Apply CS on the MR T_1–T_2 spectra with imaging of porcine spinal cord

The results of the ROI analysis on the dorsal white matter are detailed here (Fig. 4.8). The SNR in the white matter is approximately 200. Two broad peaks are observed in the T_1–T_2 spectra from the full data (preprocessed) with the myelin water (MW): f = 46.1%, gmT_2 = 23.8 ms, and gmT_1 = 837 ms and the intracellular/extracellular water (IEW): f = 53.9%, gmT_2 = 62.3 ms, and gmT_1 = 993 ms. Here, T_2 = 35 ms was used as the separation line between MW and IEW.

As with our simulations, the noisy Rician signals also introduces spurious peaks in the long-T_2 regime (red arrow in Fig. 4.8d and g), but our signal transformation scheme successfully corrects this artifact. CS performs adequately at R = 2.5, for which the correlation coefficient is 0.97 (significantly higher than the control, $p < 1\times10^{-4}$) and the contrast between the two peaks is preserved (93% for the CS, 93% for the full data, and a single peak in the control). At R = 4.0, the two peaks

are still visible although the correlation coefficient (0.91) is lower than the control (0.93) now. Interestingly, the CS reconstruction does well at preserving the MW relative fraction (biases ≤0.41%), though with larger variance, for which the underestimation can be as large as 1.8% in the control at $R = 4.0$. Student's *t*-test was performed on the results of MW relative fraction from both the CS reconstruction and the control with the null hypothesis that their means are equal to the result from full data. The hypothesis is accepted by the results from CS reconstruction ($p \geq 0.15$) expect for $R = 4.0$ ($p = 0.02$), while it is rejected by all the results from the control ($p < 1\times10^{-7}$).

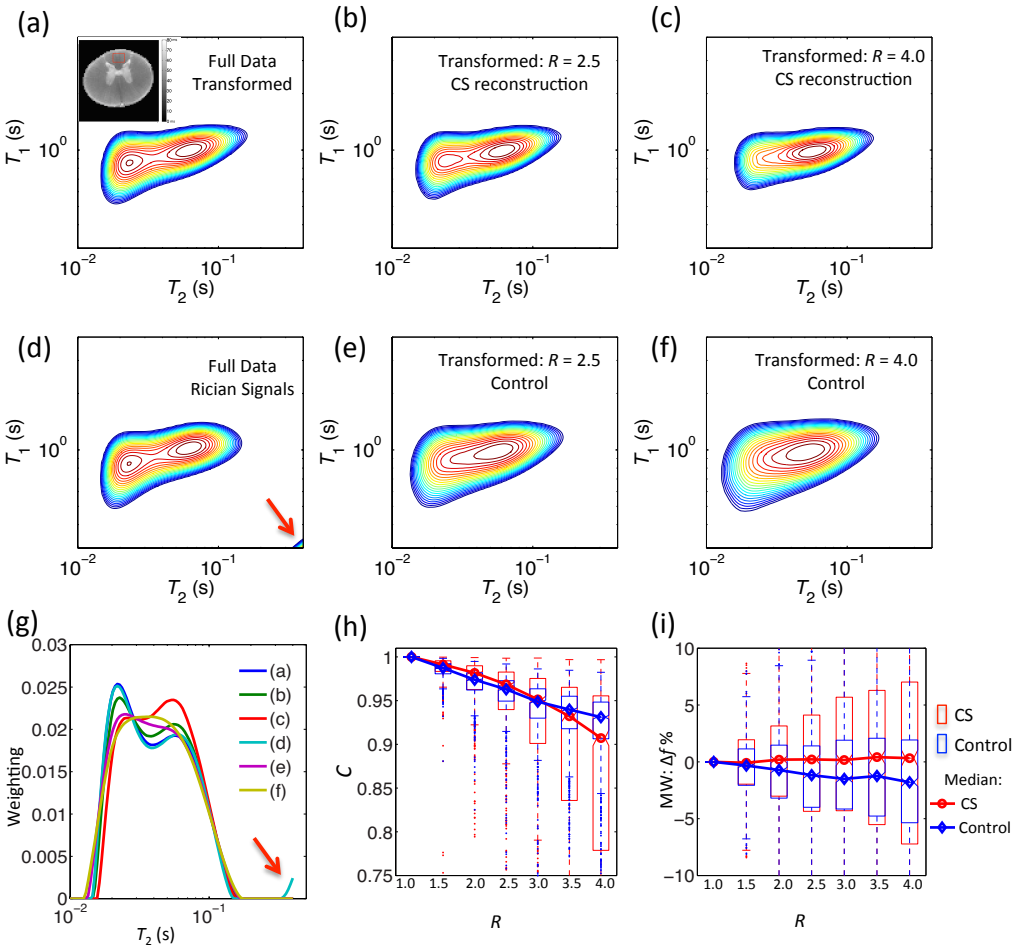

Figure 4.8. The T_1–T_2 spectra of (d) the original magnitude data in the dorsal porcine white matter, (a) full data with transformed signal, (b) CS reconstruction from the transformed data at R = 2.5 and (c) at R = 4.0, (e) and (f) the corresponding control. (g) The normalized 1D T_2 projections of (a–f). (h–g) The results of (h) the correlation coefficients and (i) the MW fraction as a function of the acceleration factor R, where the red are the CS reconstructions and the blue are the corresponding controls. The map of the gmT_2 from 10 ms to 400 ms of the spinal cord and the ROI in the dorsal white matter (red curve) are shown at the upper left corner of (a).

4.7 Discussions and conclusions

In this work, our main objective was to design a pipeline to accelerate the acquisition of 2D relaxation spectra using compressed sensing and then to test and validate its efficiency in maintaining the quality of the 2D distributions with both simulations and acquired NMR and MRI experimental data.

Clearly, compared with 1D relaxation spectra, more information can be obtained from the 2D relaxation spectra, even in simple well-defined systems like the urea/water mixture studied here. The 2D spectra can uncover and distinguish different relaxation components that may be hidden in the 1D spectra. For example, only one peak can be observed in the T_1 spectra of the urea/water phantom, whereas two peaks are well defined in the T_1–T_2 relaxation spectra. Furthermore, exchange information between different components can also be extracted from 2D relaxation spectra whereas this is not possible in the 1D case. In T_2–T_2 relaxometry of the urea/water phantom, the off-diagonal peaks provide direct evidence of exchange between the protons on the urea and water molecules; these rates of exchange can be then be quantitatively characterized by modeling and fitting the intensities of the peaks. This information cannot be obtained from 1D T_2 spectra alone.

The 2D-ILT algorithm proposed by Venkataramanan et al. is very sensitive to the SNR and the type of noise. For example, in the simulations, either the change in noise type from Gaussian to Rician or the decreasing of SNR from 10000 to 200 will significantly affect the quality of the 2D relaxometry. In T_2–T_2 relaxometry of the urea/water phantom, the off-diagonal peaks showed a little smaller T_2 values than the on-diagonal peaks in the x-axis, which might caused by some systematical

noise/artifacts we don't know yet. Normally, a high SNR with Gaussian noise is required for good performance. These conditions can be easily achieved for most NMR experiments with large sample sizes at high fields. However, for MRI applications, the SNR is typically lower and the noisy amplitude signal should be transformed from a Rician to a Gaussian distribution. Higher SNR in MRI can be achieved by performing ROI analysis in homogeneous regions.

In both simulations and the MRI experiments on the spinal cord, the presence of Rician noise introduces spurious peaks in the long T_2 regime because the rectification of the complex MR signal produces a "noise floor" which, uncorrected, is fit by the 2D-ILT routine in both dimensions. This baseline signal biases the signal decay, leading to the appearance of artifactually long-T_2 components and decreasing the contrast between existing peaks. This phenomenon is quite similar to the one we observed previously in the 1D T_2 spectra from noisy MRI magnitude data. A signal transformation framework we proposed previously for 1D T_2 spectra in multi-echo MRI is successfully applied here to the 2D relaxation spectra obtained from MRI data to remedy biases caused by Rician noise. While the method is not perfect, these biases are significantly reduced.

CS reconstruction was successfully carried out on the simulated 2D relaxation spectra data, experimental NMR data on a well-characterized urea/water phantom, and the IR-ME MRI data from the porcine spinal cord. With the CS reconstruction, the size of the data matrix can be reduced significantly without compromising the quality of the final 2D relaxation spectra. Compared with the controls, 2D relaxation spectra obtained from subsamples using CS reconstruction shows a better

approximation to the ground truth or to the results from full data, as demonstrated by the higher global correlation coefficient; better contrast between local peaks; and more accurate relative volume fraction and relaxation parameters. A disadvantage of the CS reconstruction is that it admits more outliers at higher R, where the noise in some subsamples causes the CS reconstruction to fail. However, the number of these problematic subsamples becomes negligibly small as a function of the number of data points collected [322]. Additionally, the CS-reconstruction algorithm proposed here is very fast with processing time around several seconds for each reconstruction on an Apple Desktop computer with 4 cores.

The maximum acceleration factor, R that can be achieved using CS reconstruction depends on the noise amplitude, noise type, the experimental design of the MR data acquisition protocol, and the underlying ground truth. In the simulation, better T_1–T_2 spectra are obtained at a high SNR (2000) than at a low SNR (800) at the same acceleration factor. In the T_2–T_2 spectra of the urea/water phantom, R = 12 can be achieved at a mixing time, τ_m = 50 ms, but the maximum R at a mixing time τ_m = 1000 ms is 9, for which the SNR is around 5 times lower and the relaxometry spectra appear more complex. As for the simulations of the 2D relaxation spectra with MRI, the maximum R is around 5 even after the noise correction, since CS is performed with an already small data matrix.

Two distinguishable peaks were observed in the T_1–T_2 spectra of the white matter from the porcine spinal cord, which were assigned to be myelin water (shorter relaxation times) and intracellular/extracellular water (longer relaxation times). These results were consistent with previous 1D T_2 spectra measures in the white matter *in*

vivo or *ex vivo* [178,254,260,325]. Here the maximum R that can be achieved is equal to or less than 4.0, which is smaller than in the simulations. Several reasons may contribute to this reduction: (1) the SNR is lower in the experiments since the number of voxels in the ROI is less than 100; (2) the noise is still not Gaussian even after preprocessing since there might be some systematic artifacts; (3) heterogeneities may exist among voxels and ROI-type analysis might not be the best way; (4) the underlying ground truth of the T_1-T_2 relaxation spectra of the biological tissue is still poorly known, thus there might be biases in the T_1-T_2 relaxation spectra when the complete data set is used. Interestingly, even with a decreased correlation coefficient, CS reconstruction corrects the bias in estimating the MW and IEW fraction with the conventional 2D ILT method, though with larger variance.

The biggest obstacle to migrating 2D relaxation spectra measurement to *in vivo* preclinical and clinical MRI scanning applications is the long acquisition time. For example, the total acquisition time for the IR-ME experiments in this experiment was ~21 hours. With CS, the time can be reduced to ~6 hours by an acceleration factor $R = 3.5$, but these times are still too long for *in vivo* applications. However, the parameters chosen in our time-consuming IR pulse sequences were conservative, leading to a long pre-scan delay. There are other MRI pulse sequences with shorter acquisition time, such as the saturation-recovery prepared multi-echo (SR-ME) with echo-planer (EPI) acquisition pulse sequences, proposed by Does and Gore [294], whose total acquisition time is about 1 hour. If the same acceleration factor $R = 3.5$ can be achieved there, the total acquisition time could be reduced to 17 minutes. In

addition, even higher acceleration factors will be possible as SNR increases with improvements in scanner hardware.

One practical concern of the CS reconstruction is the random sampling, which might be limited by the natural structure of the CPMG or multi-echo pulse trains, i.e., the reduction of the scan time is only achievable in the first dimension of the three pulse sequences (Fig. 4.1) used in this study. However, in high-field MRI scanners, safety concerns, primarily power deposition in tissue owing to a high specific absorption rate (SAR), limits the total number of 180° pulses that can be applied per unit time. Therefore, a practical alternative would be to use a single echo or a few echoes with a fast MRI acquisition, such as EPI; parallel imaging; multi-band excitation, etc. In these cases, acceleration provided by CS reconstruction could play an important role in reducing the acquisition time further, making 2D relaxation spectrum MRI measurements clinically feasible. Though the three pulse sequences in this study can't be directly applied to *in vivo* preclinical and clinical studies, but the data from these sequences represents the general 2D relaxometry data structure and the findings in "compressing" the 2D data will be helpful for future pulse sequence designs and data analysis.

In this work, the CS reconstruction was carefully validated in simulations and a limited number of biological samples. For *in vivo* MRI applications, much work is still required, such as reaching a deeper understanding of the ground truth of the 2D relaxation spectra in different biological tissues, better modeling and correction of the noise within MRI acquisitions, and hardware improvements that will increase the SNR. Only 2D T_1-T_2 and T_2-T_2 MR relaxometry were validated here, but this pipeline

can be easily adapted to other 2D spectra, such as D-T_2, D-D, T_1-T_1, etc., provided that the application of the successive "filters" results in a relationship between the measured magnetization and the relaxation parameters that is given by a 2D Fredholm equation. Moreover, higher dimensional (nD) relaxometry studies can also be used because compression efficiency can increase in CS with increased dimensionality particularly when spectral data are sparse and compactly supported, as appears to be the case with many experimental relaxation spectra. In addition, further data compression can be achieved if CS is used both in the Laplace domain, as is done here, and in the Fourier domain to reduce the number of MRI acquisitions required for spatial localization.

4.8 Algorithm detail: recover $\widetilde{\boldsymbol{M}}$ from incomplete measurements with compressed sensing

Let us start with the minimization problem in Eq. 4.3. With the SVD in Eq. 4.4, Eq. 4.3 can be rewritten as [311,322]

$$\begin{aligned}\hat{F} &= \arg\min_{\hat{F}\geq 0} \|M - K_1 F K_2'\|^2 + \alpha\|F\|^2 \\ &= \arg\min_{\hat{F}\geq 0} \left\|U_1\widehat{M}U_2' - U_1U_1'K_1FK_2'U_2U_2'\right\|^2 + \|M\|^2 - \left\|U_1\widehat{M}U_2'\right\|^2 + \alpha\|F\|^2 \\ &= \arg\min_{\hat{F}\geq 0} \left\|\widehat{M} - (S_1V_1')F(S_2V_2')'\right\|^2 + \alpha\|F\|^2\end{aligned} \tag{4.7}$$

where the third line comes from U_1 and U_2 having orthogonal columns, and the second and the third items in the second line being independent of F. The target of the CS reconstruction is to search for a matrix X to well approximates the ground truth

$\widetilde{M}_{\mathbf{0}} \equiv (S_1 V_1')F(S_2 V_2')' \in \mathbb{R}^{s_1 \times s_2}$ with the given subsamples *y*, which was chosen from the full data *M* on random entries

$$y = \mathcal{R}_\Omega\left(\widetilde{M}_{\mathbf{0}}\right) + \epsilon \tag{4.8}$$

where $\Omega \subset \{1, \dots, N_1\} \times \{1, \dots, N_2\}$ is the set of random indices where we observe *M* with $|\Omega| = m$ and the indices ordered as $\Omega = \{(i_k, j_k)\}_{k=1}^{m}$, and $\mathcal{R}_\Omega$ is the sampling operator

$$\begin{aligned} \mathcal{R}_\Omega &: \mathbb{R}^{s_1 \times s_2} \to \mathbb{R}^{m} \\ \mathcal{R}_\Omega(X) &= \mathcal{A}_\Omega(U_1 X U_2') \end{aligned} \tag{4.9}$$

Here $\mathcal{A}_\Omega$ is a linear operator with random sampling

$$\begin{aligned} \mathcal{A}_\Omega &: \mathbb{R}^{N_1 \times N_2} \to \mathbb{R}^{m} \\ \left(\mathcal{A}_\Omega(X)\right)_k &= X_{i_k, j_k} \end{aligned} \tag{4.10}$$

Our CS reconstruction is based on low-rank matrix completion and the reconstruction step takes the form

$$\begin{aligned} \min \quad & \|X\|_* := \textstyle\sum_{i=0}^{r} \sigma_i(X) \\ \text{such that} \quad & \|\mathcal{R}_\Omega(X) - y\|_{\,2} \le \epsilon \end{aligned} \tag{4.11}$$

where $\sigma_i(X)$ is the *i*th singular value of a rank *r* matrix *X* and the operator $\mathcal{R}_\Omega$ satisfies the restricted isometry property (RIP) as demonstrated in [322]. In the algorithm, instead of solving Eq. 4.11, we solved the relaxed Lagrangian form

$$\min \mu\|X\|_* + \frac{1}{2}\|\mathcal{R}_\Omega(X) - y\|_2^2 \tag{4.12}$$

Eq. 4.12 is solved using the singular value thresholding algorithm from [324,326] with a two-step iterative process. Let the matrix derivative of the L_2 norm term in Eq. 4.12 be written as

$$\begin{aligned} g(X) &= \mathcal{R}_\Omega^*(\mathcal{R}_\Omega(X) - y) \\ &= U_1'\left(\mathcal{A}_\Omega^*(\mathcal{A}_\Omega(U_1 X U_2') - y)\right)U_2 \end{aligned} \tag{4.13}$$

Another notation is the singular value thresholding operator S_v that reduces each singular value of some matrix X by v. Let us say the SVD of X is $X = U\Sigma V'$, then S_v is defined as

$$S_v(X) = U\hat{\Sigma}V', \text{ with } \hat{\Sigma}_{i,j} = \begin{cases} \max(\Sigma_{i,i} - v, 0), i = j \\ 0, \quad \text{otherwise} \end{cases} \tag{4.14}$$

The two-step iterative process is then

$$\begin{cases} Y^k = X^k - \tau g(X^k) \\ X^{k+1} = S_{\tau v}(Y^k) \end{cases} \tag{4.15}$$

With proper choices of τ and μ, for any initial condition, this method converges with a high probability to a matrix $\widehat{M}$, which is guaranteed in theorem [322] to be close to $\widetilde{M_0}$ up to a constant factor of the noise. The recovered $\widehat{M}$ is then substituted into Eq. 4.7 to solve for F. More details about this CS reconstruction process can be found in [322].

Chapter 5: A novel test bed for testing and developing direct fMRI methods using simultaneous calcium fluorescence imaging and MR of *ex vivo* organotypic brain cortical cultures

Recently, several new functional magnetic resonance imaging (fMRI) contrast mechanisms including diffusion, phase imaging, proton density, etc. have been proposed to measure neuronal activity more directly and accurately than blood-oxygen-level dependent (BOLD) fMRI. However, these approaches have proven difficult to reproduce, mainly because of the dearth of reliable and robust test systems to vet and validate them. In this chapter, we described the development and testing of such a test bed for non-BOLD fMRI. Organotypic cortical cultures were used as a stable and reproducible biological model of neuronal activity that show spontaneous activity similar to that of *in vivo* brain cortex without any hemodynamic or respiratory confounds. An open-access single-sided MR "profiler" consisting of four permanent magnets with a magnetic field of 0.32 T was used in this study to perform MR acquisition. A fluorescence microscope with long working distance objective was mounted on the top of a custom-designed chamber that keeps the organotypic culture vital, while the MR system was mounted on the bottom of the chamber to achieve real-time simultaneous calcium fluorescence optical imaging and MR acquisition on the same specimen. In this study, the reliability and performance of the proposed test bed was demonstrated by a conventional CPMG MR sequence acquired simultaneously with calcium imaging, which is a well-characterized measurement of neuronal activity. This experimental design will make it possible to directly correlate

the other candidate functional MR signals to the optical indicia of neuronal activity. This chapter was adapted from manuscript 5, which is under review by *NMR in Biomedicine* (Appendix A).

5.1 Need of a reliable and robust test system for direct fMRI

Detection of neuronal activity noninvasively and *in vivo* is a *desideratum* in medicine and in the neurosciences. As an example, the *BRAIN Initiative* (http://braininitiative.nih.gov/) was launched with the goal of advancing neuroimaging techniques that enable the measurement of brain function at multiple spatial and temporal scales. Owing to the many forms of MRI contrast, and MRI's exquisite sensitivity to water dynamics in soft tissue, functional magnetic resonance imaging (fMRI) remains a promising method for the assessment of neuronal activity. The most commonly used contrast mechanism in fMRI is based on the blood oxygenation level dependent (BOLD) effect, which measures local hemodynamic changes, a secondary effect of neuronal activity [78,79,327]. This indirect relationship between the BOLD fMRI signal and local neuronal activity confounds its interpretation and limits both its temporal and spatial resolution [80,85,86].

Over the past decade, several non-BOLD fMRI mechanisms have been proposed to detect neuronal activity directly. These methods include, but are not limited to: (a) functional diffusion MRI to detect water displacements [91–94]; (b) phase MRI of changes in local magnetic field caused by neuronal currents [95–97]; (c) Lorenz-Force-effect MRI of neuronal currents to detect displacements of neural tissue [98,99]; (d) proton–density–weighted MRI [100,101]; and (e) spin-lock MR methods [102,103]. Although proponents of these methods have reported positive

findings, most of these approaches are either still in development or have not been reproduced by a larger cohort of researchers. One obstacle in advancing this important research, e.g., convincingly demonstrating one or more of these proposed mechanisms, is the dearth of "ground truth" experiments—specifically, a means to generate reproducible neuronal activity while providing a robust and reliable MR means to detect them.

At a minimum, such an fMRI test bed should include (a) a well-characterized biological model of neuronal activity free of hemodynamic, respiratory and related confounds, and (b) an independent well-established neurophysiological method to detect neuronal activity directly and simultaneously with fMR/fMRI. *In vitro* perfused brain slices are a good choice for achieving the first goal as they have been widely used in neuroscience community as a biological model to study neural functions since 1950s [134–136] and have no hemodynamic or respiratory artifacts. Indeed, perfused brain slices have already been used in successful MR spectroscopy and imaging experiments designed to study metabolism, neurotransmitter, ions, tissue microstructure, tissue injury and even the neuronal excitation [69,70,93,124,131,137–143]

To meet the second requirement, one of the standard neurophysiological methods—which include intracellular and extracellular electro recording, intracellular calcium imaging, membrane voltage imaging, etc. [1,10]—should be used to measure neuronal activity inside the NMR/MRI system during MR acquisition. Though the close configuration and potential electromagnetic interface in MR systems make it difficult to perform these recordings together with MR acquisition, few hybrid setups

have been reported in which BOLD fMRI was recorded together with electrodes [144,145] or optical fibers [86]. In other fields, one group did perform successful experiments to study single cell or cell cultures with a very technically challenging setup involving a combination of confocal and magnetic resonance microscopy [146–149]. However, to our knowledge, a direct (non-BOLD) fMRI experiment that satisfies the two requirements discussed above has not yet been reported.

Here we propose and demonstrate the use of such a test bed in which MR experiments and calcium fluorescence imaging are performed simultaneously on organotypic cortical cultures from rat. In this system, a single-sided MR system with permanent magnets was used [150]. Such systems, developed in the last two decades, are portable and have been used primarily to study the proton density, relaxation times, and diffusion coefficients in biological samples, polymers and gels, foods, and materials [151–155]. One key attribute of single-sided MR systems is the open access to the sample they provide, a feature we exploit in our design, in which a fluorescence optical microscope with a long working distance was installed above the biological specimen to simultaneously image intracellular Ca^{2+} transients. Fluorometric Ca^{2+} imaging detects caged or bound Ca^{2+} ions released during neuronal activity and represents a direct method for detecting neuronal activity [156,157].

In this study, we performed experiments on the organotypic cultures of rat cortex, which has been widely used in neuroscience as a biological model of neuronal activity [158–162] and also has been used in MRI studies [95,140,163]. Organotypic cortical cultures largely maintain the *in vivo* cortical cytoarchitecture including cortical layers and cortical cell types, which can be grown and recorded from for

several weeks in the incubator [159,160]. More importantly, organotypic cultures *in vitro* display bursts of spontaneous neuronal activity, so-called up- and down-states, that is similar to *in vivo* nervous tissue [161,164,165]. Thus, no pharmacological manipulation is required to initiate neuronal activity and the culture remains in a long-term homeostatic state while exhibiting large transients of neuronal activity [162]. Organotypic cultures do not contain a cerebrovascular system and thus are free of artifacts of hemodynamic origin, such as pulsation and flow artifacts or artifacts associated with respiration and variable oxygenation, which are known confounds in fMRI studies *in vivo*.

In this work, we focus on the description and demonstration of this test bed to assess the direct fMRI measurement of neuronal activity. This article is organized as follows: A systematic description of each essential component of the test bed, which consists of the organotypic cortical culture, the MR system, the fluorescence calcium imaging, etc., is provided. Following that, the performance of the system, in particular, the properties and stability of the MR and fluorescence calcium signals is described. Then, the results of the experiments with simultaneous calcium fluoresce imaging and a conventional MR multi-echo pulse sequence without imaging are analyzed and discussed. Finally, the benefits of such a testing system and its potential applications for future work are discussed.

5.2 Simultaneous calcium fluorescence imaging and MR recording on the organotypic cortical cultures—setups

5.2.1. Organotypic rat-cortical culture

For the preparation of organotypic tissue cultures, somatosensory cortex was taken from acute coronal slices of newborn rats (postnatal day 0–2, Sprague Dawley). Organotypic cultures made from coronal slices maintain the layered organization of the cortex and the parallel orientation of pyramidal neurons with respect to each other. The acute slices (350 μm thickness) were attached to the #1 coverslips by using a plasma-thrombin mixture and submerged in 800 μL of culture medium and incubated at 35.0 ± 0.5 °C. The medium was replaced every 3–4 days. The tissue was cultured for up to 3 weeks, when the tissue thickness was approximately 100 – 200 μm. More details about growing this type of organotypic culture can be found in [162,328]. We commonly mounted two cortical slices close together on each coverslip to increase tissue volume within the RF coil. This approach allowed for neuronal cultures to preserve most of the architectural specificity of a cortical network.

5.2.2. Setup for simultaneous functional MR and calcium imaging

Fig. 5.1 is a schematic diagram, showing the placement of the MR and fluorescence imaging systems with respect to the *in vitro* specimen. Organotypic cultures from rat cortex were grown on a coverslip [160,328] and kept in a custom-machined environmental chamber to maintain the cultures' vitality during the experiment and to allow for perturbation of environmental conditions. The chamber was mounted on top of a single-sided MR system with permanent magnets; this setup provided open access to the tissue culture. An RF surface coil was attached directly below the coverslips to transmit and receive MR signals. An optical fluorescence microscope was mounted above the MR stage, thus enabling calcium imaging down

onto the organotypic culture. One advantage of this optical system is its long working distance objective (87 mm with the 0.63× lens), which separates the permanent magnets and the fluorescence microscope. Another advantage is its large field of view (FOV) (8.8 mm × 6.6 mm at 1× magnification), which can capture the entire tissue specimen (~ 2 mm × 4 mm for each cortex). The details of each part of this test bed are described in the following sections.

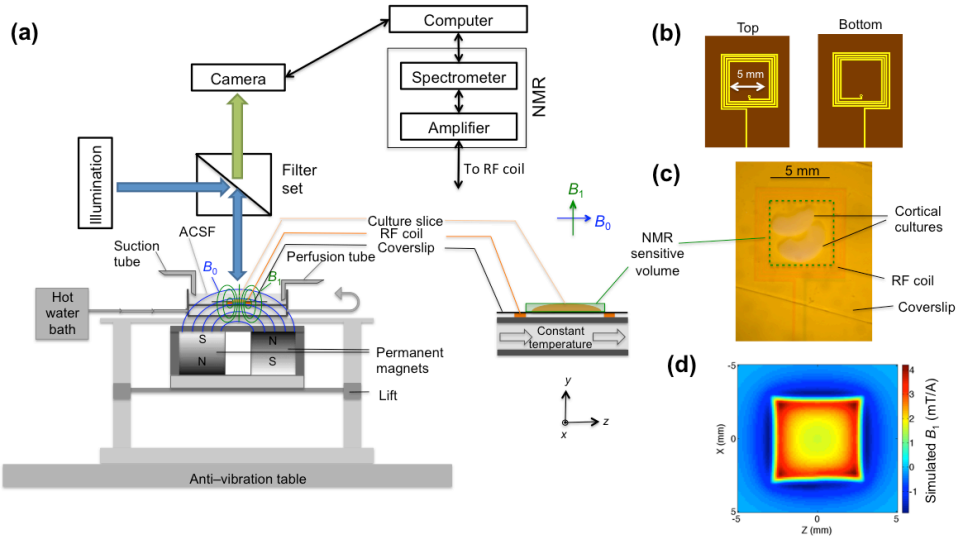

Figure 5.1. Setup for simultaneous functional MR and calcium imaging. (a) Schematic diagram of the simultaneous MR and fluorescence imaging test bed (left) and an enlargement of the components near the organotypic cultured tissue (right), which is immerged in artificial cerebral spinal fluid (ACSF). (b) Top and bottom layers of the two-layer RF surface coil. (c) A real image of the coil with the cortical culture mounted under 0.63× magnification. (d) A simulated 2D B_1 field distribution at y = 0.2 mm in the *x*-*z* plane.

5.2.2.1. Fluorescence microscope

A macro-zoom fluorescence microscope (MVX10 MacroView, Olympus Inc., USA) was modified and mounted on an optical table using a custom designed machined stainless-steel stand and a boom. A 0.63× MVX Plan Apochromat lens

(Olympus Inc., USA) with a 0.15 numerical aperture (NA) was used with total magnification ranges from 0.63× to 12.6×. A 100W Mercury Apo lamp housing and transformer were used as a light source. A color CCD camera (ProgRes® CF scan, Jenoptik, Inc., Germany) with high frame rates (51 fps for 680 × 512 pixel) was mounted on the microscope for fast fluorescence imaging.

5.2.2.2. Calcium staining and imaging

Vital calcium imaging was achieved using 50 μM Oregon Green 488 BAPTA-1 (OGB; Life Technologies, NY, USA). OGB was dissolved in 10 μL pluronic F-127 (20% in DMSO; Life Technologies, NY, USA) and 790 μL freshly prepared artificial cerebrospinal fluid (ACSF). Cultures were incubated for 45–90 minutes in a roller tube incubator and washed in ACSF for 20–60 minutes before imaging. Calcium images were acquired with GFP fluorescence filter units from Olympus (Olympus America Inc., USA), whose activity, dichroic, and emission lengths are 450–490 nm, reflection < 495 nm, and 500–550 nm, respectively. The real-time calcium imaging was acquired using ProgRes® CapturePro v2.8.8 software (Jenoptik, Germany).

5.2.2.3. Single-sided MR system

The permanent magnets of the single-sided MR system (NMR-MOUSE) were purchased from Magritek European, Aachen, Germany. A Kea spectrometer and Prospa acquisition software (Magritek, New Zealand) were used to generate and collect the MR signals. The single-sided MR system with four permanent magnets mounted in an iron yoke (Fig. 5.1, see reference [152] for details) generates a relatively uniform magnetic field (0.32 T, 15 mm × 15 mm) in the *x*-*z* plane at ~ 15 mm from the surface of the magnets. This selective volume, with thickness Δy, is

achieved by a slice-selective acquisition by controlling the acquisition time T_{acq} [150,151]:

$$\Delta y = 2\pi / G_0 T_{acq} \tag{5.1}$$

where G_0 = 650 kHz/mm is the strength of the strong and highly uniform magnetic field gradient across the selective volume in the *y*-direction. Both the MR system and the optical microscope were mounted on an anti-vibration optical table to eliminate spurious mechanical vibrations.

To reduce the MR FOV in the *x*-*z* plane so that it matched the tissue's dimensions, a homemade two-layer multi-turn micro RF surface coil (Fig. 5.1) was used with an inner dimension (5 mm) approximately the size of two cortical slices. The two-layered multi-turn RF surface coils (Fig. 5.1) were fabricated by SF Circuits Inc., San Mateo, CA, USA. On each side of the 225-μm thick polyimide board, there were 4 turns of copper conductors with 18-μm height, 200-μm width and a lateral spacing of 50 μm. The top layer and the bottom layer (Fig. 5.1b) were connected by a copper hole. A calculation based on the Biot-Savart law was performed to simulate the B_1 field distribution produced by the RF coil; this simulation can provide a good estimate of the ground truth at these low frequencies.

5.2.2.4. MR pulse sequences

The Carr-Purcell-Meiboom-Gill (CPMG) pulse sequence (Fig. 5.2a) is widely used in single-sided MR applications to measure the effective transverse relaxation time, $T_{2\text{eff}}$, which is affected by both the transverse relaxation time, T_2, and the self-diffusion coefficient, *D*, in the presence of a static field gradient, G_0 [150]:

$$\frac{1}{T_{2\text{eff}}} = \frac{1}{T_2} + \frac{1}{3}(\gamma G_0 \tau)^2 D\alpha \tag{5.2}$$

where γ is the gyromagnetic ratio of protons, τ is half the echo time, and α = 1.32 [329]. The sensitivity of the $T_{2\text{eff}}$ to T_2 and D was examined with a series of manganese chloride ($MnCl_2$) solutions while τ was adjusted [329].

A well-known feature of diffusion MRI in the cortex is the multi-exponential behavior of the diffusion signal, which is often modeled by a three-parameter biexponential function [62,69,91,93,124,330]:

$$S(b) = S_0[(1 - f_{\text{slow}})\exp(-bD_{\text{fast}}) + f_{\text{slow}}\exp(-bD_{\text{slow}})] \quad (5.3)$$

where S is the diffusion signal; b is the diffusion weighting; D_{fast} and D_{slow} are the fast and slow diffusion coefficients, respectively; and f_{slow} is the slow diffusion compartment fraction. To measure the water diffusion, we used a spin echo (SE) in the presence of a static magnetic gradient (Fig. 5.2b). CPMG echo trains were acquired and summed after the main diffusion-weighting period to improve sensitivity. In this pulse sequence, the b value is defined as [152]:

$$b = \frac{2}{3}(\gamma G_0 \tau_1)^2 \tau_1 \quad (4)$$

where τ_1 is the half echo time of the first spin echo for diffusion encoding.

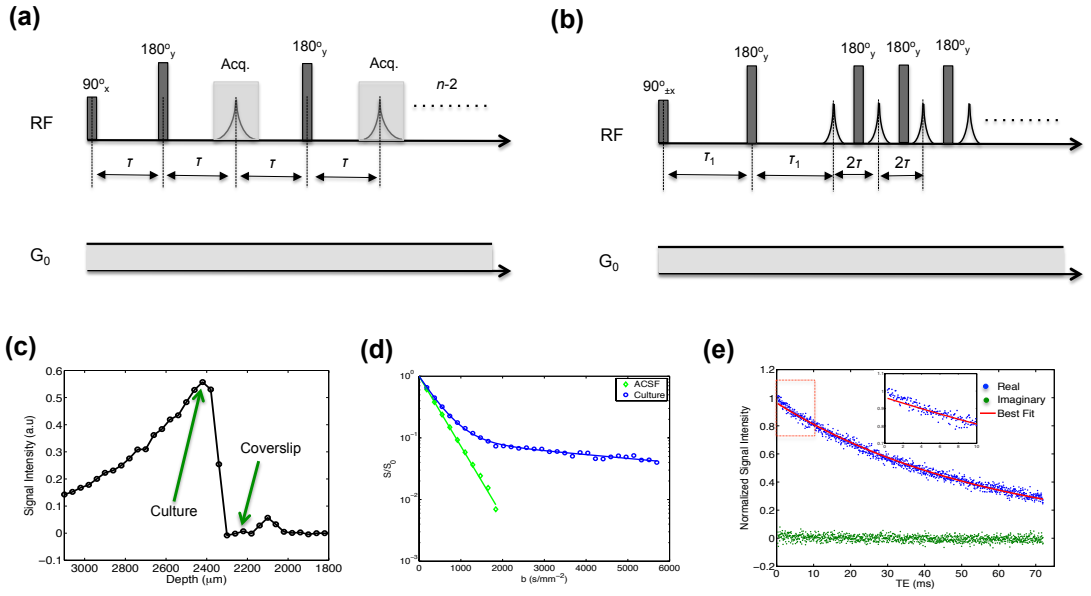

Figure 5.2. MR pulse sequences and signals. Diagrams of the two pulse sequences: (a) CPMG and (b) diffusion editing SE with CPMG detection. (c) MR spatial localization of the culture. (d) The diffusion-weighted MR signal of ACSF (green) and the culture (blue), in which the continuous curves are the fitting results with models. (e) One example of the CPMG signal of the culture, in which the continuous red curves are the fitting result with a single-exponential function. The subplot in the middle is the enlargement of the dashed red box.

5.3 Experimental protocol and data analysis methods

5.3.1 Experimental protocol

Before experiments were performed, the organotypic culture was moved from the roller incubator to the custom chamber (Fig. 5.1) after the calcium dyes were loaded. During experiments, the culture was continuously perfused with oxygenated ACSF (95% O_2 , 5% CO_2) and the temperature of the perfusate was kept constant with an inline temperature controller. A water bath, attached to the bottom of the chamber, was used to precisely control the temperature inside the chamber. Water from a large water bath outside the experimental stage circulated through this bath

and kept it at a constant temperature. A fiber-optic temperature sensor (OpSens TempSens, OpSens Inc., Quebec, Canada) was mounted near the tissues to monitor their temperature during the experiments. The temperature was kept at 34.2 ± 1.0 °C during experiments and the temperature gradient inside the RF coil was less than 0.5 °C. Of the 17 cultures scanned, 14 cultures were statistically analyzed, and three were rejected because of failure in temperature maintenance or MR acquisition software instability.

5.3.1.1 MR spatial localization

After the organotypic culture was mounted in the chamber, a 1D profile with 40-μm resolution was obtained to determine the position of the tissue. A 1D spatial profile in the *y* direction was achieved by mechanically raising and lowering the magnet with a precision lift (best resolution ~ 10 μm) and the CPMG pulse sequence with matching slice-selective acquisition. The parameters for the CPMG sequence were: TR = 2 s, 500 echoes with τ = 40 μs, and 8 repetitions. The signal intensity was defined as the average of the 500 echoes to improve the SNR. In this process, the positions of the RF coil, the chamber, and the culture were fixed while only the selective volume was raised and lowered as the magnet was moved up and down. First, the coverslip was found (Fig. 5.2c), and then the magnet was moved up 80 μm–120 μm to locate the middle of the tissue.

5.3.1.2 Diffusion MR measurements

After a central slice covering the middle portion of the tissue was identified, the SE pulse sequence was performed with 32 *b* values ranging from 0 to 5700 s/mm^2 with a step of 184 s/mm^2. The other parameters were: repetition time (TR) 4 s, 4000

echoes in the CPMG with τ = 20 μs, and 8 repetitions with a two-step phase cycling (Fig. 5.2b). The acquisition time in each echo was 16 μs with 32 sampling points, resulting in a thickness of the selective volume of ~100 μm.

5.3.1.3 Simultaneous calcium fluorescence imaging and MR recording

In the MR, the CPMG pulse sequence was used for fast recording: TR = 1 s, 1200 echoes with τ = 30 μs. The acquisition time and the corresponding thickness of the selective volume were 16 μs (32 sampling points) and 100 μm, respectively. At the beginning of each experimental session, the phase of the CPMG signal was automatically adjusted to put the entire signal into the real channel. Calcium imaging was acquired with 1× magnification, 8.8 mm × 6.6 mm FOV, 680 × 512 pixels, exposure 100 ms, and 10 frames per second. The focal plane and light intensity were adjusted at the beginning of each experiment and kept constant during the entire experiment session. The light intensity was adjusted to the minimal level that still enables distinguish neuronal activity from background noise to avoid strong photo bleaching and phototoxicity. During the experiments, both the camera frame time and the time of MR pulses (first 90° in the CPMG) were recorded with a precision of 1 ms accuracy. The total recording time ranges from 1 hr to 3 hr, which were mainly restricted by the health of the culture with calcium staining and under light shining.

5.3.2. Signal processing and data analysis

All signal processing and analysis routines were implemented in MATLAB.

5.3.2.1 Calcium signal processing

Regions of interest (ROIs) were manually selected on the two cortical slices (Fig. 5.3a) to show the spontaneous activity within and between the cultures. A

background ROI was also manually selected close to the tissue but with no tissue inside. Comparison and correlation of the calcium signal with the MR signal were also performed by manually choosing a large ROI containing all the tissues inside the RF coil. Background subtraction was further performed on the fluorescence signal from the large ROI by automatically subtracting the background. The fluorescence values were then expressed as relative percentage changes from the baseline, $\%\Delta F/F$. Formally, $\Delta F/F$ is defined as the change in fluorescence over the baseline: $\Delta F/F = (F_{ROI} - F_{ROI,0})/F_{ROI,0}$, where F_{ROI} and $F_{ROI,0}$ denote the background-corrected fluorescence intensities in the ROI and its baseline calculated from a 30-second sliding window to overcome photo bleaching artifacts. To detect calcium transients in an automated manner, a deconvolution algorithm, based on the 1D-deconvolution algorithm in MATLAB, was developed and applied to the fluorescence signal, $\%\Delta F/F$. The convolution kernel consisted of two parts: a delta function for the fast rising phase and a slow decay curve back down to the noise floor. Fluorescence decay curves were carefully fitted after neuronal activity events. A threshold was set in the deconvolved data to enable robust detection of neuronal activity events.

5.3.2.2 MR CPMG and SE signal

The first four echoes that have systematic artifacts in each CPMG echo train were automatically eliminated. The zero-order phase correction was automatically applied to all the CPMG echo trains in each experiment. As for the spontaneous MR and calcium recording, the first 10 CPMG echo trains at each long recording were automatically removed to eliminate the instability present before the steady state was reached. Three MR parameters were extracted from each CPMG echo train: $I_{0,}$ the

average of the first 5^{th} to 100^{th} echoes (real channel, mean TE (mTE) = 3.2 ms), denoted as the initial signal intensity and a representation of proton density; *R*, the weighting ratio between the average of the echoes from the 301^{rd} to the 1200^{th} (real channel, mTE = 45.0 ms) and from the 5^{th} to the 300^{th} (real channel, mTE = 9.2 ms), denoted as the decay rate; φ, the phase of the average of all the echoes, denoted as the phase of the MR signal.

In the case of the MR SE signal, the average of the entire CPMG echo train was used as the signal intensity at each b value. A trust-region-reflective nonlinear least square algorithm in the MATLAB was used for the model fitting.

5.3.2.3 Effects of neuronal activity on MR signal

The potential effects of neuronal activity on the MR signal were tested by binning the MR signal itself into two categories: active and resting states. Then, paired comparisons were performed on each active MR waveform with its corresponding resting MR waveform by subtracting each active MR signal from its corresponding resting signal.

Two types of time-series analysis were performed. Type 1, we hypothesized that each neuronal event only affects the MR signal recorded after each neuronal event in a time window *T*, with ranges from 0.1 s to 1.0 s with a step of 0.1 s. The corresponding resting MR for each active MR was the MR recording the closest in time to the moment before the neuronal event (Fig. 5.5a). The fluorescence signal for each MR signal was the average of the entire fluorescence signal within *T* prior to each MR recording. Type 2, we hypothesized that each neuronal event only affects the MR signal recorded within 2 s before and following each neuronal event. All MR

signals outside this 4 s time window were denoted as resting state (Fig. 5.5b). The fluorescence signal for each MR signal was the average of the entire fluorescence signal within 2 s before and following each MR recording. To scale the difference across cultures and perform statistics, the fluorescence signals for all MR recordings in each culture were normalized by their maximum value in the active state. Each active MR was further binned into different groups on the basis of how distant it was in time (Δ) from the neuronal event with a time step 0.2 s. For each active MR, the four resting MRs closest to it in time, both before and after, were chosen and averaged as the corresponding resting MR.

5.4 MR signal of the organotypic cortical culture

5.4.1 Micro RF coils

Tuning and matching the coil with an external circuit was achieved with a quality factor (Q) of 14 [331]. The B_1 field distribution in the selective plane (middle of the tissue, y ~ 200 μm) shows a plateau inside the RF coil with maximal sensitivity combined with a slight rise near the inner edge of the coil and a rapid decay starting at the inner edge of the coil in the lateral directions (Fig. 5.1d).

5.4.2. MR spatial localization

In the 1D profile (Fig. 5.2c), the signal intensity increased as the selective volume was lowered towards the surface of the RF coil, but the signal dropped quickly to zero as the selective volume moved onto the coverslips (thickness ~ 0.13 mm to 0.16 mm). Then, the magnet was moved up by 80 μm to 120 μm to locate the center of the culture tissues.

5.4.3. MR diffusion measurements

To confirm that the selective volume (selective thickness ~100 μm) contained the tissue, diffusion MR was performed prior to the simultaneous fluorescence and MR recording (Fig. 5.2d). The diffusion decay signals were fit well by a biexponential function with the tissue in place. In contrast, the diffusion MR signal of the ACSF itself showed a clear single-exponential decay. Statistics for the 14 cultures and the 5 ACSF samples are shown in Table 5.1.

Organotypic cortical cultures (n =14)					
D_{fast} (10^{-3} mm^2/s)	2.56 ± 0.05	D_{slow}(10^{-3} mm^2/s)	0.16 ± 0.03	f_{slow}	10.3 ± 3.1%
ACSF (n =5)					
D (10^{-3} mm^2/s)	2.66 ± 0.01				

Table 5.1. Diffusion parameter estimation with bi-exponential models for the organotypic cultures and with the single-exponential model for the ACSF.

One sample MR CPMG signal (3000 averages) from one culture is shown in Fig. 5.2e. Most of the signal intensity is in the real channel after the phase has been automatically adjusted (imaginary/real ratio is less than 0.1%). The decay curves in all the culture slices (n =14) were fit well by a single-exponential function with T_{2eff} = 59.0±2.7 ms, except for the faster decaying part at echo time (TE) < 5 ms with a fraction 2.5%±0.8% and relaxation time < 10 ms. As for the control with ACSF alone (n = 6), the decay curves were fit well by the single-exponential function over the entire TE range with T_{2eff} = 56.1±0.3 ms, which is slightly (but significantly, p < 0.001) smaller than the results of the cultures. The small, faster decaying parts in the culture slices might arise from some highly ordered water molecules (such as macromolecule-bound water) and some macromolecules (such as metabolites and proteins).

5.5 Spontaneous neuronal activity on organotypic cortical culture

In the calcium images, three ROIs were selected in each cortex region (ROI 1–6), and one ROI (ROI 7) close to the RF coil inner edge but not containing tissue was selected as background. Highly spontaneous activity was observed in all six ROIs, 1–6, (Fig. 5.3b and Fig. 5.3c), while the background ROI 7 showed low fluorescence intensity without neuronal activity information. The correlation coefficients of the fluorescence signals (30-minute recording) between all ROI's, 1−6, were no less than 0.78. The fluorescence from the large ROI containing the entire tissue inside the RF coil also showed high correlation coefficients (>= 0.88, Table 5.2) with all ROIs in the two cortexes region, which makes it as a good representative of the calcium signal of the two cortexes and was used for further correlation tests with the MR signals.

Fig. 5.3d shows 30 decay curves after neuronal activity from one experiment (solid gray lines). A biexponential function can fit the averaged decay curve very well with a fast decay component (69% ± 11%, n=13) and a slow decay component, with time constants (the time required for the signal to decay to 1/e) 0.21 ± 0.07 s and 1.67 ± 0.37 s, respectively. The failure of the single-exponential fit might be due to the large-scale imaging in which the calcium kinetics depends on local calcium concentration, neuron types, and the location of the neurons [332,333]. By implementing the biexponential decay function into the convolution kernel, our deconvolution algorithm can precisely and successfully detect the time and amplitude of each neuronal activity (Fig. 5.3e).

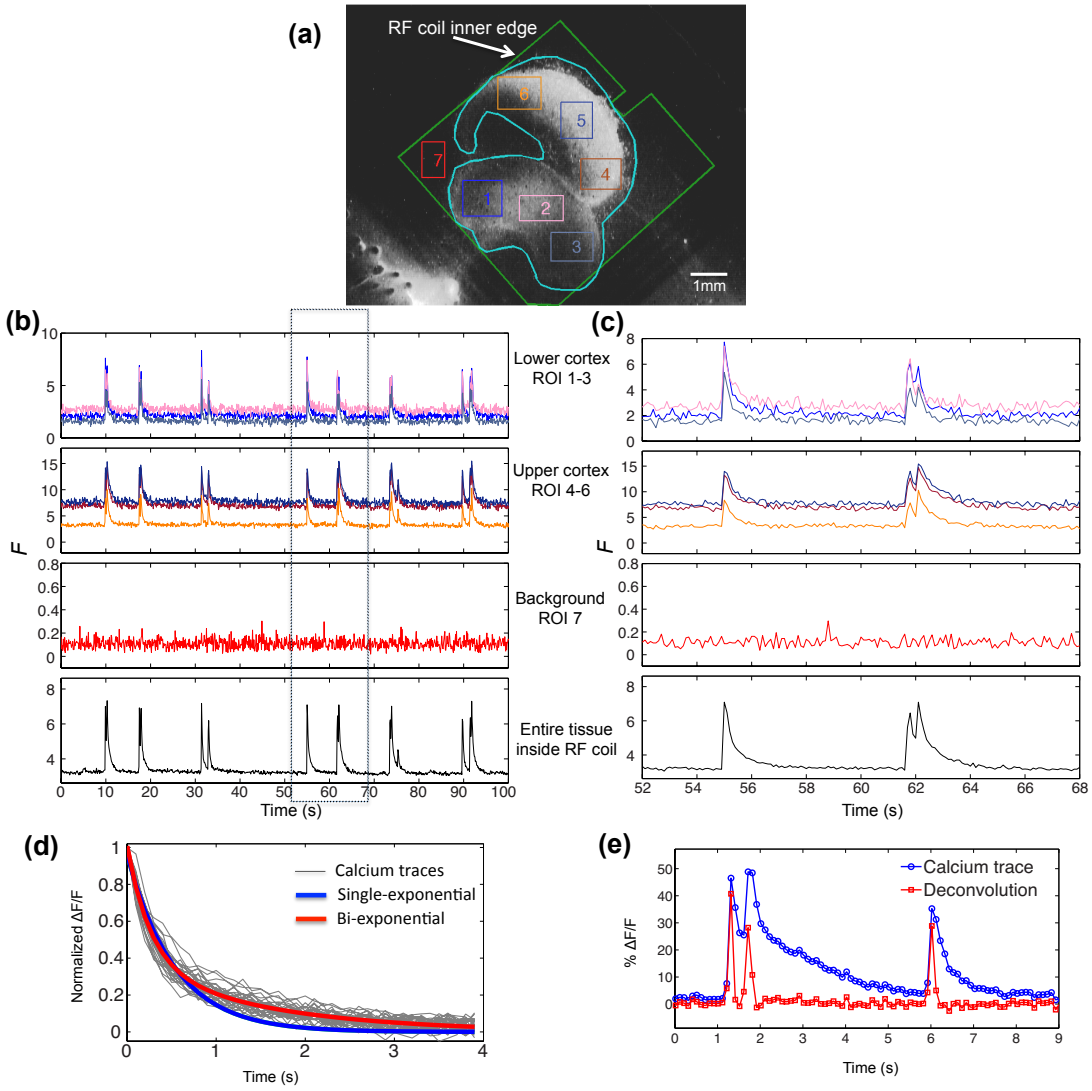

Figure 5.3. Spontaneous neuronal activity in the organotypic culture. (a) Fluorescence image of the organotypic cortical culture (2 coronal slices co-cultured) and the position of seven different ROIs. (b) The raw calcium traces of each ROI in a 100-second time window. (c) The zoomed version of the dashed box in (b). (d) The decay curves after each event and their fittings with single- and bi-exponential functions. (e) Example of the deconvolution algorithm on the calcium signals.

ROI	1	2	3	4	5	6	Entire tissue
1	1.00	0.85	0.89	0.85	0.83	0.85	0.92
2	0.85	1.00	0.82	0.81	0.80	0.81	0.88
3	0.89	0.82	1.00	0.80	0.78	0.81	0.88
4	0.85	0.81	0.80	1.00	0.93	0.93	0.96
5	0.83	0.80	0.78	0.93	1.00	0.93	0.95
6	0.85	0.81	0.81	0.93	0.93	1.00	0.96
Entire tissue	0.92	0.88	0.88	0.96	0.95	0.96	1.00

Table 5.2. Correlation coefficient table for the calcium signals from each ROI on the two cultures (Fig. 5.3) and the entire tissue inside the RF coil.

5.6 Stability of MR and calcium recording

An example of a 1.5-hour simultaneous calcium and MR recording is displayed in Fig. 5.4. For a healthy culture, good neuronal activity can last from one to several hours under continuous optical and MR recording. In this example, the neuronal activity was quite stable during the entire 1.5-hour recording. At the same time, the MR signal, which includes all three parameters (I_0, R, φ) extracted from each CPMG echo train, was also very stable.

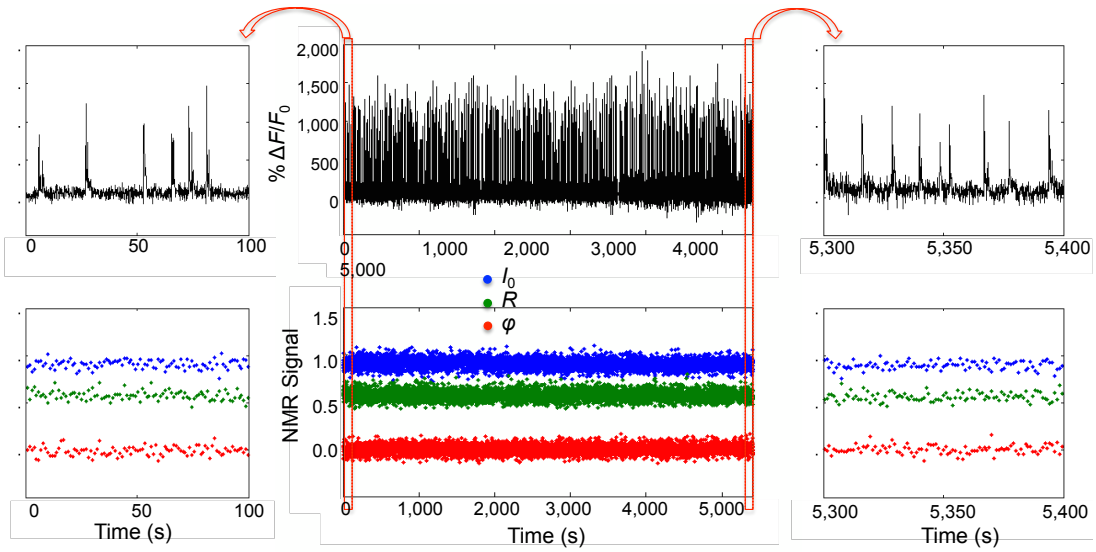

Figure 5.4. Stability of the MR and fluorescence signal. Simultaneous MR (bottom, three MR parameters) and calcium fluorescence (top) recording from one culture for ~1.5 hr. The first and last 100 s were expanded and are shown on the left and right sides of the central panel. Visual inspection does not reveal any correlations between the two.

In the above example, the signal-to-noise ratio (SNR) for I_0 and R are 12.9 and 15.0, respectively, and the standard deviation of φ is 0.04 rad (~ 6×10^{-3} parts per million (ppm) in frequency); similar noise levels were found in all admissible experiments and in two control experiments where only ACSF was present. In some experiments, there was slow-frequency (< 0.005 Hz) drift, which might be caused by small-trapped air bubbles in the ACSF line, slow motion caused by bending of the coverslips through heating, etc. The drift of I_0, R, and φ in the 1.5-hour recording session was less than 2.6%, 0.7%, and 0.02 rad (~ 3×10^{-3} ppm), respectively, for the example in Fig. 5.4 and 5.8%, 3.2%, and 0.09 rad, respectively, for all the cultures used in our statistical analysis. However, this type of drift is small and can be

neglected when active- and resting-state MR are compared in the data analysis procedure, since that time window is less than 12 s.

5.7 Effects of neuronal activity on MR signal (proton density and effective transverse relaxation time)

The potential effects of neuronal activity on the two MR parameters, I_0 and R, were further analyzed. In the Type 1 analysis, Students' *t*-tests were performed on the results from all the admissible cultures with the null hypothesis that the mean of the difference between active and resting MR was equal to 0. No significant changes were observed for any of the two MR parameters (I_0 and R) for the time window T from 0.1 s to 1.0 s ($p \geq 0.14$ for all of the tests, Fig. 5.5e), while the calcium signal showed much higher intensity in the active state (Fig. 5.5c). For the Type 2 analysis, similar Student's *t*-tests were performed on the paired comparison between the active (the entire 4 s time window without further binning) and resting MR signals, and no significant changes were observed for the two parameters either ($p \geq 0.37$, Fig. 5.5d). The time profiles of the changes in the MR parameters are shown in Fig. 5.5f. All of the averaged changes in the two MR parameters (I_0 and R) from all of the admitted cultures were less than 0.5% and 0.4%, respectively. One-way ANOVA performed on the time-profile MR results and the null hypothesis that the mean of the difference between active and resting MR in each bin were equal was also accepted ($p = 0.85$ and 0.97 for I_0 and R, respectively).

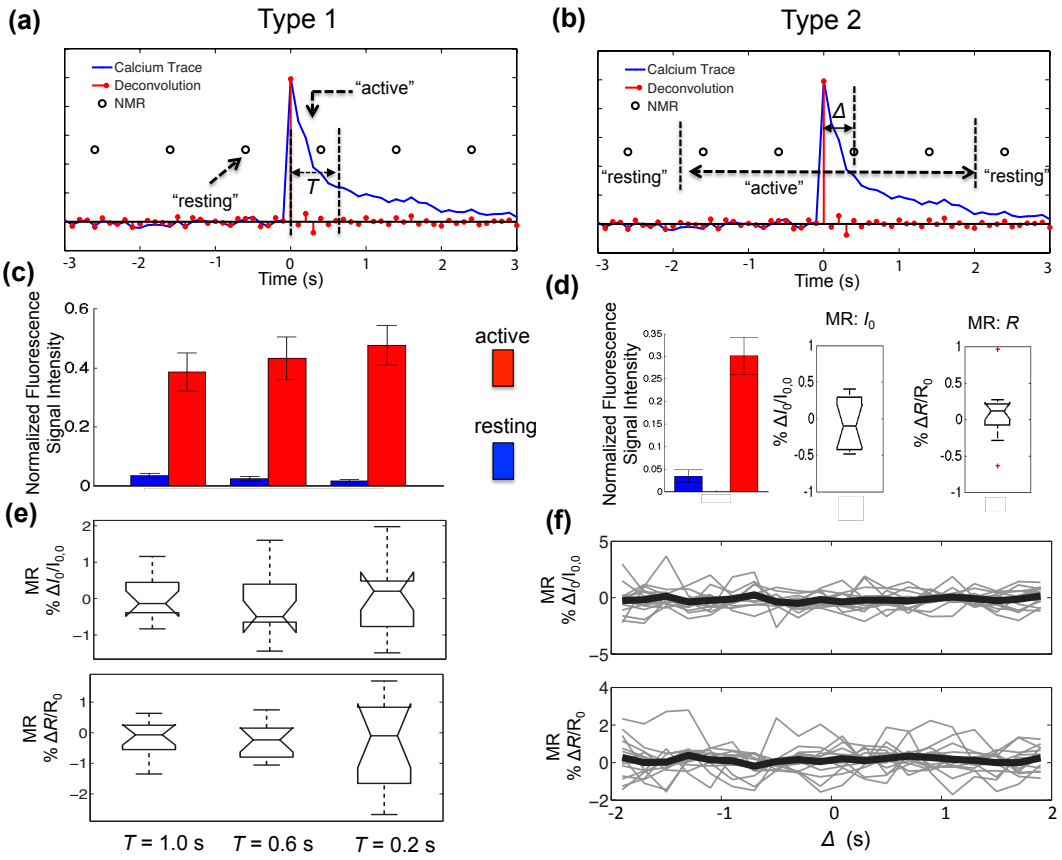

Figure 5.5. Two types of statistical methods for analysis of the potential effects of neuronal activity on the MR signal. Schematic diagram of the analysis methods: Type 1 (a) and Type 2 (b). For Type 1, bar plots of the deconvoluted fluorescence signal and boxplots of statistical results of the paired-comparison MR in the active and resting state at time window T = 1.0 s, 0.6 s, and 0.2 s are shown in (c) and (e). For Type 2, bar plots of the deconvoluted fluorescence signal and boxplots of statistical results of the paired-comparison MR in the entire active (4-second time window) and resting states are shown in (d). The time profiles of the group results for Type 2 analysis are shown in (f), where the narrow gray curves are the averaged result from each culture, and the broad black line is the average of the 14 cultures.

5.8 Immunohistochemistry to clarify cell types and densities in the organotypic cortical cultures

A subset of cultures was used for immunological identification of cell types. Cultures were rinsed in phosphate buffered saline (PBS), fixed in 4% paraformaldehyde for 40–60 minutes, and incubated for 2 hours at room temperature in blocking solution (10% normal donkey serum, 0.5% bovine serum albumin, and 1% Triton X-100 in PBS). The cultures were incubated in three primary antibodies simultaneously at 4°C overnight in a carrier solution consisting of 1% normal donkey serum, 0.5% bovine serum albumin, and 0.3% Triton X-100 in PBS: 1) mouse anti-NeuN (EMD Millipore, Temecula, CA, 1:1000); 2) rabbit anti-s100b/anti-GFAP combined (Dako, Carpinteria, CA, 1:2000 and 1:1000, respectively); 3) goat anti-Iba1 (Abcam, Cambridge, MA, 1:500). After the cultures were washed for 5 min, 15 min, and 5 min in PBS containing 1% normal donkey serum and 0.3% Triton X-100, they were incubated for 1 hour at room temperature in secondary antibodies, diluted in carrier solution: Alexa 555 donkey anti-mouse; Alexa 488 donkey anti-rabbit; Alexa 633 donkey anti-goat (1:1000, Invitrogen, NY) The cultures were then washed two more times with the wash solution for 5 min and 15 min at room temperature. Before imaging, cultures were rinsed in PBS for 5 min and mounted on coverslips with a fluorescence-preserving mounting medium (MOWIOL 4-88, EMD Millipore, Temecula, CA). Control images of cortical cell distribution were obtained with an 8-day-old rat brain fixed by transcardial perfusion. Brain slices (200 μm thick) from the same cortical region as the organotypic cultures were immunostained following the

same procedure as described above. Confocal images were obtained on an inverted Zeiss LSM 510 with a 20x Zeiss plan-apochromat dry objective (0.75NA) at the Microscopy and Imaging Core Facility, NICHD, NIH.

The confocal microscopy images of the organotypic cortical culture were shown in Fig. 5.6. In the control (acute rat-brain slices, Fig. 5.6a), all three types of cells were spatially homogenously distributed with the neuron as the dominant cell type. In the organotypic culture, a layer of astrocytes formed at the surface (Fig. 5.6b) and border of the culture (Fig. 5.6c,d) while the more susceptible neurons were predominantly found in the core of the culture at deeper imaging depths (> 10 μm, Fig. 5.6c,d). Visual inspection indicates even higher cell density of neurons at these steps than the one in the control.

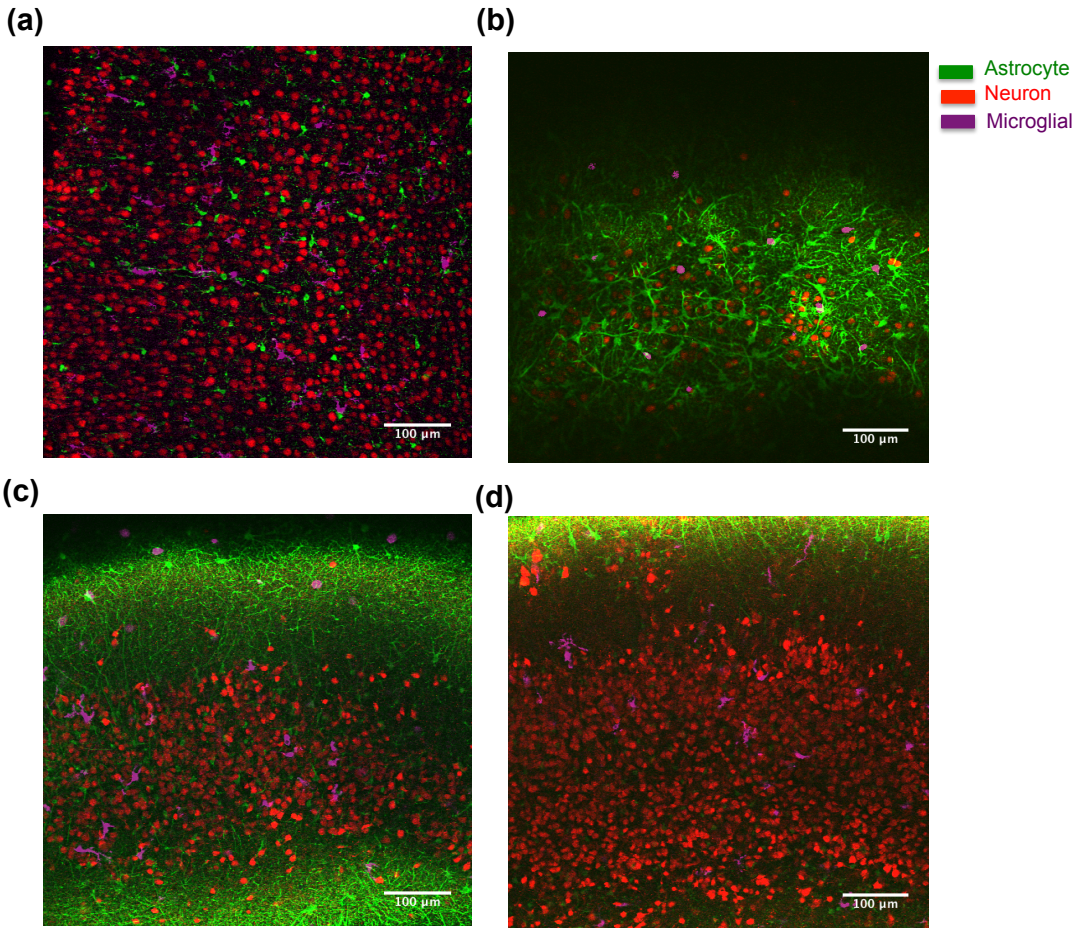

Figure 5.6. Fluorescence staining of rat brain slices with three antibodies labeled astrocytes, neurons, and microglial cells. (a) Acute brain slice from 8-day-old rat. (b-d) Organotypic cortical culture at different imaging depths (b, top layer; c, 10 µm deep; d, 20 µm deep).

5.9 Advantages and limitations of this direct fMRI test bed

Here we provide a novel, versatile and stable test bed for non-BOLD fMRI assessment consisting of 1) a well-established biological model of neuronal activity, 2) a well-controlled environmental chamber to maintain stable neuronal activity, and 3) a multimodal optical and MR means of recording neuronal activity. In our design, real-time calcium images can be acquired simultaneously with the MR signal. Calcium imaging is a well-established method for quantitatively measuring neuronal

activity [332,333]. This method allows for direct comparison of the MR signals and the calcium-based indictors of neuronal activity, and precise temporal localization of the effects of neuronal activity on MR signals.

The use of organotypic cortical cultures as a biological model of neuronal activity eliminates any possible hemodynamic contributions to the MR signal. The organotypic cultures possess healthy neurons similar to those in the *in vivo* cortex with high cell densities and extracellular matrix [159]. Moreover, spontaneous activity in organotypic cortex cultures organizes as neuronal avalanches [161], a common dynamical mode of ongoing activity also observed *in vivo* in humans and nonhuman primates [164,165]. Together, the high neuronal density and synchronized neuronal activity provide the best chance to observe changes in the MR signal due to neuronal activity, if such relationships actually exist.

Performing electrophysiology experiments inside the MRI magnet could be very technically challenging due to the electromagnetic interface [144,145]. The closed configuration and the size of the magnetic core also make it difficult to move the modern optical microscope into inside a conventional MRI scanner [146–149]. Several hybrid setups with simultaneous optical recording and fMRI were reported, but they were limited to hemodynamic based optical imaging [334,335] or a single fiber recording [86]. Here we offer an alternate solution by using the single-sided NMR system [150], which is open-access, low-cost, portable, reliable and compatible with high-resolution optical fluorescence imaging systems. Although in the MR spectroscopy experiment performed in this study an MR signal from the entire selective volume was used because MR imaging with single-sided NMR

system is currently two slow [150,336], the ultimate goal is to achieve simultaneous calcium and MR imaging within the cortical slices. Fast-imaging techniques are under development for this system [337] so that the simultaneous MR and fluorescence imaging should be feasible in future.

An obvious question is whether the results from this experimental setup can be translated to conventional pre-clinical and clinical MRI systems, which normally have much higher magnetic fields. Some MR contrasts, such as proton density, water self-diffusion, etc., are independent of the magnetic field strength, while others, such as T_1 and T_2 relaxation times, phase, Lorenz-force, etc., are strongly dependent on the magnetic field strength [50,99,338–340]. In principle, the changes in the non-field-dependent MR contrasts caused by neuronal activity observed here can be directly migrated to a high magnetic field, while the other field-dependent changes require a more careful discussion. For instance, the Lorenz-force effect can be several orders higher in the high magnetic field; therefore the expected changes here should be several orders smaller. In addition, the inhomogeneous magnetic field also makes some pulse sequences used here different from the conventional MR system and limits the application of some pulse sequences. For example, the gradient echo, which is the common MRI sequence for phase imaging [95,107], is unachievable in this system since the apparent relaxation time T_2^* is too short to detect [150]. Moreover, the presence of the static gradient also put limitations on experiments that are sensitive to diffusion direction. In addition, the baseline noise should also be considered in comparing the results from high-field MRI. For instance, the phase noise level (ppm) in our unshielded magnet is around 10 times higher than that

observed in the high-field shielded MRI system [105,107]. More detailed discussion will be provided for each specific MR contrast/sequence in our future work.

While the SNR for a single MR echo train is not high (SNR ~ 10−20 in this study) due to the low magnetic field and field inhomogeneity, here its sensitivity to the potential changes can be improved by multiple repetitions while prolonging our data recording. For example, in a 1-hour experiment, there are approximately 180 active MR waveforms within $T = 0.5$ s time window after each neuronal activity if we assume the spontaneous neuronal activity occurs every 10 s. Taking the noise level in Fig. 5.5 and a statistical power of 0.80, the sensitivity of the detectable changes in this study will be 0.53% for I_0 and 0.45% for R. Simultaneous recording on each sample can normally last no shorter than 1 hr until some epileptic activity shows or normal activity disappears in the calcium imaging due to the phototoxicity. In future, use of more neuronal-activity-sensitive and healthy fluorescence dyes and low light intensity could result in longer recording time.

Because no imaging is performed in MR, partial volume is still a problem for MR detection in the current setup as the cultured tissue cannot occupy the entire MR selective volume, even the selective volume was significantly reduced by the small custom RF coil (tissue occupies ~60% of the inner area of the coil). The non-single-exponential diffusion MR signal clearly demonstrated that the MR selective volume covers, at least partly, the two cultures. From the results of the bi-exponential fitting, D_{slow} (0.16×10^{-9} m^2/s) values obtained here are similar to those from *in vivo* rat brain and *in vitro* rat acute brain slices with imaging [69,70,93,341], while the D_{fast} (2.56×10^{-9} m^2/s) values are larger and f_{slow} (10.3%) values are smaller than the

corresponding values in the literatures. The differences are probably caused by that the fast-diffusing ACSF in the selective volume was taken as the fast diffusion component in the bi-exponential fitting.

In this study, only a conventional CPMG MR pulse sequence was applied together with calcium imaging. The two parameters extracted from each CPMG echo train correspond to different and distinct contrast mechanisms. I_0 is sensitive to the proton density and the longitudinal relaxation time T_1 (~ 1.5 s for the cultures). The weighting ratio, R, is sensitive to $T_{2\text{eff}}$, which depends both on the diffusion constant, D, and the transverse relaxation time, T_2. In the culture, two diffusion components (fast and slow) were observed using the SE sequence. However, the associated T_2 of each diffusion component and the exchange dynamics between these spin populations are still unknown and currently are beyond the scope of this article.

Statistical analysis of our results does not show statistically significant changes in the MR signals (I_0 and R) associated with neuronal activity when the active and the resting MR are compared, either by comparison of the MR signals before and after neuronal activity or inside and outside of the 4-second time window centered at the neuronal activity spike. However, it would be premature to conclude that this is a negative result for the newly proposed contrast mechanisms described in the Introduction [91,93,100], particularly as there are differences in the pulse sequences, the MR system, and the analysis methods used. As for the I_0 effect, changes in proton density might be canceled out or masked by changes in T_1. In the case of R, a similar cancelation might occur between the contributions from D and T_2. Moreover, the diffusion time in this CPMG sequence is τ = 30 μs, which is much

shorter than that in the conventional functional diffusion MRI experiments (~80 ms for clinical scanners and ~10−30 ms for preclinical scanners) [91–93,121,124]. It has been reported that diffusion MR signals from the cortex are strongly dependent on diffusion time at short diffusion time region (<=10 ms) [341,342].

More importantly, the biophysical basis of many aspects of neuronal activity is still poorly understood. MR visible effects may result from long-timescale changes, like the BOLD fMRI signal (>=10 s). In the organotypic cortical culture, spontaneous neuronal bursts occur approximately every 5 to 20 seconds. If the effect of the neuronal activity on the MR contrast lasted longer than that, the definition of the active and resting MR would need to be changed, as no resting state would exist in the entire recording. And if the effect of the neuronal activity on the MR contrast is the milliseconds scale [171], our current setup might not have enough temporal resolution to capture this effect. More experiments are still needed to address these questions.

It is often presumed that it is sufficient to understand brain function by studying the distribution and pattern of neuronal activity, while the role of astrocytes and other glial cells is often overlooked [343]. This test bed, which uses healthy organotypic brain tissue, has the potential to be used not only to study neuronal excitatory behavior, but also to assess possible changes in glial structure (with proper glial-specific calcium indicators [344]) in response to it, particularly over a longer timescale than that used in these experiments. We view these applications as important future uses of this novel test system.

Although important information can be extracted from the CPMG echo trains, the main purpose of this paper is to describe and demonstrate the successful operation of this novel test bed. The clear biexponential diffusion signal in the SE pulse sequence shows that the MR selective volume covers the tissue on the coverslip. Fig. 5.4 demonstrates the stability of both the calcium and MR signals during a long recording period. Two types of analysis methods were also provided to look for the potential effects of neuronal activity. It is important to note that because the pulse sequence design and experimental protocol are flexible to modify, it is possible to validate or test existing or newly proposed MR sequences and address open biophysical questions with this method.

Chapter 6: Can neuronal activity be detected with diffusion MRI? An *in vitro* assessment with simultaneous calcium fluorescence imaging and diffusion MR recording

Diffusion MRI was proposed recently to detect neuronal activity more directly, yet, initial findings have proven difficult to interpret and reproduce. Given that the underlying relation between water diffusion changes and neuronal activity remains unclear, the rationale for using diffusion MRI to monitor neuronal activity has yet to be clearly established. Here, we attempt to study the correlation between water diffusion and underlying neuronal activity by simultaneous calcium fluorescence imaging and diffusion magnetic resonance (MR) recording *in vitro* (details in Chapter 5). We used organotypic cortex cultures from rat brains, in which spontaneous neuronal activity free of hemodynamic and respiratory artifacts robustly emerges, as the biological model of neuronal activity. Fluorescent calcium images of spontaneous neuronal activity were then tested for a possible correlation with diffusion MR signals devoid of confounds typically encountered *in vivo*. A simultaneous increase of diffusion-weighted MR signals was observed together with the depolarization block caused by pharmacological manipulations, in which cell swelling turned out to play an important role. However, no evidence was found that diffusion MR signals were directly correlated to normal spontaneous neuronal activity. These results suggest that while current diffusion MR methods may be able monitor pathological conditions of hyperexcitability, e.g., seen in epilepsy, they do

not appear to be sensitive or specific enough to detect or follow normal neuronal activity. This chapter was adapted from our manuscript 6, which is in preparation and will be submitted for publication soon (Appendix A).

6.1 Does diffusion MRI really detect neuronal activity directly?

Noninvasive, direct *in vivo* detection of neuronal activity by imaging is one of the major challenges in the neurosciences. Progress in this area is required to improve our understanding of normal brain function, and in the clinic, to develop new tools for diagnosing disease states and disorders of the brain. fMRI has been widely used in the cognitive neuroscience community since its invention in the 1990s [78,79,105]. The most widely used fMRI method, BOLD MRI, detects hemodynamic changes in the brain. However, BOLD MRI only indirectly reflects neuronal activity, and its hemodynamic origin limits its spatial and temporal resolution, and its interpretation as a direct proxy for neuronal activity [80,85].

Recently, several MRI methods have been proposed to provide more direct measures of neuronal excitation [345]. In particular, diffusion MRI, a method to measure the apparent diffusivity of water within tissues [116–118], has been suggested as a direct functional imaging method to detect neuronal activity [91,121–123]. Early *in vivo* experiments in both humans and animals reported small but significant increases in diffusion-weighted MRI signals, which were ascribed to changes induced by underlying neuronal activity directly rather than to blood-oxygen-level changes [91,121–123]. *In vitro* experiments on brain slices [93,124] and spinal

cord [92] reported similar reductions in water diffusivity under conditions of extreme hyperexcitability achieved using strong biochemical stimulants.

However, functional diffusion MRI (fDMRI) has not been widely adopted since its introduction almost two decades ago. One reason for this may be a dearth of experiments convincingly establishing a neurophysiological basis for observed changes in diffusion MRI signals. The inability to detect predicted changes using fDMRI as well as the confounding hemodynamic contributions in fDMRI measurements *in vivo* do not argue for a robust connection between changes in diffusion MRI and underlying neuronal activity [94,125–127]. Thus, "ground truth" experiments potentially establishing a connection between the changes in diffusion MRI and underlying neuronal activity are highly relevant, particularly as they can shed light on the underlying biophysical basis of the fDMRI signal.

Recently, we developed a nonhemodynamic-based functional MRI novel test bed, in which intracellular calcium fluorescence imaging to monitor neuronal activity and MR signal acquisition can be performed simultaneously on organotypic cortex cultures from rat brains (Chapter 5). The organotypic cortex culture represents a well-characterized biological model of neuronal activity free of hemodynamic, respiratory and other physiological confounds. Not only is the *in vivo* cortical cytoarchitecture preserved including cortical layers and cortical cell types, but neuronal activity in the culture also displays bursts of spontaneous neuronal avalanches grouped into so-called up-states and separated by periods of low activity, resembling normal neuronal activity in *in vivo* [159–161,164,165]. In this experiment, Fluorometric Ca^{2+} imaging

is used to detect intracellular Ca^{2+} changes that closely follow action potential discharge in a neuron under normal conditions and thus present a direct method for detecting neuronal spiking activity in a neuronal network [156,157]. In this test bed, it becomes possible to study direct correlations between the candidate functional MR signals, which are free of *in vivo* confounds, and the underlying neuronal spiking activity by using independent calcium optical images.

In this study, diffusion MR signals were obtained simultaneously with intracellular calcium fluorescence imaging of the organotypic cortex culture. The direct effects of neuronal activity on the diffusion MR signals were studied by time-series analysis of the simultaneous calcium and MR signals during normal neuronal activity and in different pathological states, which includes hyperexcitability by kainic acid and potassium, disinhibition by picrotoxin (PTX), suppression of excitability by tetrodotoxin (TTX), and osmotic pressure modulation. On the basis of these findings, it is possible to assess the prospect of detecting normal neuronal activity with fDMRI and to better understand the relationship between fDMRI changes and biophysical mechanisms associated with neuronal activity.

6.2 Setups for simultaneous calcium fluorescence imaging and diffusion MR recording on the organotypic cortex culture

6.2.1. Preparation of organotypic rat-cortical culture

The organotypic tissue cultures were made from somatosensory cortex taken from acute coronal slices of newborn rats (postnatal day 0–2, Sprague Dawley). Two acute slices (350 μm thickness) were attached to the #1 coverslip by using a plasma-

thrombin mixture and submerged in 800 μL of culture medium and incubated at 35.0 ± 0.5 °C. The medium was replaced every 3–4 days. Cultures were grown for 2–3 weeks before being used in experiments (for details see [162,328]).

6.2.2. Simultaneous calcium optical imaging and diffusion MR

The detailed setups of this hybrid system, which enables simultaneous fluorescence imaging and MR measurements, are available in Chapter 5. Briefly, a single-sided MR "profiler" with open access was mated under a fluorescence microscope with a long working distance, in which the interface between the optical imaging and MR is small and negligible. The cultures were stained with 50 μM Oregon Green 488 BAPTA-1 (OGB; Life Technologies, NY, USA) for 1–2 hrs before the experiments were performed. A GFP fluorescence filter units from Olympus (Olympus America Inc., USA) and a color CCD camera (ProgRes® CF scan, Jenoptik, Inc., Germany) were used for the fluorescence imaging.

The single-sided MR system is made of four permanent magnets, which generate a relatively uniform magnetic field (0.32 T, 15 mm × 15 mm) in a plane at ~15 mm from the top surface of the magnets. A home-made multi-turn RF surface coil with an inner diameter of 5 mm was mounted directly under the tissue slide to match the size of the cortical cultures and improve the sensitivity. The diffusion weighting was achieved using a spin echo (SE) in the presence of a static magnetic gradient, in which CPMG echo trains were acquired and summed after the main diffusion-weighting module to improve sensitivity [152,155].

6.2.3. Experimental Protocol

In the experiments, the organotypic culture was kept in a custom chamber with constant and slow perfusion (30 mL/hr) of oxygenated (95% O_2 + 5% CO_2) ACSF (124 mM NaCl, 3.5 mM KCl, 10 mM glucose, 26.2 mM $NaHCO_3$, 0.3 mM NaH_2PO_4, 1.2 mM $CaCl_2$ and 1mM $MgSO_4$). The temperature was kept at 34.0 ± 1.0 $^{\circ}$C during experiments. During the kainate, PTX and TTX experiments, the chemical drugs were added directly into the ACSF at the given concentrations. As for the extracellular K^+ experiments, the concentration of the NaCl was reduced to maintain a constant osmotic pressure (292–296 mOsm). A 10-min drug perfusion was added in the middle of normal ACSF perfusion for each drug.

During the experiments, calcium imaging was acquired with 1× magnification, 8.8 mm × 6.6 mm FOV, 680 × 512 pixels, exposure 100 ms, and 10 frames per second. As for the diffusion MR, 5 *b*-values ranging from 0 to 2400 s/mm^2 with a step of 600 s/mm^2 were measured with a two-step phase cycling, TR = 2s, 2000 echoes with echo time 40 μs, and a selective thickness of 100 μm. As for the time profile experiments without pathological drug application, diffusion MR was acquired at a single *b* value (b = 1800 s/mm^2) with all the other settings as described above.

6.2.4. Signal processing

All the signal post processing and analyses were implemented in MATLAB.

The calcium signal (F) was defined as the average fluorescence signal inside a customer defined ROI, which contained the entire cortical tissues inside the RF coil. A background subtraction was performed on the F by automatically subtracting the signal from a manually defined background ROI. The baseline F_0 of F was calculated

from a 30-second sliding window. In the time profile experiments, the fluorescence values were then expressed as relative percentage changes from the baseline, $\%\Delta F/F_{0,}$ and a 1D deconvolution algorithm was implemented to detect the time of the neuronal activity. Details and examples are available in Chapter 5.

As for the diffusion MR signals, the first four echoes in each CPMG echo trains, which had systematic artifacts, were removed [150]. Then the average of the entire CPMG echo train was used as the signal intensity at each *b*-value.

6.3 Experiment and data analysis protocol for pharmacological manipulation

We induced hyperexcitability in the cortex cultures by bath perfusion with a high concentration of kainite (100 μM) or extracellular potassium chloride (30 mM) (for details see [139]). Kainate induces hyperexcitability by activating receptors for glutamate, an excitatory neurotransmitter in the central nervous system, while an increase in extracellular K^+ excites neurons directly by depolarizing their intracellular resting membrane potential. Concentration dependence on kainate was studied simultaneously with both the calcium imaging and diffusion MR. We also studied spontaneous neuronal activity under conditions of disinhibition, i.e., when fast synaptic inhibition was reduced with the noncompetitive $GABA_A$ receptor antagonist picrotoxin (PTX, 5 μM and 50 μM). For controls, we suppressed neuronal spiking by blocking sodium channel permeability using tetrodotoxin (TTX, 0.2 μM). Two statistical time-series analysis methods were employed to identify a time window of potential effects of normal neuronal activity on the diffusion MR signal. At the end, osmotic pressure experiments were performed to look for the contribution of the cell swelling to the changes in diffusion MR signals during the depolarization block.

In these experiments, diffusion MR measurements were performed with the static gradient spin echo NMR sequence with a single-sided NMR profiling system [152]. For the diffusion MR acquisition, 5 b-values (b = 0, 600, 1200, 1800, and 2400 s/mm^2) with TR = 2 s and a two-step phase cycling were used. The diffusion MR signal S can be well fitted by a four-parameter bicomponent model [62,67,69,91,93,124,330]:

$$S(b) = S_0[(1-f)\exp(-bD_{\text{fast}}) + f\exp(-bD_{\text{slow}})] \quad (6.1)$$

where D_{fast} and D_{slow} are the self-diffusion coefficients of the slow and fast diffusion components, respectively; f is the slow diffusion component fraction and S_0 is the MR signal without diffusion weighting. More details about this methodology can be found in [152] and in Section 6.2.

6.4 Reduction of water diffusivity in depolarization block with 100 μM kainate

A normal artificial cerebrospinal fluid (ACSF) perfusion (~ 30 mL/hr) was followed by a 10 min of perfusion with 100 μM kainate added, and then followed by a washout (Fig. 6.1). Care was taken to maintain constant perfusion speed and oxygenation of the ACSF to prevent perfusion artifacts. As shown in Fig. 6.1a, during normal activity the population intracellular calcium signal (F) was characterized by brief (1–2 s) and irregular periods of neuronal excitation. Within 2–3 minutes of kainate perfusion, however, a strong increase in F and then a change to a prolonged plateau was found, followed by a recovery close to the pre-drug baseline (F_0) levels during washout. The plateau in F indicates strong excitation of the neuronal population including potentially depolarization block throughout the spatial extent of the culture (Fig. 6.1b).

As for diffusion MR, three of the four fitting parameters in Eq. 6.1 from all of the cultures (n = 6) in this experiment during normal activity, i.e. before kainate perfusion are: f = 8.01 ± 1.68%, D_{fast} = 2.65 ± 0.04 μm^2/ms, and D_{slow} = 0.20 ± 0.05 μm^2/ms. The diffusion MR signals were observed to have simultaneous and similar changes as compared with F, the intracellular calcium signal. In the example shown in Fig. 6.1a, the slow diffusion fraction f increased from 8.47% pre-drug application to 10.38% during the kainate application. In all of the cultures scanned, increases of the diffusion MR signal at higher b values were observed during kainate perfusion, and they increased with higher b values: -0.86 ± 0.68% (p = 0.87) at b = 0 s/mm^2, 3.29 ± 1.06% (p < 0.01) at b = 600 s/mm^2, 11.2 ± 1.6% (p < 0.0005) at b = 1200 s/mm^2, 17.5 ± 2.0% (p < 0.0005) at b = 1800 s/mm^2, and 11.9 ± 5.7% (p < 0.05) at b = 2400 s/mm^2 (Fig. 6.1b). Similarly, the slow diffusion component fraction f increased significantly by 20.1 ± 3.4% (p < 0.001) with respect to the pre-drug levels (Fig. 6.1e). All of the p-values here and in the following sections were obtained by paired Student's t-Test with the drug and pre-drug data. During the wash, the diffusion MR changes returned to be close to the pre-drug levels.

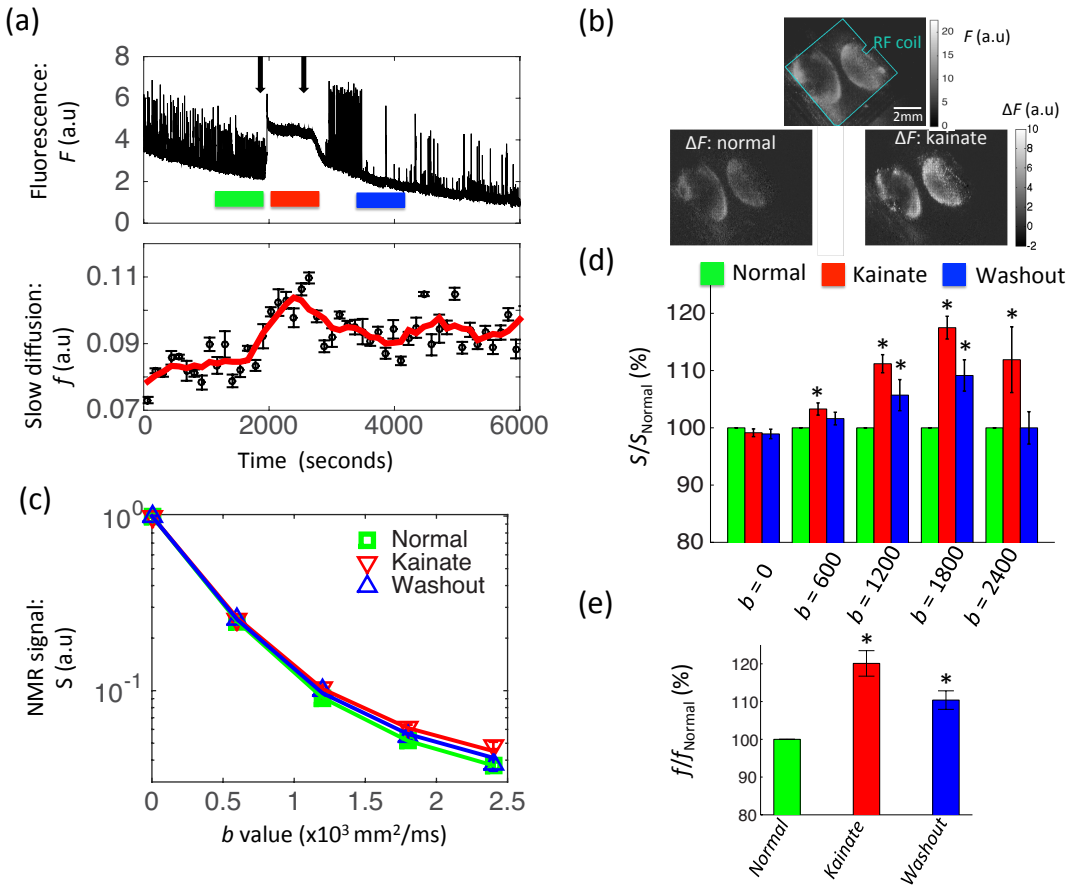

Figure 6.1. (a) The intracellular calcium fluorescence signal integrated over the entire neuronal population (top) and the slow diffusion component derived from the modeling diffusion MR signal (bottom). Red solid line: sliding data average (6 data points each). The two black arrows indicate the start of the 100-μM kainate perfusion (left) and the washout with ACSF (right). (b) Top: Large-field image of an organotypic cortex culture (two cortex slices positioned close to each other) stained with Oregon-Green BAPTA-1 (OGB-1) under fluorescence illumination with indicated position of the RF coil; Bottom: image of fluorescence changes with respect to the baseline under normal neuronal activity and kainate–induced prolonged depolarization. (c) The averaged diffusion MR signals in (a) during three phases: pre-kainate normal neuronal activity, kainate perfusion, and washout. Continuous curves are obtained from model fits. (d, e) The statistical results (n = 6) of the normalized diffusion MR signals (d) and the normalized slow diffusion component fraction (e) during three phases: normal activity, kainate perfusion, and washout. In both (d) and (e), the results were normalized with the results from the pre-kainate normal activity. $^{*}p < 0.05$ with Student's *t*-Test for MR results.

6.5 Kainate concentration dependence of diffusion MR

The observed depolarization when using 100 μM of kainite was directly related to the level of neuronal excitation in the cultures as shown by its concentration dependency. As shown in Fig. 6.2a, when kainate was used at lower concentrations than 100 μM, signal levels dropped accordingly. At 10 μM, the depolarization was still obvious but smaller than at 100 μM kainite with an increase in spontaneous population events. At 1 μM, average depolarization level was smaller than that at 10 μM kainite; however an increase in population events was clearly visible. We quantified the change in the calcium fluorescence baseline as a function of kainate as 41.7 ± 10.9% at 100 μM kainate, to 26.3 ± 5.9% (n = 6) at 10 μM kainate and 4.9 ± 11.6% (n = 6) at 1 μM kainate (Fig. 6.2b). Importantly, changes in diffusion MR signal similarly depended on the kainate concentration. For instance, the increase of the diffusion MR signals (average of the MR signals at b =1800 and 2400 s/mm^2) dropped from 14.7 ± 3.3% ($p < 0.005$) at 100 μM kainate to 4.50 ± 2.19% ($p <0.05$) at 10 μM kainate and 2.88 ± 1.26% ($p = 0.036$) at 1 μM kainate. The changes in the slow diffusion component fraction $\Delta f / f_0$, decreased from 20.1 ± 3.4% ($p < 0.001$) at 100 μM kainate to 6.34 ± 1.30% ($p < 0.005$) at 10 μM kainate and 2.47 ± 1.44% ($p = 0.07$) at 1 μM kainate.

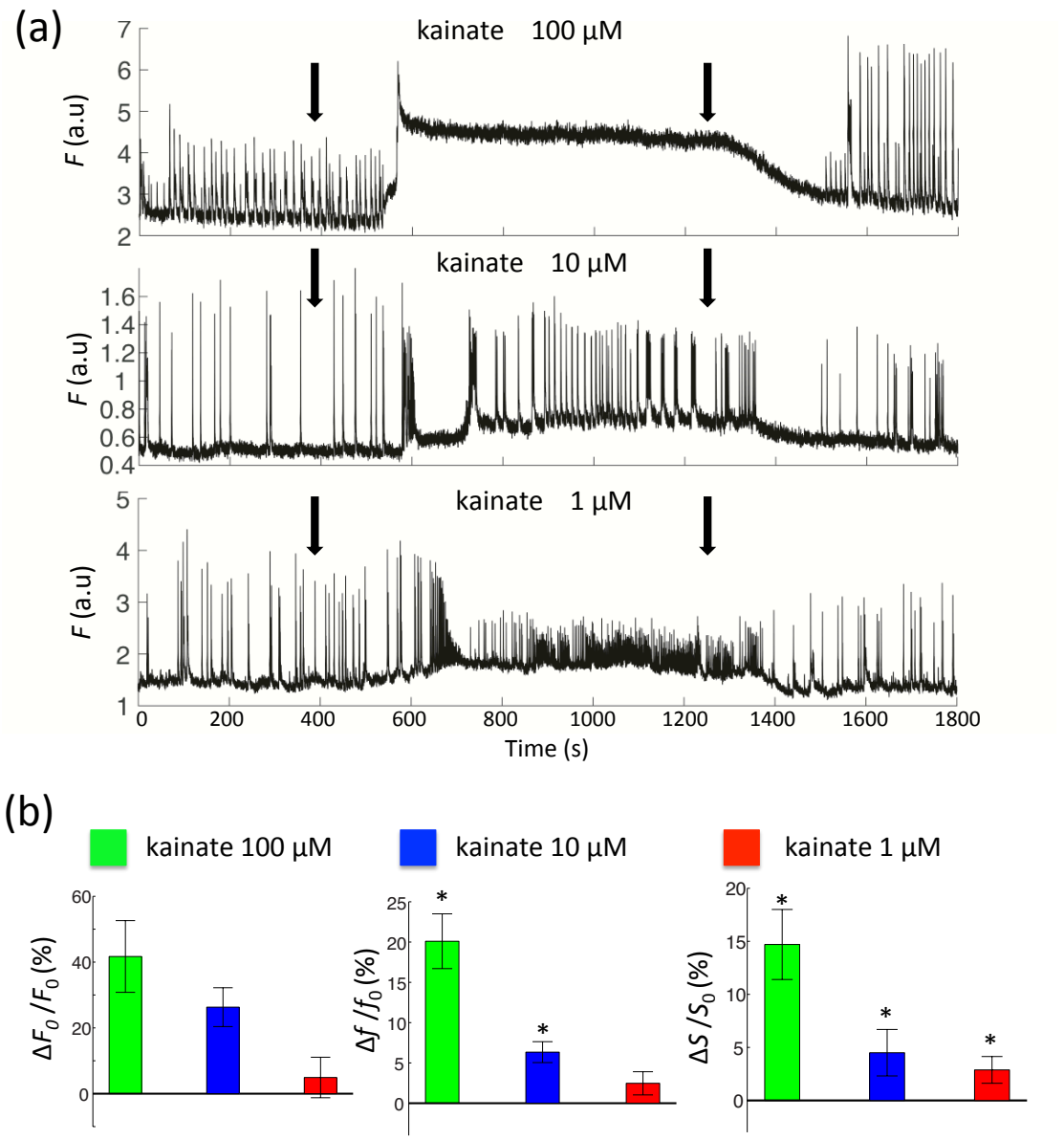

Figure 6.2. (a) The population of the intracellular calcium fluorescence signal in response to 10 min of kainate perfusion at three concentrations: 100 µM (top), 10 µM (middle) and 1 µM (bottom). The two black arrows are the start of the kainate perfusion (left) and washout with ACSF (right), respectively. (b) The changes in the fluorescence baseline (left) and the normalized changes in the diffusion MR signals (the average of MR signals at b = 1800 and 2400 s/mm^2, middle) and the slow diffusion component fraction (right) under kainate perfusion with various kainate concentrations. $^*p < 0.05$ with Student's t-Test for MR signals.

6.6 Reduction of water diffusivity in depolarization block via 30 mM extracellular K^+

A strong depolarization effect similar to that for kainite was observed during 10 min of perfusion with 30 mM potassium chloride (KCl) containing ACSF (Fig. 6.3a). The calcium baseline (F_0) increased by 72.0 ± 6.0% compared with the pre-drug baseline in all cultures (n = 4, Fig. 6.3b). The changes in diffusion MR signals were found to be similar to the calcium signal changes during high-concentration K^+ perfusion. For example, the diffusion MR signal (the average of MR signals at b = 1800 s/mm^2 and 2400 s/mm^2 increased by 9.71 ± 2.19% ($p < 0.05$) and the slow diffusion component fraction f also increased by 11.4 ± 2.4% ($p < 0.005$) compared with the pre-drug values. During the washout, both calcium signals and diffusion MR signals recovered back up toward pre-drug levels.

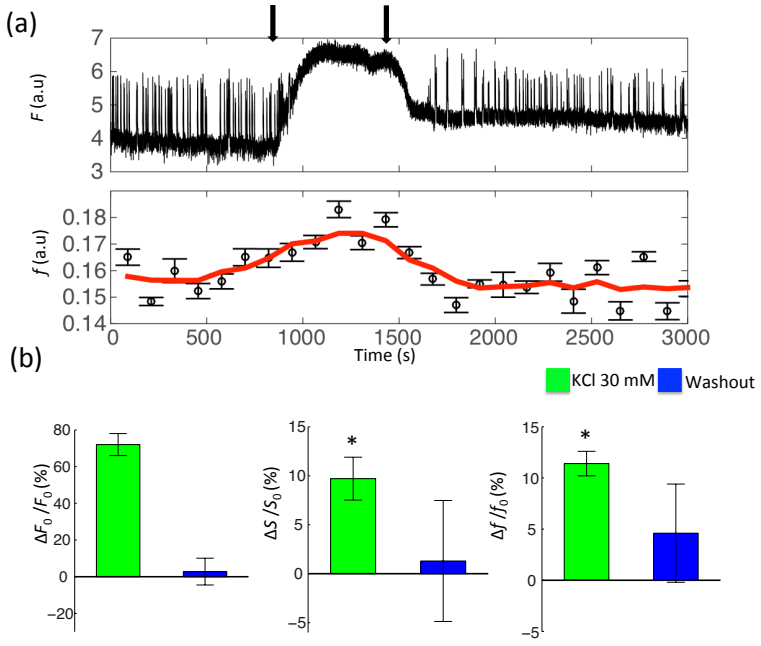

Figure 6.3. (a) An example of the population of the intracellular calcium fluorescence signal (top) and the slow diffusion component derived from modeling the diffusion MR signal (bottom) in response to a 10-min perfusion of 30 mM KCl in ACSF. Red continuous curve: sliding data average (6 data points

each). The two black arrows indicate the start of drug perfusion (left) and washout with normal ACSF (right), respectively. (b) The changes in the fluorescence baseline (left) and the normalized changes in the diffusion MR signals (the average of MR signals at b =1800 and 2400 s/mm^2, middle) and the slow diffusion component fraction (right) under perfusion of the ACSF with 30 mM KCl and washout with normal ACSF. $^*p < 0.05$ with Student's t-Test for MR signals.

6.7 Response of diffusion MR signal to inhibition modulation with picrotoxin (PTX)

Unlike the direct depolarization induced by kainate or an increase in extracellular potassium concentration, the $GABA_A$-receptor antagonist PTX enhances neuronal activity by reducing inhibitory synaptic transmission in neuronal networks leading to prolonged periods of synchronized population activity. Similar to what was found for the concentration dependency of kainate-induced neuronal activity, we found a dose-dependency for PTX. At 5 μM PTX, synchronized neuronal activity was increased as indicated by a decrease in spontaneous population events and a higher population event amplitude in the calcium imaging (Fig. 6.4a) [346,347]. There were no significant changes in either the diffusion MR signals or the slow diffusion component fraction during the 5 μM PTX application (n = 5, Fig. 6.4b). At a higher concentration (50 μM), a slight increase (32.0 ± 17.6%) in the calcium baseline signal following the PTX perfusion was observed within 2–5 mins. Importantly, at this high concentration, both the highly diffusion weighted MR signals (the average of MR signals at b=1800 and 2400 s/mm^2) and the slow diffusion component fraction f showed significant increases (n = 4): 5.95 ± 0.29% ($p < 0.0005$) and 7.07 ± 0.16% ($p < 0.0001$), respectively.

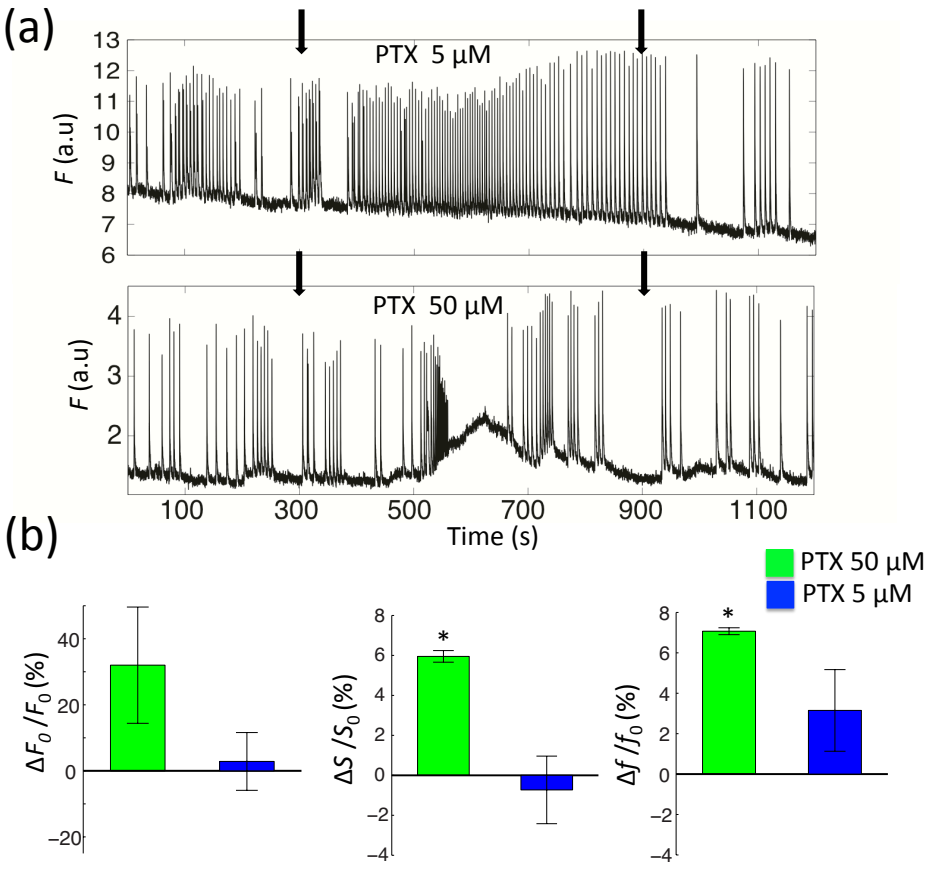

Figure 6.4. (a) Calcium fluorescence signal in response to 10-min PTX perfusion studies with two different concentrations: 5 µM (top) and 50 µM (bottom). The two black arrows are the starting times of the PTX perfusion (left) and washout with ACSF (right). (b) The changes in the fluorescence baseline (left), the normalized changes in the diffusion MR signals (the average of MR signals at b =1800 and 2400 s/mm^2, middle), and the slow diffusion component fraction (right) during PTX perfusion with various PTX concentrations. $^*p< 0.05$ with Student's t-Test for MR signals.

6.8 Suppression of normal spontaneous neuronal activity with tetrodotoxin (TTX) does not affect diffusion MR signal

We suppressed the spiking activity of the organotypic culture using a bath application of 0.2 µM TTX to demonstrate that the MRI diffusion signal does not contain residuals from normal spontaneous neuronal activity. Within 1–3 min of TTX-application, neuronal activity was almost completely suppressed with the

number of neuronal activity per minute dropping from 12.0 ± 1.7 to 0.22 ± 0.12(Fig. 6.5a). Some neuronal activity was recovered during washout in line as expected for this drug (n = 6, Fig. 6.5b). In line with our expectation that the MRI signal would not carry residual information on normal spontaneous activity, no significant changes were found in either the diffusion MR signals or the slow diffusion component fraction during the 0.2 μM TTX application (Fig. 6.5b), in which the changes were 1.06 ± 2.09% (p = 0.68) for the diffusion weighted MR signal (the average of MR signals at b=1800 and 2400 s/mm^2) and 1.33 ± 2.07% (p = 0.73) for the slow diffusion component fraction.

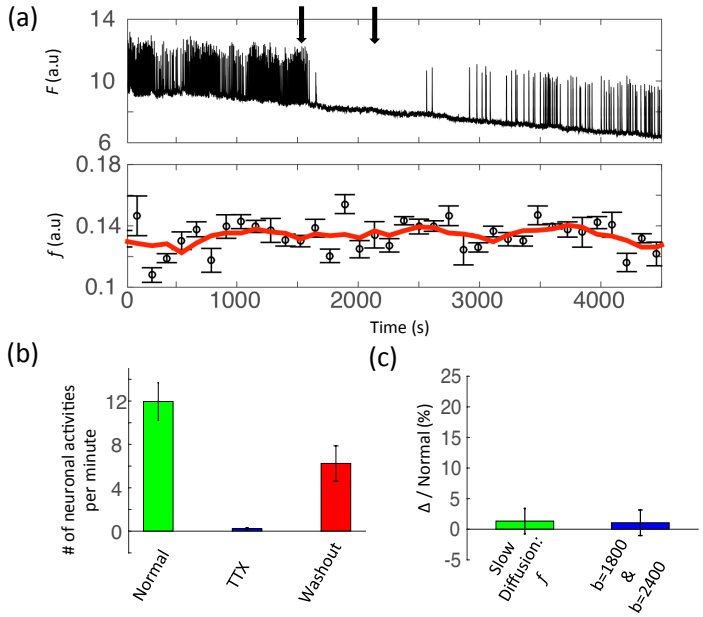

Figure 6.5. (a) An example of the population of the intracellular calcium fluorescence signal (top) and the slow diffusion component derived from modeling the diffusion MR signal (bottom) in response to a 10-min perfusion of 0.2 μM TTX in ACSF. Red continuous curve: sliding data average (6 data points each). The two black arrows indicate the start of the drug perfusion (left) and washout with normal ACSF (right), respectively. (b,c) The change in the number of neuronal firing events per minute (b), the slow diffusion component fraction and the diffusion MR signals (the average of MR signals at

b=1800 and 2400 s/mm^2) (c) under perfusion of ACSF with 0.2 μM TTX and washout with normal ACSF.

6.9 Time-series statistical analysis indicates diffusion MR unaffected by normal spontaneous neuronal activity

To identify a time window for a correlation between normal neuronal activity and the highly diffusion-weighted MR signal, 16 cultures were scanned at a single *b*-value (*b* =1800 s/mm2) under normal ACSF conditions without application of drugs. Periods of high ("active") and low ("resting") neuronal activity were identified in the population of the intracellular calcium signal, and the MR signal was binned on the basis of these two categories. Two types of time-series analysis methods were developed and applied here. For Type 1, we hypothesized that each neuronal population activity event would only affect the diffusion MR signal (active) recorded immediately after it within a time window, *T*, which was tested for *T* = 0.1 s to 1.0 s in steps of 0.1 s. The corresponding resting MR for each active MR was the MR recorded closest in time before the neuronal event (Fig. 6.6a). For Type 2, we hypothesized that each neuronal population activity event would only affect the MR signal (active) recorded within 1 s before and following it. All MR signals outside of this 2 s time window were denoted as resting state (Fig. 6.6b). The active MR signals were further binned into groups on the basis of how separate they were in time (Δ) from the neuronal event with a time step of 0.1 s. For each active MR, the four resting MRs closest to it in time, both before and after, were chosen and averaged as the corresponding resting MR.

In the Type 1 analysis, paired Student's *t*-Tests were performed on the results from all 16 cultures with the null hypothesis that the mean of the active MR signals would be larger than the resting MR signals. No significant increases were observed for all the time windows, T, from 0.1 s to 1.0 s ($p \geq 0.14$, Fig. 6.6c). For the Type 2 analysis, similar Student's *t*-Tests were performed on the paired comparisons between the active (the entire 2 s time window without further binning) and resting MR signals, and no significant increases were observed for the active signals either ($p = 0.93$). The time profiles of the changes in the diffusion MR signals are also shown in Fig. 6.6d. The increases in the diffusion MR signals in each time window, Δ, were less than 0.40%, while none showed significant increases ($p \geq 0.24$) compared with the resting MR. One-way ANOVA performed on the time-profile MR results with the null hypothesis that the mean of the changes between active and resting MR in each bin would be equal was also accepted ($p = 0.97$). These results further support our finding that the diffusion MRI signal does not carry information about normal spontaneous network events.

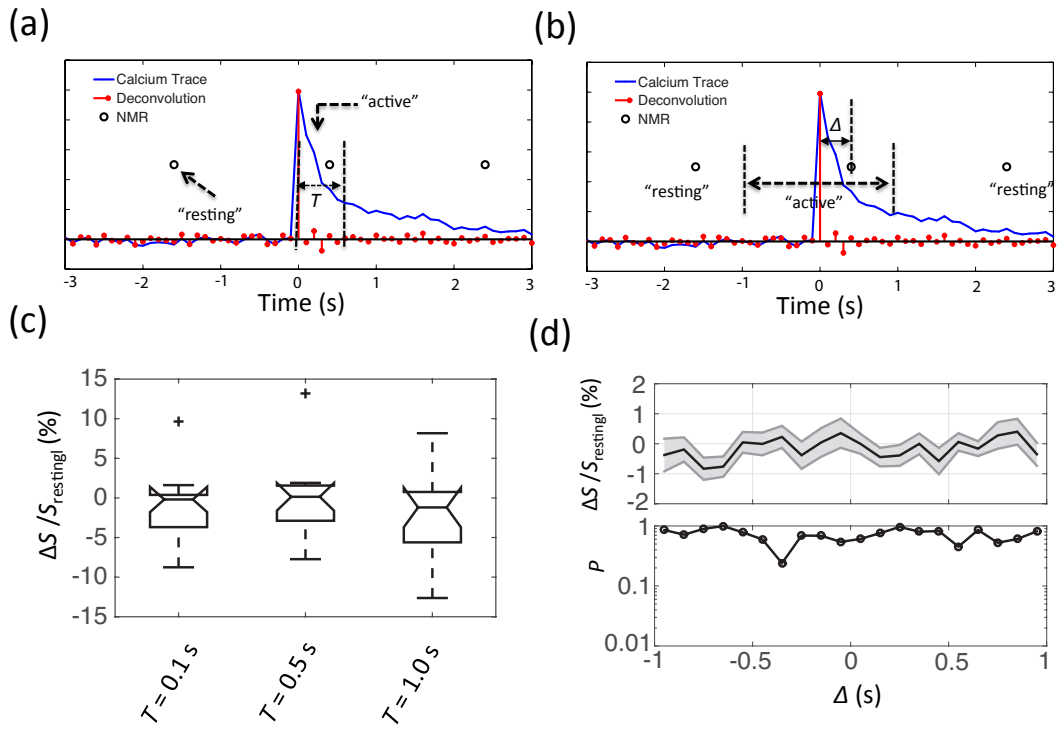

Figure 6.6. Two statistical methods were used to analyze the potential effects of neuronal activity on the MR signals. (a, b) Schematic diagram of the analysis methods: (a) Type 1 and (b) Type 2. (c) The Boxplots of statistical results of the changes in the active state with respect to the resting diffusion MR signals at time windows 0.1 s, 0.5 s, and 1.0 s. For display purposes some outliers were not plotted. (d) The time profiles of the potential effects of neuronal activity on diffusion MR signals and their corresponding *p*-values with student's *t*-Test. The black line is the mean, and the light shadow is the mean standard error in (d), top.

6.10 Cell swelling? Effects of osmotic pressure during depolarization block

It was speculated that the diffusion MR changes were the result of cell swelling during neuronal activity [62]. To investigate this hypothesis, the osmotic pressure was changed during perfusion of normal ACSF and ACSF with 100 μM kainate. The osmotic pressure of the ACSF was increased and decreased by 80 mOsm with a direct addition of mannitol or distilled water into the normal ACSF. In the

control, the following experimental protocol was performed: normal ACSF (30 min) → +80 mOsm (15 min) → normal ACSF (30 min) → -80 mOsm (15 min) → normal ACSF. The last 10-min diffusion MR data from the osmotic modulation was selected and averaged to compare with the pre-osmotic state. A significant reduction ($p < 0.05$) of both the diffusion-weighted MR signal (the average of the MR signals at b =1800 and 2400 s/mm^2, -5.75 ± 1.25%, n = 4) and the slow diffusion component fraction f (-4.84 ± 1.71%) was observed at +80 mOsm, while an significant increase ($p < 0.005$) of both parameters (15.2 ± 1.8% and 14.6 ± 1.7%, respectively) was observed at -80 mOsm (Fig. 6.7a). During the wash with normal ACSF, both the spontaneous activity in the calcium signal and the levels of the diffusion MR signals were recovered close to the pre-osmotic state (Fig. 6.8).

To study the effect of the osmotic pressure on the kainate induced diffusion MR changes, experiments were performed following the protocol: normal ACSF (20 min) → kainate 100 μM under +80 mOsm (10 min) → normal ACSF (30 min) → kainate 100 μM under normal ACSF (10 min) → normal ACSF. Compared with the results of kainate 100 μM under normal ACSF in Section 6.4, the calcium signal still showed the strong dollarization during the kainate application under +80 mOsm (Fig. 6.8). However, the change in the averaged MR signals at b = 1800 and 2400 s/mm^2 was significantly reduced ($p < 0.01$, n = 4) from 14.7 ± 3.3% to 1.39 ± 1.42% by the addition of mannitol, while the change in the slow diffusion component fraction was also significantly reduced ($p < 0.005$) from 20.1 ± 3.4% to 1.60 ± 0.92% (Fig. 6.7b). During the subsequent wash with normal ACSF, the depolarization was reduced while some spontaneous activity showing up (Fig. 6.9). The application of the second

100 μM kainate perfusion with normal ACSF also showed much higher increases in both the diffusion weighted MR signals (averages at b = 1800 and 2400 s/mm^2, 11.7 ± 1.7%, p < 0.005) and the slow diffusion component fraction (10.1 ± 1.1%, p < 0.001) than the first 100 μM kainate perfusion with +80 mOsm ACSF (Fig. 6.9).

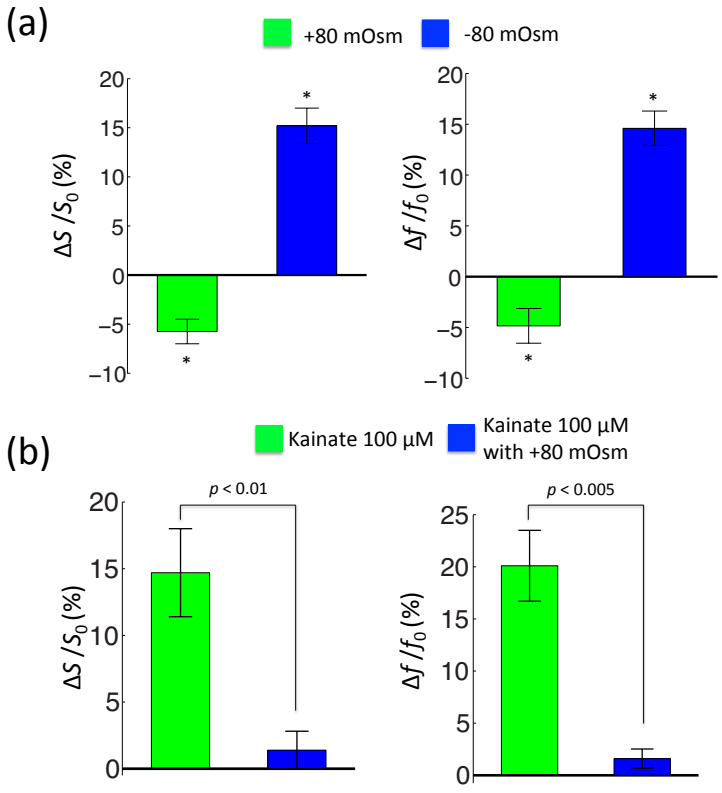

Figure 6.7. (a) The normalized changes in the diffusion-weighted MR signals (the average of the MR signals at b =1800 and 2400 s/mm^2, left) and the slow diffusion coefficients (right) in the +80 mOsm and -80 mOsm. (b) The normalized changes in the diffusion-weighted MR signals (the average of the MR signals at b =1800 and 2400 s/mm^2, left) and the slow diffusion coefficients (right) in the 100 μM kainate application with normal normal ACSF and +80 mOsm. * p < 0.05 with Student's t-Test.

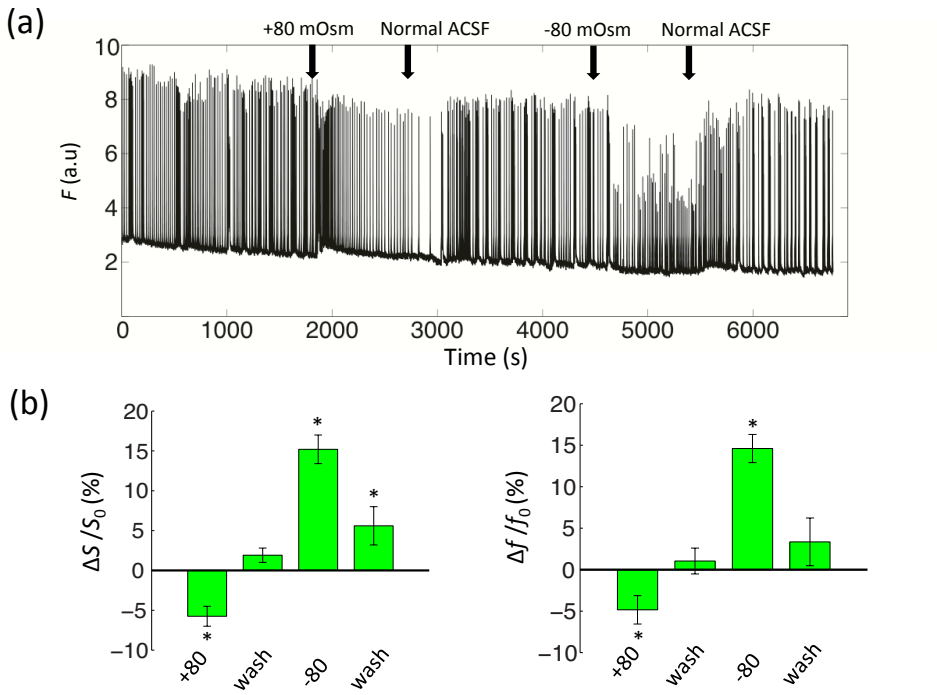

Figure 6.8. (a) The calcium fluorescence signal and (b) the normalized changes in the diffusion-weighted MR signals (the average of the MR signals at b =1800 and 2400 s/mm^2, left) and the slow diffusion coefficients (right) in the response of the osmotic pressure modulation. * $p < 0.05$ with Student's t-Test for MR results.

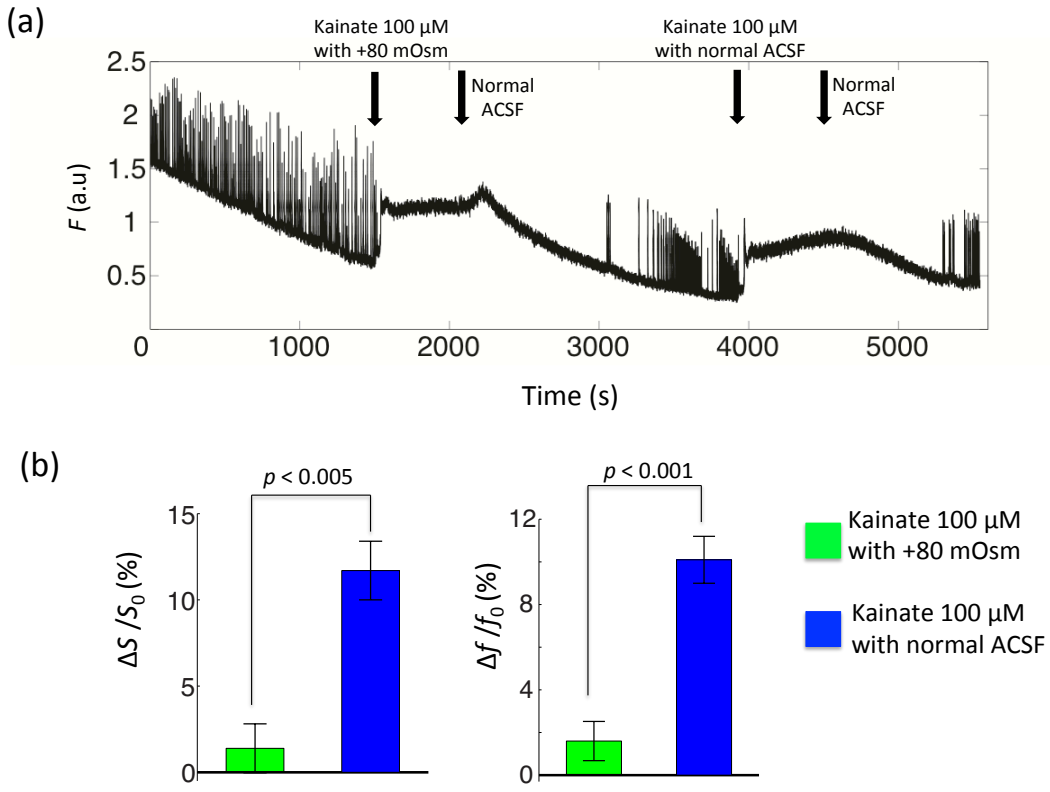

Figure 6.9. (a) The calcium fluorescence signal and (b) the normalized changes in the diffusion-weighted MR signals (the average of the MR signals at b =1800 and 2400 s/mm^2, left) and the slow diffusion coefficients (right) in the response to the perfusion of kainate 100 µM under +80 mOsm and normal ACSF. $^*p < 0.05$ with Student's t-Test for MR results.

6.11 Discussion: is current diffusion MR method sensitive enough to capture normal neuronal activity?

Our *in vitro* organotypic cortical cultures produce high-quality diffusion MR signals without any hemodynamic or respiratory effects and eliminate most potential artifacts and confounds associated with *in vivo* MRI experiments, such as subject motion, pulsation, blood volume redistribution, respiration-induced changes in oxygenation, etc. Moreover, our hybrid test bed with simultaneous monitoring of neuronal activity with intracellular calcium during acquisition of the MR signal

provides a unique opportunity for direct, spatially resolved, time-dependent comparison of the diffusion MR signals with neuronal activity.

Organotypic cortex cultures have been successfully used as a biological model of neuronal activity for decades [159–161]. These cultures have healthy neurons similar to those in the *in vivo* cortex with high cell densities and extracellular matrix [159]. More importantly, organotypic cortical cultures *in vitro* display bursts of spontaneous neuronal activity in the form of neuronal avalanches, a well-recognized dynamical mode of spontaneous activity found *in vivo* in humans and nonhuman primates during while at rest [161,164,165].

Kainate is a potent analog of glutamic acid, which is the principal excitatory neurotransmitter in the central nervous system (CNS). An application of high concentration kainate can cause prolonged depolarization of the cell membrane with an influx of Ca^{+} [348,349]; this phenomenon was clearly demonstrated in Fig. 6.1a. High-concentration extracellular K^{+} can also induce cell depolarization by changing the ions' gradient across the cell membrane [1], as shown in Fig. 6.2a. The $GABA_A$ receptor chloride channel blocker PTX was also shown to depolarize the cell at high concentration in Fig. 6.4a and [350]. In all the three conditions with depolarization blocking, the diffusion-weighted MR signals showed significant increases; these changes became larger as the *b* values increased. In other words, the slow diffusion component fraction showed significant increases in the bi-component model. Both the slow diffusion component fraction and its changes that were found in this study are smaller than the results from acute rat brain slices with imaging [93]; this difference

might the result of the partial-volume effect here and of the use of different tissue types.

Interestingly, the increases in the diffusion-weighted MR signals were found to be dependent only on the depolarization level rather than on the level of the normal neuronal population events that encoded by spikes. In the kainate concentration experiments, the changes in the diffusion-weighted signals diminished as the depolarization level decreased during the reduction of kainate concentration, in which the number of calcium neuronal population spikes increased. A similar result was found in the PTX experiments, in which significant diffusion MR signal changes were only found at the higher PTX concentration, which clearly elicited a prolonged depolarization. In the TTX experiments, the suppression of normal spontaneous neuronal activity had no significant effect on the diffusion MR signals. In the time profile experiments without a drug application, no evidence was found that each single event of normal neuronal activity correlated significantly with the highly diffusion-weighted MR signals (b = 1800 s/mm^2) within a temporal resolution of 100 ms.

The phenomenon of cell swelling induced by intense neuronal depolarization has been reported in other imaging studies [166,167,172,351–354]. Cell volume changes have also been reported in ischemia, osmotic modulation, and spreading depression [166,351,352,355]; in all of these cases diffusion-weighted MRI shows a positive response [119,120,356]. Thus, cell swelling appears to contribute to the reduced water diffusivity observed here and in other pathological states mentioned above. The contribution of cell swelling was further studied with osmotic pressure

experiments on the organotypic cultures (Fig. 6.7). In the control, the diffusion-weighted MR signals decreased at +80 mOsm and increased at -80 mOsm; these results correspond to cell shrinkage and swelling, respectively [166,351]. The adding of mannitol during perfusion of 100 μM kainate significantly reduced the changes in the diffusion MR signals caused by the depolarization block; this result suggests that cell swelling, at least in part, accounts for the reduced water diffusivity observed during cell depolarization, although the underlying mechanisms are still unclear. Some possible explanations include, but are not limited to: (a) an increase of diffusion tortuosity in the extracellular space and intracellular volume fraction [357]; (b) more "bound" water near the lipid membrane and/or macromolecules with slow diffusivity during cell swelling [62]; and (c) changes in the configuration of the cytoplasmic matrix and streaming [358].

Cell swelling has also been reported to occur during normal neuronal activity, but with a negligible amplitude that is much smaller than that caused by prolonged and strong depolarization [166,168–172]. In general, the displacement of the cell surface are on the scale of nanometers, with a maximum of several tens of nanometers, under normal electrical stimulation [168–171]. However, the surface displacement changes in the neuronal soma induced by the prolonged depolarization can be approximately one or more micrometers [166,172]. If we assume the reduction of water diffusivity is caused mainly by cell swelling, it is highly unlikely that the diffusion MRI is sensitive enough to measure the changes caused by normal neuronal activity; these changes are estimated to be approximately three or more orders of magnitude smaller than the changes observed during strong depolarization.

Most physiological processes occurring during normal neuronal activity, such as the action potential, ion-exchange, channel opening and closing, and also the cell swelling and other mechanical changes, happen on a short time scale (fractions to several milliseconds) [1,171]. However, the effect of the depolarization on the diffusion MR signals is found to be an integration phenomenon (~several min) rather than an instantaneous response. Additionally, no significant changes in the diffusion MR signals induced by a single neuronal event were found in the time-series analysis within a temporal resolution of 100 ms. In conclusion, the current diffusion MR techniques may not be sensitive and fast enough to capture single neuronal activity/spikes.

Diffusion MR signals are obtained from water molecules inside the extracellular matrix and cells including neurons, astrocytes, microglial cells, etc. The biophysical relationship between the observed diffusion MR signals and the underlying microstructure and water dynamics is still poorly understood and is currently a topic of great interest and active research. In addition to neuronal cell swelling, other physiological processes might also contribute to the changes in the diffusion MR signals. Early morphological experiments showed that the neuron cell membrane might become "leaky" under intense excitation [166,167]; this leakiness might modulate the water exchange between compartments and change the diffusion MR signals [71]. It has also been suggested that advection caused by micro streaming might change the diffusion MR signal by a process called pseudo-diffusion [92,128]. In addition, astrocytes and other glial cells also play an important role in brain function [343], and their contributions to the diffusion MR signals are still not clear.

In summary, simultaneous calcium imaging and diffusion MR measurements clearly demonstrate the direct correlation between reduced water diffusivity and depolarization of the cell membrane. Changes in diffusion MR signals are positively correlated with the amplitude of the depolarization rather than with the levels of normal neuronal activity. Current diffusion MR methods are not capable of following a single event of normal neuronal activity, either in terms of sensitivity or temporal resolution. To achieve the goal of direct MR imaging of neuronal activity, a better understanding of the physiological process of neuronal activity and the biophysics of diffusion MR in tissue and a smarter MR contrast design are still needed.

6.12 Supporting information: "stroke" model to test the performance of the test bed

The reliability and stability of this hybrid imaging system have been demonstrated in our previous work (Chapter 5). To further validate the system's ability to detect the intracellular calcium levels and the diffusion signal changes, a "stroke" model with an oxygen/glucose deprivation (OGD) protocol was tested [120,166,351]. Diffusion MRI is a gold-standard neuroimaging method to diagnose stroke clinically with increasing signal in diffusion-weighted images and a concomitant reduction in the mean apparent diffusion coefficient (ADC) [119,120]. Another phenomenon associated with ischemia caused by acute stroke is depolarization of the cell membrane and calcium uptake by neurons [355,359]. These two phenomena were both observed in this hybrid system: clearly there were increases in the diffusion-weighted MR signals ($b \geq 600$ s/mm^2), decreases in the

ADC, and increases in the calcium signal in the absence of normal neuronal spikes in the optical imaging, as the OGD started (Fig. 6.10).

In the OGD protocol, glucose was removed to the feed stream (NaCl was added to maintain the osmotic pressure) and the ACSF saturation was maintained with 95% N_2 + 5% O_2 [120,166,351]. The culture was perfused under OGD at a faster perfusion speed (60 mL/hr) for 15 minutes at the beginning of the protocol to remove the remaining oxygen and glucose from the tissue at the beginning (during this period no MR recording was performed), and then the perfusion speed was set back to 30 mL/hr for another 2 hrs.

Calcium imaging revealed clear increases in the calcium signals as the OGD started in all the admissible cultures (n = 3). The calcium signal kept increasing until the photo bleaching effect dominated while the normal neuronal spikes were suppressed (Fig. 6.10a). The followed washout with normal ACSF did not recover result in normal neuronal activity returning. In the control (normal ACSF perfusion), the calcium signal kept decreasing while normal neuronal activity took place during the entire 2.5-hr recording.

In diffusion MR, the diffusion-weighted MR signals started increasing as the OGD started. As shown in Fig. 6.10a and Fig. 6.10c, greater increases of the diffusion MR signals were observed at higher b values and longer OGD perfusion times. Additionally, the washout did not result in the recovery of the diffusion signal back to the pre-OGD levels. The ADC was calculated at b = 1800 s/mm^2 with the equation:

$$\text{ADC} = -\frac{1}{b}\exp\left(\frac{S(b)}{S(b=0)}\right) \tag{6.2}$$

The ADC dropped from 1.35 ± 0.08 μm^2/ms by 4.99 % at the first 30-min OGD perfusion and kept decreasing until in reached 14.9% at the end of the 2-hr OGD perfusion. The washout did not cause the ADC to recover either.

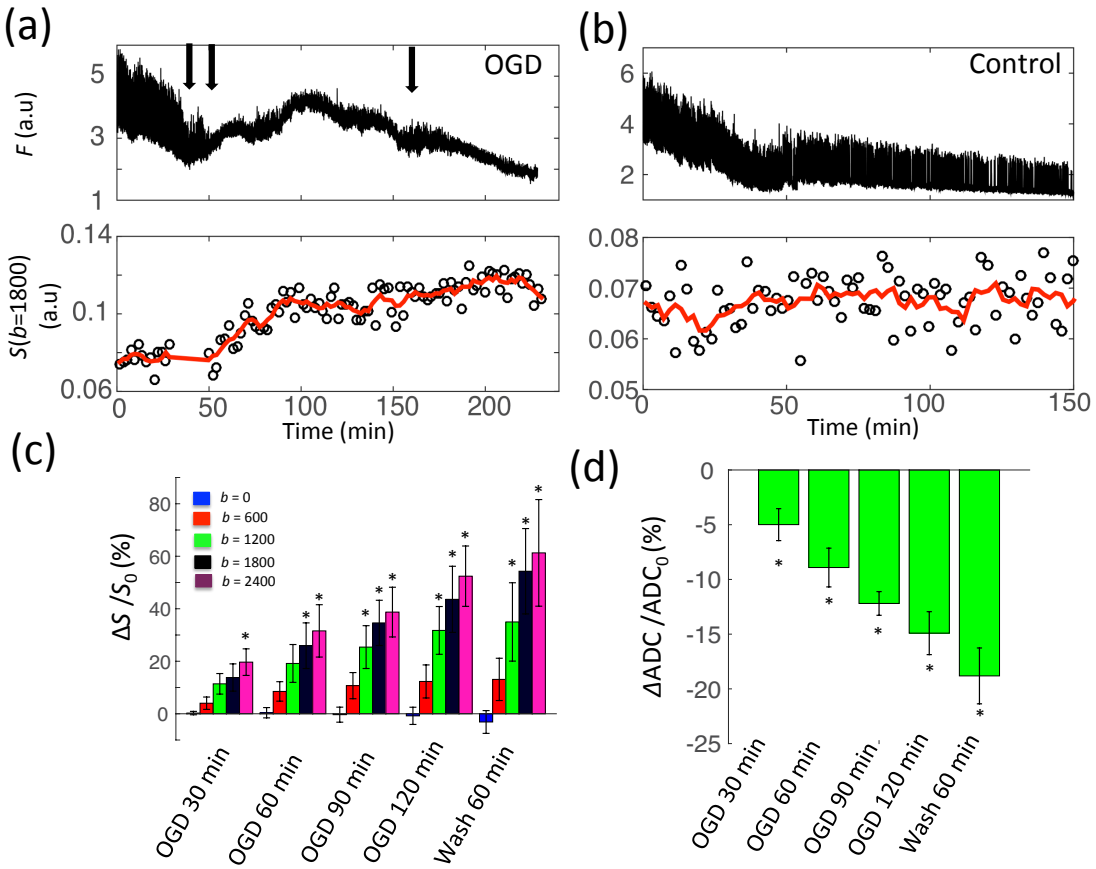

Figure 6.10. (a,b) The calcium fluorescence signal (top) and the diffusion MR signal at b = 1800 s/mm^2 in the response of OGD (a) and the normal ACSF (b, control). In the lower section of panels (a) and (b), the red continuous curves are the average of the data with a step of 6 data points. The three black arrows in (a) indicate for the starting time of the faster OGD perfusion, normal OGD perfusion and washout with normal ACSF, respectly. (c) The changes in the diffusion MR signals at various b values and various time points in the OGD model. (d) The changes in ADC at various time points in the OGD model. $^*p < 0.05$ with Student's t-Test for MR results.

Chapter 7: Discussion and future work

In this final chapter, we summarize the results of three candidate fMRI methods (i.e., diffusion, proton density, and relaxation time) using the novel test bed we built specifically for non-BOLD fMRI. Next, we explain the fundamental knowledge about water dynamics in living tissue required to understand the findings in this study and to design new non-BOLD fMRI methods in future. Then, we discuss requirements and our plans to further promote the use of multidimensional MR diffusion/relaxation to characterize complex water dynamics in living tissue. Finally, the potential applications in other fields of this novel test bed for non-BOLD fMRI and the new MR methods we developed are briefly discussed.

7.1 Vetted non-BOLD fMRI methods: diffusion, proton density, and relaxation time

In Chapter 6, diffusion MR signals were shown to be sensitive to depolarization block induced by pharmacological manipulations, but were not able to detect normal spontaneous neuronal activity. These results suggest that while current diffusion MR methods can monitor pathological conditions of hyperexcitability, e.g., such as those seen in epilepsy, they do not appear to be sensitive or specific enough to detect or follow normal neuronal activity.

In Chapter 5, the potential effect of normal spontaneous neuronal activity on proton density and the efficient transverse relaxation time, $T_{2\text{eff}}$, were studied via an MR CPMG sequence, in which no significant effects were observed. In a depolarization block experiment with 100 μM kainate (not shown in Chapter 5), there

were still no significant changes in proton density (-0.12 ± 0.27%, $p = 0.68$, n = 7). A small change was observed in $T_{2\text{eff}}$ (0.84 ± 0.23%, $p < 0.01$, n=7) during the depolarization block; this change might come mainly from the contribution of water self-diffusion in the MR CPMG sequence via Eq. 5.2.

In conclusion, none of the three vetted fMRI mechanisms (i.e., proton density, transverse relaxation times, and diffusion) are capable of detecting or tracking normal neuronal activity at the sensitivities currently available. Diffusion fMRI shows promise in following depolarization block experiments, but the underlying biophysical mechanisms remain still unclear, and whether the method can be improved to detect normal neuronal activity in future remains doubtful.

7.2 Cell swelling or other physiological processes: more knowledge needed

Cell swelling has been proposed as one of the possible explanations for the reduced water diffusivity observed in the depolarization block and in other pathological states (e.g., stroke). Our osmotic pressure modulation experiments indicate that the cell swelling matters, at least in part, for the reduced water diffusivity during prolonged depolarization. To further confirm the important role of cell swelling in the diffusion MRI signal, more osmotic experiments with different osmolyte types and compositions will be systematically studied in the future.

On the other hand, the underlying biophysical mechanisms of cell swelling and its effect on water diffusion are still unclear. Cell swelling has also been reported to occur during normal neuronal activity [166,168–172]. Thus, the further study of the underlying biophysical mechanisms would help us design smarter fMRI methods that would be sensitive enough to detect or track neuronal activity directly.

Some possible explanations for the effect of cell swelling include, but are not limited to: (a) an increase of diffusion tortuosity in the extracellular space [357]; (b) more bound water near the lipid membrane with slow diffusivity during cell swelling [62]; and (c) changes in the configuration of the cytoplasmic matrix and microstreaming [358]. In our opinion, the slow diffusion water in the cortex might come mainly from the strongly restricted water located inside the neuropil, i.e., an area composed of compartments with small diameters, such as dendrites, axons, glial processes, etc., whose size is much smaller than the mean diffusion displacement of water (~1–5 μm at most diffusion MR sequences, Eq. 1.12). The swelling of these compartments would induce more water into the slow diffusion region, as has been observed in the depolarization block state in Chapter 6.

In addition to neuronal cell swelling, there are other physiological processes that may also change the diffusion MR signals. Early morphological experiments showed that the neuron cell membrane might become "leaky" under intense excitation [166,167]; this leakiness might modulate the water exchange between intracellular cytoplasm and the extracellular matrix. In addition to Brownian motion, there are also some water translational motions caused by some active biophysical processes, such as microstreaming, that might contribute to the changes in the diffusion MR signals by creating pseudo-diffusion or other mechanisms [92,128].

Clearly, we must understand the complex water dynamics occurring in living tissue, including their relation to the underlying microstructure, tissue heterogeneity, water exchange among different microenvironments, active water motion, etc., before we can fully understand the MR signal we are detecting and then design better MR

methods for detection. To the best of our knowledge, current MR studies and methods are still far from accomplishing this task.

We propose two strategies for future studies in an attempt to better characterize the water dynamics in living tissue. First, as discussed in Chapter 2, one way to simplify the complexity of tissue is by using biomimetic models. Such models allow the characterization of chemical and other properties of living tissue and the isolation of different components inside the tissue. The hydrogels used in Chapter 2 with properties similar to those of intracellular cytoplasm are a good choice. On the other hand, cell membrane also plays a very important role in water dynamics in living tissue by restricting the translational motion of water, controlling the water exchange between intracellular and extracellular spaces, inducing active water motion in some physiological processes, etc. A good candidate biomimetic model for cell membrane is an emulsion of liposomes, vesicles with one or multiple lipid bilayers, which mimics the chemical structure and spatial configuration of the cell membrane [360]. The methods for synthesizing and preparing liposomes are fairly mature now, and their size, configuration, and permeability to water can be well controlled and characterized [360–363]. A well-controlled liposome phantom may be very helpful in understanding the role of cell membrane in the water dynamics in living tissue.

Another strategy is to design new MR methods to better detect the water dynamics in living tissue. The multidimensional MR diffusion/relaxation spectra, originally developed in a porous medium to study pore structure and composition and to track water pore-to-pore exchange [185,191,295], show promise in characterizing the microenvironments for water in biological tissue and monitoring the motion of

water molecules among different microenvironments. Although our work in transferring this method from NMR spectroscopy to MRI with imaging (Chapter 3) and accelerating its acquisition speed with compressed sensing (Chapter 4) promotes its application in living tissue, substantial effort is still needed before this method can be used to characterize water dynamics in living tissue. The work required is discussed in the following section. Additionally, diffusion time dependence and directional correlation of the diffusion MR signal have also drawn us to study water diffusion anisotropy at multiple length scales, e.g., diffusion anisotropy caused by local macromolecules, cell membranes, etc., in future.

7.3 Promoting multidimensional MR diffusion/relaxation spectra to characterize the complex water dynamics in living tissue

As discussed in Section 7.2, there are still several steps needed to apply multidimensional MR diffusion/relaxation spectra method to characterize the complex water dynamics in living tissue. A description of these steps follows.

Step 1: Develop a mathematical framework to identify quantitatively the microenvironments of water and to characterize the water exchange process among these microenvironments in tissue. As shown in Fig. 1.2, the very heterogeneous nature of tissue causes a broad distribution of the relaxation spectra and complicates the problem of identifying distinct microenvironments. The currently available mathematical methods can only describe the exchange process between two or three water sites that have very narrow and distinguishable diffusion/relaxation distributions. To deal with the multidimensional spectra of tissue, its heterogeneous nature must be considered, and broad distributions rather than a single component

should be used to characterize both the diffusion/relaxation properties and the exchange process in the tissue.

Step 2: Further accelerate multidimensional MR acquisition and processing by compressed sensing and other data reduction methods. One significant obstacle to apply these 2D relaxometry for preclinical and clinical imaging is the large amount of data and long MR acquisition times required. We recently developed a new MR pipeline for 2D relaxometry that incorporates compressed sensing as a means to vastly reduce the amount of 2D relaxation data needed for tissue characterization without compromising the data. In the future, other data reduction methods will be developed, based upon the use of *a priori* information as well as the use of physically based constraints. These methods might further accelerate the data acquisition by another factor of ~5. Together with fast acquisition MR pulse sequence design, there methods might reduce the acquisition time of these types of multidimensional diffusion/relaxation MR to make this method feasible for preclinical and clinical applications.

Step 3: Migrate more of these types of pulse sequences from MR spectroscopy to imaging. Currently, there are no commercially available MRI sequences for measuring multidimensional diffusion/relaxation maps. We have only developed the T_1–T_2 MRI sequences in our 7T Bruker microimaging system. In the future, some other multidimensional diffusion/relaxation MR spectroscopy sequences will also be adapted to work with 2D or 3D imaging, which include, but are not limited to, T_2–T_2, D–D, T_2^*–T_2^*, D–T_2^*, etc.

Step 4: Develop multimodal imaging with histology validation. Double-PFG diffusion methods developed in our lab can provide information about the axon diameter distribution (ADD) [289]. Multidimensional MR diffusion/relaxation spectra can provide the volume fraction of water microenvironments and their exchange process. All of this information can be combined to create realistic kinetic models based on diffusion motion to provide more microstructure information, such as the surface-to-volume ratio, cell membrane permeability, etc. This additional information might make it possible to quantify the cell-type distribution and grade the health of the cells. Histology with high-resolution optical imaging will further validate these newly developed methods.

7.4 Potential applications in other fields

MRI is a very powerful, noninvasive brain-imaging tool for both research and clinical diagnosis. However, the most important applications of MRI are for brain anatomy and, currently, it is difficult to extract detailed information about cellular physiological processes from MRI measurements. On the other hand, fluorescence optical images show great advantages for the study of the fine structure of tissue and the details of cell functions at the cellular and subcellular levels. The hybrid fluorescence imaging and MR system we built will be a bridge to connect these two important techniques and help transform the findings from fluorescence imaging into useful biomarkers that can be used in MRI to track physiological processes or diagnose diseases.

One possible application that has attracted our attention is the study of the role of glial cells in brain function. A recent study found that, although glial cells do not

work in the same way as neurons, their role in brain function and connectivity may be as important as that of neurons [343]. The hybrid system we built here, which uses healthy organotypic brain tissue, has the potential to be used not only to study neuronal excitatory behavior, but also to assess possible changes in glial structure (with proper glial-specific calcium indicators [344]) in response to this behavior, particularly over a longer timescale than that used in these experiments. We view these applications as important future uses of this novel test system.

The multidimensional MR diffusion/relaxation spectra methods developed here also have the potential to help explore the detailed physiological processes of some diseases and then to aid in the development of more efficient clinical diagnosis biomarkers. One particularly interesting area is stroke. Diffusion MRI is a gold-standard for diagnosing stroke clinically with an increasing signal in the diffusion-weighted image and a reduction in the mean ADC [119,120]. However, some detailed physiological processes, such as the failure of ion pumps, cell swelling, cell membrane integrity, cell death, etc., are hard to distinguish in conventional clinical diffusion MRI scans. As a result it is difficult to grade the stages of the disease and provide a proper prognosis. On the other hand, the multidimensional MR diffusion/relaxation spectra methods have the potential to characterize water motions through the cell membrane, cell volume fractions, etc.; this method might shed light on how to detect cellular details of stroke with MRI techniques. Their applications in other brain diseases, such as tumors, brain trauma, epilepsy, etc., will also be considered in the future.

Appendix A: list of publications

1. **R. Bai**, P.J. Basser, R.M. Briber, F. Horkay, NMR water self-diffusion and relaxation studies on sodium polyacrylate solutions and gels in physiologic ionic solutions, J. Appl. Polym. Sci. 131 (2014) 1–7. doi:10.1002/app.40001.

2. **R. Bai**, C.G. Koay, E. Hutchinson, P.J. Basser, A framework for accurate determination of the T2 distribution from multiple echo magnitude MRI images, J. Magn. Reson. 244 (2014) 53–63. doi:10.1016/j.jmr.2014.04.016.

3. A. Cloninger, W. Czaja, **R. Bai**, P.J. Basser, Solving 2D Fredholm integral from incomplete measurements using compressive sensing, SIAM J. Imaging Sci. 7 (2014) 1775–1798. doi:10.1137/130932168.

4. **R. Bai**, A. Cloninger, W. Czaja, P.J. Basser, Efficient 2D MRI relaxometry using compressed sensing, J. Magn. Reson. 255 (2015) 88–99. doi:10.1016/j.jmr.2015.04.002.

5. **R. Bai**, A. Klaus, T. Bellay, C. Stewart, S. Pajevic, U. Nevo, H. Merkle, D. Plenz, P. J. Basser, Simultaneous MR and calcium fluorescence imaging of *ex vivo* organotypic cortical cultures: a new test bed for functional MRI, NMR in Biomedicine (under review).

6. **R. Bai**, C. Stewart, D. Plenz, P. J. Basser, Can neuronal activity be detected by diffusion MRI? An *in vitro* assesment with simultanous calcium fluorescence imaging and diffusion MR recording: a new test bed for functional MRI. Manuscript.

Bibliography

[1] M.F. Bear, B.W. Connors, M.A. Paradiso, Neuroscience, Third, Lippincott Williams & Wilkins, Baltimore, 2007.

[2] Mental disorders, Fact sheet N°396, World Health Organization, (2014).

[3] "Nervous System Diseases". Healthinsite.gov.au., (n.d.).

[4] The top 10 causes of death, Fact sheet N°310,World Health Organization, (2014).

[5] D. Aur, M.S. Jog, Neuroelectrodynamics: Understanding the Brain Language, IOS Press, 2010.

[6] J.G. Nicholls, From Neuron to Brain, Sinauer Associates, 2012.

[7] E.T. Whittaker, A History of the Theories of Aether and Electricity from the Age of Descartes to the Close of the Nineteenth Century, Longmans, Green and Company, 1910.

[8] From Molecules to Networks: An Introduction to Cellular and Molecular Neuroscience, Academic Press, 2014.

[9] O. Shimomura, F.H. Johnson, Y. Saiga, Extraction, Purification and Properties of Aequorin, a Bioluminescent Protein from the Luminous Hydromedusan,Aequorea, J. Cell. Comp. Physiol. 59 (1962) 223–239. doi:10.1002/jcp.1030590302.

[10] F. Helmchen, A. Konnerth, Imaging in Neuroscience: A Laboratory Manual, Cold Spring Harbor Laboratory Press, 2011.

[11] N.S. Ward, R.S.J. Frackowiak, Towards a new mapping of brain cortex function., Cerebrovasc. Dis. 17 Suppl 3 (2004) 35–8. doi:10.1159/000075303.

[12] P.A. Bandettini, What's new in neuroimaging methods?, Ann. N. Y. Acad. Sci. 1156 (2009) 260–93. doi:10.1111/j.1749-6632.2009.04420.x.

[13] A.C. Papanicolaou, Fundamentals of Functional Brain Imaging: A Guide to the Methods and their Applications to Psychology and Behavioral Neuroscience, CRC Press, 1998.

[14] W.W. Orrison, Functional Brain Imaging, Mosby, 1995.

[15] S.A. Huettel, A.W. Song, G. McCarthy, Functional Magnetic Resonance Imaging, Freeman, 2009.

[16] B.E. Swartz, The advantages of digital over analog recording techniques, Electroencephalogr. Clin. Neurophysiol. 106 (1998) 113–117. doi:10.1016/S0013-4694(97)00113-2.

[17] L.F. Haas, Hans Berger (1873-1941), Richard Caton (1842-1926), and electroencephalography., J. Neurol. Neurosurg. Psychiatry. 74 (2003) 9.

[18] D. Cohen, Magnetoencephalography: evidence of magnetic fields produced by alpha-rhythm currents., Science. 161 (1968) 784–6.

[19] M. Hämäläinen, R. Hari, R.J. Ilmoniemi, J. Knuutila, O. V. Lounasmaa, Magnetoencephalography—theory, instrumentation, and applications to noninvasive studies of the working human brain, Rev. Mod. Phys. 65 (1993) 413–497. doi:10.1103/RevModPhys.65.413.

[20] Electroencephalography: Basic Principles, Clinical Applications, and Related Fields, Lippincott Williams & Wilkins, 2005.

[21] O.D. Creutzfeldt, S. Watanabe, H.D. Lux, Relations between EEG phenomena and potentials of single cortical cells. I. Evoked responses after thalamic and epicortical stimulation, Electroencephalogr. Clin. Neurophysiol. 20 (1966) 1–18. doi:10.1016/0013-4694(66)90136-2.

[22] A.W. Toga, J.C. Mazziotta, Brain Mapping: The Methods, Academic Press, 2002.

[23] R. Grech, T. Cassar, J. Muscat, K.P. Camilleri, S.G. Fabri, M. Zervakis, et al., Review on solving the inverse problem in EEG source analysis., J. Neuroeng. Rehabil. 5 (2008) 25. doi:10.1186/1743-0003-5-25.

[24] P.L. Nunez, R. Srinivasan, Electric Fields of the Brain: The Neurophysics of EEG, Oxford University Press, 2006.

[25] Y. Hoshi, Functional near-infrared spectroscopy: current status and future prospects., J. Biomed. Opt. 12 (2007) 062106. doi:10.1117/1.2804911.

[26] B. Chance, Z. Zhuang, C. UnAh, C. Alter, L. Lipton, Cognition-activated low-frequency modulation of light absorption in human brain., Proc. Natl. Acad. Sci. 90 (1993) 3770–3774. doi:10.1073/pnas.90.8.3770.

[27] A. Villringer, J. Planck, C. Hock, L. Schleinkofer, U. Dirnagl, Near infrared spectroscopy (NIRS): A new tool to study hemodynamic changes during

activation of brain function in human adults, Neurosci. Lett. 154 (1993) 101–104. doi:10.1016/0304-3940(93)90181-J.

[28] T. Kato, A. Kamei, S. Takashima, T. Ozaki, Human visual cortical function during photic stimulation monitoring by means of near-infrared spectroscopy., J. Cereb. Blood Flow Metab. 13 (1993) 516–20. doi:10.1038/jcbfm.1993.66.

[29] Y. Hoshi, M. Tamura, Detection of dynamic changes in cerebral oxygenation coupled to neuronal function during mental work in man, Neurosci. Lett. 150 (1993) 5–8. doi:10.1016/0304-3940(93)90094-2.

[30] S.C. Bunce, M. Izzetoglu, K. Izzetoglu, B. Onaral, K. Pourrezaei, Functional near-infrared spectroscopy, IEEE Eng. Med. Biol. Mag. 25 (2006) 54–62. doi:10.1109/MEMB.2006.1657788.

[31] S.L. Jacques, Optical properties of biological tissues: a review., Phys. Med. Biol. 58 (2013) R37–61. doi:10.1088/0031-9155/58/11/R37.

[32] W.F. Cheong, S.A. Prahl, A.J. Welch, A review of the optical properties of biological tissues, IEEE J. Quantum Electron. 26 (1990) 2166–2185. doi:10.1109/3.64354.

[33] D.A. Boas, C. Pitris, N. Ramanujam, Handbook of Biomedical Optics, CRC Press, 2011.

[34] D.T. Delpy, M. Cope, P. van der Zee, S. Arridge, S. Wray, J. Wyatt, Estimation of optical pathlength through tissue from direct time of flight measurement, Phys. Med. Biol. 33 (1988) 1433–1442. doi:10.1088/0031-9155/33/12/008.

[35] H. Boecker, C.H. Hillman, L. Scheef, H.K. Strüder, eds., Functional Neuroimaging in Exercise and Sport Sciences, Springer New York, New York, NY, 2012. doi:10.1007/978-1-4614-3293-7.

[36] I. Miederer, H. Boecker, PET: Theoretical Background and Practical Aspects, in: H. Boecker, C.H. Hillman, L. Scheef, H.K. Strüder (Eds.), Funct. Neuroimaging Exerc. Sport Sci., Springer New York, New York, NY, 2012: p. 318. doi:10.1007/978-1-4614-3293-7.

[37] W.W. Orrison, J.D. Lewine, J.A. Sanders, M.F. Hartshorne, Functional Brain Imaging, Elsevier, 1995. doi:10.1016/B978-0-8151-6509-5.50009-6.

[38] A. Kumar, H.T. Chugani, Functional imaging: PET., Handb. Clin. Neurol. 111 (2013) 767–76. doi:10.1016/B978-0-444-52891-9.00079-8.

[39] G. Muehllehner, J.S. Karp, Positron emission tomography., Phys. Med. Biol. 51 (2006) R117–37. doi:10.1088/0031-9155/51/13/R08.

[40] S.I. Ziegler, Positron Emission Tomography: Principles, Technology, and Recent Developments, Nucl. Phys. A. 752 (2005) 679–687. doi:10.1016/j.nuclphysa.2005.02.067.

[41] J. Greenberg, M. Reivich, A. Alavi, P. Hand, A. Rosenquist, W. Rintelmann, et al., Metabolic mapping of functional activity in human subjects with the [18F]fluorodeoxyglucose technique, Science. 212 (1981) 678–680. doi:10.1126/science.6971492.

[42] J.C. Mazziotta, M.E. Phelps, R.E. Carson, D.E. Kuhl, Tomographic mapping of human cerebral metabolism: Auditory stimulation, Neurology. 32 (1982) 921–37. doi:10.1212/WNL.32.9.921.

[43] M. Phelps, D. Kuhl, J. Mazziota, Metabolic mapping of the brain's response to visual stimulation: studies in humans, Science. 211 (1981) 1445–1448. doi:10.1126/science.6970412.

[44] R.M. Kessler, J.C. Goble, J.H. Bird, M.E. Girton, J.L. Doppman, S.I. Rapoport, et al., Measurement of Blood-Brain Barrier Permeability with Positron Emission Tomography and [68Ga]EDTA, J. Cereb. Blood Flow Metab. 4 (1984) 323–328. doi:10.1038/jcbfm.1984.48.

[45] L. Farde, H. Hall, E. Ehrin, G. Sedvall, Quantitative analysis of D2 dopamine receptor binding in the living human brain by PET, Science. 231 (1986) 258–261. doi:10.1126/science.2867601.

[46] D.E. Kuhl, R.A. Koeppe, S. Minoshima, S.E. Snyder, E.P. Ficaro, N.L. Foster, et al., In vivo mapping of cerebral acetylcholinesterase activity in aging and Alzheimer's disease, Neurology. 52 (1999) 691–699. doi:10.1212/WNL.52.4.691.

[47] K. Yoshinaga, R. Klein, N. Tamaki, Generator-produced rubidium-82 positron emission tomography myocardial perfusion imaging-From basic aspects to clinical applications., J. Cardiol. 55 (2010) 163–73. doi:10.1016/j.jjcc.2010.01.001.

[48] P.T. Callaghan, Principles of Nuclear Magnetic Resonance Microscopy, Oxford University Press, New York, 1991. doi:10.1118/1.596918.

[49] F. Bloch, Nuclear Induction, Phys. Rev. 70 (1946) 460–474. doi:10.1103/PhysRev.70.460.

[50] N. Bloembergen, E. Purcell, R. Pound, Relaxation effects in nuclear magnetic resonance absorption, Phys. Rev. 73 (1948) 679–712. doi:10.1103/PhysRev.73.679.

[51] P.A. Bottomley, T.H. Foster, R.R. Argersinger, L.M. Pfeifer, A review of normal tissue hydrogen NMR relaxation times and relaxation mechanisms from 1-100MHz: Dependence on tissue type, NMR frequency, temperature, species, extinction and age, Med. Phys. 11 (1984) 425–449. doi:10.1118/1.595535.

[52] B.C. Thompson, M.R. Waterman, G.L. Cottam, Evaluation of the water environments in deoxygenated sickle cells by longitudinal and transverse water proton relaxation rates, Arch. Biochem. Biophys. 166 (1975) 193–200. doi:10.1016/0003-9861(75)90380-X.

[53] C. Laule, I.M. Vavasour, S.H. Kolind, D.K.B. Li, T.L. Traboulsee, G.R.W. Moore, et al., Magnetic resonance imaging of myelin., Neurotherapeutics. 4 (2007) 460–84. doi:10.1016/j.nurt.2007.05.004.

[54] R.D. Dortch, G. a. Apker, W.M. Valentine, B. Lai, M.D. Does, Compartment-specific enhancement of white matter and nerve ex vivo using chromium., Magn. Reson. Med. 64 (2010) 688–697. doi:10.1002/mrm.22460.

[55] R.A. Horch, J.C. Gore, M.D. Does, Origins of the ultrashort-T2 1H NMR signals in myelinated nerve: a direct measure of myelin content?, Magn. Reson. Med. 66 (2011) 24–31. doi:10.1002/mrm.22980.

[56] A.N. Dula, D.F. Gochberg, H.L. Valentine, W.M. Valentine, M.D. Does, Multiexponential T2, magnetization transfer, and quantitative histology in white matter tracts of rat spinal cord., Magn. Reson. Med. 63 (2010) 902–9. doi:10.1002/mrm.22267.

[57] J.D. Quirk, G.L. Bretthorst, T.Q. Duong, A.Z. Snyder, C.S. Springer, J.J.H. Ackerman, et al., Equilibrium water exchange between the intra- and extracellular spaces of mammalian brain., Magn. Reson. Med. 50 (2003) 493–9. doi:10.1002/mrm.10565.

[58] F.R. Fenrich, C. Beaulieu, P.S. Allen, Relaxation times and microstructures., NMR Biomed. 14 (2001) 133–9.

[59] A. Einstein, Über die von der molekularkinetischen Theorie der Wärme geforderte Bewegung von in ruhenden Flüssigkeiten suspendierten Teilchen, Ann. Phys. 322 (1905) 549–560. doi:10.1002/andp.19053220806.

[60] A. Einstein, Investigations on the Theory of the Brownian Movement, Courier Corporation, 1956.

[61] P.T. Callaghan, Translational Dynamics and Magnetic Resonance: Principles of Pulsed Gradient Spin Echo NMR, OUP Oxford, 2011.

[62] D. Le Bihan, The “wet mind”: water and functional neuroimaging., Phys. Med. Biol. 52 (2007) R57–90. doi:10.1088/0031-9155/52/7/R02.

[63] U.F. Hazlewood, H.E. Rorschach, C. Lin, Diffusion of water in tissues and MRI, Magn. Reson. Med. 19 (1991) 214–216. doi:10.1002/mrm.1910190204.

[64] K.C. Chen, C. Nicholson, Changes in brain cell shape create residual extracellular space volume and explain tortuosity behavior during osmotic challenge., Proc. Natl. Acad. Sci. U. S. A. 97 (2000) 8306–11. doi:10.1073/pnas.150338197.

[65] P.J. Basser, E. Özarslan, Introduction to diffusion MRI, in: H. Johansen-Berg, T.E.. Behrens (Eds.), Diffus. MRI, Elsevier, 2014: pp. 3–9. doi:10.1016/B978-0-12-396460-1.00001-9.

[66] P.J. Basser, J. Mattiello, D. LeBihan, MR diffusion tensor spectroscopy and imaging., Biophys. J. 66 (1994) 259–67. doi:10.1016/S0006-3495(94)80775-1.

[67] D. Le Bihan, Molecular diffusion, tissue microdynamics and microstructure, NMR Biomed. 8 (1995) 375–386. doi:10.1002/nbm.1940080711.

[68] C.A. Clark, D. Le Bihan, Water diffusion compartmentation and anisotropy at high b values in the human brain., Magn. Reson. Med. 44 (2000) 852–9. http://www.ncbi.nlm.nih.gov/pubmed/11108621.

[69] D.L. Buckley, J.D. Bui, M.I. Phillips, T. Zelles, B.A. Inglis, H.D. Plant, et al., The effect of ouabain on water diffusion in the rat hippocampal slice measured by high resolution NMR imaging., Magn. Reson. Med. 41 (1999) 137–42. http://www.ncbi.nlm.nih.gov/pubmed/10025621.

[70] T.M. Shepherd, S.J. Blackband, E.D. Wirth, Simultaneous diffusion MRI measurements from multiple perfused rat hippocampal slices., Magn. Reson. Med. 48 (2002) 565–9. doi:10.1002/mrm.10241.

[71] J.-H.H. Lee, C.S. Springer, Effects of equilibrium exchange on diffusion-weighted NMR signals: The diffusigraphic “shutter-speed,” Magn. Reson. Med. 49 (2003) 450–458. doi:10.1002/mrm.10402.

[72] J. Pfeuffer, U. Flögel, W. Dreher, D. Leibfritz, Restricted diffusion and exchange of intracellular water: theoretical modelling and diffusion time dependence of 1H NMR measurements on perfused glial cells., NMR Biomed. 11 (1998) 19–31. http://www.ncbi.nlm.nih.gov/pubmed/9608585 (accessed May 23, 2014).

[73] E. Fieremans, D.S. Novikov, J.H. Jensen, J.A. Helpern, Monte Carlo study of a two-compartment exchange model of diffusion., NMR Biomed. 23 (2010) 711–24. doi:10.1002/nbm.1577.

[74] S. Ogawa, T.M. Lee, A.R. Kay, D.W. Tank, Brain magnetic resonance imaging with contrast dependent on blood oxygenation, Proc. Natl. Acad. Sci. U. S. A. 87 (1990) 9868–72. doi:10.1073/pnas.87.24.9868.

[75] S. Ogawa, T.-M. Lee, Magnetic resonance imaging of blood vessels at high fields:In vivo andin vitro measurements and image simulation, Magn. Reson. Med. 16 (1990) 9–18. doi:10.1002/mrm.1910160103.

[76] S. Ogawa, T.M. Lee, A.S. Nayak, P. Glynn, Oxygenation-sensitive contrast in magnetic resonance image of rodent brain at high magnetic fields., Magn. Reson. Med. 14 (1990) 68–78.

[77] P.A. Bandettini, E.C. Wong, R.S. Hinks, R.S. Tikofsky, J.S. Hyde, Time course EPI of human brain function during task activation, Magn. Reson. Med. 25 (1992) 390–397. doi:10.1002/mrm.1910250220.

[78] K.K. Kwong, J.W. Belliveau, D.A. Chesler, I.E. Goldberg, R.M. Weisskoff, B.P. Poncelet, et al., Dynamic magnetic resonance imaging of human brain activity during primary sensory stimulation, Proc. Natl. Acad. Sci. U. S. A. 89 (1992) 5675–5679.

[79] S. Ogawa, D.W. Tank, R. Menon, J.M. Ellermann, S.G. Kim, H. Merkle, et al., Intrinsic signal changes accompanying sensory stimulation: functional brain mapping with magnetic resonance imaging, Proc. Natl. Acad. Sci. 89 (1992) 5951–5955. doi:10.1073/pnas.89.13.5951.

[80] N.K. Logothetis, What we can do and what we cannot do with fMRI., Nature. 453 (2008) 869–78. doi:10.1038/nature06976.

[81] A. Mechelli, C.J. Price, K.J. Friston, Nonlinear coupling between evoked rCBF and BOLD signals: a simulation study of hemodynamic responses., Neuroimage. 14 (2001) 862–72. doi:10.1006/nimg.2001.0876.

[82] K.L. Miller, W.-M. Luh, T.T. Liu, A. Martinez, T. Obata, E.C. Wong, et al., Nonlinear temporal dynamics of the cerebral blood flow response, Hum. Brain Mapp. 13 (2001) 1–12. doi:10.1002/hbm.1020.

[83] D.J. Heeger, D. Ress, What does fMRI tell us about neuronal activity?, Nat. Rev. Neurosci. 3 (2002) 142–51. doi:10.1038/nrn730.

[84] T.L. Davis, K.K. Kwong, R.M. Weisskoff, B.R. Rosen, Calibrated functional MRI: mapping the dynamics of oxidative metabolism., Proc. Natl. Acad. Sci. U. S. A. 95 (1998) 1834–9. doi:10.1073/pnas.95.4.1834.

[85] N.K. Logothetis, The ins and outs of fMRI signals., Nat. Neurosci. 10 (2007) 1230–2. doi:10.1038/nn1007-1230.

[86] K. Schulz, E. Sydekum, R. Krueppel, C.J. Engelbrecht, F. Schlegel, A. Schröter, et al., Simultaneous BOLD fMRI and fiber-optic calcium recording in rat neocortex, Nat. Methods. 9 (2012) 597–602. doi:10.1038/nMeth.2013.

[87] R.S. Menon, S.-G. Kim, Spatial and temporal limits in cognitive neuroimaging with fMRI, Trends Cogn. Sci. 3 (1999) 207–216. doi:10.1016/S1364-6613(99)01329-7.

[88] P.A. Bandettini, N. Petridou, J. Bodurka, Direct detection of neuronal activity with MRI: Fantasy, possibility, or reality?, Appl. Magn. Reson. 29 (2005) 65–88. doi:10.1007/BF03166956.

[89] R.S. Menon, B.G. Goodyear, Submillimeter functional localization in human striate cortex using BOLD contrast at 4 Tesla: implications for the vascular point-spread function., Magn. Reson. Med. 41 (1999) 230–5. http://www.ncbi.nlm.nih.gov/pubmed/10080267 (accessed July 24, 2015).

[90] S. Engel, Retinotopic organization in human visual cortex and the spatial precision of functional MRI, Cereb. Cortex. 7 (1997) 181–192. doi:10.1093/cercor/7.2.181.

[91] D. Le Bihan, S. Urayama, T. Aso, T. Hanakawa, H. Fukuyama, Direct and fast detection of neuronal activation in the human brain with diffusion MRI., Proc. Natl. Acad. Sci. U. S. A. 103 (2006) 8263–8. doi:10.1073/pnas.0600644103.

[92] N. Tirosh, U. Nevo, Neuronal activity significantly reduces water displacement: DWI of a vital rat spinal cord with no hemodynamic effect., Neuroimage. 76 (2013) 98–107. doi:10.1016/j.neuroimage.2013.02.065.

[93] J. Flint, B. Hansen, P. Vestergaard-Poulsen, S.J. Blackband, Diffusion weighted magnetic resonance imaging of neuronal activity in the hippocampal slice model., Neuroimage. 46 (2009) 411–418. doi:10.1016/j.neuroimage.2009.02.003.

[94] K.L. Miller, D.P. Bulte, H. Devlin, M.D. Robson, R.G. Wise, M.W. Woolrich, et al., Evidence for a vascular contribution to diffusion FMRI at high b value., Proc. Natl. Acad. Sci. U. S. A. 104 (2007) 20967–20972. doi:10.1073/pnas.0707257105.

[95] N. Petridou, D. Plenz, A.C. Silva, M. Loew, J. Bodurka, P.A. Bandettini, Direct magnetic resonance detection of neuronal electrical activity, Proc. Natl. Acad. Sci. U. S. A. 103 (2006) 16015–20. doi:10.1073/pnas.0603219103.

[96] J. Bodurka, P.A. Bandettini, Toward direct mapping of neuronal activity: MRI detection of ultraweak, transient magnetic field changes, Magn. Reson. Med. 47 (2002) 1052–8. doi:10.1002/mrm.10159.

[97] L.M. Parkes, F.P. de Lange, P. Fries, I. Toni, D.G. Norris, Inability to directly detect magnetic field changes associated with neuronal activity., Magn. Reson. Med. 57 (2007) 411–6. doi:10.1002/mrm.21129.

[98] T.-K. Truong, A.W. Song, Finding neuroelectric activity under magnetic-field oscillations (NAMO) with magnetic resonance imaging in vivo., Proc. Natl. Acad. Sci. U. S. A. 103 (2006) 12598–601. doi:10.1073/pnas.0605486103.

[99] B.J. Roth, P.J. Basser, Mechanical model of neural tissue displacement during Lorentz effect imaging., Magn. Reson. Med. 61 (2009) 59–64. doi:10.1002/mrm.21772.

[100] M.C. Ng, K.K. Wong, G. Li, S. Lai, E.S. Yang, Y. Hu, et al., Proton-density-weighted spinal fMRI with sensorimotor stimulation at 0.2 T., Neuroimage. 29 (2006) 995–9. doi:10.1016/j.neuroimage.2005.08.011.

[101] T.H. Jochimsen, D.G. Norris, H.E. Möller, Is there a change in water proton density associated with functional magnetic resonance imaging?, Magn. Reson. Med. 53 (2005) 470–3. doi:10.1002/mrm.20351.

[102] T. Witzel, F.-H. Lin, B.R. Rosen, L.L. Wald, Stimulus-induced Rotary Saturation (SIRS): a potential method for the detection of neuronal currents with MRI., Neuroimage. 42 (2008) 1357–65. doi:10.1016/j.neuroimage.2008.05.010.

[103] F. De Luca, Direct fMRI by random spin-lock along the neural field., Magn. Reson. Imaging. 29 (2011) 951–957. doi:10.1016/j.mri.2011.04.003.

[104] R. Hobbie, B.J. Roth, Intermediate Physics for Medicine and Biology, Springer Science & Business Media, 2007. https://books.google.com/books?id=iD4mC6FGTBgC&pgis=1 (accessed July 25, 2015).

[105] G.. Scott, M.L.. Joy, R.. Armstrong, R.. Henkelman, Sensitivity of magnetic-resonance current-density imaging, J. Magn. Reson. 97 (1992) 235–254. doi:10.1016/0022-2364(92)90310-4.

[106] M. Joy, G. Scott, M. Henkelman, In vivo detection of applied electric currents by magnetic resonance imaging, Magn. Reson. Imaging. 7 (1989) 89–94. doi:10.1016/0730-725X(89)90328-7.

[107] J. Bodurka, A. Jesmanowicz, J.S. Hyde, H. Xu, L. Estkowski, S.J. Li, Current-induced magnetic resonance phase imaging., J. Magn. Reson. 137 (1999) 265–71. doi:10.1006/jmre.1998.1680.

[108] H. Kamei, K. Iramina, K. Yoshikawa, S. Ueno, Neuronal current distribution imaging using magnetic resonance, IEEE Trans. Magn. 35 (1999) 4109–4111. doi:10.1109/20.800771.

[109] D. Konn, P. Gowland, R. Bowtell, MRI detection of weak magnetic fields due to an extended current dipole in a conducting sphere: a model for direct detection of neuronal currents in the brain., Magn. Reson. Med. 50 (2003) 40–9. doi:10.1002/mrm.10494.

[110] J. Xiong, P.T. Fox, J.-H. Gao, Directly mapping magnetic field effects of neuronal activity by magnetic resonance imaging., Hum. Brain Mapp. 20 (2003) 41–49. doi:10.1002/hbm.10124.

[111] R. Chu, J.A. de Zwart, P. van Gelderen, M. Fukunaga, P. Kellman, T. Holroyd, et al., Hunting for neuronal currents: absence of rapid MRI signal changes during visual-evoked response., Neuroimage. 23 (2004) 1059–67. doi:10.1016/j.neuroimage.2004.07.003.

[112] A.W. Song, A.M. Takahashi, Lorentz effect imaging, Magn. Reson. Imaging. 19 (2001) 763–767. doi:10.1016/S0730-725X(01)00406-4.

[113] T.-K. Truong, J.L. Wilbur, A.W. Song, Synchronized detection of minute electrical currents with MRI using Lorentz effect imaging., J. Magn. Reson. 179 (2006) 85–91. doi:10.1016/j.jmr.2005.11.012.

[114] R.S. Wijesinghe, B.J. Roth, Lorentz effect imaging of ionic currents in solution using correct values for ion mobility., J. Magn. Reson. 204 (2010) 225–7. doi:10.1016/j.jmr.2010.02.024.

[115] N.W. Halpern-Manners, V.S. Bajaj, T.Z. Teisseyre, A. Pines, Magnetic resonance imaging of oscillating electrical currents., Proc. Natl. Acad. Sci. U. S. A. 107 (2010) 8519–24. doi:10.1073/pnas.1003146107.

[116] D. Le Bihan, E. Breton, Imagerie de diffusion in-vivo par résonance magnétique nucléaire, Comptes-Rendus l'Académie des Sci. 93 (1985) 27–34. https://hal.archives-ouvertes.fr/hal-00350090/ (accessed July 16, 2015).

[117] K.-D. Merboldt, W. Hanicke, J. Frahm, Self-diffusion NMR imaging using stimulated echoes, J. Magn. Reson. 64 (1985) 479–486. doi:10.1016/0022-2364(85)90111-8.

[118] D.G. Taylor, M.C. Bushell, The spatial mapping of translational diffusion coefficients by the NMR imaging technique, Phys. Med. Biol. 30 (1985) 345–349. doi:10.1088/0031-9155/30/4/009.

[119] A.E. Baird, S. Warach, Magnetic resonance imaging of acute stroke., J. Cereb. Blood Flow Metab. 18 (1998) 583–609. doi:10.1097/00004647-199806000-00001.

[120] C. Van Pul, W. Jennekens, K. Nicolay, K. Kopinga, P.F.F. Wijn, Ischemia-induced ADC changes are larger than osmotically-induced ADC changes in a neonatal rat hippocampus model, Magn. Reson. Med. 53 (2005) 348–355. doi:10.1002/mrm.20353.

[121] T. Tsurugizawa, L. Ciobanu, D. Le Bihan, Water diffusion in brain cortex closely tracks underlying neuronal activity, Proc. Natl. Acad. Sci. 110 (2013) 11636–11641. doi:10.1073/pnas.1303178110/-/DCSupplemental.www.pnas.org/cgi/doi/10.1073/pnas.1303178110.

[122] J. Zhong, O.A.C. Petroff, L.A. Pleban, J.C. Gore, J.W. Prichard, Reversible, reproducible reduction of brain water apparent diffusion coefficient by cortical electroshocks, Magn. Reson. Med. 37 (1997) 1–6. doi:10.1002/mrm.1910370102.

[123] A. Darquié, J.B. Poline, C. Poupon, H. Saint-Jalmes, D. Le Bihan, Transient decrease in water diffusion observed in human occipital cortex during visual stimulation., Proc. Natl. Acad. Sci. U. S. A. 98 (2001) 9391–5. doi:10.1073/pnas.151125698.

[124] J.D. Bui, D.L. Buckley, M.I. Phillips, S.J. Blackband, Nuclear magnetic resonance imaging measurements of water diffusion in the perfused hippocampal slice during N-methyl-d-aspartate-induced excitotoxicity, Neuroscience. 93 (1999) 487–490. doi:10.1016/S0306-4522(99)00191-8.

[125] T. Jin, S.-G. Kim, Functional changes of apparent diffusion coefficient during visual stimulation investigated by diffusion-weighted gradient-echo fMRI., Neuroimage. 41 (2008) 801–12. doi:10.1016/j.neuroimage.2008.03.014.

[126] J.A.A. Autio, J. Kershaw, S. Shibata, T. Obata, I. Kanno, I. Aoki, High b-value diffusion-weighted fMRI in a rat forepaw electrostimulation model at 7 T., Neuroimage. 57 (2011) 140–8. doi:10.1016/j.neuroimage.2011.04.006.

[127] T. Jin, F. Zhao, S.-G. Kim, Sources of functional apparent diffusion coefficient changes investigated by diffusion-weighted spin-echo fMRI., Magn. Reson. Med. 56 (2006) 1283–92. doi:10.1002/mrm.21074.

[128] U. Nevo, E. Ozarslan, M.E. Komlosh, C.G. Koay, J.E. Sarlls, P.J. Basser, A system and mathematical framework to model shear flow effects in biomedical DW-imaging and spectroscopy., NMR Biomed. 23 (2010) 734–44. doi:10.1002/nbm.1591.

[129] C.R. Figley, J.K. Leitch, P.W. Stroman, In contrast to BOLD: signal enhancement by extravascular water protons as an alternative mechanism of endogenous fMRI signal change., Magn. Reson. Imaging. 28 (2010) 1234–43. doi:10.1016/j.mri.2010.01.005.

[130] P.W. Stroman, V. Krause, K.L. Malisza, U.N. Frankenstein, B. Tomanek, Extravascular proton-density changes as a non-BOLD component of contrast in fMRI of the human spinal cord., Magn. Reson. Med. 48 (2002) 122–7. doi:10.1002/mrm.10178.

[131] P.W. Stroman, A.S. Lee, K.K. Pitchers, R.D. Andrew, Magnetic resonance imaging of neuronal and glial swelling as an indicator of function in cerebral tissue slices., Magn. Reson. Med. 59 (2008) 700–6. doi:10.1002/mrm.21534.

[132] P.W. Stroman, B. Tomanek, V. Krause, U.N. Frankenstein, K.L. Malisza, Functional magnetic resonance imaging of the human brain based on signal enhancement by extravascular protons (SEEP fMRI)., Magn. Reson. Med. 49 (2003) 433–9. doi:10.1002/mrm.10831.

[133] T. Jin, P. Wang, M. Tasker, F. Zhao, S.-G. Kim, Source of nonlinearity in echo-time-dependent BOLD fMRI., Magn. Reson. Med. 55 (2006) 1281–90. doi:10.1002/mrm.20918.

[134] C.-L. Li, H. McIlwain, Maintenance of resting membrane potentials in slices of mammalian cerebral cortex and other tissues in vitro., J. Physiol. 139 (1957) 178–90.

[135] C. Yamamoto, H. McIlwain, Electrical activities in thin sections from the mammalian brain maintained in chemically-defined media in vitro., J. Neurochem. 13 (1966) 1333–43.

[136] K.K. Skrede, R.H. Westgaard, The transverse hippocampal slice: a well-defined cortical structure maintained in vitro, Brain Res. 35 (1971) 589–593. doi:10.1016/0006-8993(71)90508-7.

[137] K.J. Brooks, R.A. Kauppinen, S.R. Williams, H.S. Bachelard, T.E. Bate, D.G. Gadian, Ammonia causes a drop in intracellular pH in metabolizing cortical

brain slices. A [31P]- and [1H]nuclear magnetic resonance study, Neuroscience. 33 (1989) 185–192. doi:10.1016/0306-4522(89)90320-5.

[138] R. Badar-Goffer, P. Morris, N. Thatcher, H. Bachelard, Excitotoxic amino acids cause appearance of magnetic resonance spectroscopy-observable zinc in supervised cortical slices, J. Neurochem. 62 (2008) 2488–2491. doi:10.1046/j.1471-4159.1994.62062488.x.

[139] J.J. Flint, C.H. Lee, B. Hansen, M. Fey, D. Schmidig, J.D. Bui, et al., Magnetic resonance microscopy of mammalian neurons, Neuroimage. 46 (2009) 1037–1040. doi:10.1016/j.neuroimage.2009.03.009.

[140] T.M. Shepherd, B. Scheffler, M.A. King, G.J. Stanisz, D.A. Steindler, S.J. Blackband, MR microscopy of rat hippocampal slice cultures: a novel model for studying cellular processes and chronic perturbations to tissue microstructure., Neuroimage. 30 (2006) 780–6. doi:10.1016/j.neuroimage.2005.10.020.

[141] M.M. Cohen, J.W. Pettegrew, S.J. Kopp, N. Minshew, T. Glonek, P-31 nuclear magnetic resonance analysis of brain: Normoxic and anoxic brain slices, Neurochem. Res. 9 (1984) 785–801. doi:10.1007/BF00965666.

[142] T.M. Shepherd, P.E. Thelwall, S.J. Blackband, B.R. Pike, R.L. Hayes, E.D. Wirth, Diffusion magnetic resonance imaging study of a rat hippocampal slice model for acute brain injury., J. Cereb. Blood Flow Metab. 23 (2003) 1461–70. doi:10.1097/01.WCB.0000100852.67976.C2.

[143] T.M. Shepherd, E.D. Wirth, P.E. Thelwall, H.-X. Chen, S.N. Roper, S.J. Blackband, Water diffusion measurements in perfused human hippocampal slices undergoing tonicity changes., Magn. Reson. Med. 49 (2003) 856–63. doi:10.1002/mrm.10456.

[144] N.K. Logothetis, J. Pauls, M. Augath, T. Trinath, a Oeltermann, Neurophysiological investigation of the basis of the fMRI signal., Nature. 412 (2001) 150–157. doi:10.1038/35084005.

[145] D.-S. Kim, I. Ronen, C. Olman, S.-G. Kim, K. Ugurbil, L.J. Toth, Spatial relationship between neuronal activity and BOLD functional MRI., Neuroimage. 21 (2004) 876–85. doi:10.1016/j.neuroimage.2003.10.018.

[146] R.A. Wind, K.R. Minard, G.R. Holtom, P.D. Majors, E.J. Ackerman, S.D. Colson, et al., An integrated confocal and magnetic resonance microscope for cellular research., J. Magn. Reson. 147 (2000) 371–7. doi:10.1006/jmre.2000.2212.

[147] R.A. Wind, P.D. Majors, K.R. Minard, E.J. Ackerman, D.S. Daly, G.R. Holtom, et al., Combined confocal and magnetic resonance microscopy, Appl. Magn. Reson. 22 (2002) 145–158. doi:10.1007/BF03166099.

[148] P.D. Majors, K.R. Minard, E.J. Ackerman, G.R. Holtom, D.F. Hopkins, C.I. Parkinson, et al., A combined confocal and magnetic resonance microscope for biological studies, Rev. Sci. Instrum. 73 (2002) 4329. doi:10.1063/1.1517146.

[149] K.R. Minard, G.R. Holtom, L.E. Kathmann, P.D. Majors, B.D. Thrall, R.A. Wind, Simultaneous 1H PFG-NMR and confocal microscopy of monolayer cell cultures: effects of apoptosis and necrosis on water diffusion and compartmentalization., Magn. Reson. Med. 52 (2004) 495–505. doi:10.1002/mrm.20179.

[150] F. Casanova, J. Perlo, B. Blümich, Single-Sided NMR, Springer, Berlin, 2011. http://books.google.com/books?hl=en&lr=&id=IWErGhyPyqQC&pgis=1 (accessed May 31, 2012).

[151] E. Danieli, B. Blümich, Single-sided magnetic resonance profiling in biological and materials science., J. Magn. Reson. (2012) 1–13. doi:10.1016/j.jmr.2012.11.023.

[152] D.G. Rata, F. Casanova, J. Perlo, D.E. Demco, B. Blümich, Self-diffusion measurements by a mobile single-sided NMR sensor with improved magnetic field gradient., J. Magn. Reson. 180 (2006) 229–35. doi:10.1016/j.jmr.2006.02.015.

[153] R. Haken, B. Blümich, Anisotropy in tendon investigated in vivo by a portable NMR scanner, the NMR-MOUSE., J. Magn. Reson. 144 (2000) 195–199. doi:10.1006/jmre.2000.2040.

[154] E. Rössler, C. Mattea, A. Mollova, S. Stapf, Low-field one-dimensional and direction-dependent relaxation imaging of bovine articular cartilage, J. Magn. Reson. 213 (2011) 112–118. doi:10.1016/j.jmr.2011.09.014.

[155] R. Bai, P.J. Basser, R.M. Briber, F. Horkay, NMR water self-diffusion and relaxation studies on sodium polyacrylate solutions and gels in physiologic ionic solutions., J. Appl. Polym. Sci. 131 (2014) 1–7. doi:10.1002/app.40001.

[156] M.J. Berridge, P. Lipp, M.D. Bootman, The versatility and universality of calcium signalling., Nat. Rev. Mol. Cell Biol. 1 (2000) 11–21. doi:10.1038/35036035.

[157] R.W. Tsien, R.Y. Tsien, Calcium channels, stores, and oscillations., Annu. Rev. Cell Biol. 6 (1990) 715–60. doi:10.1146/annurev.cb.06.110190.003435.

[158] L. Stoppini, P.-A. Buchs, D. Muller, A simple method for organotypic cultures of nervous tissue, J. Neurosci. Methods. 37 (1991) 173–182. doi:10.1016/0165-0270(91)90128-M.

[159] M. Caeser, A. Schüz, Maturation of neurons in neocortical slice cultures: A light and electron microscopic study on in situ and in vitro material., J. Hirnforsch. 33 (1992) 429–443.

[160] V.C. Karpiak, D. Plenz, Preparation and maintenance of organotypic cultures for multi-electrode array recordings., Curr. Protoc. Neurosci. Chapter 6 (2002) Unit 6.15. doi:10.1002/0471142301.ns0615s19.

[161] J.M. Beggs, D. Plenz, Neuronal avalanches are diverse and precise activity patterns that are stable for many hours in cortical slice cultures., J. Neurosci. 24 (2004) 5216–29. doi:10.1523/JNEUROSCI.0540-04.2004.

[162] C. V Stewart, D. Plenz, Homeostasis of neuronal avalanches during postnatal cortex development in vitro., J. Neurosci. Methods. 169 (2008) 405–16. doi:10.1016/j.jneumeth.2007.10.021.

[163] N. Daviaud, E. Garbayo, N. Lautram, F. Franconi, L. Lemaire, M. Perez-Pinzon, et al., Modeling nigrostriatal degeneration in organotypic cultures, a new ex vivo model of Parkinson's disease., Neuroscience. 256 (2014) 10–22. doi:10.1016/j.neuroscience.2013.10.021.

[164] O. Shriki, J. Alstott, F. Carver, T. Holroyd, R.N.A. Henson, M.L. Smith, et al., Neuronal avalanches in the resting MEG of the human brain., J. Neurosci. 33 (2013) 7079–7090. doi:10.1523/JNEUROSCI.4286-12.2013.

[165] S. Yu, H. Yang, H. Nakahara, G.S. Santos, D. Nikolić, D. Plenz, Higher-order interactions characterized in cortical activity., J. Neurosci. 31 (2011) 17514–17526. doi:10.1523/JNEUROSCI.3127-11.2011.

[166] R.D. Andrew, M.W. Labron, S.E. Boehnke, L. Carnduff, S. a. Kirov, Physiological evidence that pyramidal neurons lack functional water channels, Cereb. Cortex. 17 (2007) 787–802. doi:10.1093/cercor/bhk032.

[167] M. Maulucci-Gedde, D.W. Choi, Cortical neurons exposed to glutamate rapidly leak preloaded 51chromium, Exp. Neurol. 96 (1987) 420–429. doi:10.1016/0014-4886(87)90059-8.

[168] K. Iwasa, I. Tasaki, R. Gibbons, Swelling of nerve fibers associated with action potentials, Science (80-.). 210 (1980) 338–339. doi:10.1126/science.7423196.

[169] I. Tasaki, K. Iwasa, Rapid pressure changes and surface displacements in the squid giant axon associated with production of action potentials., Jpn. J. Physiol. 32 (1982) 69–81. doi:10.2170/jjphysiol.32.69.

[170] I. Tasaki, P.M. Byrne, Rapid structural changes in nerve fibers evoked by electric current pulses, Biochem. Biophys. Res. Commun. 188 (1992) 559–564. doi:10.1016/0006-291X(92)91092-5.

[171] I. Tasaki, Rapid structural changes in nerve fibers and cells associated with their excitation processes., Jpn. J. Physiol. 49 (1999) 125–138.

[172] W.C. Risher, R.D. Andrew, S.A. Kirov, Real-time passive volume responses of astrocytes to acute osmotic and ischemic stress in cortical slices and in vivo revealed by two-photon microscopy, Glia. 57 (2009) 207–221. doi:10.1002/glia.20747.

[173] G.H. Pollack, Cells, Gels and the Engines of Life: A New, Unifying Approach to Cell Function, Ebner & Sons, 2001.

[174] I. Tasaki, Spread of discrete structural changes in synthetic polyanionic gel : A model of propagation of a nerve impulse, J. Theor. Biol. 218 (2002) 497–505. doi:10.1006/yjtbi.3095.

[175] I. Tasaki, Repetitive abrupt structural changes in polyanionic gels: a comparison with analogous processes in nerve fibers., J. Theor. Biol. 236 (2005) 2–11. doi:10.1016/j.jtbi.2005.02.011.

[176] I. Tasaki, On the Reversible Abrupt Structural Changes in Nerve Fibers Underlying Their Excitation, in: G.H. Pollack, W.C. Chin (Eds.), Phase Transit. Cell Biol., Springer, 2008: pp. 1–21.

[177] A. Mackay, K. Whittall, J. Adler, D. Li, D. Paty, D. Graeb, In vivo visualization of myelin water in brain by magnetic resonance, Magn. Reson. Med. 31 (1994) 673–677. doi:10.1002/mrm.1910310614.

[178] A. MacKay, C. Laule, I. Vavasour, T. Bjarnason, S. Kolind, B. Mädler, Insights into brain microstructure from the T2 distribution, Magn. Reson. Imaging. 24 (2006) 515–525.

[179] K. Gersonde, L. Felsberg, T. Tolxdorff, D. Ratzel, B. Ströbel, Analysis of multiple T2 proton relaxation processes in human head and imaging on the basis of selective and assigned T2 values., Magn. Reson. Med. 1 (1984) 463–477. doi:10.1097/00004728-198503000-00068.

[180] S. Peled, D.G. Cory, S.A. Raymond, D.A. Kirschner, A. Jolesz, Water diffusion, T2 , and compartmentation in frog sciatic nerve, Magn. Reson. Med. 42 (1999) 911–918.

[181] C.J.G. Bakker, J. Vriend, Multi-exponential water proton spin-lattice relaxation in biological tissues and its implications for quantitative NMR imaging, Phys. Med. Biol. 29 (1984) 509–518. doi:10.1088/0031-9155/29/5/003.

[182] M. Prange, Y.-Q. Song, Understanding NMR T2 spectral uncertainty, J. Magn. Reson. 204 (2010) 118–123.

[183] K.D. Harkins, A.N. Dula, M.D. Does, Effect of intercompartmental water exchange on the apparent myelin water fraction in multiexponential T2 measurements of rat spinal cord., Magn. Reson. Med. 67 (2012) 793–800. doi:10.1002/mrm.23053.

[184] G.S. Rule, T.K. Hitchens, Fundamentals of Protein NMR Spectroscopy, Springer, Dordrecht, 2006.

[185] P.T. Callaghan, C.H. Arns, P. Galvosas, M.W. Hunter, Y. Qiao, K.E. Washburn, Recent Fourier and Laplace perspectives for multidimensional NMR in porous media., Magn. Reson. Imaging. 25 (2007) 441–444. doi:10.1016/j.mri.2007.01.114.

[186] P.T. Callaghan, I. Furó, Diffusion-diffusion correlation and exchange as a signature for local order and dynamics., J. Chem. Phys. 120 (2004) 4032–4038. doi:10.1063/1.1642604.

[187] A.M. Olaru, J. Kowalski, V. Sethi, B. Blümich, Exchange relaxometry of flow at small Péclet numbers in a glass bead pack., J. Magn. Reson. 220 (2012) 32–44. doi:10.1016/j.jmr.2012.04.015.

[188] Y. Qiao, P. Galvosas, T. Adalsteinsson, M. Schönhoff, P.T. Callaghan, Diffusion exchange NMR spectroscopic study of dextran exchange through polyelectrolyte multilayer capsules, J. Chem. Phys. 122 (2005) 214912. doi:10.1063/1.1924707.

[189] L. Venturi, N. Woodward, D. Hibberd, N. Marigheto, A. Gravelle, G. Ferrante, et al., Multidimensional cross-correlation relaxometry of aqueous protein systems, Appl. Magn. Reson. 33 (2008) 213–234. doi:10.1007/s00723-008-0066-z.

[190] L. Monteilhet, J.-P. Korb, J. Mitchell, P. McDonald, Observation of exchange in micropore water in cement pastes by two-dimensional T2-T2 nuclear magnetic resonance relaxometry, Phys. Rev. E. 74 (2006) 061404. doi:10.1103/PhysRevE.74.061404.

[191] K. Washburn, P. Callaghan, Tracking pore to pore exchange using relaxation exchange spectroscopy, Phys. Rev. Lett. 97 (2006) 175502. doi:10.1103/PhysRevLett.97.175502.

[192] M. Gratz, M. Wehring, P. Galvosas, F. Stallmach, Multidimensional NMR diffusion studies in microporous materials, Microporous Mesoporous Mater. 125 (2009) 30–34. doi:10.1016/j.micromeso.2009.02.014.

[193] G. Bernardo, Diffusivity of alcohols in amorphous polystyrene, J. Appl. Polym. Sci. 127 (2013) 1803–1811. doi:10.1002/app.37918.

[194] W.P. Hsu, K.S. Ho, Solvent diffusion in a modified polyaniline, J. Appl. Polym. Sci. 66 (1997) 2095–2101.

[195] G. Van Zee, J. De Graauw, Determination of the diffusivity in elastomer solutions by batch sorption studies from a dilute liquid phase, J. Appl. Polym. Sci. 66 (1997) 347–353.

[196] Y. Qiu, K. Park, Environment-sensitive hydrogels for drug delivery., Adv. Drug Deliv. Rev. 53 (2001) 321–39.

[197] S.S. Shah, Y. Cha, Poly(glycolic acid-co-DL-lactic acid): diffusion or degradation controlled durg delivery, J. Control. Release. 18 (1992) 261–270.

[198] F. Horkay, I. Tasaki, P.J. Basser, Osmotic swelling of polyacrylate hydrogels in physiological salt solutions., Biomacromolecules. 1 (2000) 84–90. http://www.ncbi.nlm.nih.gov/pubmed/11709847.

[199] F. Horkay, I. Tasaki, P.J. Basser, Effect of monovalent-divalent cation exchange on the swelling of polyacrylate hydrogels in physiological salt solutions., Biomacromolecules. 2 (2001) 195–9.

[200] R. Skouri, F. Schosseler, J.P. Munch, S.J. Candau, Swelling and elastic properties of polyelectrolyte gels, Macromolecules. 28 (1995) 197–210. doi:10.1021/ma00105a026.

[201] D.-W. Yin, F. Horkay, J.F. Douglas, J.J. de Pablo, Molecular simulation of the swelling of polyelectrolyte gels by monovalent and divalent counterions., J. Chem. Phys. 129 (2008) 129–140. doi:10.1063/1.2991179.

[202] S. Khodadadi, J.H. Roh, A. Kisliuk, E. Mamontov, M. Tyagi, S.A. Woodson, et al., Dynamics of biological macromolecules: not a simple slaving by hydration water., Biophys. J. 98 (2010) 1321–1326. doi:10.1016/j.bpj.2009.12.4284.

[203] J.H. Roh, R.M. Briber, A. Damjanovic, D. Thirumalai, S. a Woodson, a P. Sokolov, Dynamics of tRNA at different levels of hydration., Biophys. J. 96 (2009) 2755–2762. doi:10.1016/j.bpj.2008.12.3895.

[204] H. Frauenfelder, P.. Fenimore, B.. McMahon, Hydration, slaving and protein function, Biophys. Chem. 98 (2002) 35–48. doi:10.1016/S0301-4622(02)00083-2.

[205] P.W. Fenimore, H. Frauenfelder, B.H. McMahon, R.D. Young, Bulk-solvent and hydration-shell fluctuations, similar to alpha- and beta-fluctuations in glasses, control protein motions and functions., Proc. Natl. Acad. Sci. U. S. A. 101 (2004) 14408–14413. doi:10.1073/pnas.0405573101.

[206] A.L. Tournier, J. Xu, J.C. Smith, Translational hydration water dynamics drives the protein glass transition, Biophys. J. 85 (2003) 1871–1875.

[207] S.-H. Chen, L. Liu, E. Fratini, P. Baglioni, A. Faraone, E. Mamontov, Observation of fragile-to-strong dynamic crossover in protein hydration water., Proc. Natl. Acad. Sci. U. S. A. 103 (2006) 9012–9016. doi:10.1073/pnas.0602474103.

[208] C. Rocchi, A.R. Bizzarri, S. Cannistraro, Water dynamical anomalies evidenced by molecular-dynamics simulations at the solvent-protein interface, Phys. Rev. A. 57 (1998) 3315–3325.

[209] A.R. Bizzarri, S. Cannistraro, U. Infm, S. Ambientali, U. Tuscia, I.- Viterbo, Molecular dynamics of water at the protein-solvent interface, J. Phys. Chem.B. 106 (2002) 6617–6633.

[210] C. Casieri, F. De Luca, P. Fantazzini, Pore-size evaluation by single-sided nuclear magnetic resonance measurements: Compensation of water self-diffusion effect on transverse relaxation, J. Appl. Phys. 97 (2005) 043901. doi:10.1063/1.1833572.

[211] S. Ghoshal, C. Mattea, P. Denner, S. Stapf, Heterogeneities in gelatin film formation using single-sided NMR., J. Phys. Chem.B. 114 (2010) 16356–16363. doi:10.1021/jp1068363.

[212] O. Neudert, S. Stapf, C. Mattea, Diffusion exchange NMR spectroscopy in inhomogeneous magnetic fields., J. Magn. Reson. 208 (2011) 256–261. doi:10.1016/j.jmr.2010.11.014.

[213] R.I. Chelcea, R. Fechete, E. Culea, D.E. Demco, B. Blümich, Distributions of transverse relaxation times for soft-solids measured in strongly inhomogeneous magnetic fields., J. Magn. Reson. 196 (2009) 178–190. doi:10.1016/j.jmr.2008.11.004.

[214] J. Perlo, F. Casanova, B. Blümich, Profiles with microscopic resolution by single-sided NMR., J. Magn. Reson. 176 (2005) 64–70. doi:10.1016/j.jmr.2005.05.017.

[215] R.B. Lauffer, Paramagnetic metal complexes as water proton relaxation agents for NMR imaging: theory and design, Chem. Rev. 87 (1987) 901–927. doi:10.1021/cr00081a003.

[216] W. Nordhøy, H.W. Anthonsen, M. Bruvold, P. Jynge, J. Krane, H. Brurok, Manganese ions as intracellular contrast agents: proton relaxation and calcium interactions in rat myocardium., NMR Biomed. 16 (2003) 82–95. doi:10.1002/nbm.817.

[217] L. Masaro, X.X. Zhu, Physical models of diffusion for polymer solutions , gels and solids, Prog. Polym. Sci. 24 (1999) 731–775.

[218] J.S. Mackie, P. Meares, The Diffusion of Electrolytes in a Cation-Exchange Resin Membrane. I. Theoretical, Proc. R. Soc. A. 232 (1955) 498–509. doi:10.1098/rspa.1955.0234.

[219] B. Jonsson, H. Wennerstrom, P. Nilsson, Self-diffusion of small molecules in colloidal systems, Colloid Polym. Sci. 264 (1986) 77–88.

[220] J.S. Vrentas, J.L. Duda, H.-C. Ling, A.-C. Hou, Free-volume theories for self-diffusion in polymer–solvent systems. I. Conceptual differences in theories, J. Polym. Sci. Part B Polym. Phys. 23 (1985) 275–288. doi:10.1002/pol.1985.180230204.

[221] J.H. Wang, Theory of the self-diffusion of water in protein solutions. a new method for studying the hydration and shape of protein molecules, J. Am. Chem. Soc. 76 (1954) 4755–4763. doi:10.1021/ja01648a001.

[222] E. Geissler, A.M. Hecht, Translational and collective diffusion in semi-dilute gels, J. Phys. Lettres. 40 (1979) 173–176. doi:10.1051/jphyslet:01979004007017300.

[223] F. Mariette, D. Topgaard, B. Jönsson, O. Soderman, 1H NMR diffusometry study of water in casein dispersions and gels., J. Agric. Food Chem. 50 (2002) 4295–302. http://www.ncbi.nlm.nih.gov/pubmed/12105961.

[224] M. Jonstromer, B. Jonsson, B. Lindman, Self-diffusion in nonionic surfactant-water systems, J. Phys. Chem. 95 (1991) 3293–3300.

[225] R. Colsenet, F. Mariette, M. Cambert, NMR relaxation and water self-diffusion studies in whey protein solutions and gels., J. Agric. Food Chem. 53 (2005) 6784–90. doi:10.1021/jf050162k.

[226] J.M. Zielinski, J.L. Duda, Predicting polymer / solvent diffusion coefficients using free-volume theory, AIChE J. 38 (1992) 405–415.

[227] J.S. Vrentas, C.-H. Chu, Free-volume analysis of solvent self-diffusion in polymer solutions, J. Colloid Interface Sci. 130 (1989) 293–295. doi:10.1016/0021-9797(89)90105-7.

[228] T.S. Frick, W.J. Huang, M. Tirrell, T.P. Lodge, Probe diffusion in polystyrene/toluene solutions, J. Polym. Sci. Part B Polym. Phys. 28 (1990) 2629–2649. doi:10.1002/polb.1990.090281311.

[229] J.M. Zielinski, H. Sillescu, I.H. Romdhane, 1,3,5-triisopropylbenzene diffusion in polystyrene solutions, J. Polym. Sci. Part B Polym. Phys. 34 (1996) 121–130. doi:10.1002/(SICI)1099-0488(19960115)34:1<121::AID-POLB10>3.0.CO;2-G.

[230] M.B. Wisnudel, J.M. Torkelson, Small-molecule probe diffusion in polymer solutions: studies by Taylor dispersion and phosphorescence quenching, Macromolecules. 29 (1996) 6193–6207. doi:10.1021/ma960635b.

[231] R.A. Yapel, L. DuDa, X. Lin, E. Meerwall, Mutual and self-diffusion of water in gelatin : experimental measurement and predictive test of free-volume theory, Polymer (Guildf). 35 (1994) 2411–2416.

[232] K.S. Stojilkovic, A.M. Berezhkovskii, V.Y. Zitserman, S.M. Bezrukov, Conductivity and microviscosity of electrolyte solutions containing polyethylene glycols, J. Chem. Phys. 119 (2003) 6973. doi:10.1063/1.1605096.

[233] P.S.H. Nmr, S. Matsukawa, I. Ando, A Study of Self-Diffusion of Molecules in Polymer Gel by Pulsed-Gradient Spin-Echo 1H NMR, Macromolecules. 3 (1996) 7136–7140.

[234] J.S. Vrentas, J.L. Duda, H.-C. Ling, A.-C. Hou, Free-volume theories for self-diffusion in polymer–solvent systems. II. Predictive capabilities, J. Polym. Sci. Part B Polym. Phys. 23 (1985) 289–304. doi:10.1002/pol.1985.180230205.

[235] F. Horkay, A.M. Hecht, E. Geissler, The effects of cross-linking on the equation of state of a polymer solution, J. Chem. Phys. 91 (1989) 2706. doi:10.1063/1.456980.

[236] E. Geissler, F. Horkay, A.M. Hecht, Scattering from network polydispersity in polymer gels, Phys. Rev. Lett. 71 (1993) 645–648. doi:10.1103/PhysRevLett.71.645.

[237] J. Pleštil, Y.M. Ostanevich, V.Y. Bezzabotonov, D. Hlavatá, J. Labský, Small-angle scattering from polyelectrolyte solutions: Dimensions of

poly(methacrylic acid) chains in salt-free solutions, Polymer (Guildf). 27 (1986) 839–842. doi:10.1016/0032-3861(86)90291-0.

[238] J.R.C. Van der Maarel, D. Lankhorst, J. De Bleijser, J.C. Leyte, Water dynamics in polyelectrolyte solutions from deuterium and oxygen-17 nuclear magnetic relaxation, Macromolecules. 20 (1987) 2390–2397. doi:10.1021/ma00176a011.

[239] B.P. Hills, S.F. Takacs, P.S. Belton, The effects of proteins on the proton N.M.R. transverse relaxation times of water, Mol. Phys. 67 (1989) 903–918. doi:10.1080/00268978900101531.

[240] K.J. Packer, D.A.T. Dick, D.R. Wilkie, The dynamics of water in heterogeneous systems, Philos. Trans. R. Soc. B Biol. Sci. 278 (1977) 59–87. doi:10.1098/rstb.1977.0031.

[241] H.T. Edzes, E.T. Samulski, The measurement of cross-relaxation effects in the proton NMR spin-lattice relaxation of water in biological systems: Hydrated collagen and muscle, J. Magn. Reson. 31 (1978) 207–229. doi:10.1016/0022-2364(78)90185-3.

[242] J.R. Zimmerman, W.E. Brittin, Nuclear magnetic resonance studies in multiple phase systems: lifetime of a water molecule in an adsorbing phase on silica gel, J. Phys. Chem. 61 (1957) 1328–1333. doi:10.1021/j150556a015.

[243] L.M. Cedex, M.E. Kuil, J.G. Hollander, C. Le Bon, T. Nicolai, Self-diffusion and cooperative diffusion of globular proteins in solution, J. Phys. Chem. B. 103 (1999) 10294–10299. doi:10.1021/jp991345a.

[244] M.B. Mustafa, D.L. Tipton, M.D. Barkley, P. Ruaso, F.D. Blum, Dye diffusion in isotropic and liquid crystalline aqueous dye diffusion in (hydroxypropyl) cellulose, Macromolecules. 26 (1993) 370–378.

[245] A. Hecht, A. Guillermo, H. Simon, J.F. Legrand, E.G. J, Structure and dynamics of a poly (dimethylsi1oxane) network : a comparative investigation of gel and solution, Macromolecules. 25 (1992) 3677–3684.

[246] S. Mallam, F. Horkay, A.M. Hecht, E. Geissler, Scattering and swelling properties of inhomogeneous polyacrylamide gels, Macromolecules. 22 (1989) 3356–3361. doi:10.1021/ma00198a029.

[247] F. Horkay, A.M. Hecht, I. Grillo, P.J. Basser, E. Geissler, Experimental evidence for two thermodynamic length scales in neutralized polyacrylate gels, J. Chem. Phys. 117 (2002) 9103. doi:10.1063/1.1522399.

[248] D.W. McCall, D.C. Douglass, The effect of Ions on the self-diffusion of Water. I. concentration dependence, J. Phys. Chem. 69 (1965) 2001–2011. doi:10.1021/j100890a034.

[249] J.N. Sachs, H. Nanda, H.I. Petrache, T.B. Woolf, Changes in phosphatidylcholine headgroup tilt and water order induced by monovalent salts: molecular dynamics simulations., Biophys. J. 86 (2004) 3772–82. doi:10.1529/biophysj.103.035816.

[250] X. Chen, W. Hua, Z. Huang, H.C. Allen, Interfacial water structure associated with phospholipid membranes studied by phase-sensitive vibrational sum frequency generation spectroscopy., J. Am. Chem. Soc. 132 (2010) 11336–42. doi:10.1021/ja1048237.

[251] Y. Zhang, S. Furyk, D.E. Bergbreiter, P.S. Cremer, Specific ion effects on the water solubility of macromolecules: PNIPAM and the Hofmeister series., J. Am. Chem. Soc. 127 (2005) 14505–10. doi:10.1021/ja0546424.

[252] F.X. Quinn, V.J. Mcbrierty, A.C. Wilson, G.D. Friends, Water in hydrogels. 3. poly(hydroxyethy1 methacrylate) / saline solution systems, Macromolecules. 23 (1990) 4576–4581.

[253] F. Horkay, A.M. Hecht, C. Rochas, P.J. Basser, E. Geissler, Anomalous small angle x-ray scattering determination of ion distribution around a polyelectrolyte biopolymer in salt solution., J. Chem. Phys. 125 (2006) 234904. doi:10.1063/1.2402921.

[254] R. Bai, C.G. Koay, E. Hutchinson, P.J. Basser, A framework for accurate determination of the T2 distribution from multiple echo magnitude MRI images., J. Magn. Reson. 244 (2014) 53–63. doi:10.1016/j.jmr.2014.04.016.

[255] Y.-Q. Song, Focus on the physics of magnetic resonance on porous media, New J. Phys. 14 (2012) 055017. doi:10.1088/1367-2630/14/5/055017.

[256] M.M. Britton, R.G. Graham, K.J. Packer, Relationships between flow and NMR relaxation of fluids in porous solids, Magn. Reson. Imaging. 19 (2001) 325–331. doi:10.1016/S0730-725X(01)00244-2.

[257] B. Hills, Magnetic Resonance Imaging in Food Science, Wiley, New York, 1998.

[258] B. Blumich, NMR Imaging of Materials, Oxford University Press, Oxford, 2000.

[259] J.E.M. Snaar, H. Van As, Probing water compartments and membrane permeability in plant cells by 1H NMR relaxation measurements, Biophys. J. 63 (1992) 1654–1658.

[260] R. Harrison, M.J. Bronskill, R.M. Henkelman, Magnetization transfer and T2 relaxation components in tissue., Magn. Reson. Med. 33 (1995) 490–496. doi:10.1002/mrm.1910330406.

[261] S.C.L. Deoni, T.M. Peters, B.K. Rutt, High-resolution T1 and T2 mapping of the brain in a clinically acceptable time with DESPOT1 and DESPOT2., Magn. Reson. Med. 53 (2005) 237–41. doi:10.1002/mrm.20314.

[262] Y. Xia, Relaxation anisotropy in cartilage by NMR microscopy (μMRI) at 14-μm resolution, Magn. Reson. Med. 39 (1998) 941–949. doi:10.1002/mrm.1910390612.

[263] F. Eckstein, D. Burstein, T.M. Link, Quantitative MRI of cartilage and bone: degenerative changes in osteoarthritis., NMR Biomed. 19 (2006) 822–54. doi:10.1002/nbm.1063.

[264] R.M. Henkelman, Measurement of signal intensities in the presence of noise in MR images., Med. Phys. 12 (1985) 232–233. doi:10.1118/1.595711.

[265] C.B. Ahn, Z.H. Cho, A new phase correction method in NMR imaging based on autocorrelation and histogram analysis., IEEE Trans. Med. Imaging. 6 (1987) 32–6. doi:10.1109/TMI.1987.4307795.

[266] J.G. Pipe, Motion correction with PROPELLER MRI: application to head motion and free-breathing cardiac imaging., Magn. Reson. Med. 42 (1999) 963–9.

[267] M.H. Buonocore, L. Gao, Ghost artifact reduction for echo planar imaging using image phase correction, Magn. Reson. Med. 38 (1997) 89–100. doi:10.1002/mrm.1910380114.

[268] C.G. Koay, P.J. Basser, Analytically exact correction scheme for signal extraction from noisy magnitude MR signals., J. Magn. Reson. 179 (2006) 317–22. doi:10.1016/j.jmr.2006.01.016.

[269] H. Gudbjartsson, S. Patz, The Rician distribution of noisy MRI data, Magn. Reson. Med. 34 (1995) 910–914. doi:10.1002/mrm.1910340618.

[270] O.T. Karlsen, R. Verhagen, W.M. Bovée, Parameter estimation from Rician-distributed data sets using a maximum likelihood estimator: application to T1 and perfusion measurements., Magn. Reson. Med. 41 (1999) 614–23.

[271] T.A. Bjarnason, C.R. McCreary, J.F. Dunn, J.R. Mitchell, Quantitative T2 analysis: the effects of noise, regularization, and multivoxel approaches., Magn. Reson. Med. 63 (2010) 212–7. doi:10.1002/mrm.22173.

[272] C.R. McCreary, T.A. Bjarnason, V. Skihar, J.R. Mitchell, V.W. Yong, J.F. Dunn, Multiexponential T2 and magnetization transfer MRI of demyelination and remyelination in murine spinal cord, Neuroimage. 45 (2009) 1173–1182.

[273] E.P. Minty, T.A. Bjarnason, C. Laule, A.L. MacKay, Myelin water measurement in the spinal cord., Magn. Reson. Med. 61 (2009) 883–92. doi:10.1002/mrm.21936.

[274] C.G. Koay, E. Özarslan, P.J. Basser, A signal transformational framework for breaking the noise floor and its applications in MRI, J. Magn. Reson. 197 (2009) 108–119.

[275] T.A. Bjarnason, C. Laule, J. Bluman, P. Kozlowski, Temporal phase correction of multiple echo T2 magnetic resonance images, J. Magn. Reson. 231 (2013) 22–31.

[276] E. Özarslan, T.M. Shepherd, C.G. Koay, S.J. Blackband, P.J. Basser, Temporal scaling characteristics of diffusion as a new MRI contrast: Findings in rat hippocampus, Neuroimage. 60 (2012) 1380–1393.

[277] M.A. Bernstein, Improved detectability in low signal-to-noise ratio magnetic resonance images by means of a phase-corrected real reconstruction, Med. Phys. 16 (1989) 813. doi:10.1118/1.596304.

[278] W.A. Edelstein, A signal-to-noise calibration procedure for NMR imaging systems, Med. Phys. 11 (1984) 180. doi:10.1118/1.595484.

[279] L.-C. Chang, G.K. Rohde, C. Pierpaoli, An automatic method for estimating noise-induced signal variance in magnitude-reconstructed magnetic resonance images, in: J.M. Fitzpatrick, J.M. Reinhardt (Eds.), Med. Imaging, International Society for Optics and Photonics, 2005: pp. 1136–1142. doi:10.1117/12.596008.

[280] J. Sijbers, D. Poot, A.J. den Dekker, W. Pintjens, Automatic estimation of the noise variance from the histogram of a magnetic resonance image., Phys. Med. Biol. 52 (2007) 1335–48. doi:10.1088/0031-9155/52/5/009.

[281] C.G. Koay, E. Özarslan, C. Pierpaoli, Probabilistic Identification and Estimation of Noise (PIESNO): A self-consistent approach and its applications in MRI, J. Magn. Reson. 199 (2009) 94–103.

[282] P.-L. Liu, A. Der Kiureghian, Multivariate distribution models with prescribed marginals and covariances, Probabilistic Eng. Mech. 1 (1986) 105–112.

[283] S.J. van Albada, P.A. Robinson, Transformation of arbitrary distributions to the normal distribution with application to EEG test–retest reliability, J. Neurosci. Methods. 161 (2007) 205–211.

[284] K.P. Whittall, A.L. MacKay, Quantitative interpretation of NMR relaxation data, J. Magn. Reson. 84 (1989) 134–152. doi:10.1016/0022-2364(89)90011-5.

[285] C.L. Lawson, R.J. Hanson, Solving Least Squares Problems, Prentice-Hall, Englewood Cliffs, NJ, 1974.

[286] J.P. Butler, J.A. Reeds, S. V. Dawson, Estimating solutions of first kind integral equations with nonnegative constraints and optimal smoothing, SIAM J. Numer. Anal. 18 (1981) 381–397. doi:10.1137/0718025.

[287] V.A. Morozov, Methods for Solving Incorrectly Posed Problems, Springer New York, New York, NY, 1984. doi:10.1007/978-1-4612-5280-1.

[288] E.J. Fordham, A. Sezginer, L.D. Hall, Imaging multiexponential relaxation in the (y, LogeT1) plane, with application to clay filtration in rock cores, J. Magn. Reson. Ser. A. 113 (1995) 139–150.

[289] M.E.E. Komlosh, E. Özarslan, M.J.J. Lizak, I. Horkayne-Szakaly, R.Z.Z. Freidlin, F. Horkay, et al., Mapping average axon diameters in porcine spinal cord white matter and rat corpus callosum using d-PFG MRI, Neuroimage. 78 (2013) 210–216. doi:10.1016/j.neuroimage.2013.03.074.

[290] P. Kozlowski, J. Liu, A.C. Yung, W. Tetzlaff, High-resolution myelin water measurements in rat spinal cord., Magn. Reson. Med. 59 (2008) 796–802. doi:10.1002/mrm.21527.

[291] S.O. Rice, Mathematical analysis of random noise, Bell Syst. Tech. J., Vol. 23, P. 282-332. 23 (1944) 282–332.

[292] J. Sijbers, A.J. den Dekker, Maximum likelihood estimation of signal amplitude and noise variance from MR data., Magn. Reson. Med. 51 (2004) 586–94. doi:10.1002/mrm.10728.

[293] R. Bai, A. Cloninger, W. Czaja, P.J. Basser, Efficient 2D MRI relaxometry using compressed sensing., J. Magn. Reson. 255 (2015) 88–99. doi:10.1016/j.jmr.2015.04.002.

[294] M.D. Does, J.C. Gore, Compartmental study of T 1 and T 2 in rat brain and trigeminal nerve In vivo, Magn. Reson. Med. 47 (2002) 274–283. doi:10.1002/mrm.10060.

[295] P. Galvosas, Y. Qiao, M. Schönhoff, P.T. Callaghan, On the use of 2D correlation and exchange NMR spectroscopy in organic porous materials., Magn. Reson. Imaging. 25 (2007) 497–500. doi:10.1016/j.mri.2006.11.009.

[296] A.E. English, K.P. Whittall, M.L.G. Joy, R.M. Henkelman, Quantitative two-dimensional time correlation relaxometry, Magn. Reson. Med. 22 (1991) 425–434. doi:10.1002/mrm.1910220250.

[297] G. Saab, R.T. Thompson, G.D. Marsh, P.A. Picot, G.R. Moran, Two-dimensional time correlation relaxometry of skeletal muscle In vivo at 3 tesla, Magn. Reson. Med. 46 (2001) 1093–1098.

[298] D. van Dusschoten, C.T.W. Moonen, P.A. de Jager, H. Van As, Unraveling diffusion constants in biological tissue by combining Carr-Purcell-Meiboom-Gill imaging and pulsed field gradient NMR, Magn. Reson. Med. 36 (1996) 907–913.

[299] J.G. Seland, M. Bruvold, H. Anthonsen, H. Brurok, W. Nordhøy, P. Jynge, et al., Determination of water compartments in rat myocardium using combined D-T1 and T1-T2 experiments., Magn. Reson. Imaging. 23 (2005) 353–354. doi:10.1016/j.mri.2004.11.062.

[300] J. Warner, S. Donell, K. Wright, L. Venturi, B. Hills, The characterisation of mammalian tissue with 2D relaxation methods., Magn. Reson. Imaging. 28 (2010) 971–981. doi:10.1016/j.mri.2010.03.015.

[301] L. Venturi, J. Warner, B. Hills, Multisliced ultrafast 2D relaxometry., Magn. Reson. Imaging. 28 (2010) 964–970. doi:10.1016/j.mri.2010.03.024.

[302] P.S. Belton, A.M. Gil, G.A. Webb, D. Rutledge, Magnetic Resonance in Food Science: Latest Developments, Royal Society of Chemistry, Bedford, UK, 2003.

[303] M.D. Hürlimann, L. Burcaw, Y.-Q. Song, Quantitative characterization of food products by two-dimensional D-T2 and T1-T2 distribution functions in a static gradient., J. Colloid Interface Sci. 297 (2006) 303–311. doi:10.1016/j.jcis.2005.10.047.

[304] A.R. Mutina, M.D. Hürlimann, Correlation of transverse and rotational dffusion coefficient: A probe of chemical composition in hydrocarbon oils, J. Phys. Chem. A. 112 (2008) 3291–3301. doi:10.1021/jp710254d.

[305] M.D. Hürlimann, M. Flaum, L. Venkataramanan, C. Flaum, R. Freedman, G.J. Hirasaki, Diffusion-relaxation distribution functions of sedimentary rocks in different saturation states, Magn. Reson. Imaging. 21 (2003) 305–310. doi:10.1016/S0730-725X(03)00159-0.

[306] R.D. Dortch, R.A. Horch, M.D. Does, Development, simulation, and validation of NMR relaxation-based exchange measurements., J. Chem. Phys. 131 (2009) 164502. doi:10.1063/1.3245866.

[307] L. Venturi, K. Wright, B. Hills, Ultrafast T1-T2 relaxometry using FLOP sequences., J. Magn. Reson. 205 (2010) 224–234. doi:10.1016/j.jmr.2010.05.003.

[308] B. Sun, K.-J. Dunn, A global inversion method for multi-dimensional NMR logging., J. Magn. Reson. 172 (2005) 152–160. doi:10.1016/j.jmr.2004.10.003.

[309] D. Bernin, D. Topgaard, NMR diffusion and relaxation correlation methods: New insights in heterogeneous materials, Curr. Opin. Colloid Interface Sci. 18 (2013) 166–172. doi:10.1016/j.cocis.2013.03.007.

[310] Y.-Q. Song, L. Venkataramanan, M.D. Hürlimann, M. Flaum, P. Frulla, C. Straley, T(1)--T(2) correlation spectra obtained using a fast two-dimensional Laplace inversion., J. Magn. Reson. 154 (2002) 261–268. doi:10.1006/jmre.2001.2474.

[311] L. Venkataramanan, Y. Song, M.D. Hürlimann, Solving Fredholm integrals of the first kind with tensor product structure in 2 and 2.5 dimensions, J. Magn. Reson. 50 (2002) 1017–1026.

[312] N. Marigheto, L. Venturi, D. Hibberd, K.M. Wright, G. Ferrante, B.P. Hills, Methods for peak assignment in low-resolution multidimensional NMR cross-correlation relaxometry., J. Magn. Reson. 187 (2007) 327–342. doi:10.1016/j.jmr.2007.04.016.

[313] E.W. Abel, T.P.J. Coston, K.G. Orrell, V. Sik, D. Stephenson, Two-dimensional NMR exchange spectroscopy . quantitative treatment of multisite exchanging systems, J. Magn. Reson. 70 (1986) 34–53.

[314] J. Mitchell, T.C. Chandrasekera, L.F. Gladden, Numerical estimation of relaxation and diffusion distributions in two dimensions., Prog. Nucl. Magn. Reson. Spectrosc. 62 (2012) 34–50. doi:10.1016/j.pnmrs.2011.07.002.

[315] E.J. Candes, M.B. Wakin, An introduction to compressive sampling, IEEE Signal Process. Mag. 25 (2008) 21–30. doi:10.1109/MSP.2007.914731.

[316] M. Doneva, P. Börnert, H. Eggers, C. Stehning, J. Sénégas, A. Mertins, Compressed sensing reconstruction for magnetic resonance parameter mapping., Magn. Reson. Med. 64 (2010) 1114–1120. doi:10.1002/mrm.22483.

[317] C. Huang, C.G. Graff, E.W. Clarkson, A. Bilgin, M.I. Altbach, T2 mapping from highly undersampled data by reconstruction of principal component coefficient maps using compressed sensing, Magn. Reson. Med. 67 (2012) 1355–1366. doi:10.1002/mrm.23128.

[318] M. Lustig, D. Donoho, J.M. Pauly, Sparse MRI: The application of compressed sensing for rapid MR imaging., Magn. Reson. Med. 58 (2007) 1182–1195. doi:10.1002/mrm.21391.

[319] M.I. Menzel, E.T. Tan, K. Khare, J.I. Sperl, K.F. King, X. Tao, et al., Accelerated diffusion spectrum imaging in the human brain using compressed sensing, Magn. Reson. Med. 66 (2011) 1226–1233. doi:10.1002/mrm.23064.

[320] C. Prieto, M.E. Andia, C. von Bary, D.C. Onthank, T. Schaeffter, R.M. Botnar, Accelerating three-dimensional molecular cardiovascular MR imaging using compressed sensing., J. Magn. Reson. Imaging. 36 (2012) 1363–1371. doi:10.1002/jmri.23763.

[321] E. Candès, J. Romberg, Sparsity and incoherence in compressive sampling, Inverse Probl. 23 (2007) 969–985. doi:10.1088/0266-5611/23/3/008.

[322] A. Cloninger, W. Czaja, R. Bai, P.J. Basser, Solving 2D Fredholm integral from incomplete measurements using compressive sensing, SIAM J. Imaging Sci. 7 (2014) 1775–1798. doi:10.1137/130932168.

[323] R.A. Horch, M.D. Does, Aqueous urea as a model system for bi-exponential relaxation, Magn. Reson. Mater. Physics, Biol. Med. 20 (2007) 51–56. doi:10.1007/s10334-006-0064-9.

[324] J.-F. Cai, E.J. Candès, Z. Shen, A singular value thresholding algorithm for matrix completion, SIAM J. Optim. 20 (2010) 1956–1982. doi:10.1137/080738970.

[325] A.R. Travis, M.D. Does, Selective excitation of myelin water using inversion-recovery-based preparations., Magn. Reson. Med. 54 (2005) 743–747. doi:10.1002/mrm.20606.

[326] S. Ma, D. Goldfarb, L. Chen, Fixed point and Bregman iterative methods for matrix rank minimization, Math. Program. 128 (2009) 321–353. doi:10.1007/s10107-009-0306-5.

[327] P.A. Bandettini, A. Jesmanowicz, E.C. Wong, J.S. Hyde, Processing strategies for time-course data sets in functional MRI of the human brain, Magn. Reson. Med. 30 (1993) 161–173. doi:10.1002/mrm.1910300204.

[328] D. Plenz, C. V Stewart, W. Shew, H. Yang, A. Klaus, T. Bellay, Multi-electrode array recordings of neuronal avalanches in organotypic cultures., J. Vis. Exp. (2011). doi:10.3791/2949.

[329] Y.-Q. Song, Categories of coherence pathways for the CPMG sequence, J. Magn. Reson. 157 (2002) 82–91. doi:10.1006/jmre.2002.2577.

[330] R.M. Henkelman, G.J. Stanisz, J.K. Kim, M.J. Bronskill, Anisotropy of NMR properties of tissues., Magn. Reson. Med. 32 (1994) 592–601. http://www.ncbi.nlm.nih.gov/pubmed/21669302.

[331] J. Watzlaw, S. Glöggler, B. Blümich, W. Mokwa, U. Schnakenberg, Stacked planar micro coils for single-sided NMR applications., J. Magn. Reson. 230 (2013) 176–85. doi:10.1016/j.jmr.2013.02.013.

[332] H.J. Koester, B. Sakmann, Calcium dynamics associated with action potentials in single nerve terminals of pyramidal cells in layer 2/3 of the young rat neocortex, J. Physiol. 529 (2000) 625–646. doi:10.1111/j.1469-7793.2000.00625.x.

[333] F. Helmchen, K. Imoto, B. Sakmann, Ca2+ buffering and action potential-evoked Ca2+ signaling in dendrites of pyramidal neurons., Biophys. J. 70 (1996) 1069–81. doi:10.1016/S0006-3495(96)79653-4.

[334] A. Kleinschmidt, H. Obrig, M. Requardt, K.D. Merboldt, U. Dirnagl, A. Villringer, et al., Simultaneous recording of cerebral blood oxygenation changes during human brain activation by magnetic resonance imaging and near-infrared spectroscopy., J. Cereb. Blood Flow Metab. 16 (1996) 817–26. doi:10.1097/00004647-199609000-00006.

[335] D.J. Mehagnoul-Schipper, B.F.W. van der Kallen, W.N.J.M. Colier, M.C. van der Sluijs, L.J.T.O. van Erning, H.O.M. Thijssen, et al., Simultaneous measurements of cerebral oxygenation changes during brain activation by near-infrared spectroscopy and functional magnetic resonance imaging in healthy young and elderly subjects., Hum. Brain Mapp. 16 (2002) 14–23.

[336] J. Perlo, F. Casanova, B. Blumich, 3D imaging with a single-sided sensor: an open tomograph, J. Magn. Reson. 166 (2004) 228–235. doi:10.1016/j.jmr.2003.10.018.

[337] A. Liberman, E. Bergman, Y. Sarda, U. Nevo, Faster imaging with a portable unilateral NMR device., J. Magn. Reson. 231 (2013) 72–78. doi:10.1016/j.jmr.2013.03.009.

[338] H.W. Fischer, P.A. Rinck, Y. van Haverbeke, R.N. Muller, Nuclear relaxation of human brain gray and white matter: Analysis of field dependence and implications for MRI, Magn. Reson. Med. 16 (1990) 317–334. doi:10.1002/mrm.1910160212.

[339] W.D. Rooney, G. Johnson, X. Li, E.R. Cohen, S.-G. Kim, K. Ugurbil, et al., Magnetic field and tissue dependencies of human brain longitudinal 1H2O relaxation in vivo, Magn. Reson. Med. 57 (2007) 308–318. doi:10.1002/mrm.21122.

[340] J.H. Duyn, P. van Gelderen, T.-Q. Li, J. a de Zwart, A.P. Koretsky, M. Fukunaga, High-field MRI of brain cortical substructure based on signal phase., Proc. Natl. Acad. Sci. U. S. A. 104 (2007) 11796–801. doi:10.1073/pnas.0610821104.

[341] N. Pyatigorskaya, D. Le Bihan, O. Reynaud, L. Ciobanu, Relationship between the diffusion time and the diffusion MRI signal observed at 17.2 tesla in the healthy rat brain cortex., Magn. Reson. Med. 00 (2013) 1–9. doi:10.1002/mrm.24921.

[342] T. Niendorf, D.G. Norris, D. Leibfritz, Detection of apparent restricted diffusion in healthy rat brain at short diffusion times., Magn. Reson. Med. 32 (1994) 672–7.

[343] R.D. Fields, D.H. Woo, P.J. Basser, Glial regulation of the neuronal connectome through local and long-distant communication, Neuron. 86 (2015) 374–386. doi:10.1016/j.neuron.2015.01.014.

[344] H. Hirase, L. Qian, P. Barthó, G. Buzsáki, Calcium dynamics of cortical astrocytic networks in vivo., PLoS Biol. 2 (2004) E96. doi:10.1371/journal.pbio.0020096.

[345] P.A. Bandettini, Seven topics in functional magnetic resonance imaging, J. Integr. Neurosci. 8 (2009) 371–403.

[346] J.M. Beggs, D. Plenz, Neuronal Avalanches in Neocortical Circuits, J. Neurosci. 23 (2003) 11167–77.

[347] W.L. Shew, H. Yang, S. Yu, R. Roy, D. Plenz, Information capacity and transmission are maximized in balanced cortical networks with neuronal avalanches., J. Neurosci. 31 (2011) 55–63. doi:10.1523/JNEUROSCI.4637-10.2011.

[348] E. Berdichevsky, N. Riveros, S. Sánchez-Armáss, F. Orrego, Kainate, N-methylaspartate and other excitatory amino acids increase calcium influx into rat brain cortex cells in vitro, Neurosci. Lett. 36 (1983) 75–80. doi:10.1016/0304-3940(83)90489-5.

[349] J.H. Robinson, S.A. Deadwyler, Kainic acid produces depolarization of CA3 pyramidal cells in the in vitro hippocampal slice, Brain Res. 221 (1981) 117–127. doi:10.1016/0006-8993(81)91067-2.

[350] U. Czubayko, D. Plenz, Fast synaptic transmission between striatal spiny projection neurons., Proc. Natl. Acad. Sci. U. S. A. 99 (2002) 15764–15769. doi:10.1073/pnas.242428599.

[351] R.D. Andrew, B. a MacVicar, Imaging cell volume changes and neuronal excitation in the hippocampal slice., Neuroscience. 62 (1994) 371–383. doi:0306-4522(94)90372-7 [pii].

[352] N. Zhou, G.R.J. Gordon, D. Feighan, B.A. MacVicar, Transient swelling, acidification, and mitochondrial depolarization occurs in neurons but not astrocytes during spreading depression, Cereb. Cortex. 20 (2010) 2614–2624. doi:10.1093/cercor/bhq018.

[353] D.W. Choi, Excitotoxic cell death, J. Neurobiol. 23 (1992) 1261–1276. doi:10.1002/neu.480230915.

[354] F.B. Meyer, Calcium, neuronal hyperexcitability and ischemic injury, Brain Res. Rev. 14 (1989) 227–243. doi:10.1016/0165-0173(89)90002-7.

[355] U. Dirnagl, C. Iadecola, M.A. Moskowitz, Pathobiology of ischaemic stroke: an integrated view, Trends Neurosci. 22 (1999) 391–397. doi:10.1016/S0166-2236(99)01401-0.

[356] E. Busch, M.L. Gyngell, M. Eis, M. Hoehn-Berlage, K.A. Hossmann, Potassium-induced cortical spreading depressions during focal cerebral ischemia in rats: contribution to lesion growth assessed by diffusion-weighted NMR and biochemical imaging., J. Cereb. Blood Flow Metab. 16 (1996) 1090–9. doi:10.1097/00004647-199611000-00002.

[357] L.L. Latour, K. Svoboda, P.P. Mitra, C.H. Sotak, Time-dependent diffusion of water in a biological model system., Proc. Natl. Acad. Sci. 91 (1994) 1229–1233. doi:10.1073/pnas.91.4.1229.

[358] R.M. Dijkhuizen, R.A. de Graaf, K.A. Tulleken, K. Nicolay, Changes in the diffusion of water and intracellular metabolites after excitotoxic injury and global ischemia in neonatal rat brain., J. Cereb. Blood Flow Metab. 19 (1999) 341–9. doi:10.1097/00004647-199903000-00012.

[359] D.W. Choi, Calcium-mediated neurotoxicity: relationship to specific channel types and role in ischemic damage, Trends Neurosci. 11 (1988) 465–469. doi:10.1016/0166-2236(88)90200-7.

[360] J. Katsaras, T.A. Harroun, J. Pencer, M.-P. Nieh, "Bicellar" lipid mixtures as used in biochemical and biophysical studies., Naturwissenschaften. 92 (2005) 355–66. doi:10.1007/s00114-005-0641-1.

[361] N. Carbon, C. Temp, S.P. The, D. Dipalmitoyl, A. Catalog, Liposome Preparation, 0 (n.d.).

[362] P.S. Vol, LIPOSOMES PREPARATION METHODS, 19 (1996) 65–77.

[363] A. Baszkin, W. Norde, Physical Chemistry of Biological Interfaces, CRC Press, 1999.